Inaugural-Dissertation

zur

Erlangung der Doktorwürde

der

Naturwissenschaftlich-Mathematischen Gesamtfakultät

der

Ruprecht-Karls-Universität

Heidelberg

vorgelegt von

Pavel Hron

aus Příbram, Tschechische Republik

Tag der mündlichen Prüfung

21.7 2015

Numerical Simulation of Multi-Phase Multi-Component Reactive Flow in Porous Media

Gutachter: Prof. Dr. Peter Bastian

Acknowledgments

I would like to gratefully acknowledge the financial support which enabled the research presented in this thesis. Funding was received from the German Research Foundation (DFG) through the Research Group FOR 831 “Dynamic Capillary Fringes: A Multidisciplinary Approach (DyCap)” (Project Ba 1498/7-2). I would like to thank the Faculty of Mathematics and Computer Sciences, the Heidelberg Graduate School for Mathematical and Computational Modeling (HGS) and the Interdisciplinary Center for Scientific Computing (IWR) at the Heidelberg University for providing me an excellent infrastructure.

I would like to use this opportunity to express my gratitude to all the people who supported me and helped me while I was working on this thesis. First of all my gratitude goes to my main supervisor Peter Bastian and my mentor Olaf Ippisch, for giving me the opportunity to work on this interesting interdisciplinary project. They helped me with many productive discussions, suggestions and valuable comments concerning this work and they always took the time to sit down and discuss, even if they actually had no time at all. Without their deep knowledge and valuable suggestions this thesis would not have been possible. I am also very glad for the interdisciplinary work in the DyCap project and I would like to thank all the involved co-workers, particularly to Daniel Jost, Christina Haberer and Samuel Kumahor for their valuable experimental data and great collaboration. For all the nice discussions, a great time together, excellent atmosphere, shared coffee, trips to the shop and all their help I am grateful to Steffen Müthing, Rebecca de Cuveland, Adrian Ngo, Felix Heimann, Jurgis Pods, Ole Klein, Dominic Kempf, Marian Piatkowski and all the other members of the AG Wissenschaftliches Rechnen. This work would not have been possible without the software library DUNE thus my thank goes to all developers, particularly to the developers of module PDELab.

Moreover, my gratitude goes to my proof readers, especially to Steffen, Johannes, Robert, Lydia and Megan who read everything again and again. I would like to thank all my flatmates Elena, Timo, Niko, Stefan and Franziska for fruitful discussions about anything and everything, many cooking evenings and a never-ending barbecue season. I would like to thank my parents for their continued and never wavering support throughout my long studies. Most of all, I want to thank my girlfriend Eliška for her patience and support during the last seven years.

Abstract

In this thesis we develop a multi-component multi-phase reactive transport simulator to facilitate the investigation of a large variety of phenomena in porous media including component transport, diffusion, microbiological growth and decay, cell attachment and detachment and phase exchange. The coupled problem is solved using operator splitting approach. This approach enables us to use higher-order schemes and reduce numerical diffusion, which can result in an overestimation of phase exchange and reaction processes. Furthermore, this approach allows a flexible adaptation of the solution strategy to the concrete problem. We conduct an in-depth comparison of the fully-coupled and splitting approaches in order to derive criteria for the most efficient scheme depending on the relative importance of advection, diffusion and reaction.

We discuss theoretical, numerical and implementation-related aspects and examine applications of our model to simulate laboratory experiments in an unsaturated porous medium. To obtain transport parameters and reaction rates from the experiments, we incorporate parameter estimation into our model framework. The comparison of simulation results and experimental data on flow and transport processes, chemical reactions and microbial activity is used to detect deficiencies of the model and to receive suggestions for its improvement. Although the model parameters are estimated using data from batch experiments with aqueous solutions, the numerical model is able to describe and predict the laboratory experiments with porous media reasonably well without additional calibration.

Zusammenfassung

In dieser Dissertation entwickeln wir einen reaktiven Mehrkomponenten-Mehrphasenströmungs-Simulator, der die makroskopische Simulation von verschiedenen Prozessen in porösen Medien erleichtert. Unter anderem erlaubt er die Beschreibung von Komponententransport, Diffusion, mikrobiellem Wachstum und Zerfall, Adhäsion der Zellen und Phasenwechsel. Wir lösen das globale Problem mit einem Operator-Splitting-Ansatz. Dieser Ansatz erlaubt es uns numerische Schemata höherer Ordnung zu implementieren und so die numerische Diffusion zu verringern, welche zur Überschätzung von Phasenwechseln und Reaktionen führen kann. Des Weiteren ermöglicht uns dieser Ansatz eine flexible Anpassung der Lösungstrategien an das konkrete Problem. Wir vergleichen die verschiedenen Operator-Splitting-Ansätze eingehend mit dem global impliziten Ansatz um Kriterien zur Auswahl des effizientesten Verfahrens in Abhängigkeit der Bedeutung von Advektion, Diffusion und Reaktion zu finden.

Wir diskutieren theoretische und numerische Aspekte und untersuchen Anwendungen unseres Modells, um Laborexperimente in einem ungesättigten porösen Medium zu simulieren. Um Transportparameter und Reaktionsraten aus den Experimenten zu schätzen, verwenden wir Methoden der Parameterschätzung. Der Vergleich von gemessenen und simulierten Daten des Phasenflusses, des Komponententransports, der chemischen Reaktionen und mikrobieller Aktivität gibt Aufschluss über Defizite des Modells und liefert Hinweise für Verbesserungen. Obwohl die Modellparameter mit Hilfe von Daten aus Batchexperimenten in wässrigen Lösungen geschätzt wurden, beschreibt und prognostiziert das numerische Modell Laborexperimente mit porösen Medien - ohne zusätzliche Kalibrierung - verhältnismäßig gut.

Table of Contents

List of Acronyms

Notation	Description	Page
ADRE	advection-diffusion-reaction equation	22
AE	algebraic equation	19
BTC	breakthrough curve	92
CCFV	cell-centered finite volume method	29
CFL	Courant-Friedrichs-Lewy	38
CFT	colloid filtration theory	92
CF	capillary fringe	98
DG	discontinuous Galerkin method	46
DOC	dissolved oxygen carbon	107
DOF	degree of freedom	37
DSA	direct substitution approach	21
FI	fluorescence intensity	119
FTC	flow-through cell	98
GIA	global implicit approach	21
LB	lysogeny broth medium	107
LMA	Levenberg-Marquard algorithm	46
MSO	multi-step outflow experiment	92
NP	panoparticle	91
ODE	ordinary differential equation	19
OD	optical density	107
OS	operator splitting	22
PDE	partiall differential equation	19
REV	representative elementary volume	6
RKF45	Runge-Kutta-Fehlbert 4(5) method	39
RK	Runge-Kutta method	29
RK-IMEX	Runge-Kutta implicit-explicit method	29
SIA	sequential iterative approach	23
SNIA	sequential non-iterative approach	22
TVD	total variation diminishing	35

List of Symbols

Notation	Description	SI Units	Page
Greek letters			
α	van Genuchten parameter	$[\mathrm{kg}^{-1}\,\mathrm{m}\,\mathrm{s}^2]$	9
β	shape factor for retention of nanoparticles along the flow path	$[-]$	93
β_e	mass transfer coefficient	$[\mathrm{m}\,\mathrm{s}^{-1}]$	115
γ	face in the spatial discretization	$[-]$	30
θ	parameter in the minmod limiter	$[-]$	35
θ_α	volumetric fraction of phase α	$[-]$	8
κ	fraction of the air bubble surface area exposed to mobile water	$[-]$	116
λ_{bc}	Brooks and Corey pore size distribution index	$[-]$	9
λ_r	reaction rate	$[\mathrm{s}^{-1}]$	55
μ_α	dynamic viscosity of the fluid	$[\mathrm{kg}\,\mathrm{m}^{-1}\,\mathrm{s}^{-1}]$	8
μ_a	specific aerobic growth rate	$[\mathrm{s}^{-1}]$	109
μ_{an}	specific anaerobic growth rate	$[\mathrm{s}^{-1}]$	109
$\mu_{max,a}$	aerobic maximum growth rate	$[\mathrm{s}^{-1}]$	109
$\mu_{max,an}$	anaerobic maximum growth rate	$[\mathrm{s}^{-1}]$	108
ν	CFL number	$[-]$	40
ν_α	mole density of phase α	$[\mathrm{kg}\,\mathrm{m}^{-3}]$	11
ν_l	CFL-like number	$[-]$	40
ρ_α	mass density of phase α	$[\mathrm{kg}\,\mathrm{m}^{-3}]$	8
ρ_b	bulk density	$[\mathrm{kg}\,\mathrm{m}^{-3}]$	93
τ	splitting time step	$[\mathrm{s}]$	22
ϕ	porosity of porous medium	$[-]$	7
Ω	domain in $\mathbb{R}^d$	$[-]$	13
Latin letters			
$a_{\alpha,\kappa}$	interaction between liquid and solid phase	$[\mathrm{kg}\,\mathrm{m}^{-3}\,\mathrm{s}^{-1}]$	18
a_{gw}	specific effective interface	$[\mathrm{m}^{-1}]$	115
B_{si}	Contois saturation constant for substrate s_i	$[-]$	108
$C_{\alpha,\kappa}$	concentration of component κ in phase α	$[\mathrm{kg}\,\mathrm{m}^{-3}]$	10
$C^m_{\alpha,\kappa}$	molar concentration of κ in phase α	$[\mathrm{mol}\,\mathrm{m}^{-3}]$	10
C_{np}	concentration of nanoparticles	$[\mathrm{kg}\,\mathrm{m}^{-3}]$	93
Da	transport Damköhler number	$[-]$	56
Da_a	advection Damköhler number	$[-]$	56
Da_d	diffusion Damköhler number	$[-]$	56
$D_{\alpha,\kappa}$	diffusion coeffiecient	$[\mathrm{m}^2\,\mathrm{s}^{-1}]$	12

Notation	Description	SI Units	Page
$e_{\alpha,\kappa}$	phase exchange term	$[\mathrm{kg\,m^{-3}\,s^{-1}}]$	18
E	element in the spatial discretization	$[-]$	29
E_{rr}	difference between the exact and the operator splitting or numerical solution respectively	$[-]$	55
g	gravitational acceleration	$[\mathrm{m\,s^{-2}}]$	8
h	mesh size	$[\mathrm{m}]$	29
$j_{\alpha,\kappa}$	diffusive flux	$[\mathrm{kg\,m^{-2}\,s}]$	12
k_{att}	attachment rate	$[\mathrm{s^{-1}}]$	93
k_{det}	detachment rate	$[\mathrm{s^{-1}}]$	93
k_H	Henry's law constant	$[\mathrm{mol\,m^{-3}\,Pa^{-1}}]$	12
k_H^{cc}	dimensionless Henry's law constant	$[-]$	12
$k_{r\alpha}$	relative permeability function	$[-]$	8
K	absolute soil permeability	$[\mathrm{m^2}]$	8
K_α	effective permeability	$[\mathrm{m^2}]$	8
$\mathcal{K}_\alpha$	set of components in phase α	$[-]$	10
K_{si}	half-saturation constant for substrate s_i	$[\mathrm{kg\,m^{-3}}]$	108
l	characteristic length	$[\mathrm{m}]$	55
L	domain length	$[\mathrm{m}]$	76
L_1^r	normalized error in the L_1-norm	$[-]$	55
m	van Genuchten parameter	$[-]$	9
m_α	mass of phase α	$[\mathrm{kg}]$	11
$m_{\alpha,\kappa}$	mass of component κ in phase α	$[\mathrm{kg}]$	10
m_o	maintenance rate for oxygen	$[\mathrm{m^3\,s^{-1}\,kg^{-1}}]$	110
M	total mass of the exact solution	$[-]$	53
M_{err}	total mass error in the operator splitting solution	$[-]$	53
M_α	average molar mass of phase α	$[\mathrm{kg\,mol^{-1}}]$	11
M_κ	molar mass of component κ	$[\mathrm{kg\,mol^{-1}}]$	11
n	outward unit normal	$[\mathrm{m}]$	31
$\hat{n}$	van Genuchten parameter	$[-]$	9
N_α	number of moles in phase α	$[\mathrm{mol}]$	11
$N_{\alpha,\kappa}$	number of moles of κ in phase α	$[\mathrm{mol}]$	10
N_h	number of cells in mesh triangulation	$[-]$	29
p_α	macroscopic fluid pressure	$[\mathrm{kg\,m^{-1}\,s^{-2}}]$	8
p_c	capillary pressure	$[\mathrm{kg\,m^{-1}\,s^{-2}}]$	9
p_d	mean sand particle diameter	$[\mathrm{m}]$	93
p_e	entry pressure	$[\mathrm{kg\,m^{-1}\,s^{-2}}]$	9
$\mathcal{P}$	set of all phases in porous medium	$[-]$	7
Pe	Péclet number	$[-]$	55
$\mathrm{Pe_g}$	grid Péclet number	$[-]$	41
$\mathcal{P}_f$	set of fluid phases (liquid and gas)	$[-]$	7
r_d	decay rate	$[\mathrm{s^{-1}}]$	109
$r_{\alpha,\kappa}$	reaction term for component κ in phase α	$[\mathrm{kg\,m^{-3}\,s^{-1}}]$	18
R	retardation in reactive transport	$[-]$	33

Notation	**Description**	SI Units	**Page**
$\mathcal{R}$	objective function (residuum)	[−]	45
$\mathcal{R}^2$	coefficient of determination	[−]	45
s_α	saturation of phase α	[−]	8
$s_{e,\alpha}$	effective saturation of phase α	[−]	8
$s_{r,\alpha}$	residual saturation of phase α	[−]	8
S_{np}	concentration of attached nanoparticles	[−]	93
t	time	[s]	7
$\mathcal{T}_h$	mesh triangulation	[−]	29
v	transport velocity	$[\mathrm{m\,s^{-1}}]$	33
v_α	phase transport velocity	$[\mathrm{m\,s^{-1}}]$	8
V_α	volume of phase α in REV	$[\mathrm{m^3}]$	7
V_{ps}	volume of pore space in REV	$[\mathrm{m^3}]$	7
V_R	volume of the REV	$[\mathrm{m^3}]$	7
x	position vector in $\mathbb{R}^d$	$[\mathrm{m}]^\mathrm{d}$	7
$Y_{S,\cdot}$	yield coefficient for substrate S	[−]	114
Subscripts			
α	phase		7
κ	component		10
g	gas phase		7
l	liquid phase		7
s	solid phase		7

List of Figures

List of Tables

Chapter 1

Introduction

In the past decades, understanding and prediction of multi-phase multi-component reactive flow and transport in the subsurface has received increasing attention by the scientific community due to the widespread increase of awareness of alarming contemporary problems such as water contamination by organic solvents, contaminants and waste disposal (Xu et al., 1999a). Additionally, the steady increase in available computing power allows for the development of more complex, reliable, and accurate mathematical models capable of simulating such complicated problems.

1.1 Motivation

The simultaneous flow of multi-component immiscible fluids in porous media occurs in a wide variety of applications. Over the past decades, the most concentrated research in the field of multi-phase flows has focused on flows in underground petroleum reservoirs (Aziz et al., 1979; Chavent and Jaffré, 1986; Peaceman, 1977), capturing and storing of carbon dioxide (Bielinsky, 2006; Lauser, 2014) and on saturated and unsaturated groundwater flows in general (Bastian et al., 2005). Most recently, multi-phase multi-component flows have generated serious interest among engineers concerned with deep geological repository for radioactive waste (Bourgeat et al., 2009).

Reactive transport modeling is also an essential tool for the understanding of microbial growth and transport in the subsurface (Steefel et al., 2005). The transport of bio-chemically reacting contaminants in unsaturated and saturated porous media is a very active field of research, including the research in this thesis. Microbial activity is of significant interest in various environmental applications such as *in situ* bioremediation (Lee et al., 2009), biodegradation of pollutants (Bauer et al., 2008), dispersal of pathogenic microorganisms (Unc and Goss, 2004), protection of drinking water supplies, and for subsurface geochemistry in general.

The design of bioremediation schemes requires an understanding of the processes governing the growth, fate, attachment to solid surfaces and transport of the microbes under the particular physical, biological, and geochemical conditions involved (Ginn et al., 2002). The ongoing processes can be influenced e.g. by the properties of the porous medium and the microbial species as well as the composition of pore water and gas (Amy and Halderman, 1997; Or et al., 2007).

Bacterial growth in soil usually depends on bio-available water content (Chang and Halverson, 2003; Skopp et al., 1990), temperature (Bell et al., 2008; Trevors, 1991) and other physical or environmental parameters like pressure, pH (Fernández-Calviño et al., 2011) or bio-geochemical

redox processes (Borch et al., 2010). In addition to water saturation, the most important factors controlling bacterial growth are the availability of substrate or nutrients (Reischke et al., 2013) and the availability of electron acceptors, like oxygen for aerobic or facultative anaerobic bacteria (Sierra and Renault, 1995).

While there are many factors influencing the behavior of microbial growth and transport in porous media, an in-depth description of all processes is an exacting task. To investigate and quantify the most relevant processes, researchers often conduct various laboratory experiments (Fig. 1.1), e.g. in flow-through chambers filled with sand (Jost et al., 2010, 2011, 2014b). The goal of said laboratory experiments is to gain insight into the simplified system, to better understand the pertinent processes and to try to find suitable mathematical models for the full problem.

Mathematical modeling is a crucial tool for the study of nutrient fluxes in soils, the assessment of bioremediation and intrinsic biodegradation in the subsurface and the planning of related experiments. The parameters for microbial growth and transport are typically determined by means of independent laboratory experiments fitting the model parameters to experimental data. After model calibration, the obtained parameters are often used to predict the retention and transport of microorganisms under natural conditions using appropriate numerical models (Clement and Peyton, 1997; Schäfer et al., 1998b,c). The lack of agreement between theoretical mathematical models and experimental measurements often leads to important advances as better theories are developed. An example of a comparison between microbial concentration measured in the laboratory experiment and numerical simulation is shown in Fig. 1.2.

The importance of mathematical modeling lies in the fact that a model may help to explain a system and to study the effects of different system components, and to make predictions about behavior. It is often difficult to measure all quantities in the whole laboratory setup during execution of the experiment and modeling helps to get this type of information.

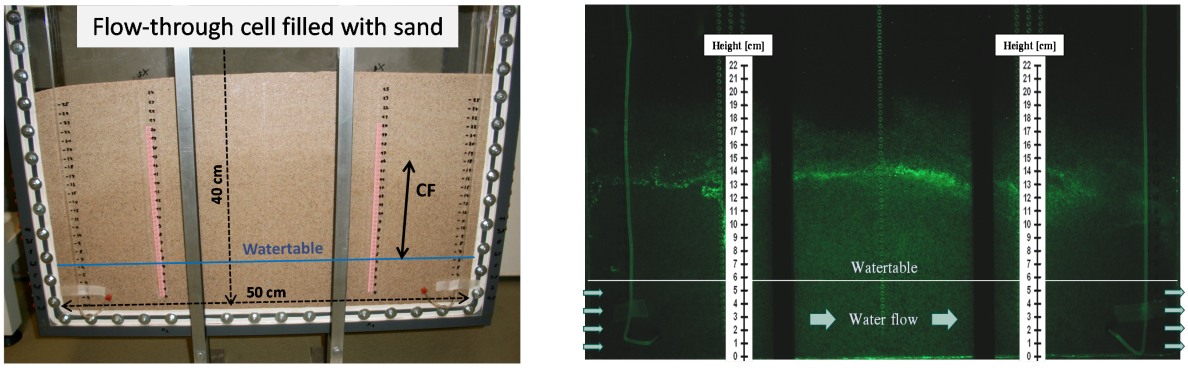

Fig. 1.1: Flow-through chamber filled with sand with saturated and unsaturated regions (left) and bacteria in this cell producing green fluorescent protein (right), pictures by D. Jost.

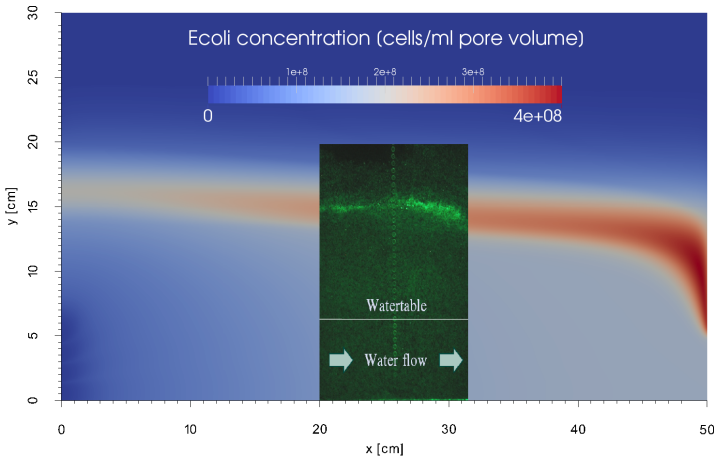

Fig. 1.2: Comparison of numerical simulation and data from laboratory experiments. Growth and transport of microorganisms in saturated and unsaturated porous medium.

1.2 Research Results

The primary purpose of this dissertation thesis is to develop a numerical simulator for multi-phase multi-component reactive flow using modern mathematical methods with application to the processes in highly dynamic regions of saturated and unsaturated porous medium.

When modeling the controlling processes in reactive transport, it is common practice to combine a non-reactive transport model with a suitable reaction model to obtain a reactive transport capability. Current numerical simulators are very well developed either in the flow part or in the reaction part of the solution algorithm. However, the compatibility of the conceptual models developed for conservative transport on the one hand, with models developed for bio-chemical reactions on the other, has only been partially understood for the most part.

The solution approach of the presented multi-phase multi-component reactive flow model is based on an operator splitting technique and leads to the two types of problems described above: phase and component transport and bio-chemical reactions. Moreover, the derivation of the mathematical model reveals the sources of the operator splitting error. We answer the question under which circumstances we can use this type of coupling/decoupling and investigate the applicability of operator splitting schemes to prototypical problem classes. Furthermore, the accuracy of numerical methods in the context of reactive transport has been explored little in the literature. For this reason, we discuss the accuracy of various numerical methods applied to reactive transport problems.

Reactive interactions of compounds are limited by mutual mixing of the compounds. Numerical diffusion introduced by the scheme for advective transport may lead to an overestimation of the related reaction rates. Therefore, we use higher-order schemes to reduce the numerical diffusion. We determine the error which occurs in the numerical discretization and compare it to the error arising in the operator splitting. One of the most important findings is the fact that the operator splitting error for almost all kinds of kinetically controlled reactions in advection-dominated regime is much lower than the discretization error.

After validating the implementation of the described numerical methods, we apply our model to both the forward and the inverse reactive transport modeling of setups given by laboratory experiments and measured data. Inverse models involve fitting various dynamic quantities (e.g. reaction rates) to data like solute or nanoparticle concentrations distributed in space and/or in time. We develop sub-models which are able to sufficiently describe the measured data, e.g. the breakthrough curves in flow-through experiments or the microbial growth in batch cultures. This data is used to calibrate and validate the sub-models in advance of predictive modeling. We also determine and analyze the most important processes in modeling microbial growth and transport in the saturated and the unsaturated zone of porous media and apply the numerical simulator to forecast future events. We simulate laboratory experiments in a flow-through cell, including several models of the phase and component transport, microbial growth, adhesion and phase exchange.

In summary, the major contributions of this work are:

- development of a new model for multi-phase multi-component reactive flow in porous media;
- implementation of this model using various numerical methods in the DUNE framework;
- quantification of errors arising in the operator splitting approach and errors in the numerical discretization;
- provide a guideline in which situations to use a concrete solution strategy in reactive transport problems;
- application of the developed numerical simulator to model laboratory experiments;
- parameter estimation for microbial growth, adhesion and transport of nanoparticles;
- forecasting of microbial growth and transport of microorganisms in highly dynamic zones in porous media, particularly in the capillary fringe.

1.3 Outline

The structure of this thesis is as follows. In Chapter 2 we describe the multi-phase multi-component reactive model in porous media and the basic terminology. In principle, this model is composed of a set of partial differential equations that describe the flow of the participating components in all phases and of a set of algebraic equations. There are many approaches for solving this underlying problem, which we discuss in Chapter 3. We introduce the operator splitting technique at various levels to solve the global model problem.

The numerical solution described in Chapter 4 of the transport sub-problems employs a space discretization on a structured grid using a cell-centered finite volume method and a fully implicit time discretization for the two-phase problem to achieve unconditional stability. To solve the solute transport in advection dominated cases, we use a second order Godunov reconstruction of upwind fluxes together with explicit schemes. The system equations describing chemical reactions are solved element wise.

Operator splitting significantly simplifies the numerical solution process. Unfortunately, the separate treatment of the various sub-processes creates a splitting error. The magnitude of this error must be controlled to prevent an unstable solution process, e.g. by creating negative concentrations. In Chapter 5 we examine this error for the first- and second-order non-iterative splitting method applied to advection-diffusion-reaction problems. The splitting error is studied with respect to characteristic time scales represented by dimensionless Damköhler and Péclet numbers.

In Chapter 6 we investigate the performance of the various discretization schemes described in Chapter 4, which we apply to problems like the ones introduced in Chapter 5 and quantify the size of both the discretization error and the operator splitting error. We also extract guidelines for optimal discretization choices depending on various transport and reaction conditions.

The first application of the developed numerical simulator to laboratory experiments is described in Chapter 7. We investigate the transport of nanoparticles in unsaturated porous media and oxygen transport in a flow-through cell. Furthermore, we study the influence of numerical diffusion in a two-dimensional transport example with non-trivial velocity field.

In the final chapter, we develop a model for aerobic and anaerobic growth of microorganisms based on experiments without porous media in batch cultures. We use inverse modeling to estimate a unique set of parameters which is able to approximately describe all batch experiments under various conditions. This growth model is combined with a transport model, a phase exchange model and an adhesion model, and applied to simulate laboratory experiments in a flow-through cell under steady-state and transient conditions.

Chapter 2

Model Development

In this chapter we provide an introduction to the mathematical modeling of multi-phase multi-component reactive flow in a porous medium. We introduce the fundamental mathematical relationships that are used to describe the relevant processes in saturated and unsaturated porous media together with the essential terminology.

We present a general conceptual model based on a *representative elementary volume* (REV) approach (Bear, 1972; Lichtner et al., 1996) which serves as a basis for the formulation of reactive transport models. Within this approach, the actual discrete physical system, consisting of porous media with aggregates of mineral grains, fractures, and interstitial pore space filled with fluids, is replaced by a continuous system in which physical variables describing the system vary continuously in space. We provide governing equations for multi-phase multi-component reactive flow on the REV scale based on mass balance and discuss limitations and simplifications of the mathematical model.

2.1 Continuum Approach

In the modeling of reactive flow in saturated and unsaturated porous media, it is important to consider different length scales ranging from the macroscale through to the microscale and to the molecular nanoscale.

Since many of the physical, chemical, and biological processes actually take place at the pore scale, developing averaging approaches for these coupled processes at larger scales is essential (Steefel et al., 2005). In the continuum representation of a porous medium, the physical variables describing the system, which are discontinuous at the microscale or pore scale, are replaced by functions which are continuous at the macroscale. This is not to say that microscale properties are not important. In fact, the macroscale properties are defined by the microscale properties averaged over a REV. The REV is assigned to each point of the macroscale continuum (Bear, 1972). The REV volume is sufficiently large to statistically estimate all relevant parameters of the void space configuration and small enough to be considered a negligible portion of the total volume from the macroscopic scale. The dimensions of a REV are usually large compared to the grain size, but small compared to the characteristic length scale over which the quantities of interest change. If such a REV cannot be found, then the represented macroscopic theory of flow in porous media cannot be applied.

This description is not valid at the pore scale where the Navier-Stokes equations derived from fluid mechanics are required and where it is necessary to capture microscopic scale gradients in concentration resulting from transport and a non-uniform distribution of reactive material.

Basic assumptions invoked in the REV formulation are:

- liquid, gaseous, and solid phases all occupy the same physical space of control volume at the same time;
- the coexistence of any number of species within each phase is permitted;
- reactions involving two separate phases which interact across a common interface are treated as homogeneous reactions uniformly distributed throughout the REV;
- the fluid and solid phases are well-mixed and therefore without concentration gradients, thus resulting in uniform reaction rates within the control volume.

Another approach for the passage from the microscopic level to the macroscopic one is known as *mathematical homogenization* (Bear and Cheng, 2010). This technique is based on the mathematical theory of asymptotic functional expansions (Hornung, 1997) and is generally acknowledged to be more appropriate for handling multiple scale heterogeneity. The REV approach uses smoothing and spatial averaging formulas, whereas the homogenization does the upscaling by letting the microscale tend to zero. We use the REV approach, because it is generally convenient for the description of large-scale problems where some effects stemming from the micro-structure of the material like fracturing or granular flow are not important.

2.2 Multi-Phase Multi-Component Flow

In this section we study the basics of multi-phase multi-component flow in a porous medium, but the respective qualities can be generalized for a multi-phase flow formulation as well. We provide here the fundamental definitions and explanations presented in Bear (1972) and Bear and Cheng (2010). The model is based on the assumptions discussed below.

The porous medium consists of three phases $\mathcal{P} = \{s, l, g\}$: a rigid solid phase s, an incompressible liquid phase l and a compressible gas phase g (as in Allen (1985)). We denote the fluid phases by $\mathcal{P}_f = \{l, g\}$.

2.2.1 Porosity and Phase Content

The total volume of REV centered at x, V_R, can be divided into a volume of pore space in REV, V_{ps}, and a volume of the fluid phase α, V_α.

Porosity ϕ is a macroscopic quantity that describes the ratio of void space within a volume of a porous material to the total volume

$$\phi(x,t) = \frac{V_{ps}(x,t)}{V_R(x,t)}$$

In the unsaturated zone, the void space is partly filled by air and partly by water. To describe the relative quantity of water at a certain time in the vicinity of a point in a porous medium

domain, (i.e., in an REV for which this point is a centroid) we define the saturation of the fluid phase α as

$$s_\alpha(x,t) = \frac{V_\alpha(x,t)}{V_{ps}(x,t)}, \quad \alpha \in \mathcal{P}_f,$$

and the volumetric fraction of phase α as

$$\begin{aligned}\theta_\alpha(x,t) &= s_\alpha(x,t)\phi(x,t), \quad \alpha \in \mathcal{P}_f,\\ \theta_s(x,t) &= 1-\phi.\end{aligned}$$

From their definitions, the volume fractions and saturations clearly must fulfill the constraints

$$\theta_l + \theta_g + \theta_s = 1, \qquad s_l + s_g = 1.$$

Residual and Effective Saturation

It is well known that a pre-existing fluid phase cannot be displaced entirely from a porous medium creating what is called a *residual saturation* $s_{r,l}$, which denotes the minimal water saturation that remains in the void space after a drainage process in the form of pendular rings around the grain contact points and relatively immobile thin films. Additionally, a residual saturation $s_{r,g}$ can also be defined for the gas phase when the air is present in the form of isolated bubbles. If the phase saturation falls below the residual saturation $s_{r,\alpha}$, the phase α is immobile. The effective saturation $s_{e,\alpha}$ describes only the volumetric portions of the fluid phase that can be displaced mechanically and is given by

$$s_{e,\alpha} = \frac{s_\alpha - s_{r,\alpha}}{1 - s_{r,l} - s_{r,g}}.$$

2.2.2 Extended Darcy Law

The liquids in porous medium flow in negative direction of the pressure gradient and the macroscopic phase velocities in an *isotropic* porous medium are related to the phase pressures p_α via the extended Darcy law

$$v_\alpha = -\frac{1}{\mu_\alpha} K_\alpha \left(\nabla p_\alpha - \rho_\alpha g\right), \tag{2.1}$$

where K_α is the effective permeability, μ_α is the dynamic viscosity of the fluid, ρ_α is the mass phase density and g is the gravitational acceleration vector. The effective permeability can be expressed as

$$K_\alpha = k_{r\alpha} K,$$

where $k_{r\alpha}$ is the non-linear relative permeability function depending on the phase saturation (see Section 2.2.4) and K is the scalar absolute permeability at full water saturation ($s_l = 1$). The absolute permeability is a property of the porous medium alone and not of the fluid. In the case of an *anisotropic* porous medium, the absolute permeability depends on the direction of flow and is represented as tensor (Bear, 1972; Helmig, 1997).

The Darcy law is valid only for slow flows of Newtonian fluids through porous medium, when the flow is *laminar*. In this thesis we assume that (2.1) holds in all considered cases.

2.2.3 Macroscopic Capillary Pressure

In order to describe the macroscopic effect of the microscale capillary forces and to close the equation set for multi-phase flow models, we introduce the *macroscopic capillary pressure* p_c as the difference between the macroscale liquid phase pressure p_l and the gas phase pressure p_g by

$$p_c = p_g - p_l. \tag{2.2}$$

The dependence of the capillary pressure on the saturation s_l is obtained by measuring the phase pressures difference during slow drainage or imbibition laboratory experiments.

We use the following two static capillary pressure-saturation models. Brooks and Corey (1964) proposed a mathematical model for the p_c/s_l relation in the form

$$s_{e,l}(p_c) = \left(\frac{p_c}{p_e}\right)^{\lambda_{bc}} \qquad \text{for } p_c \geq p_e, \tag{2.3}$$

where the parameter λ_{bc} describes the pore distribution of the grains in a porous material and p_e is the entry pressure, which is the minimum value of p_c on a drainage capillary pressure curve at which a continuous air phase exists in the void space.

Another model, proposed by Genuchten (1980), treats the capillary pressure-saturation relationship as

$$s_{e,l}(p_c) = \left[1 + (\alpha p_c)^{\hat{n}}\right]^{m} \qquad \text{for } p_c \geq 0. \tag{2.4}$$

The parameter m is often chosen as $m = \frac{\hat{n}-1}{\hat{n}}$ and therefore only two free parameters $\hat{n}$ and α remain to be fitted. These parameters characterize the pore structure of the porous medium.

These models are used in the modeling of multi-phase flow independently of the flow conditions as long as the hysteretic effects can be neglected. The capillary pressure-saturation relationship holds only under static conditions, i.e., in the state of thermodynamic equilibrium of the system. When the system is not in equilibrium, the dynamic effects on capillary pressure-saturation relationship should be taken into account, see (Fučík et al., 2010; Hassanizadeh et al., 2002). However, the relevant experimental data describing the dynamic effects is not easy to measure. In our applications, the dynamic effects are neglected, but the model can be extended easily.

2.2.4 Relative Permeability

The relative permeability is a convenient and commonly used concept for multi-phase flows in porous medium. It describes the fact that the flow paths of a fluid are hindered by the presence of other phases. A number of models have been developed to predict the relationship between saturation and relative permeability based upon the capillary pressure-saturation information, see Bear and Cheng (2010). We state the two most common approaches defining the relative permeability $k_{r\alpha}$.

The *Burdine* mathematical model for the relative permeability $k_{r\alpha}$ of the phase α has the form

$$k_{rl}\left(s_l\right) = s_{e,l}{}^{\frac{2+3\lambda_{bc}}{\lambda_{bc}}}, \tag{2.5a}$$

$$k_{rg}\left(s_l\right) = \left(1 - s_{e,l}\right)^2 \left(1 - s_{e,l}{}^{\frac{2+\lambda_{bc}}{\lambda_{bc}}}\right), \tag{2.5b}$$

where the parameter λ_{bc} is the same as in (2.3). It is common to refer to (2.5) in conjunction with (2.3) as the *Brooks and Corey model*.

The *Mualem* mathematical model for relative permeability functions is given by

$$k_{rl}(s_l) = s_{e,l}{}^{\frac{1}{2}} \left(1 - \left(1 - s_{e,l}{}^{\frac{1}{m}}\right)^m\right)^2, \tag{2.6a}$$

$$k_{rg}(s_l) = \left(1 - s_{e,l}\right)^{\frac{1}{3}} \left(1 - s_{e,l}{}^{\frac{1}{m}}\right)^{2m}. \tag{2.6b}$$

Together with (2.4), it is usually referred to as the *van Genuchten model*.

2.2.5 Phase Composition

Each fluid or solid phase that occupies (a part of) the porous medium is composed of multiple species of interest. It is therefore necessary to consider the composition of each individual phase. We use the term *component* to denote a chemical species that belongs to the minimum number of independent chemical species necessary to completely describe the composition of a given phase (Bear and Cheng, 2010). Note that the set of components is not unique. When chemical equilibrium is not assumed, all species are defined to be components. Each phase α can be a set of several components $\kappa \in \mathcal{K}_\alpha$, where a component κ can be present in one or both of the mobile phases, in the solid phase or in the solid and in the liquid phase.

The chemical species is referred to as a *solvent* if it is the predominant species in a phase, or as a *solute* if it constitutes only a small portion of a phase. A solvent can be e.g. the solid matrix minerals in the solid phase or water in the liquid phase, because the liquid phase is comprised primarily of water.

The concentration of a component indicates its quantity in a unit volume of a fluid or a solid phase. It can be measured in different ways, depending on the selected units for quantity and volume.

Phase composition is expressed in terms of a *mass concentration* or a *molar concentration*. The molar concentration $C^m_{\alpha,\kappa}$ of component κ expresses the number of moles of κ, $N_{\alpha,\kappa}$, per unit volume of the phase α, V_α, as

$$C^m_{\alpha,\kappa} = \frac{N_{\alpha,\kappa}}{V_\alpha}$$

and the mass concentration expresses the mass of κ-species, $m_{\alpha,\kappa}$, per unit volume of phase α as

$$C_{\alpha,\kappa} = \frac{m_{\alpha,\kappa}}{V_\alpha}.$$

The phase mole density (total molar concentration) is given by

$$\nu_\alpha = \frac{N_\alpha}{V_\alpha} = \sum_{\kappa \in \mathcal{K}_\alpha} C^m_{\alpha,\kappa}$$

and the phase mass density is defined by

$$\rho_\alpha = \frac{m_\alpha}{V_\alpha} = \sum_{\kappa \in \mathcal{K}_\alpha} C_{\alpha,\kappa},$$

where N_α is the total number of mole in phase α and m_α is the mass of phase α.

The phase mass and mole densities are related by

$$\rho_\alpha = \sum_{\kappa \in \mathcal{K}_\alpha} M_\kappa C^m_{\alpha,\kappa} = \nu_\alpha \sum_{\kappa \in \mathcal{K}_\alpha} M_\kappa \frac{N_{\alpha,\kappa}}{N_\alpha} = \nu_\alpha M_\alpha, \tag{2.7}$$

where M_κ is the molar mass of compound κ and M_α is the average molar mass of mixtures

$$M_\kappa = \frac{m_{\alpha,\kappa}}{N_{\alpha,\kappa}}, \qquad M_\alpha = \sum_{\kappa \in \mathcal{K}_\alpha} M_\kappa \frac{N_{\alpha,\kappa}}{N_\alpha}. \tag{2.8}$$

The relationship between mass and molar concentration is

$$C^m_{\alpha,\kappa} = \frac{C_{\alpha,\kappa}}{M_\kappa}.$$

2.2.6 Thermodynamic Relationships and Restrictions

In contrast to e.g. Class and Helmig (2002); Class et al. (2002) and Xu et al. (2006), we consider only isothermal conditions. In our applications, the temperature is given and the pressure of the gas phase is close to the standard atmospheric pressure. Thus, the real gas can be approximated by an *ideal gas*.

The ideal gas obeys the ideal gas law

$$\nu_g = \frac{p_g}{RT}, \tag{2.9}$$

where $R = 8.314\,\mathrm{J\,mol^{-1}\,K^{-1}}$ is the universal gas constant and T is the thermodynamic temperature.

Total pressure in the gas phase is related to the sum of the partial pressures (Dalton's law)

$$\sum_{\kappa \in \mathcal{K}_g} p_{g,\kappa} = p_g \tag{2.10}$$

and the partial pressures relate to molar concentrations as (Molins and Mayer, 2007)

$$p_{g,\kappa} = RTC^m_{g,\kappa}. \tag{2.11}$$

Henry's Law

Mass transfer between liquid and gas phase occurs at the phase interface. For gases with a low solubility, like oxygen in water, the solubility of a gas in a liquid phase is directly proportional to the partial pressure of the gas above the liquid

$$p_{g,\kappa} k_H = C^{*,m}_{l,\kappa}, \tag{2.12}$$

where $p_{g,\kappa}$ is the partial pressure of the solute in the gas phase, k_H is the Henry's law constant and $C^{*,m}_{l,\kappa}$ is the equilibrium molar concentration in liquid phase. Introducing a dimensionless constant $k^{cc}_H = k_H \cdot RT$, Henry's law (2.12) is given by (Sander, 1999)

$$C^{*,m}_{l,\kappa} = k^{cc}_H C^m_{g,\kappa}. \tag{2.13}$$

2.2.7 Macroscopic Diffusive Flux

There are two basic processes controlling the macroscopic diffusive flux of solutes in porous media: mechanical dispersion and molecular diffusion.

The mechanical dispersion refers to the spreading and mixing caused by the variations in velocities with which the fluid phases moves at different scales. The dispersion normally depends on the water velocity and the direction of flow. In flow direction the dispersivity is typically larger than the dispersivity in the directions perpendicular to the flow direction, for details see (Bear, 1972).

Molecular diffusion is a mass transfer process caused by the random Brownian motion of solute particles in fluids. The mass transfer model assumes that the flux is proportional to the negative concentration gradient. The macroscopic diffusive flux of the component κ is described by the averaged *Fick's first law*

$$j_{\alpha,\kappa} = -D_{\alpha,\kappa} \nabla C_{\alpha,\kappa}, \tag{2.14}$$

where the diffusion coefficient depends on the type of solute, the saturation and phase composition

$$D_{\alpha,\kappa} = D_{\alpha,\kappa}(x, t, s_\alpha, C_{\alpha,\kappa}, \ldots).$$

In this work (unless stated otherwise), we use the Fick's law to describe the diffusive fluxes $j_{\alpha,\kappa}$ with the second model of Millington and Quirk for the dependence of the effective diffusion coefficient on phase saturation (Jin and Jury, 1996) and one obtains

$$j_{\alpha,\kappa} = -s^2_\alpha \phi^{\frac{4}{3}} D_{\alpha,\kappa} \nabla C_{\alpha,\kappa}. \tag{2.15}$$

Constraints on Diffusive Flux

We assume as in Allen et al. (1992); Miller et al. (1998) and Class et al. (2002) that the sum of the diffusive fluxes for all components in each phase is zero

$$\sum_{\kappa \in \mathcal{K}_\alpha} j_{\alpha,\kappa} = 0, \tag{2.16}$$

which ensures that the sum of all components of a phase moves with the phase velocity v_α. The constraint (2.16) holds when all components are at dilute concentration, except for the solvent component.

The molecular diffusion coefficients of gas components are assumed to be equal to their respective binary diffusion coefficients in air. This is done only for simplification; the calculation of multi-component diffusion coefficients is complicated and it is not clear at all that such calculations will improve the accuracy of the simulations (Adenekan et al., 1993). The theory of diffusion in multi-component gases is discussed by Cussler (1997) and diffusion in liquid mixtures in Rehfeldt and Stichlmair (2007).

2.2.8 Mass Balance Equations

A rigorous mathematical description of compositional multi-phase flow in the subsurface is based upon mass balance equations for each component present in the system.

The macroscopic differential mass balance equations for components may be obtained by averaging the microscopic balance equations (Bear and Cheng, 2010) for the mass of chemical species in fluid phases that fully or partly occupy the void space and of chemical species in the solid phase.

For each phase $\alpha \in \mathcal{P}$ and for each component $\kappa \in \mathcal{K}_\alpha$, the general macroscopic mass conservation equations describing the transport and reaction of fluid and solid phase species are written as (Abriola and Pinder, 1985; Aziz et al., 1979; Miller et al., 1998)

$$\frac{\partial(\theta_\alpha C_{\alpha,\kappa})}{\partial t} + \nabla \cdot \{C_{\alpha,\kappa} v_\alpha + j_{\alpha,\kappa}\} = q_{\alpha,\kappa} + R_{\alpha,\kappa} \quad \text{in } \Omega \times [0,T], \tag{2.17}$$

where Ω is the spatial domain and $[0,T]$ is the time interval under consideration.

The system of equations (2.17) includes general species reaction terms $R_{\alpha,\kappa}$, each expressing the rate at which the mass of that species is added to the phase and/or changed within the phase by a particular process. Amongst others, these processes may include chemical reactions among various species, adsorption, ion exchange, mineral precipitation, dissolution, interphase mass transfer, microbiological growth and decay, and bio-transformation. The term $q_{\alpha,\kappa}$ accounts for component mass change in the phase α and denotes the gain or loss of mass due to external sources and sinks (mass added from outside the system), e.g. injection. In the case of solid components, the advection and diffusion parts in (2.17) vanish.

The reactions here are in a rate formulation, but equilibrium reactions are also possible. Steefel and Lasaga (1994) describe the mechanism of how to obtain a rate expression for equilibrium reactions. In our applications, the equilibrium reactions will be introduced through the operator splitting technique described in Chapter 3.

2.3 Discussion

Richards' Assumption

Very often, only the flow of the water is considered and the air flow is neglected. The assumption of a passive gas phase underlying many models is that the resistance to flow in the gas phase is negligible everywhere. Because air density is very small, the gas phase is assumed to be everywhere at atmospheric pressure (Richards' assumption).

It is certainly not justified when air flow is produced by air injection and/or extraction as part of contaminant cleanup operations, e.g. gas production and consumption by microorganisms (Bear and Cheng, 2010). Advective gas transport by itself is not likely to affect the flow solution, since gas pressures are small, but it may influence the reactive transport solution significantly. The correct solution of the fully transient problem is only possible using a compositional approach, which considers advective and diffusive transport processes in both the aqueous and gaseous phases simultaneously with geochemical reactions. In our applications, a full two-phase flow model is required as gas can be entrapped or gas density can depend on the phase composition. Thus, we have to solve a mass balance equation for the air.

Restrictions and Limitations

The incompressible liquid phase with constant density is considered to be always present, whereas the gaseous phase may vanish. The dissolved components in liquid phase are considered as tracers, i.e. their concentrations are small and the density of the liquid phase is that of water. The reactive processes at the microscale may change macroscale parameters such as porosity, permeability, fluid viscosity, and reactive surface area of the porous media. Although these dependencies are not considered in the model, it can be straightforwardly extended. In our applications, aqueous species are subject to local chemical interactions with the solid and gaseous phase or are assumed to be at local equilibrium. Direct interactions between solid and gas phase or within the solid phase are not considered in the model.

Chapter 3

Solution Approaches of Model Equations

In this chapter we consider a general compositional formulation of multi-phase reactive flow with multi-component solute transport. The term *compositional formulation* denotes that the solution includes both the composition and the volumetric fraction of each phase as a function of space and time and not merely the volumetric fraction distribution of each phase in space in time (Miller et al., 1998).

We briefly discuss several mathematical formulations for multi-phase multi-component transport and introduce model formulation based on operator splitting. Additionally, we compare different approaches for coupling between solute transport and chemical reactions together with a discussion about existing codes for modeling of reactive transport.

In general, the solution approaches in multi-phase multi-component reactive flow can be classified with respect to:

1. the solution strategy for solving the original coupled problem;
2. the primary variables used;
3. the discretization schemes employed for the system or subsystems.

3.1 Mathematical Formulations

The governing equations (2.17) may be written in a number of forms. While the formulations are mathematically equivalent, the numerical models based on each formulation differ in flexibility and efficiency. We review here two different formulations; each formulation offers inherent advantages and disadvantages w.r.t. numerical approximation and in model flexibility.

3.1.1 Fully Coupled Formulation

In a fully coupled formulation (also called a simultaneous formulation), the governing equations (2.17), the relationships between the phase pressures and the fluid saturations, and the component concentrations within each phase are described through a single set of equations.

This formulation is the most straightforward and leads to a numerical approximation which does not need any iterative procedures. However, this approach is computationally expensive, since all unknown variables are approximated in a single step and the system of equations

resulting from the numerical discretization of this model formulation is large and highly non-linear.

The numerical schemes of the solution of models based on this formulation are not expected to be very efficient for systems with multiple phases and many components. Examples of the simultaneous solution method may be found in e.g. Adenekan et al. (1993); Class et al. (2002); Lenhard et al. (1995); Mayer and Miller (1996); Sleep (1995); Sleep and Sykes (1993); White et al. (1995).

To solve the system of equations (2.17), different sets of variables can be chosen as primary variables to solve the system unambiguously. However, the choice is not unique and can even change during the simulation, for details we refer the reader to literature listed below. The problem in the simultaneous formulation arises when a phase appears or disappears. In this case, there are these main strategies to resolve this issue: extending the saturation to negative values (Abadpour and Panfilov, 2009), using suitable sets of primary variables (Neumann, 2015; Neumann et al., 2013), complementarity constraints (Jaffré and Sboui, 2010; Lauser, 2014), local switching of primary variables depending on present phases (Adenekan et al., 1993; Class et al., 2002; Forsyth and Simpson, 1991; Lauser, 2014) and flash calculations (Fuller et al., 2006; Polívka and Mikyška, 2014).

The simultaneous formulation is often used to model multi-phase multi-component flow in porous media with a special regard to CO_2 sequestration (Bielinsky, 2006; Lauser, 2014; Neumann et al., 2013). In this case, the mobile phases are comprised only from a low number of components and the phase properties are highly dependent on the phase composition.

The numerical discretization of models based on the simultaneous formulation is often based on a fully implicit time discretization and a full upwinding technique (Adenekan et al., 1993; Bielinsky, 2006), which may introduce numerical diffusion in the system (Huber and Helmig, 1999).

3.1.2 Decoupled Formulation

An alternative formulation may be developed if the equations describing the movement of the phases are separated from those describing the transport of components within the fluid phases. This formulation produces two sets of non-linear equations, which are weakly coupled by compositionally dependent fluid properties and by mass exchange terms.

In general, a computationally decoupled formulation offers advantages in terms of model flexibility, as any number of components may be studied without changing the solution of the phase balance equations or the solution approach for the component balance equations.

For equivalent problems, a computationally decoupled formulation is expected to be more efficient from the numerical point of view than the simultaneous formulation due to the solution of smaller problems. Unfortunately, the operator splitting scheme proposed for a computationally decoupled model introduces additional errors into the solution of the equations. The errors can be reduced e.g. by iterating between the phase balance equations and the component balance equations (Reeves and Abriola, 1994) or controlled by limiting the time step size in order to constrain the mass transfer and saturation changes during a single time step (Mayer and Miller, 1996).

3.2 Model Formulation Based on Operator Splitting

The operator splitting model formulation presented in this thesis is a computationally decoupled formulation. In a first step, the set of equations (2.17) describing the reactions in the solid phase are separated from those describing the transport of components within the fluid phases. Then the system (2.17) is split into a transport part for fluid phases

$$\frac{\partial(\theta_\alpha C_{\alpha,\kappa})}{\partial t} + \nabla \cdot \{C_{\alpha,\kappa} v_\alpha + j_{\alpha,\kappa}\} = q_{\alpha,\kappa}, \quad \kappa \in \mathcal{K}_\alpha,\, \alpha \in \mathcal{P}_f, \tag{3.1a}$$

and into a reaction part (for all phases)

$$\frac{\partial(\theta_\alpha C_{\alpha,\kappa})}{\partial t} = R_{\alpha,\kappa}, \quad \kappa \in \mathcal{K}_\alpha,\, \alpha \in \mathcal{P}. \tag{3.1b}$$

Further, the transport part (3.1a) is split again in a phase transport and in a phase composition part.

3.2.1 Phase Transport

Summation of the transport part (3.1a) over all components of each fluid phase and using assumption (2.16) yields a balance equation for each mobile phase

$$\frac{\partial\left(\theta_\alpha \rho_\alpha\right)}{\partial t} + \nabla \cdot \{\rho_\alpha v_\alpha\} = \sum_\kappa q_{\alpha,\kappa} = q_\alpha, \quad \alpha \in \mathcal{P}_f, \tag{3.2}$$

where q_α denotes the total source/sink term in phase α (now without reactions). The liquid mass phase density remains constant, while the gas phase density ρ_g may depend on the phase composition. By solving (3.2), we obtain the fluid velocities and saturation distributions.

In the case of unsaturated groundwater flow it is often assumed that the gas phase is mobile enough to always be at atmospheric pressure, i.e. $p_g = const$. The liquid phase pressure can subsequently be computed via the capillary pressure function, and gas and liquid phase transport are decoupled. Assuming incompressibility of the liquid phase we obtain from (3.2) a single equation for liquid phase which is called Richard's equation (Richards, 1931).

3.2.2 Component Transport

To formulate component transport equations, we select a reference non-reactive component $\kappa_{\alpha,0} \in \mathcal{K}_\alpha$ in each phase, e.g. water in the liquid phase, air in the gas phase and porous material in the solid phase. The balance transport equations for the remaining N_α components in the fluid phases have the form

$$\frac{\partial(\theta_\alpha C_{\alpha,\kappa})}{\partial t} + \nabla \cdot \{C_{\alpha,\kappa} v_\alpha + j_{\alpha,\kappa}\} = q_{\alpha,\kappa}, \quad \kappa \in \mathcal{K}_\alpha \setminus \{\kappa_{\alpha,0}\},\, \alpha \in \mathcal{P}_f. \tag{3.3}$$

We use the resulting $N_l + N_g = |\mathcal{K}_l| + |\mathcal{K}_g| - 2$ concentrations in the fluid phases, that are a

result of component transport (3.3), together with $N_s = |\mathcal{K}_s| - 1$ concentrations in the solid phase to compute the chemical reaction problem.

3.2.3 Reaction

All reactive species are subject to local chemical interactions with the aqueous, gaseous, and solid phase by

$$\frac{\partial C_{\alpha,\kappa}}{\partial t} = \frac{1}{\theta_\alpha} R_{\alpha,\kappa} = r_{\alpha,\kappa} + e_{\alpha,\kappa} \ + a_{\alpha,\kappa} \ , \quad \kappa \in \mathcal{K}_\alpha \setminus \{\kappa_{\alpha,0}\}, \, \alpha \in \mathcal{P}. \tag{3.4}$$

The right-hand side of (3.4) includes all reactions; it can be divided into a chemical and/or biological reaction part $r_{\alpha,\kappa}$, a phase exchange between fluids $e_{\alpha,\kappa}$ and an interaction between the liquid and solid phases $a_{\alpha,\kappa}$.

3.2.4 Coupling of Component Transport and Reaction

Because the component transport and reactions are coupled, equations (3.3) and (3.4) can be merged to get the advection-diffusion-reaction system

$$\frac{\partial(\theta_\alpha C_{\alpha,\kappa})}{\partial t} + \nabla \cdot \{C_{\alpha,\kappa} v_\alpha + j_{\alpha,\kappa}\} = q_{\alpha,\kappa} + R_{\alpha,\kappa}, \quad \kappa \in \mathcal{K}_\alpha \setminus \kappa_{\alpha,0}, \, \alpha \in \mathcal{P}. \tag{3.5}$$

Also note that the two-phase equations (3.2) and reactive transport equations (3.5) are coupled, because the density of the gas phase can be concentration composition dependent.

3.2.5 Chemical Equilibrium

Internal reactions which are slow in comparison with the transport process are described by ordinary differential equations (3.4). In the mathematical description of reversible reactions, which are relatively fast with respect to transport, the assumption of local equilibrium can be introduced.

For each pair of components involved in the equilibrium process we obtain one algebraic equilibrium equation, see Herzer and Kinzelbach (1989). The set of $|\mathcal{K}_e|$ equilibrium equations is given by

$$F_j(C_{l,\kappa_1}, \ldots, C_{l,\kappa_{N_l}}, C_{g,\kappa_1}, \ldots, C_{g,\kappa_{N_g}}, C_{s,\kappa_1}, \ldots, C_{s,\kappa_{N_s}}) = 0, \quad j \in \mathcal{K}_e, \tag{3.6}$$

where the function F_j is in general a non-linear function of the involved concentrations.

If the system contains both the slow reactions, characterized by kinetic rate laws, and the fast reactions, which are assumed to be at the local equilibrium, the reactive transport model is described by the system of partial differential and algebraic equations (3.5-3.6).

3.2.6 Primary Variables

The model (2.17) split into (3.1-3.6) is a mixture of two sets of non-linear partial differential equations (PDE), one set of ordinary differential equations (ODE) and set of algebraic equations (AE). Different choices of primary variables are possible for the solution of the PDEs and ODEs. The remaining unknowns can be computed from the algebraic equations.

In this thesis we use the fluid pressures p_l, p_g or the liquid phase and capillary pressures p_l, p_c as the primary variables for the two-phase balance equations (3.2) and the component concentrations $C_{\alpha,\kappa}$ of all but one component $\mathcal{K}_\alpha \setminus \{\kappa_{\alpha,0}\}$ for each phase as primary variables. A discussion about alternative formulations of two-phase flow models can be found in Section 3.3.

Given these primary variables, the remaining quantities can be computed as follows: the water saturation is determined via the inverse function p_c^{-1} of (2.2). As the liquid density is assumed to be constant, the concentration $C_{l,0}$ can be calculated from ρ_l and the $|\mathcal{K}_l| - 1$ known concentrations.

For the gas phase we use the ideal gas law (2.9) to calculate the molar density of the gas phase ν_g, which is assumed to be constant. Using ν_g, the known concentrations and molar masses M_κ, we can calculate the concentration $C_{g,0}$ from

$$C_{g,0} = \frac{1}{M_{g,0}} \cdot \left[\nu_g - \sum_{\kappa \in \mathcal{K}_g \setminus \{\kappa_{g,0}\}} \frac{C_{g,\kappa}}{M_\kappa} \right]$$

and finally the gas phase density from

$$\rho_g = \sum_{\kappa \in \mathcal{K}_g} C_{g,\kappa}.$$

Both the PDEs and ODEs are subject to appropriate initial conditions. Additionally, the formulation of PDEs has to be supplement by the boundary conditions, see Chapter 4 for details.

3.3 Remarks on Two-Phase Flow

Multi-phase models for the simulation of processes in the subsurface are widely used in different fields of technical applications. Since the late 1950s, researchers in the oil industry have developed numerical models in order to help optimize oil recovery, see the classical texts by Aziz et al. (1979); Peaceman (1977) and Chavent and Jaffré (1986).

In this thesis, we use a formulation based on fluid pressures or capillary/liquid pressures. This choice of primary variables is motivated by our applications: we apply the model to simulate two-phase flow (with water and air) in laboratory flow-through experiments, where the diameter of the computational domain is less than 1 meter. In that case, no sharp saturation fronts occur, because the transition zone between full saturated and completely dry sand occupies

several centimeters, see Chapters 7 and 8. Furthermore, the gas phase is compressible and can disappear, while the liquid phase is incompressible and is always present.

Nevertheless, the model concept introduced in this work can be adapted to a concrete situation without major changes. In general, the two-phase flow equations are of elliptic/hyperbolic, elliptic/parabolic or parabolic/parabolic type, depending on whether or not the phases are compressible and whether or not capillary pressure is considered.

The global implicit approach (also called fully coupled/fully implicit approach), where the two equations (3.2) are solved simultaneously is very robust and is the standard choice in industrial simulators, often based on a pressure-saturation formulation. It is used in combination with finite volume (Dawson et al., 1997) and finite element (Forsyth, 1991; Helmig, 1997) discretization schemes.

However, this approach has some drawbacks. The large-scale non-linear systems of algebraic equations may be difficult to solve. Good progress has been reported on this point with Newton-Krylov methods (Bergamaschi et al., 2012; Dawson et al., 1997; Knoll and Rider, 1999) and multigrid methods (Bastian and Helmig, 1999; Molenaar, 1995). A second and more severe drawback is that only first-order full upwinding is typically restricted to the mobilities. In the elliptic/hyperbolic regime, this leads to a very poor accuracy of sharp saturation fronts due to numerical dispersion (Huber and Helmig, 1999).

In this regime the sequential approach, called IMPES (implicit pressure explicit saturation) performs better. It is a very powerful method for the numerical treatment of incompressible two-phase flow. The general phase balance equations are combined to eliminate the saturation unknowns and the equation for pressure is separated from that for saturation, see Chen (2007) for details. The coupling between the fluid saturations and pressure is lagged by one solution step. This method has one drawback: a small time step for the saturation equation is required in order to keep the explicit method stable. However, it is typically possible to execute multiple transport steps per pressure update, which reduces the computing time significantly. An adaptive implicit procedure to take the advantage of the efficiency of the IMPES formulation while retaining the stability of the simultaneous formulation was proposed by Forsyth and Sammon (1986).

A formulation based on the so-called „global" pressure by Chavent and Jaffré (1986) allows an effective decoupling of the elliptic pressure equation and the (nearly) hyperbolic saturation equation, making it possible to apply appropriate discretization schemes for each equation. One choice that has been used very successfully by several groups is the mixed finite element method for the elliptic equation in combination with cell-centered finite volume methods (higher order Godunov scheme) for the hyperbolic equation (Chavent and Jaffré, 1986; Durlofsky, 1993; Huber and Helmig, 1999). Other approaches in this regime are non-linear characteristic and front tracking methods (Karlsen and Risebro, 1998; Mulder and Meyling, 1993; Risebro and Tveito, 1991).

3.4 Approaches for Coupling Reaction and Solute Transport

It is beyond the scope of this thesis to provide a thorough review of the development of reactive transport modeling. We refer the reader to e.g. Kirkner and Reeves (1988); Reeves

and Kirkner (1988); Rubin (1983); Steefel and Lasaga (1994) and Lichtner et al. (1996) for an in-depth discussion of the general philosophy of multi-component reactive transport modeling. In addition, authors of a review article Steefel et al. (2005) discuss the historical development and the current status of reactive transport modeling and its application to real problems.

In general, the multi-component transport and reaction models in porous media lead to a large set of coupled PDEs for mobile species, ODEs for immobile species and AEs for equilibrium reactions (Saaltink et al., 1998, 2001; Schäfer et al., 1998b). We can use an operator notation to describe the solute transport and reaction for a set of components with concentrations C by

$$\frac{\partial C(t)}{\partial t} = \mathcal{L}\left(C(t)\right) + \mathcal{R}\left(C(t)\right), \tag{3.7}$$

where $\mathcal{L}$ is the spatial operator representing the transport (advection and diffusion) and the operator $\mathcal{R}$ includes all chemical reactions.

In our case, the reactive transport model (3.7) is described by the system of transport-reaction equations (3.5) and by the equilibrium equations (3.6). The equations (3.5) can be split into the transport part (3.3) and into the reactive part (3.4).

We can solve the arising coupled system with two different approaches that are well known for reactive transport modeling:

1. the global approach, in which both transport and chemical operators are solved simultaneously (Fahs et al., 2008; Hammond et al., 2002; Steefel and MacQuarrie, 1996; Steefel and Lasaga, 1994; Valocchi et al., 1981);
2. the operator splitting approach, in which transport and chemical reactions are solved separately (Carrayrou et al., 2010, 2004; Lagneau and van der Lee, 2010; van der Lee and Windt, 2001; Parkhurst and Appelo, 2013).

In view of the fact that the solution strategies have an influence on the accuracy and the efficiency of the numerical solution, we discuss their implementation and the associated implications in detail.

3.4.1 Global Approach

One way to solve the coupled system (3.7) is the global implicit approach (GIA), sometimes called one-step global approach. All governing equations are discretized implicitly in time and the resulting large set of non-linear algebraic equations is solved iteratively, e.g. by Newton's method. Global methods are often based on a direct substitution approach (DSA), which reduces the number of unknowns in the system by eliminating components in equilibrium (Yeh and Tripathi, 1989, 1991). Additional reduction approaches can be found in (Friedly and Rubin, 1992; Kräutle and Knabner, 2005, 2007; Saaltink et al., 1998).

3.4.2 Operator Splitting Approach

The mathematical properties of each operator in reactive transport are very different: parabolic and hyperbolic PDEs for advection-diffusion equations, non-linear AEs for instantaneous equi-

librium chemistry and stiff ODEs for kinetic chemistry. It is therefore interesting to separate each operator using operator splitting (OS) methods (Carrayrou, 2009; Carrayrou et al., 2004; Ropp and Shadid, 2005; Schäfer et al., 1998b), which can lead to a very efficient method, since one can treat each part of the original operator independently with an appropriate numerical method.

In the OS approach, a single time step consists of a transport step followed by a reaction step using the transported concentrations. The simplest variant of OS is the sequential non-iterative approach (SNIA) where each sub-model is solved exactly once per global splitting time step τ.

First-Order Splitting

To solve (3.7) using first-order splitting (also called Lie-Trotter splitting) we first solve the transport problem from time $\tilde{t}$ to time $\tilde{t}+\tau$

$$\frac{\partial C_t(t)}{\partial t} = \mathcal{L}\left(C_t(t)\right), \quad C_t(\tilde{t}) = C(\tilde{t}), \tag{3.8a}$$

followed by the solution of the reaction operator

$$\frac{\partial C_r(t)}{\partial t} = \mathcal{R}\left(C_r(t)\right), \quad C_r(\tilde{t}) = C_t(\tilde{t}+\tau), \tag{3.8b}$$

where the initial concentration for (3.8b) is given by the solution of (3.8a). The concentration $C(\tilde{t}+\tau)$ is than the solution C_r of (3.8b) at time $\tilde{t}+\tau$. The Lie-Trotter splitting (3.8) is not symmetric with respect to the operators $\mathcal{L}$ and $\mathcal{R}$.

Strang Splitting

It is possible to reduce some of the splitting errors associated with the SNIA approach by using a symmetrical Strang splitting (Strang, 1968). By a small modification of (3.8) it is possible to make the splitting algorithm second-order accurate. This is done by surrounding the reaction step by two transport steps. The Strang splitting algorithm to solve the original problem (3.7) from time $\tilde{t}$ to time $\tilde{t}+\tau$ is as follows: the transport is solved with a time step $\tau/2$

$$\frac{\partial C_t(t)}{\partial t} = \mathcal{L}\left(C_t(t)\right), \quad C_t(\tilde{t}) = C(\tilde{t}), \tag{3.9a}$$

followed by a reaction step

$$\frac{\partial C_r(t)}{\partial t} = \mathcal{R}\left(C_r(t)\right), \quad C_r(\tilde{t}) = C_t(\tilde{t}+\tau/2), \tag{3.9b}$$

which is in turn followed by another $\tau/2$ transport step

$$\frac{\partial C(t)}{\partial t} = \mathcal{L}\left(C(t)\right), \quad C(\tilde{t}+\tau/2) = C_r(\tilde{t}+\tau). \tag{3.9c}$$

The Strang splitting (3.9) has second-order accuracy, but the convergence order of Strang splitting for general ADRE can be reduced due to the effect of stiff reaction terms or bound-

ary conditions (Faou et al., 2014; Hundsdorfer and Verwer, 1995, 2003). We compare the performance of both splitting techniques mentioned above in Chapter 5.

Sequential Iteration Approach

The error introduced by the decoupling of the component transport and the chemical reactions can be decreased by the sequential iteration approach (SIA) where all sub-models are iterated until convergence in each global splitting time step. The two sets of equations are coupled by sink/source terms which are updated during the iterative cycle (Steefel and MacQuarrie, 1996; Šimůnek and Suarez, 1994; Walter et al., 1994).

Although the SIA methods appear attractive because they can be modularized as SNIA, they have several disadvantages. The iterative procedure is not unconditionally stable, due to the explicit nature of the approach; difficulties in the convergence can arise and small splitting times are required (de Dieuleveult et al., 2009; Fahs et al., 2008; Herzer and Kinzelbach, 1989). To overcome this difficulty, many improvements of SIA methods were proposed in the literature, see e.g. Carrayrou et al. (2004); Tebes-Stevens et al. (1998). Another possible disadvantage to the SIA approach is dependence on an implicit solution of the transport equations in order to get a fully implicit solution of the overall reaction-transport problem (Steefel and MacQuarrie, 1996). Carrayrou et al. (2004) conclude that standard SIA schemes should not be used; they may exhibit convergence or stability problems and the OS errors are still present even if the iterative algorithm converges.

3.4.3 Discussion

Both the one-step methods and the OS methods have several advantages and disadvantages in solving of ADREs. The choice of the most appropriate methods depends on multiple factors including among others

- complexity and character of chemical reactions;
- dominance of considered processes (physical transport or chemical reactions) based on their time scales;
- dimension of the given problem and time steps required;
- memory requirements, CPU time and code parallelism.

GIA is often used with full upwinding of the convective terms (in convective-dominated cases) to avoid unphysical oscillations of the concentrations. This results in a large amount of numerical diffusion for the component transport. Since reactions only take place when components mix, and components might mix mainly due to numerical diffusion, the simulation may overestimate the reaction (Cirpka et al., 1999).

Another potential limitation of GIA is the need to compute, store and invert the Jacobian matrix. This becomes problematic for large systems with many components in two- and three-dimensional field scale simulations, because the increased size of the Jacobian matrix results

in greater memory usage and more CPU time is needed to solve the resulting system of linear equations within the Newton iterations. Because of its high memory requirements, the global approach was initially rejected (Yeh and Tripathi, 1989), but the memory capacity of modern computers has greatly improved so that a high memory requirement is no longer the major drawback. The GIA method was originally used only for small reaction systems in one dimension, but since the beginning of the 21^{th} century, GIA has been used for complex bio-chemical reaction models coupled to 3D groundwater flow, e.g. (Wagner et al., 2002).

On the other hand, GIA has some important advantages. The global convergence properties of the fully coupled method may be better than those of multi-step iteration methods. Using Newton's method to solve the full set of equations, we expect to achieve quadratic convergence in the vicinity of the solution, while we can expect linear convergence at best from the iterative OS methods. Moreover, it is possible to take larger time steps with GIA, because the time step size is limited only by the convergence of Newton's method and the accuracy of the discretization methods. This is particularly true for stiff transient problems converging to a steady state (Verwer et al., 2004). Nevertheless, the GIA approach is considered to be more robust for chemically complex systems and it is the preferred scheme in practice (Cirpka and Helmig, 1997; de Dieuleveult and Erhel, 2009; de Dieuleveult et al., 2009; Kanney et al., 2003; Podgorney et al., 2012; Saaltink et al., 2001; Steefel and Lasaga, 1994).

The OS approach is used in order to avoid the large computational cost of GIA. It takes advantage of the fact that only the physical transport equations are spatially coupled while the chemical equations are strictly coupled at each point in the system. This leads to a smaller system than the GIA methods; the transport problem can be solved independently for each component. The coupling between transport and chemistry is done on a per-element (or per-node) basis, which is beneficial in parallel computing. One can also use different numerical discretization schemes for multi-component transport and for chemical reaction that are optimized for a given situation. Within the OS approach high resolution schemes for hyperbolic transport equations can be utilized (Cockburn and Shu, 1998; Dawson, 1991; LeVeque, 2002) which introduce less numerical diffusion compared to the GIA methods. The decoupled methods, therefore, offer greater flexibility and even allow for the integration of existing codes for non-reactive transport and chemical reactions.

However, although OS methods show many advantages, the splitting procedure generates operator splitting errors. The OS errors for kinetically-controlled reactions will be investigated and discussed in Chapter 5.

Comparison

The numerical efficiency of SNIA, SIA and GIA approaches has been compared by Lichtner et al. (1996); Xu et al. (1999b) and Saaltink et al. (2001). They concluded that GIA performs better than OS methods for chemically complex, small dimensional reactive transport problems but is outperformed by OS approaches for chemically simple, large-dimensional problems. Although GIA is both more difficult to implement than the OS approach and very demanding in terms of computing time and memory requirements, it does not introduce any operator splitting error. The results in Fahs et al. (2008) show that in combination with an efficient sparse direct solver, GIA performs better than SIA and SNIA even for chemically simple problems. Cirpka

and Helmig (1997) compared the computational times for a system containing slow and fast chemical reactions. The SIA scheme was less efficient than GIA, because SIA required a very high number of time steps. The most efficient method based on OS was multiple times faster than GIA. However, the OS solution for fast reactions showed significant fronting, see also Section 5.4.1.

3.4.4 Reactive Transport Codes

There is a variety of computer codes for simulating flow and solute transport in porous media in combination with bio-chemical reactions. In the following, we briefly describe several numerical codes used in the simulation of reactive transport codes based on the REV formulation. The review article Steefel et al. (2014) presents a general description of the mathematical and numerical formulations used in reactive transport. Furthermore, the authors compared the features of several reactive transport modeling codes w.r.t.

- their general features of the flow and transport:
  - domain dimension
  - isothermal/non-isothermal flow
  - saturated/unsaturated flow
  - one/multi-phase flow
  - Richards' assumption
  - the type of advection and diffusion processes
- the type of geochemical and microbial process which can be treated in each code
- the numerical and computational features:
  - solution approaches (GIA, SNIA, SIA)
  - spatial and temporal discretization
  - inverse modeling and parameter estimation
  - code parallelization

We will not discuss the reactive transport codes listed in Steefel et al. (2014) in detail and refer to this article, which compares the following codes: PHREEQC (Parkhurst and Appelo, 2013; Zhu et al., 2001), HPx (Šimůnek et al., 2013), PHT3D (Appelo and Rolle, 2010; Prommer et al., 2003), OpenGeoSys (Kolditz et al., 2012), HYTEC (van der Lee et al., 2003), ORCHESTRA (Meeussen, 2003), TOUGHREACT(Xu et al., 2006, 2008, 2011), eSTOMP (White and Oostrom, 1996), HYDROGEOCHEM (Yeh and Tripathi, 1990), CrunchFlow (Steefel, 2008), MIN3P (Mayer et al., 2002), and PFLOTRAN (Lichtner et al., 2013a,b).

Other reviews on reactive transport codes can be found e.g. in van der Lee and Windt (2001); Mao et al. (2006) and (Wissmeier and Barry, 2008). There are also other codes used in reactive transport modeling, some of the relevant codes regarding to this work are discussed below.

SPECY

SPECY is a reactive transport code based on SNIA, where even advection and dispersion are split. The key feature of this code is the use of specific numerical methods to solve each part of the reactive transport equation. The code employs an explicit discontinuous Galerkin finite element method to obtain a good description of sharp reactive fronts associated with certain chemical phenomena. The diffusion operator is solved with an implicit mixed finite element method. The combination of these two methods has been adapted to reactive transport in the case of SIA. The equilibrium chemistry is solved using a combined algorithm based on Newton's method that reduces computing time and improves convergence, see Carrayrou (2009). SPECY was tested against the 1D reference solution of the reactive MoMaS problem (Carrayrou et al., 2010) including instantaneous equilibrium chemistry, kinetic rate laws and precipitation-dissolution reactions. Another code tested in the MoMaS benchmark is GDAE1D (de Dieuleveult and Erhel, 2009), based on the finite volume method with full upwinding and GIA without DSA. This code uses efficient and robust differential algebraic equations solvers, but the arising linear system is solved by a dense direct solver and the performance of the code was tested only for 1D domains.

TBC

Schäfer et al. (1998b,c) developed the very flexible parallel code TBC including chemical (kinetic and equilibrium) reactions, bio-chemical reactions and transport for saturated groundwater flow in three dimensions. It is based on a standard finite element method with explicit and fully implicit time integration. The coupled problem is solved using the SIA method. The authors assume that all microorganisms reside in an immobile bio-phase (bio-film model). Bio-chemical reactions only take place in the bio-phase, i.e. all relevant substrates first have to change phases from the liquid to the bio-phase before they can take part in the bio-chemical reactions. The growth of microbial populations is described by Monod-type kinetics with one or more respiratory pathways (e.g. aerobic and anaerobic).

CORE

The computer code CORE (Samper et al., 2009), which is an extended and improved version of an earlier code called TRANQUI (Xu et al., 1999b) solves two-dimensional groundwater flow, solute, and heat transport equations with a finite element method. Flow in variably saturated media is solved in terms of pressure heads. The authors solve the Richard's equation to get the velocity distribution. Samper and Zhang (2006) extended the original code and coupled the water flow and microbial reactive transport in BIO-CORE. Coupled transport and chemical equations are solved using SNIA and many variants of SIA, e.g. sequential partly iterative approach, which improves the accuracy of the traditional SNIA approach and in several situations is more efficient than the general SIA, see Samper et al. (2009).

RT3D

Another code that is capable of simulating multi-species reactive transport of different types of contaminants is the three-dimensional model RT3D (Clement et al., 1998), using external computed liquid velocities. The authors analyzed different types of subsurface contaminant reactions, microbial metabolisms, and microbial transport kinetics. The non-iterative OS strategy is separated into four steps: advection, diffusion, source/sink terms and chemical reactions. The advection part is solved by the method of characteristics or by an upstream finite difference method and the diffusion is discretized with an explicit finite difference approximation. After the transport time step, all reaction equations are solved implicitly employing multiple reaction time steps.

FEREACT

A reactive transport finite element method code FEREACT examines the coupled effects of two-dimensional steady-state groundwater flow, equilibrium aqueous speciation reactions, and kinetically-controlled interphase reactions. Transport and chemical reactions are coupled by the SIA-1 method which improves the convergence behavior of the traditional SIA approach (Tebes-Stevens et al., 1998).

RETRASO

The code RETRASO simulates reactive transport of dissolved and gaseous species in non-isothermal saturated and unsaturated problems. For the solution of the reactive transport equations it uses GIA with DSA (Saaltink et al., 2004). One, two and three-dimensional finite element methods can be used for the spatial discretization.

3.5 Summary

In this chapter, we presented basic solution approaches for multi-phase multi-component reactive flow in porous media based on continuum representation. This field of study is under intensive scientific investigation; for more detailed insight into this very complex topic we refer the reader to the literature cited in the whole chapter. The general application of one solution approach is not possible; the choice of the most appropriate solution approach depends on many factors, particularly on the model applications. The simultaneous compositional formulation is used for modeling CO_2 sequestration, because the phase properties are strongly dependent on the phase composition and the coupling plays an important role. Most of the models describing multi-phase reactive transport in porous media use decoupled formulations. Not only the phase flow and component transport can be decoupled, but also component transport and chemical reactions can be computed separately.

The resulting system of equations arising in the simultaneous formulation for and in GIA for reactive transport might be very large and the (non)-linear system may be difficult to solve.

This could become problematic for large systems with many components in two- and three-dimensional field scale simulations. The increased size of the Jacobian matrix results in a greater memory usage and more CPU time is needed to solve the resulting system of linear equations within the Newton iterations. On the other hand, these approaches are very robust and no operator splitting error occurs.

In this thesis, we present a model based on the decoupled formulation, where the phase transport, component transport and reactions are separated. The operator splitting approach enables the use of different numerical methods to solve each sub-problem; the spatial and temporal discretization schemes can be designed in such a way that the error arising in the numerical discretization is reduced significantly, see Chapter 4. On the other hand, the OS approach introduces an operator splitting error to the solution procedure. In our applications, we use almost only kinetically controlled chemical reactions. The OS error can be reduced by controlling the splitting time step depending on transport velocity and rates of chemical reactions, see Chapter 5 for details. As an alternative to the SNIA scheme for advection-diffusion-reaction systems, we can also use GIA in situations without sharp fronts in concentrations. Particularly in quasi steady-state problems, where the transient error associated with the concentration front propagation is absent, GIA performs reasonably well, because it allows larger time steps and the simulation time can be reduced significantly without loss of accuracy in the solution.

Chapter 4

Numerical Discretization

In this chapter we describe the numerical discretization of problems defined in Chapter 3. The application problems to be treated in this thesis involve only simple geometries. Therefore we decided to use a cell-centered finite volume scheme (CCFV) for both, the two-phase flow problem and for the component transport. This method is locally mass-conservative, which is a general requirement for a physically meaningful solution and a necessity for the solution of reactive transport.

We focus on the so-called *method of lines* in which the evolution problem is first semi-discretized in space yielding a system of coupled ordinary differential equations (ODEs), which is afterwards discretized in time. For the time discretization, we consider explicit and implicit Runge-Kutta methods (RK). For reactive transport, implicit-explicit Runge-Kutta methods (RK-IMEX) provide an alternative to the classical RK schemes.

The splitting concept introduced in Chapter 3 is, however, independent of the discretization of the sub-problems. Therefore, other spatial and temporal discretization methods can be implemented during future model development without a major reorganization of the code.

4.1 Preliminary Definitions

In this section we present the main ingredients needed for the spatial discretization on structured grids with conforming interfaces. The considered domain $\Omega \subset \mathbb{R}^d$, $d \in \{2,3\}$ with boundary $\partial\Omega$ is a rectangle in two space dimensions or a rectangular cuboid in case of $d = 3$.

Let $\mathcal{T}_h$ be a structured and regular tessellation of Ω into N_h mesh elements (cells) fulfilling

$$\begin{aligned} \mathcal{T}_h &= \{E_0, \dots, E_{N_h-1}\}, \\ \overline{\Omega} &= \bigcup_{j=0}^{N_h-1} \overline{E}_j, \quad \overline{E}_i \neq \overline{E}_j \quad \forall i \neq j, \end{aligned}$$

with cell volume $|E|$ and mesh size h computed as

$$|E| = \int_E 1 \, dx, \quad h = \max\{\mathrm{diam}(E) \,|\, E \in \mathcal{T}_h\}.$$

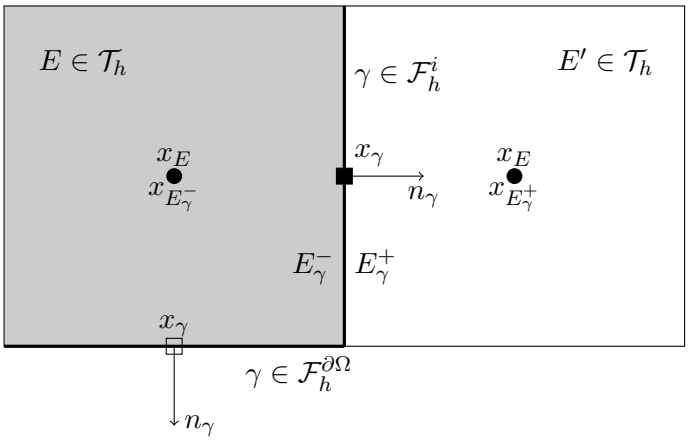

Fig. 4.1: Definition of the cell, face and boundary face geometry in two space dimensions.

The (d-1)-dimensional cell intersections form the set of interior and boundary faces

$$\mathcal{F}_h^i = \{\gamma_{e,f} = \partial E_e \cap \partial E_f \,;\, E_e, E_f \in \mathcal{T}_h, e \neq f \text{ and } |\,\gamma_{e,f}| > 0\},$$
$$\mathcal{F}_h^{\partial\Omega} = \{\gamma_e = \partial E_e \cap \partial\Omega \,;\, E_e \in \mathcal{T}_h \text{ and } |\gamma_e| > 0\},$$

where $|\gamma|$ denotes the volume of face γ. For an interior face, which is a common face of cells E and E', we arbitrarily fix a unit normal direction n_γ and we denote by E_γ^+ the cell where the normal points to and by E_γ^- the cell in the opposite direction, see Fig. 4.1. For boundary faces, n_γ is chosen to be the unit outer normal to $\partial\Omega$. For a cell $E \in \mathcal{T}_h$ and for a face $\gamma \in \mathcal{F}_h^i \cup \mathcal{F}_h^{\partial\Omega}$, we denote by x_E and x_γ the cell center and the face center, respectively. The cells are such that points on an interior face γ have equal distance to the centers of both cells E_γ^+ and E_γ^- and the vector $x_{E_\gamma^+} - x_{E_\gamma^-}$ is perpendicular to the face γ. The Euclidean distance $d_{E,\gamma}$ of cell centers of two adjacent elements E_γ^+ and E_γ^- to the face γ is given by

$$d_{E,\gamma} = |x_{E_\gamma^+} - x_{E_\gamma^-}| \quad \forall\gamma \in \mathcal{F}_h^i, \quad d_{E,\gamma} = |x_{E_\gamma^+} - x_\gamma| \quad \forall\gamma \in \mathcal{F}_h^{\partial\Omega}.$$

The space of piecewise constant functions on $\mathcal{T}_h$ is defined by

$$P_0(\mathcal{T}_h) = \{u \in L_2(\Omega) \,:\, u|_E = \text{constant} \quad \forall E \in \mathcal{T}_h\}.$$

Functions in $P_0(\mathcal{T}_h)$ may be discontinuous on the interior faces $\mathcal{F}_h^i$: for the value on each side of the intersection γ we set

$$u_\gamma^+(x) = \lim_{\varepsilon\to 0^+} u(x + \varepsilon n_\gamma), \quad u_\gamma^-(x) = \lim_{\varepsilon\to 0^-} u(x + \varepsilon n_\gamma). \tag{4.1}$$

The jump and the average of the function $u \in P_0(\mathcal{T}_h)$ for $x \in \gamma \in \mathcal{F}_h^i$ are then given by

$$[u](x) = u_\gamma^+(x) - u_\gamma^-(x), \quad \langle u\rangle(x) = \frac{1}{2}\left(u_\gamma^+(x) + u_\gamma^-(x)\right).$$

These definitions are extended to the domain boundary $\partial\Omega$ by

$$[v](x) = \langle v \rangle(x) = v(x) \qquad \forall x \in \gamma, \quad \gamma \in \mathcal{F}_h^{\partial\Omega}.$$

4.2 Two-Phase Flow Problem

Now we discretize the two-phase flow problem (3.2) based on a pressure-pressure formulation. In particular we describe how to combine upwinding and averaging of mobilities such that media discontinuities can be treated properly. For an introduction to different formulations of the multi-phase flow equations see also (Aziz et al., 1979; Chavent and Jaffré, 1986; Helmig, 1997; Peaceman, 1977) and (Bastian, 1999).

The phase balance equations (3.2) for $\alpha \in \mathcal{P}_f$ together with Darcy's law (2.1) are given by

$$\frac{\partial(\theta_\alpha \rho_\alpha)}{\partial t} + \nabla \cdot \{\rho_\alpha v_\alpha\} = q_\alpha \text{ in } \Omega \times [0,T], \tag{4.2a}$$

$$v_\alpha = -\frac{k_{r\alpha}}{\mu_\alpha} K \left(\nabla p_\alpha - \rho_\alpha g\right), \tag{4.2b}$$

supplemented by boundary and initial conditions

$$p_\alpha = p_\alpha^D \text{ on } \Gamma_\alpha^D, \qquad \rho_\alpha v_\alpha \cdot n = \eta_\alpha \text{ on } \Gamma_\alpha^N, \qquad p_\alpha(x,0) = p_{\alpha,0}(x) \text{ in } \Omega. \tag{4.2c}$$

The boundary of the domain $\partial\Omega$, where the boundary conditions are stated, is divided into disjoint parts with Neumann boundary Γ_α^N and Dirichlet boundary Γ_α^D.

Definition 4.1 (Semi-discrete finite volume method)
The semi-discrete finite volume approximation of (4.2) utilizing continuous in time solution representation, $t \in [0,T]$, and piecewise constant solution representation in space, $p_{\alpha h}(t) \in P_0(\mathcal{T}_h)$, $\alpha \in \mathcal{P}_f$, such that

$$p_{\alpha h}(t)|_E = \frac{1}{|E|} \int_E p_\alpha(x,t)\, dx$$

with initial data

$$p_{\alpha h}(0)|_E = \frac{1}{|E|} \int_E p_{\alpha,0}(x)\, dx$$

is given by the following system of ordinary differential equations:

$$\frac{d}{dt} \sum_{E \in \mathcal{T}_h} \int_E \theta_\alpha \rho_\alpha u \, dx + \sum_{\gamma \in \mathcal{F}_h^i} \int_\gamma \rho_\alpha v_\alpha \cdot n_\gamma [u] \, ds + \sum_{\gamma \in \mathcal{F}_h^{\partial\Omega} \cap \Gamma_\alpha^D} \int_\gamma \rho_\alpha v_\alpha \cdot n_\gamma u \, ds$$
$$+ \sum_{\gamma \in \mathcal{F}_h^{\partial\Omega} \cap \Gamma_\alpha^N} \int_\gamma \eta_\alpha u \, ds = \sum_{E \in \mathcal{T}_h} \int_E q_\alpha u \, dx \quad \forall u \in P_0(\mathcal{T}_h) \quad \alpha \in \mathcal{P}_f.$$

which can be abbreviated as

$$\frac{d}{dt} m_h(p_{\alpha h}, u) + a_h(p_{\alpha h}, u) = f_h(u) \quad \forall u \in P_0(\mathcal{T}_h) \quad \alpha \in \mathcal{P}_f. \tag{4.3}$$

To derive the semi-discrete form (4.3), we multiplied the original problem (4.2) by a test function $u \in P_0(\mathcal{T}_h)$, integrated over Ω and applied integration by parts on each cell. For simplicity, we suppress the subscript h.

All integrals in (4.3) are now evaluated numerically by applying the midpoint rule. The crucial term to evaluate is the interior flux term

$$v_\alpha|_\gamma \cdot n_\gamma = \underbrace{\frac{k_{r\alpha}(s_\alpha)}{\mu_\alpha(p_\alpha)} K}_{\xi_{\alpha,\gamma}} \underbrace{(-\nabla p_\alpha + \rho_\alpha g) \cdot n_\gamma}_{w_{\alpha,\gamma}}, \tag{4.4}$$

which we divide into two parts: mobility $\xi_{\alpha,\gamma}$ and flow direction $w_{\alpha,\gamma}$. Due to the simple element geometry, the normal derivative of the pressure can be evaluated by finite differences which then yields the flow direction:

$$w_{\alpha,\gamma} \approx -\frac{p_\alpha(x_{E_\gamma^+}) - p_\alpha(x_{E_\gamma^-})}{d_{E,\gamma}} + \frac{\rho_\alpha(x_{E_\gamma^+}) + \rho_\alpha(x_{E_\gamma^-})}{2} g \cdot n_\gamma = -\frac{[p_\alpha]}{d_{E,\gamma}} + \langle \rho_\alpha \rangle g \cdot n_\gamma.$$

Using this direction we can upwind the capillary pressure

$$p_{c,\gamma} = \begin{cases} p_g(x_{E_\gamma^-}) - p_l(x_{E_\gamma^-}) & w_{\alpha,\gamma} \geq 0, \\ p_g(x_{E_\gamma^+}) - p_l(x_{E_\gamma^+}) & w_{\alpha,\gamma} < 0, \end{cases}$$

and from that we can compute the saturations on adjacent elements:

$$\begin{aligned} s_{l,\gamma}^- &= \left(p_c^-\right)^{-1}(p_{c,\gamma}) & s_{g,\gamma}^- &= 1 - s_{l,\gamma}^-, \\ s_{l,\gamma}^+ &= \left(p_c^+\right)^{-1}(p_{c,\gamma}) & s_{g,\gamma}^+ &= 1 - s_{l,\gamma}^+. \end{aligned}$$

Finally, we perform a harmonic averaging of the mobility

$$\xi_{\alpha,\gamma}^- = \frac{{k_{r\alpha}}^-(s_{\alpha,\gamma}^-) K(x_{E_\gamma^-})}{\mu_\alpha(p_\alpha(x_{E_\gamma^-}))}, \qquad \xi_{\alpha,\gamma}^+ = \frac{k_{r\alpha}^+(s_{\alpha,\gamma}^+) K(x_{E_\gamma^+})}{\mu_\alpha(p_\alpha(x_{E_\gamma^+}))}, \qquad \xi_{\alpha,\gamma} = \frac{2\xi_{\alpha,\gamma}^- \xi_{\alpha,\gamma}^+}{\xi_{\alpha,\gamma}^- + \xi_{\alpha,\gamma}^+}.$$

This upwinding scheme in capillary pressure can handle material discontinuities that result in discontinuities in capillary pressure-saturation curves and relative permeability functions in neighboring elements (Ippisch, 2014).

4.2.1 Velocity Field

To ensure the local mass conservation for the component transport, we require that the velocity field belongs to the functional space $H(\mathrm{div}, \Omega)$, which is the space of functions with square-integrable weak divergences,

$$H(\mathrm{div}, \Omega) = \{v \in [L^2(\Omega)]^d;\ \nabla \cdot v \in L^2(\Omega)\},$$

which imposes the continuity of the normal trace across all faces.

The CCFV scheme on axis-parallel grids yields the normal velocities $v_\alpha|_\gamma \cdot n_\gamma$ on the midpoints of all faces, which can be directly used to construct the lowest-order Raviart-Thomas element space $\mathcal{RT}_0(E)$. The $\mathcal{RT}_0(E)$ space has the form

$$v_i = a_i + b_i x_i, \quad a_i, b_i \in \mathbb{R}, \quad i = 1, \ldots, d,$$

where subscript i denotes the i-th component of the vectors v and x, respectively. The velocity $v_\alpha \in \mathcal{RT}_0(E)$ can be easily evaluated component-wise by a linear interpolation between the normal velocities on opposing face midpoints, which are computed by (4.4). Note, that the polynomial space for $\mathcal{RT}_0(E)$ defined by

$$\mathcal{RT}_0(\mathcal{T}_h, \Omega) = \{v \in [L^2(\Omega)]^d;\, v|_E \in \mathcal{RT}_0(E) \quad \forall E \in \mathcal{T}_h\}$$

is a subspace of $H(\mathrm{div}, \Omega)$.

Furthermore, the interpolation of phase velocities into the $\mathcal{RT}_0$ space has two practical advantages:

1. the calculation of the solute transport can be performed on a grid not identical to the grid used in the two-phase calculations;
2. repetitive evaluation of (4.4) to solve the component transport problem is rather expensive; the interpolation saves many function evaluations in (4.4) and improves the code performance.

4.3 Component Transport Problem

The sets of equations (3.1a) and (3.3) are both advection-diffusion-reaction equations (ADREs) in the form

$$\frac{\partial (RC)}{\partial t} + \nabla \cdot j = q \text{ in } \Omega \times [0, T], \tag{4.5a}$$

$$j = vC - D\nabla C, \tag{4.5b}$$

which are subject to the boundary conditions

$$C = C^D \text{ on } \Gamma^D, \qquad j \cdot n = \eta \text{ on } \Gamma^N, \qquad j \cdot n = (vC - D\nabla C) \cdot n \text{ on } \Gamma^O, \tag{4.5c}$$

and initial conditions

$$C(x, 0) = C_0(x) \text{ in } \Omega. \tag{4.5d}$$

Model (4.5) describes the transport of a component, or a system of components with concentration(s) C via the flux j including advection with velocity v and diffusion with coefficient D, whereas reactions are modeled using the source-sink term q. The term R denotes fluid content, but it can also express the retardation caused by processes like adhesion.

The special case of the Neumann boundary conditions for $\eta = 0$ is known as the *no-flux* condition. For pure advection, the specification of the values on the inflow boundary, where

$v \cdot n < 0$, is sufficient. However, for the advection-diffusion problem with small diffusion coefficient, where the Péclet number (see Section 4.4.6) is large, the Dirichlet condition at the outflow boundary, where $v \cdot n > 0$, will give rise to a *boundary layer* problem, see Hundsdorfer and Verwer (2003). In this case the outflow boundary condition with $D = 0$ is applied, which is essentially a *do-nothing* boundary condition and allows the solute to leave the domain freely.

4.3.1 Space Semi-Discretization

The semi-discrete CCFV scheme for solving the transport equation (4.5) in either its hyperbolic or parabolic form is given as follows: Find a piecewise constant solution representation in space and continuous in time $C_h(t) \in P_0(\mathcal{T}_h)$ that for all $u \in P_0(\mathcal{T}_h)$ function C_h solves the equation

$$\begin{aligned} &\frac{\partial}{\partial t} \sum_{E \in \mathcal{T}_h} \int_E R C_h u \, dx + \sum_{\gamma \in \mathcal{F}_h^i} \int_\gamma C_h v \cdot n_\gamma [u] \, ds - \sum_{\gamma \in \mathcal{F}_h^i} \int_\gamma D \nabla C_h \cdot n_\gamma [u] \, ds \\ &+ \sum_{\gamma \in \mathcal{F}_h^{\partial\Omega} \cap (\Gamma^D \cup \Gamma^O)} \int_\gamma (C_h v - D \nabla C_h) \cdot n_\gamma u \, ds + \sum_{\gamma \in \mathcal{F}_h^{\partial\Omega} \cap \Gamma^N} \int_\gamma \eta u \, ds = \sum_{E \in \mathcal{T}_h} \int_E q u \, dx. \end{aligned} \tag{4.6}$$

All integrals in (4.6) are again evaluated numerically by applying the midpoint rule. To evaluate the flux $S_{E,\gamma}$ through the face γ, the normal derivative of the concentration is evaluated by central finite differences and the diffusion coefficient is computed as an harmonic average:

$$-\int_\gamma D \nabla C_h \cdot n_\gamma \, ds \approx S_{E,\gamma} = -\frac{2D(x_{E_\gamma^+}) D(x_{E_\gamma^-})}{D(x_{E_\gamma^+}) + D(x_{E_\gamma^-})} \frac{|\gamma|}{d_{E,\gamma}} \left(C_h(x_{E_\gamma^+}) - C_h(x_{E_\gamma^-}) \right). \tag{4.7}$$

4.3.2 Upwinding

In order to preserve stability of the numerical scheme, we use the standard *first-order upwind method*. The concentration C_h for $x_\gamma \in \gamma$ in the advection term $C_h v \cdot n_\gamma$ is given by

$$C_h(x_\gamma) = \begin{cases} {C_h}^-(x_\gamma) & \text{if } v(x_\gamma) \cdot n_\gamma \geq 0 \\ {C_h}^+(x_\gamma) & \text{else,} \end{cases} \tag{4.8}$$

where the face concentrations ${C_h}^-$ and ${C_h}^+$ are given by (4.1). Full upwinding is a monotonicity preserving linear method but is only first-order accurate. It achieves its greater stability compared to the central differences by adding numerical diffusion (Steefel and Lasaga, 1994). In diffusion dominated cases, we can approximate the concentration as $C_h = \left({C_h}^- + {C_h}^+ \right)/2$, which corresponds to central differences in the finite difference method.

4.3.3 Slope Limiters for Linear Reconstruction

Even for linear advection problems, first-order accurate schemes are generally considered too inaccurate for most quantitative calculations, unless the mesh resolution is made excessively fine, thus rendering the schemes inefficient. The problem of numerical diffusion is most severe

in multi-dimensional problems where flow can be diagonal to rather than along the face orientations and in problems where transient, sharp concentration fronts occur (Steefel and Lasaga, 1994).

According to Godunov's theorem (LeVeque, 2002) there are no monotone linear schemes of order greater than one. This limitation of monotone linear schemes has motivated the development of non-linear higher-order accurate schemes which are still monotone and reduce the numerical diffusion significantly. The main idea of higher-order schemes is to reconstruct a piecewise polynomial function from cell averages. Considering element $E \in \mathcal{T}_h$ with barycenter x_E, the function representing the linear reconstruction can be written as

$$C_h^*(x) = C_h(x_E) + \sum_{i=1}^{d} \sigma_i \left(x - x_E\right)_i ,$$

where the slopes σ_i do not influence the average and thus the method is conservative:

$$\frac{1}{|E|} \int_E C_h^*(x)\, dx = C_h(x_E).$$

The function C_h^* is then used in the evaluation of the upwind values in (4.8) instead of C_h. The slopes σ_i have to be chosen in such a way that the total variation diminishing (TVD) property is maintained, for details we refer to Pietro and Ern (2012).

The slope limiter in the d-dimensional case for simple grid geometries can be seen as a sequence of d one-dimensional limiters. We define the upwind and downwind slopes as

$$\sigma_i^{\mathrm{up}} = \frac{C_h(x_E) - C_h(x_u)}{|x_E - x_u|}, \quad \sigma_i^{\mathrm{dw}} = \frac{C_h(x_d) - C_h(x_E)}{|x_E - x_d|},$$

where x_u and x_d denote the barycenter of neighbor elements of E in the i^{th} upwind and downwind direction, respectively. We compute the limited slopes σ_i on element E by the following limiters:

1. van-Leer's one-parameter family of minmod limiters (Kurganov and Tadmor, 2000; van Leer, 1979):
$$\sigma_i = \mathrm{minmod}\left(\theta\sigma_i^{up}, \theta\sigma_i^{dw}, \frac{\sigma_i^{up} + \sigma_i^{dw}}{2}\right), \tag{4.9}$$
where parameter $\theta \in [1, 2]$ determines the resulting slope;

2. superbee limiter by Roe (1986):
$$\sigma_i = \mathrm{maxmod}\left(\sigma_i^1, \sigma_i^2\right), \tag{4.10}$$
where
$$\sigma_i^1 = \mathrm{minmod}\left(\sigma_i^{up}, 2\sigma_i^{dw}\right), \qquad \sigma_i^2 = \mathrm{minmod}\left(2\sigma_i^{up}, \sigma_i^{dw}\right).$$

The generalized minmod function for real numbers $z_1, \dots, z_k$ is defined as

$$\operatorname{minmod}(z_1, \dots, z_k) = \begin{cases} a \min(|z_1|, \dots, |z_k|) & \text{if } a = \operatorname{sgn}(z_1) = \cdots = \operatorname{sgn}(z_k), \\ 0 & \text{otherwise.} \end{cases}$$

while the maxmod function for real numbers a and b is given by

$$\operatorname{maxmod}(a, b) = \begin{cases} a & \text{if } |a| \geq |b| \\ b & \text{otherwise.} \end{cases}$$

In this work we use only the two limiters described above that guarantee second-order accuracy for smooth solutions while still satisfying the TVD property. With $\theta = 1$ the limiter (4.9) corresponds to the ubiquitous minmod limiter (LeVeque, 1990; Roe, 1986). For parameter $\theta > 1$, the slopes are steeper and the limiter is less dissipative.

4.3.4 Finite Volume Reconstruction

Because the discrete solution C_h is cell-wise constant, the regularity of the solution is low. In order to be able to compare the CCFV solution to an analytical solution or with other discretization methods, we require a higher regularity of the CCFV solution. Inspired by results of Eymard et al. (2001); Vohralík (2007) and Vohralík (2008), we locally postprocess the approximate solution C_h to get a postprocessed approximation solution $\tilde{C}_h$, which preserves exactly the given discrete diffusive fluxes and whose mean value in each cell is identical to the original constant approximation C_h.

In the postprocessing, we use some additional knowledge that we have from the CCFV scheme: the fluxes $S_{E,\gamma}$ defined in (4.7). For element-wise constant diffusion coefficients, we define $\tilde{C}_h$ as the weak solution of the following local problems:

$$-D\nabla \tilde{C}_h|_E \cdot n = \frac{S_{E,\gamma}}{|\gamma|} \quad \forall \gamma \in \partial E, \quad \forall E \in \mathcal{T}_h, \tag{4.11a}$$

$$\frac{1}{|E|} \int_E \tilde{C}_h \, dx = C_h \quad \forall E \in \mathcal{T}_h. \tag{4.11b}$$

For regular tetrahedral meshes, $\tilde{C}_h$ given by (4.11) is a piecewise second-order polynomial of the form

$$\tilde{C}_h(x) = \sum_{j=1}^{d} \left(a_{E,j} x_j^2 + b_{E,j} x_j \right) + c_E \quad \forall x \in E, \tag{4.12}$$

where the coefficients $a_{E,j}, b_{E,j}, c_E$ in the postprocessing are computed locally on element E.

Vohralík (2008) originally presented this postprocessing to obtain a potential suitable for energy error measuring (the piecewise gradient of the original cell-wise constant approximation is zero). Furthermore, it can be used for a posteriori error estimate of residual type, which are fully computable, so that it can serve both as an indicator for adaptive refinement and for the actual control of the error (Vohralík, 2008). In this work, we use the postprocessing only for ADREs

in numerical experiments, where the solution computed by the CCFV method is compared to an analytical solution or with other discretization methods.

4.4 Time Discretization

So far we have only discussed the spatial discretization of two-phase and component transport problems, leading to semi-discrete systems of ODEs for the solution vector $U = U(t)$

$$U'(t) = L(U(t)), \quad 0 < t < T, \quad U(0) = U_0, \tag{4.13}$$

with $U(t) = (U_j(t))_{j=1}^m \in \mathbb{R}^m$, m being proportional to the number of degrees of freedom (DOF) in the semi-discrete system. For the two-phase problem (4.2) together with CCFV we have $m = 2N_h$ and for the semi-discretization of the transport problem (4.5) containing N_c components, there are $N_c N_h$ DOFs. The initial solution U_0 is given by the initial conditions of the original PDEs.

The time interval $[0, T]$ is subdivided into a finite number of time steps t^k, $0 = t^0 < t^1 < \cdots < t^M = T$, with time steps $\Delta t^n = t^{n+1} - t^n$. A superscript n indicates the value of a function at the discrete time t^n, so that, e.g. $f^n = f(t^n)$.

4.4.1 Implicit Runge-Kutta Methods

To discretize the ODEs arising from the semi-discretization of the two-phase flow or reactive transport, we employ general diagonally implicit Runge-Kutta (DIRK) one step schemes, because they are A-stable and useful for stiff problems. They also exhibit a significant computational advantage, because the coefficient matrix is lower triangular with all diagonal elements equal and the stages can be computed independently.

In addition to the standard implicit Euler and Crank-Nicolson scheme, we also evaluated a strongly S-stable DIRK of order 2 in 2 stages and of order 3 in 3 stages (for details see Alexander, 1977); they are denoted as Alexander2 and Alexander3 in this work.

4.4.2 Explicit Runge-Kutta Methods

As an alternative to the DIRK methods when solving ADREs, explicit time integration can be used. The explicit methods avoid the solution of the (non-)linear system of equations, but the maximal time step size is restricted to ensure numerical stability.

Applying the explicit Euler time integration to (4.13) yields the fully-discrete form

$$U^{n+1} = U^n + \Delta t^n L(U^n). \tag{4.14}$$

The forward Euler time discretization is stable with respect to the L^∞-norm, i.e.

$$\|U^{n+1}\|_\infty \leq \|U^{n+1}\|_\infty \quad \forall n \geq 0, \tag{4.15}$$

for a sufficiently small time step Δt^n dictated by the CFL condition

$$\Delta t^n \leq \Delta t_{cfl}. \tag{4.16}$$

Here, Δt_{cfl} is the largest allowable step size that will guarantee that the stability property above will hold for forward Euler with the given PDE and spatial discretization. The time step restriction for explicit methods is discussed in details in Section 4.4.5.

The transport problem was subsequently extended to second-order accuracy in space using slope limiter techniques. In order to fully exploit this improvement in spatial accuracy, we also need to improve the accuracy in time by switching to higher-order accurate time integration methods. A class of higher-order accurate time integration methods that preserve stability properties of the fully-discrete scheme with explicit Euler time integration (4.14) is referred to as *Strong Stability Preserving* (SSP) methods (Gottlieb and Gottlieb, 2003; Gottlieb et al., 2001). These methods were originally developed by Shu (1988) and called TVD Runge-Kutta methods.

A general m stage RK-SSP method can be algorithmically represented as

$$\tilde{U}^0 = U^n, \tag{4.17a}$$

$$\tilde{U}^i = \sum_{k=0}^{i-1} \left(\alpha_{ik} \tilde{U}^k + \Delta t^n \beta_{ik} L(\tilde{U}^k) \right), \quad i = 1, \ldots, m, \tag{4.17b}$$

$$U^{n+1} = \tilde{U}^m, \tag{4.17c}$$

where $\alpha_{ik} \geq 0$ and $\alpha_{ik} = 0$ only if $\beta_{ik} = 0$. This representation of RK methods can be converted to a standard Butcher form, but the conversion is not unique and for consistency we require $\sum_{k=0}^{i-1} \alpha_{ik} = 1$ (Pareschi and Russo, 2005). If the explicit scheme can be written in the form (4.17) with non-negative coefficients β_{ik} then it is a convex combination of explicit Euler steps with step sizes $\frac{\beta_{ik}\Delta t^n}{\alpha_{ik}}$. SSP-RK methods are called optimal if the time step restriction corresponds to the time step restriction for explicit Euler method, which is formalized in the following theorem (Shu, 1988):

Theorem 1 (SSP optimal methods)
If the explicit Euler method (4.14) *is* L^∞*-stable subject to the* CFL *condition* (4.16)*, then every optimal SSP-RK method is* L^∞*-stable under the same time step restriction.*

Furthermore, SSP methods up to (and including) third-order for ODEs with non-linear operators L do not require any additional stages or function evaluations compared to general explicit RK methods (Gottlieb et al., 2001). We use the second- and third-order non-linear SSP-RK methods given in Shu (1988), denoted by Heun and Shu3, respectively, for details see Appendix A.1.1. Both of these methods are optimal in the sense given above.

4.4.3 IMEX Runge-Kutta Methods

As a general rule, it is best to solve non-stiff problems using explicit methods. This should be expected to achieve acceptable accuracy with minimal costs. However, as problems become

increasingly stiff, stability rather than accuracy becomes the dominant consideration, and implicit methods become the more appropriate choice.

The most simple decoupling of the main processes in ADRE from one another is to use the OS technique. However, using OS techniques can give rise to large splitting errors (Verwer et al., 2004). For many reactive transport processes, the natural splitting is into two parts: a) one of which is non-stiff, or mildly stiff, and suited for explicit treatment and b) a stiff term, which is suited for implicit time integration. The RK-IMEX methods consist of suitable mixtures of implicit and explicit methods and are used without formal splitting.

Suppose that the semi-discrete system is given by

$$U'(t) = L_1(t, U(t)) + L_2(t, U(t)), \tag{4.18}$$

where L_1 is a non-stiff term suitable for explicit discretization (e.g. discretized advection), and L_2 is a stiff term requiring an implicit treatment (e.g. diffusion or stiff reactions).

A simple example of RK-IMEX methods is the θ-RK-IMEX method Koto (2008b) defined by

$$\frac{U^{n+1} - U^n}{\Delta t^n} = L_1(t^n, U^n) + (1-\theta)L_2(t^n, U^n) + \theta L_2(t^{n+1}, U^{n+1}), \tag{4.19}$$

with parameter $\theta \geq \frac{1}{2}$. Here, the explicit Euler method is combined with the A-stable implicit θ-method and is of first-order in accuracy. Other RK-IMEX methods used in this work are summarized in appendix A.1.2. Trapez-IM, Alexander2-IM and Pareschi2 belong to second-order schemes, whereas Ascher3 is third-order accurate in time.

Boscarino et al. (2013) used RK-IMEX methods to solve advection-diffusion equation, where the linear diffusion was solved fully implicitly and non-linear advection was solved using explicit time integration. Numerical results showed that this approach is able to capture the correct behavior of the system at lower computational costs than explicit schemes, because the CFL restriction for the parabolic part (diffusion) can be removed. Furthermore, their scheme avoids implicit solves of non-linear algebraic equations.

The RK-IMEX method remains stable for time steps much longer than those that would be possible for a purely explicit methods. However, the analysis of the stability of RK-IMEX methods is still under investigation; the stability of several methods is examined in Calvo et al. (2001); Koto (2008a,b); Pareschi and Russo (2000) among others. Note, that the stability of explicit method for explicit part and stability of implicit methods for stiff part do not imply the stability of the RK-IMEX scheme.

4.4.4 Reaction Problem

In case of full operator splitting, when the reaction term is not handled in (3.2), we solve the system of ODEs (3.1b) element-wise using an embedded Runge-Kutta-Fehlberg (RKF45) method (Hairer et al., 1993). This method allows for an automatically determined adaptive step size to reduce error in the solution. For highly stiff ODEs or for a system of differential-algebraic equations, implicit time integration together with Newton's method can be used instead of RKF45.

4.4.5 CFL-like Condition

If the component transport equation (4.5) is discretized with an explicit method in time, then the time step needs to be restricted to preserve stability. The principle behind the time step restriction is the physical transport on a given grid. If a tracer is moving across a discrete spatial grid, the time step duration must be less than the time for the tracer to travel to adjacent elements. Specifically, if the tracer is able to flow through one grid element in one time step.

The time step restriction is typically associated with an upper boundary for the Courant-Friedrichs-Lewy (CFL) number ν. The CFL condition relates the length of the time step to a function of the interval lengths of the spatial discretization and of the maximum speed with which information can travel in the physical space.

Based on the CCFV spatial discretization for ADRE (4.5), we define the outflow flux function on an element $E \in \mathcal{T}_h$ by

$$O(E) = \sum_{\gamma \in \partial E} \left(L_g \max(0, v \cdot n_\gamma) + \frac{D}{d_{E,\gamma}} \right) |\gamma|, \tag{4.20}$$

where $L_g > 0$ denotes the Lipschitz constant of the hyperbolic numerical flux; for limiters discussed in Section 4.3.3 a reasonable value for L_g is 2 (Verwer et al., 2004), whereas for upwind schemes without flux reconstruction $L_g = 1$. The function (4.20) measures the numerical outflow flux from the grid cell E. The specific time T_s needed by the tracer to leave the grid cell E is given by

$$T_s(E) = \frac{R|E|}{O(E)}. \tag{4.21}$$

To ensure that the tracer concentration does not turn negative in any mesh cell in one time step and to fulfill the condition on maximal travel distance, we define a CFL-like number ν_l by

$$\nu_l = \frac{\Delta t}{\min_{E \in \mathcal{T}_h} T_s(E)}. \tag{4.22}$$

The maximal CFL-like number value of 1 indicates that the tracer is able to flow through one grid element during one time step.

The time step restriction (4.22) can also be computed for one-dimensional problems. Since the measure of γ is not defined, we set $|\gamma| = 1$. For regular grids with mesh size h together with an upwind scheme the CFL-like condition (4.22) leads to the well know CFL condition. For pure advection ($D = 0$), one obtains

$$\nu = \frac{v \Delta t}{h} \tag{4.23}$$

and for pure diffusion ($v = 0$) the CFL condition is given by

$$\nu = \frac{2D \Delta t}{h^2}. \tag{4.24}$$

Thus, Δt is of the order h^2 for large D and of the order h for $D \leq h$. In cases where the

diffusion coefficient is larger than the mesh size, it is therefore advisable to use an implicit scheme which completely eliminates the stability breakdown problem due to time step size.

4.4.6 Péclet Number

The ratio of the rate of physical advection by the flow to the rate of diffusion regarding to the element size h is defined by a dimensionless grid Péclet number

$$\mathrm{Pe}_{\mathrm{g}} = \frac{hv}{D}. \tag{4.25}$$

The grid Péclet number can be used to decide whether the transport process in ADRE (4.5) is locally (in the grid cell) advection or diffusion dominated. It also imposes a restriction on the mesh size independent of the time step for central differences instead of upwinding in the advection term, see Section 4.3.2. For $\mathrm{Pe}_{\mathrm{g}} < 2$ the central difference formulation is unconditionally stable. On the other hand, for grid Péclet numbers greater than 2, the central differences are not stable and spurious oscillations can occur.

A combination between central differences and upstream weighting (upwind) formulation is a power law scheme proposed by Patankar (1980), where the solution approach switches between a fully centered form at $\mathrm{Pe}_{\mathrm{g}} < 2$ to an upwind formulation at $\mathrm{Pe}_{\mathrm{g}} > 10$.

4.5 Implementation

All numerical methods, algorithms and discretization schemes described in this chapter have been implemented and the numerical simulations were performed in the C++ framework DUNE (Bastian et al., 2008a,b), particularly in the discretization module dune-pdelab (Bastian et al., 2010).

Grid

Our problems are limited to simple (rectangular, axis-parallel) geometries, so we were able to use the structured rectangular grid YaspGrid for all simulations. The overlapping domain decomposition methods with the Schwarz overlap allows us to simulate problems involving large grids on parallel computers. The overlap of one cell was chosen for all parallel computations.

Non-Linear Solver

The arising non-linear equations are linearized with an inexact Newton's method, the Jacobi matrix is derived through one-sided numerical differentiation. To increase the convergence region of Newton's method, we employ a line search strategy (Hackbusch and Reusken, 1989).

In order to improve control over the non-negativity constraint of the concentrations to solve the ADR systems (4.5) in the GIA approach, the original Newton's method is slightly modified. The resulting vector after each iteration of Newton's method is controlled and negative values

are set to zero. This modification improves the convergence behavior for ADR systems and bigger time steps are allowed without controlling the solution after each time step. Another solution for this issue would be to use logarithmic value of the concentration as in Samper et al. (2009) and Amir and Kern (2010). However, evaluating the logarithmic functions can be very demanding.

Linear Solvers

The resulting linear system is solved with a BiCGStab iterative solver with a SSORk preconditioner or an algebraic multigrid preconditioner (Blatt, 2010). Smaller matrix problems were solved using the direct solver SuperLU.

4.6 Solution Procedure

We use a sequentially coupled non-iterative methodology to solve the multi-phase flow, multi-component transport and chemical reactions similar to Xu and Pruess (2001) implemented in code TOUGHREACT and to Lichtner (1996) implemented in code MULTIFLO. The solution algorithm for two-phase flow and reactive transport is represented in Fig. 4.2. At each new time step, we first solve simultaneously the flow equations (3.2) in order to obtain the pressure, saturation and velocity flow field as functions of position. Second, we solve the transport model (3.3) including advection and diffusion on a component basis. In the third step, the resulting cell concentrations obtained from the transport are substituted into the chemical reaction model (3.4). The alternative to the second and third steps is GIA to solve system (3.5) fully implicitly. This three-step approach (two-step in the case of GIA) can be justified based on the different time scales of the processes involved.

4.6.1 Adaptive Time Stepping

We provide an adaptive time stepping scheme which ensures a reliable, robust and effective solution of the non-linear equations describing two-phase flow and reactive transport based on the present difficulty of the concrete problem. Without the adaptation strategy the simulation of complicated problems would not be possible. In the overall scheme the time step Δt_f for the two-phase system may be larger than the time step Δt_c for the reaction-transport part and several steps for the reactive transport are applied per two-phase time step.

Two-Phase Flow

In the first step, the two-phase problem with time step Δt_f is solved. We control the time step size for the two-phase flow problem using a simple but efficient scheme: the size of the time increment Δt_f is determined based on the absolute change in saturation and the convergence of Newton's method during the last time step. To reduce the operator splitting error between phase transport and component transport, the maximal absolute change per-cell saturation in one time step Δt_f is limited to 0.1. This choice is suitable for our applications, because

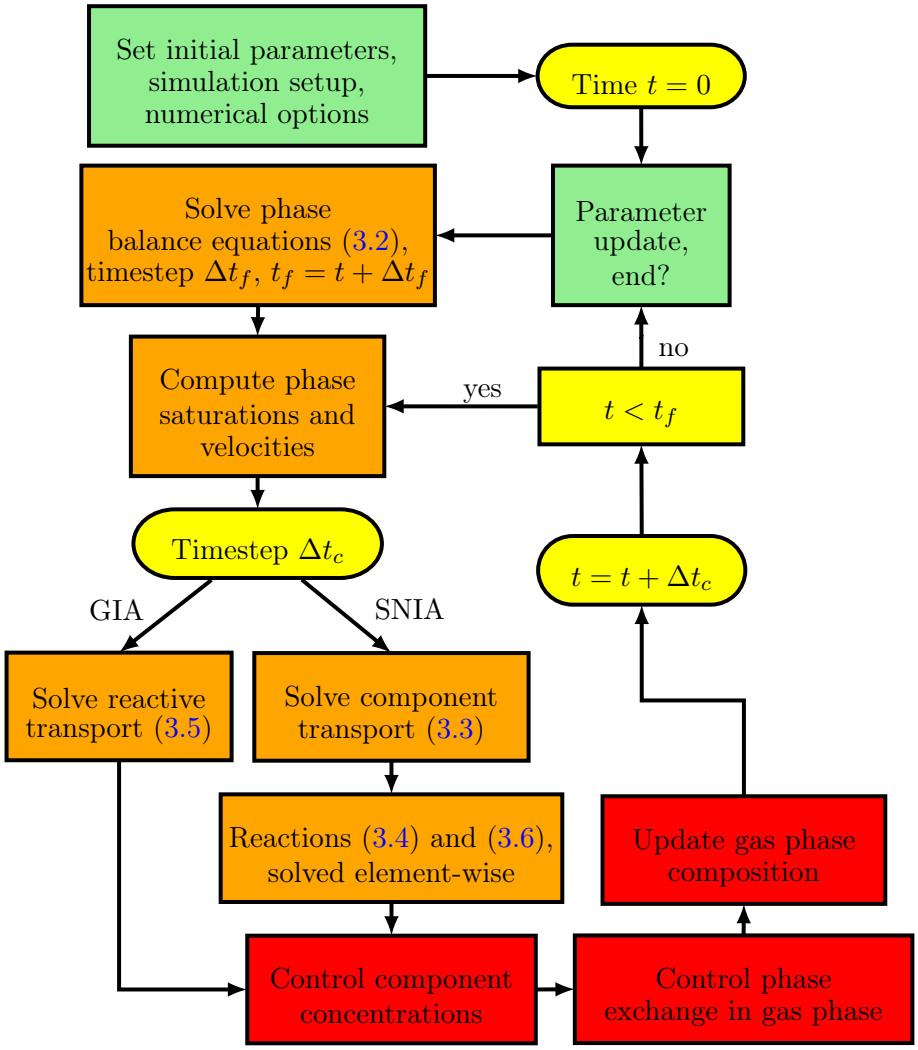

Fig. 4.2: Flow chart summarizing solution algorithm.

the system contains water and air and sharp saturation fronts are not expected. For other application (e.g. DNAPL infiltration in field-scale studies) this criterion should be modified and further investigated.

We detect non-convergence of the time step based on the number of Newton's iterations, line search iterations and linear solver breakdown; in this case, we retry the time step with a reduced time increment $c_r \Delta t_f$. This algorithm ensures that the only possibility for complete convergence failure is if the solution does not converge for the specified minimum time step. On the other hand, if Newton's method converges in less than 6 iterations and the time step was not reduced in the previous time step, next time step will increase to $c_i \Delta t_f$. The constants $c_r < 1$ and $c_i > 1$ can be specified by the user, the choice $c_r = 0.6$ and $c_i = 2$ is used for all two-phase simulations.

Reactive Transport

The time step Δt_c for the reactive and transport part is chosen based on the transport velocity and the rate of chemical reactions to reduce the splitting error between component transport and reactions in the SNIA variant. For details about the choice of Δt_c see Chapter 5.

For GIA-based methods Δt_c is restricted by the convergence of Newton's method and a similar strategy to the solution of the two-phase problem can be applied. However, because we use GIA together with full upwinding and implicit time integration, it is prone to add numerical diffusion in advection-dominated cases for large time steps and the maximum time step needs to be capped at $\Delta t_{c,max}$. In order to reduce numerical diffusion, $\Delta t_{c,max}$ should not exceed time step corresponding to the CFL number $\nu = 10$ for pure advection problem computed by (4.23). We prefer GIA during periods of quasi steady-state, when the concentration changes in the system are slow and greater time steps can be expected to reduce computational effort time.

If the flow in the liquid phase is advection-dominated and exhibits sharp concentration fronts, we prefer SNIA and explicit time discretization together with higher-order space discretization. Transport equations for each liquid component are solved with time step Δt_t, which is defined as the maximal time step satisfying the CFL-like condition (4.22) for all liquid components. In the gas phase, transport is often diffusion dominated and can be solved using implicit methods. The transport time step Δt_t is smaller than Δt_c and it holds $\Delta t_c = \sum \Delta t_t$. The reaction time step Δt_r in the third part of the solution approach is automatically chosen with the predictor-corrector method RKF45.

Solution Control

In order to verify the consistency of the reaction and transport step, we control the resulting values of concentrations and retry with a smaller time step value in case of failure. While negative concentration values only occur very rarely if $\Delta t_c, \Delta t_t$ and Δt_r were chosen correctly, this control step is crucial to guarantee the correctness of the solution.

The gas density depends on the gas composition and is updated based on the new component concentrations in the gas phase after each transport step followed by the gas velocity update. If the gaseous composition is not taken into account, we compute the phase velocities only one time per two-phase time step Δt_f.

If there is high phase exchange in the system and gas molecules are added to or removed from the gas phase, the time step Δt_f needs to be reduced. The element-wise loss or win of gas molecules during the phase exchange needs to incorporated into the solution of the two-phase problem as an inner source term. We will investigate this part of splitting algorithm in the future model development; in this work we assume a constant mole density ν_g in the gas phase.

4.6.2 Transport of Gaseous Components

The non-standard difficulty for transport in the gaseous phase is that the gas saturation may be zero in some parts of the domain. We require that the following assumption holds: *If the*

gas saturation in some cell $E \in \mathcal{T}_h$ is non-zero at time t then it is also non-zero at $t+\Delta t_f$ after the two-phase flow step. In practice, non-zero is replaced by $s_g > \epsilon$. This can be ensured by setting the relative permeability to zero for non-zero but small saturation, which is equivalent to a small residual saturation of the gas phase $s_{r,g}$.

All cells with $s_g \leq \epsilon$ at $t + \Delta t_f$ are treated as "dry cells" and omitted in the transport step (for advection as well as for diffusion). For implicit time discretizations, trivial equations are assembled. For the "wet cells" with $s_g > \epsilon$ at $t + \Delta t_f$ the usual component transport equations (3.3) for gaseous species are solved.

4.7 Parameter Estimation

In this work, we investigate several different kinetically controlled bio-chemical reactions. However, the kinetically controlled reactions have one drawback: if the kinetic rates are not known from the literature (which is often the case), they need to be determined based on laboratory experiments and observed data. Parameter estimation techniques allow us to determine the rates of chemical reactions and compare the level of correspondence between measured data and solution of given problem with estimated parameters.

Model Problem

The temporal development of a dynamic system with the components $z_1, \ldots, z_n$ is given by a system of ordinary differential equations (in vector notation)

$$\frac{\mathrm{d}\boldsymbol{z}}{\mathrm{d}t} = f\left(\boldsymbol{z}; \boldsymbol{\theta}; t\right), \quad \boldsymbol{z}(0) = \boldsymbol{z}_0$$

with dependent variables $\boldsymbol{z} = (z_1, \ldots, z_n)^T$ and parameters $\boldsymbol{\theta} = (\theta_1, \ldots, \theta_p)^T$. Let $y_{i,j}$ denote measurements (or functions of the measurements) taken at time points $t_j, j = 1, \ldots, m$. We assume the measurement errors to be normally distributed with mean 0 and standard deviation w_{ij}.

The problem to be solved is the minimization of the objective function (residuum)

$$\mathcal{R}(\boldsymbol{\theta}) = \sum_{i=1}^{n} \mathcal{R}_i(\boldsymbol{\theta}) = \sum_{i=1}^{n} \sum_{j=1}^{m} \left(\frac{z_{ij}(\boldsymbol{\theta}, t_j) - y_{ij}}{w_{ij}} \right)^2 \tag{4.26}$$

over the set of admissible parameter values with appropriate weighting factors w_{ij}. The index j in z_{ij} denotes the value of component z_i at time point j. Eq. (4.26) can also be interpreted as a log-likelihood estimator for the parameters, see Seber and Wild (2003).

The coefficient of determination $\mathcal{R}^2$, a number that indicates how well data fits a model, is computed as

$$\mathcal{R}^2(\boldsymbol{\theta}) = 1 - \frac{\sum_{i=1}^{n} \sum_{j=1}^{m} \left(z_{ij}(\boldsymbol{\theta}, t_j) - y_{ij}\right)^2}{\sum_{i=1}^{n} \sum_{j=1}^{m} \left(y_{ij}\right)^2}. \tag{4.27}$$

To minimize the residuum $\mathcal{R}$ and to solve the optimization problem, we use the Levenberg-Marquardt-Algorithm (LMA) (Moré, 1978) with the sensitivities derived by numerical differentiation. The code for parameter estimation was originally implemented by Olaf Ippisch in a computer code fitphi and applied in Ippisch et al. (2006). The parameter estimation is independent of the forward problem which can be a system of ODEs or PDEs.

4.8 Final Remarks

In this chapter we have described the used numerical schemes in detail. We solve the two-phase problem using CCFV space discretization together with unconditionally stable implicit methods. The component transport problem is solved using first- and second-order CCFV methods. For the simulation of advection-diffusion problems in diffusion dominated cases we use CCFV with implicit time integrators, which enables large time steps.

In advection-dominated cases we use explicit one-step methods for the time discretization. The time step is always restricted by a CFL condition, see Section 4.4.5. Furthermore, upwinding is needed for stability reasons which is only first-order accurate. For this reason we use CCFV with a second-order Godunov reconstruction of upwind fluxes and slope limiters. These limiters guarantee second-order accuracy for smooth solutions while still satisfying the TVD property. Most TVD schemes also satisfy the strict maximum principle, even in multi-dimensions. TVD schemes can be designed for any formal order of accuracy for solutions in smooth, monotone regions. Unfortunately, TVD schemes locally degenerate to piecewise constant approximations at smooth extrema which locally degrades the accuracy (Osher et al., 1985).

To overcome this difficulty, other schemes were developed in the literature: essentially non-oscillatory (ENO) reconstruction schemes (Harten et al., 1987) and weighted ENO schemes (WENO) (Liu et al., 1994). These schemes do not insist on strict TVD properties, therefore they do not satisfy the maximum principle. On the other hand, they can be designed to be arbitrarily higher-order accurate for smooth solutions. The advantage of WENO schemes is that they do not create oscillations for solutions with strong shocks even for complicated meshes. Therefore, WENO schemes are often used as limiters not only for CCFV, but also for discontinuous Galerkin method (DG) (Zhu et al., 2008). We do not use the WENO schemes in this work, but they can be tested in a future model development.

Although we apply the numerical simulator in problems involving only simple geometries (see Chapters 6, 7 and 8), the operator splitting concept is independent of the chosen numerical scheme. On complicated geometries unstructured grids with discretization schemes like DG can be used for both the two-phase problem (Bastian, 2014) and the component transport problem (Bastian, 2003). The choice of numerical methods for the simulation of a specific problem has a significant impact on the obtained accuracy. We discuss this impact in Chapter 6 in more detail. We compare the performance of CCFV and DG with linear basis functions to solve the ADRE problem (Eq. 4.5) in advection-dominated cases. The implementation of DG is described in detail in Bastian (2003). The unphysical oscillations in higher-order DG schemes are suppressed by slope limiters. The slope limiters in DG are applied after each stage in the Runge-Kutta time stepping scheme. That is the difference compared to the CCFV scheme, where the flux reconstruction is used before each stage in the Runge-Kutta method.

Chapter 5

Operator Splitting

In the operator splitting approach for reactive transport, the physical transport and reactive processes are generally decoupled. In this chapter we will take a look at the operator splitting (OS) of the ADR problem (4.5) and answer the question in which situations and under which circumstances the operator splitting method works well. From the theoretical point of view, the viability of any OS method is primarily determined by the splitting error introduced by solving the sub-problems one after another in a decoupled manner.

The first part of this chapter deals with theory about operator splitting. We conclude this theoretical part with a theorem describing the conditions under which no operator splitting error arises in ADR problems. In the second part we describe some possibilities of operator splitting techniques for ADRE, define the measures for errors in the OS and characterize the time scales for each process based on a dimensionless numbers. We also describe the solution strategy eliminating the discretization error in the solution of each operator in ADRE which is subsequently used in the last part of this chapter where we analyze the OS error for simple one-dimensional problems which are relevant for reactive transport modeling of real applications.

5.1 Operator Splitting Theory

This section is based on work by D. Lanser (Lanser, 2002) about operator splitting and applications in air pollution modeling. The results are also well applicable to problems in reactive transport in porous media. We present an introduction to the analysis of operator splitting and provide insight into the splitting error for ADR problems in greater detail. These general ideas are independent of the particular spatial and temporal discretization used.

5.1.1 Linear ODE Problem

Let us first illustrate the notion of splitting by considering a linear, homogeneous ODE problem

$$\frac{\mathrm{d}C(t)}{\mathrm{d}t} = AC(t), \quad t \in [0,T], \quad C(0) = C_0, \tag{5.1}$$

and assume a two-term splitting for A, $A = A_1 + A_2$. The system (5.1) may be seen as e.g. a semi-discretization of a linear transport problem (4.6) with homogeneous boundary conditions. The solution of (5.1) at time $t^{n+1} = t^n + \tau$ is given by

$$C(t^{n+1}) = e^{\tau A} C(t^n). \tag{5.2}$$

If we apply A_1 and A_2 separately using first-order splitting (3.8), instead of the full A, then (5.2) can be approximated by

$$C^{n+1} = e^{\tau A_2} e^{\tau A_1} C^n \tag{5.3}$$

with C^n approximating $C(t^n)$.

The exponential of the matrix is defined by the power series and we have

$$e^{\tau A} = I + \tau(A_1 + A_2) + \frac{\tau^2}{2}(A_1 + A_2)^2 + \ldots,$$
$$e^{\tau A_2} e^{\tau A_1} = I + \tau(A_1 + A_2) + \frac{\tau^2}{2}(A_1^2 + 2A_2A_1 + A_2^2) + \ldots.$$

Replacing (5.2) by (5.3) normally introduces an operator splitting error. Inserting the exact solution C of the original problem (5.1) into (5.3) gives

$$C(t^{n+1}) = e^{\tau A_2} e^{\tau A_1} C(t^n) + \tau \rho_n, \tag{5.4}$$

with local truncation error ρ_n. The error thus satisfies

$$\rho_n = \frac{1}{\tau}\left(e^{\tau A} - e^{\tau A_2} e^{\tau A_1}\right) C(t^n) = \frac{\tau}{2}\left[A_1, A_2\right] C(t^n) + \mathcal{O}(\tau^2), \tag{5.5}$$

where

$$[A_1, A_2] = A_1A_2 - A_2A_1$$

is the commutator of A_1 and A_2. We can see that the splitting (5.3) is a first-order process unless A_1 and A_2 commute. When both matrices commute, we have

$$e^{\tau A_2} e^{\tau A_1} = e^{\tau A_2 + \tau A_1} = e^{\tau A}, \tag{5.6}$$

the splitting (5.3) is exact and it leaves no splitting error. It can be seen by using the power series expansion for the exponential function, see Hundsdorfer and Verwer (2003).

5.1.2 Abstract Initial Value Problem

We discussed the first-order time splitting for linear ODE problems (5.1). However, this discussion can also be extended to PDE. Considering directly the PDE problem will make it more clear in which cases the time splitting will be exact. We study the initial value problem for abstract autonomous systems

$$\frac{\mathrm{d}C(x,t)}{\mathrm{d}t} = f(x, C(x,t)), \quad t \in [0,T], \quad x \in \mathbb{R}^d, \quad C(x,0) = C_0(x). \tag{5.7}$$

With this abstract problem we may associate any ODE or PDE initial value problem in autonomous form without boundary conditions. In the case of a linear ODE problem, Eq. (5.7) simplifies to (5.1).

In the PDE case, the function f is to be seen as a spatial partial differential operator, e.g. for

the advection-diffusion-reaction system (4.5):

$$f(C) = -\nabla \cdot (vC) + \nabla \cdot (D\nabla C) + q(C), \tag{5.8}$$

where $C = C(x,t)$.

For simplicity we do not explicitly write the dependency of C and f on x. We assume C is from the function space $\mathcal{U}$ which is a real, sufficiently often differentiable space.

If the solution of (5.7) at time t^n is known, we define the solution operator $\mathcal{S}_\tau$ acting on $\mathcal{U}$ such that the solution of (5.7) at time $t^{n+1} = t^n + \tau$ is given by

$$C(t^{n+1}) = \mathcal{S}_\tau(C(t^n)). \tag{5.9}$$

This operator generalizes the exponential operator $e^{\tau A}$ of the linear ODE problem (5.1).

For simplicity, we assume a two-term splitting for f, $f = f_1 + f_2$, but the presented techniques can be generalized to multi-component splittings (Hundsdorfer and Verwer, 2003). We associate with f_1 and f_2 the solution operators $\mathcal{S}_{\tau,1}$ and $\mathcal{S}_{\tau,2}$. In the case of first-order splitting (3.8), the abstract initial value problem (5.7) then becomes

$$C^{n+1} = \mathcal{S}_{\tau,2}\left(\mathcal{S}_{\tau,1}(C^n)\right), \tag{5.10}$$

with C^n approximating $C(t^n)$. As above, by inserting the exact solution C of (5.7) into (5.10) and using Taylor expansion of $C(t^{n+1})$ around $t = t^n$, we obtain a relation similar to (5.4) for linear ODE problems

$$C(t^{n+1}) = \mathcal{S}_{\tau,2}\left(\mathcal{S}_{\tau,1}(C^n)\right) + \tau\rho_n, \tag{5.11}$$

where the local truncation error is given by

$$\rho_n = \frac{\tau}{2}\left[\frac{\partial f_1}{\partial C} f_2 - \frac{\partial f_2}{\partial C} f_1\right](C(t^n)) + \mathcal{O}(\tau^2). \tag{5.12}$$

In analogy to the linear ODE case, we call this bracketed term the commutator of the operators f_1 and f_2

$$[f_1, f_2](C) = \left[\frac{\partial f_1}{\partial C} f_2 - \frac{\partial f_2}{\partial C} f_1\right](C). \tag{5.13}$$

An important observation is that the local error in the splitting (5.10) is a first-order process unless operators f_1 and f_2 commute, similarly as for the linear ODE case. One can also prove by means of a Lie operator formalism the fact that the splitting process (5.10) leaves no splitting error if the commutator (5.13) is zero. We refer the reader to Lanser and Verwer (1999) and Hundsdorfer and Verwer (2003) for technical details.

5.1.3 Splitting for ADR in Initial Value Problems

We discuss in which situations an OS error occurs, when the influence of boundary conditions is not considered. Throughout the following analysis, we assume that (5.8) is linear with respect to advection and diffusion, but non-linear in the chemical reaction term q.

The commutativity of the advection, diffusion and reaction operators was studied in (Lanser, 2002; Lanser and Verwer, 1999) and can be summarized in the following theorem:

Theorem 2 (Splitting for ADRE**)**

1. *Advection commutes with diffusion if both v and D are independent of x.*
2. *Advection commutes with reaction if*
   a) q is independent of x and the velocity field is divergence-free ($\nabla \cdot v = 0$), or
   b) q is independent of x and linear in C.
3. *Diffusion commutes with reaction if q is linear in C and independent of x.*

This commutativity is of great importance: when the corresponding processes commute, we do not have any splitting error. As a consequence of Theorem 2, no splitting error of ADRE exists if all terms (v, D and q) are independent of x and q is linear in C. Note that the requirement q independent of x does not mean that q is independent of $C = C(x,t)$.

Advection and Diffusion

In real-world applications, v and D will not be independent of x and thus the splitting error does not vanish. For this reason, the second-order symmetrical Strang splitting is preferred.

Transport and Reaction

If we split transport (advection and diffusion) and reaction, and solve transport followed by reaction, the local truncation error has the form (Hundsdorfer and Verwer, 2003)

$$\rho_n = \frac{\tau}{2}\left[-\nabla\cdot(vq(C)) + \nabla\cdot(D\nabla q(C)) + q'(C)(\nabla\cdot(vC)) - q'(C)(\nabla\cdot(D\nabla C))\right](t^n) + \mathcal{O}(\tau^2). \tag{5.14}$$

A similar truncation error can be found for the second-order symmetrical Strang splitting scheme (Lanser, 2002). In practical applications, the reaction term q typically depends on C in a non-linear fashion $q(C) = LC + \tilde{q}(C)$: a linear part L plus a non-linearity $\tilde{q}$. If the linear operator L is independent of x, then the linear part drops out of the commutator, and the truncation error for the first-order splitting becomes

$$\rho_n = \frac{\tau}{2}\left[-\nabla\cdot(v\tilde{q}(C)) + \nabla\cdot(D\nabla\tilde{q}(C)) + \tilde{q}'(C)(\nabla\cdot(vC)) - \tilde{q}'(C)(\nabla\cdot(D\nabla C))\right](t^n) + \mathcal{O}(\tau^2). \tag{5.15}$$

In addition, if the velocity field is divergence-free and the reaction term q is independent of x (non-linearity of q is still allowed), the expression for the splitting error simplifies to

$$\rho_n = \frac{\tau}{2}\left[\nabla\cdot(D\nabla\tilde{q}(C)) - \tilde{q}'(C)(\nabla\cdot(D\nabla C))\right](t^n) + \mathcal{O}(\tau^2). \tag{5.16}$$

5.1.4 Boundary Value Problem

Until now we have assumed homogeneous boundary conditions. However, the major difficulties with operator splitting methods occur in problems where the boundary conditions are important. We note that the inhomogeneous boundary conditions will give an inhomogeneous term in the system disturbing the commutativity of the operators even if the assumptions required by Theorem 2 are fulfilled. Thus, traditional OS schemes are known to incur an error when a non-zero mass flux across the domain boundary is present (Kaluarachchi and Morshed, 1995; Simpson et al., 2005; Valocchi and Malmstead, 1992).

The boundary conditions may also affect the accuracy of splitting methods and even the order of Strang splitting may be reduced (Hundsdorfer and Verwer, 2003). This loss of convergence order caused by boundary conditions is often the main reason for the disappointing convergence behavior with splitting methods.

5.1.5 Summary

In this section we have shown that the error in the operator splitting depends on the size of the involved commutators. In situations satisfying the assumption of Theorem 2 no operator splitting errors arise. Otherwise we are able to describe the arising OS error in one splitting time step τ: e.g., equations (5.14-5.16) express the error for the first-order splitting if we split transport and reaction. However, we are not able to predict the accumulation and the propagation of the OS error during the whole simulation. Moreover, if we consider a PDE problem with inhomogeneous boundary conditions, the boundary conditions for the splitting sub-steps are missing. In the following, we study the arising OS errors in concrete problems.

5.2 Splitting Errors and Quantification

In order to get a better insight into the applicability of the OS methods, we investigate OS error in some simplified examples depending on the splitting time step τ, the type and the character of chemical reactions and the solute transport velocity. Table 5.1 contains a summary of the considered splitting strategies under investigation. The most popular schemes are A-D-R, where all three operators are solved separately (Clement et al., 1998), and the two-step scheme (AD-R), where the reaction follows the transport (Valocchi and Malmstead, 1992).

In the literature, one can also find other splitting schemes that differ in the sequence of the solution of each operator (e.g. Simpson et al., 2005). However, the difference is remarkable only in one splitting time step. Thus, the solution order of the involved operators has a negligible impact on the solution of given problem when more splitting time steps are used.

5.2.1 Mass Balance Errors

Firstly, we study the limitations of OS techniques based on total mass balance. The mass balance error in ADREs is a specific measure for the splitting error which was investigated

OS Approach	Solution Algorithm	Splitting Time Step
AD-R	1. advection-diffusion	τ
	2. reaction	τ
AD-RS	1. advection-diffusion	$\tau/2$
	2. reaction	τ
	3. advection-diffusion	$\tau/2$
A-D-R	1. advection	τ
	2. diffusion	τ
	3. reaction	τ
A-DR	1. advection	τ
	2. diffusion-reaction	τ
A-DRS	1. advection	$\tau/2$
	2. diffusion-reaction	τ
	3. advection	$\tau/2$
A-DS-RS	1. advection	$\tau/2$
	2. diffusion	$\tau/2$
	3. reaction	τ
	4. diffusion	$\tau/2$
	5. advection	$\tau/2$

Table 5.1: Investigated splitting methods for ADRE.

by many authors, e.g., Valocchi and Malmstead (1992). The one-dimensional ADRE with first-order reaction in a semi-infinite domain $\Omega = [0, \infty)$ can be written as

$$\frac{\partial C}{\partial t} + \nabla \cdot (vC - D\nabla C) = q = -\lambda C, \tag{5.17}$$

where C is the concentration of the solute, v is a constant velocity and D is the diffusion coefficient. The reaction term q models a first-order linear decay with reaction rate λ. The initial concentration is 0 in the whole domain, and at the inflow boundary a solute with concentration C_0 is added. The boundary condition can be of the Dirichlet type, where the inflow concentration is fixed

$$C(0, t) = C_0, \tag{5.18}$$

or of the Robin type (mixed boundary condition), which has the form

$$\left(vC - D\frac{\partial C}{\partial x}\right)(0, t) = vC_0. \tag{5.19}$$

Eq. (5.17) with either type of boundary condition on a semi-infinite one-dimensional domain has an analytical solution (Genuchten, 1981). We can also prescribe a Neumann boundary condition at the inflow (flux), but the concentration flux is hard to measure in experiments. For this reason we only consider ADR problem with boundary condition (5.18) or (5.19).

The choice of the boundary condition also influences the choice of OS technique. For the

Dirichlet boundary condition (5.18), the A-D-R and AD-R schemes applied to the advection-diffusion equation generally result in a different solution. This difference is caused by the splitting error in the A-D-R scheme, which occurs at the boundary. For advection dominated cases, the diffusion directly at the domain inflow is often negligible. In practical situations (laboratory experiments with solute inflow) we are not able to distinguish between the advection and the diffusion part of the transport and we prefer the Robin boundary condition (5.19), which includes the inflow solute concentration. Similarly, if we do not take into account the diffusion at the domain boundary in the A-D-R splitting scheme, A-D-R and AD-R schemes with Robin boundary condition result in the same solution.

Valocchi and Malmstead (1992) only considered Robin boundary condition and analytically derived the mass balance errors after the first splitting time step τ for AD-R and AD-RS schemes. Integrating the governing equation (5.17) together with (5.19) over the one-dimensional domain Ω, and using the fact that $C(x \to \infty) \to 0$, they obtain the ODE problem

$$\frac{\mathrm{d}M(t)}{\mathrm{d}t} = vC_0 - \lambda M(t), \quad M(0) = 0, \tag{5.20}$$

where $M(t)$ is the total mass in Ω computed as

$$M(t) = \int_\Omega C \mathrm{d}x = \int_0^\infty C \mathrm{d}x. \tag{5.21}$$

The ODE for the total mass (5.20) has the analytical solution $M(t) = \frac{vC_0}{\lambda}(1 - e^{-\lambda t})$. To compare the error in the OS approach to the exact solution, we define the relative mass error as

$$M_{err} = \frac{M - M_{os}}{M}, \tag{5.22}$$

where M_{os} is the total mass of the solution obtained using the operator splitting approach. The relative mass error after one splitting time step τ can be computed analytically, see Valocchi and Malmstead (1992) for details, and is expressed as

$$M_{err}(\tau) = 1 - \frac{\lambda\tau e^{-\lambda\tau}}{1 - e^{-\lambda\tau}} \text{ for AD-R}, \quad M_{err}(\tau) = 1 - \frac{\lambda\tau}{2}\frac{1 + e^{-\lambda\tau}}{1 - e^{-\lambda\tau}} \text{ for AD-RS}. \tag{5.23}$$

Figure 5.1a shows a plot of the magnitude of the relative mass error over one time step τ versus the factor $\lambda\tau$ for AD-R and AD-RS schemes. AD-RS has much smaller mass balance errors than AD-R for values of $\lambda\tau$ less than 1. The AD-R method overestimates the reaction rate which results in positive values of M_{err}, whereas the relative error in AD-RS remains negative, see also Table 5.2.

The analysis of the analytically computed mass error can be continued recursively. Kaluarachchi and Morshed (1995) have calculated the mass for (5.17) with (5.19) after n splitting time steps τ. The value of the mass for AD-R is then given by

$$M_{os}(n\tau) = \frac{vC_0\tau}{\lambda} e^{-\lambda\tau} \left(1 - e^{-n\lambda\tau}\right)$$

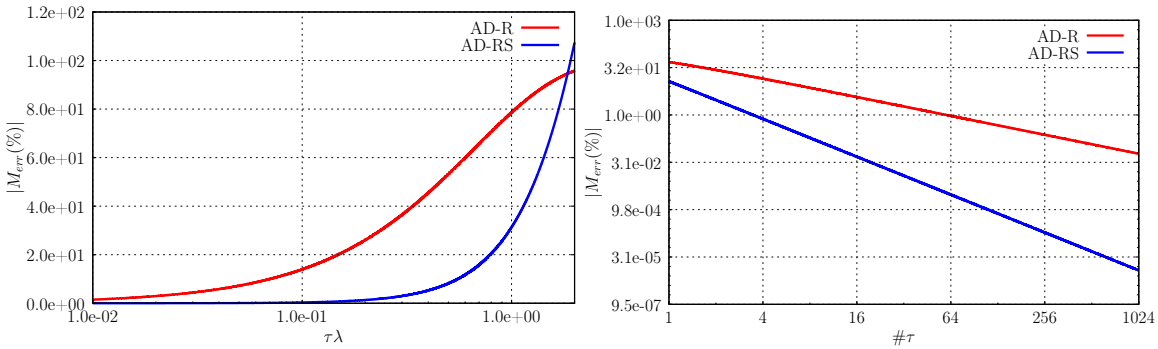

(a) (b)

Fig. 5.1: (a) Absolute value of relative mass error $M_{err}(\%)$ after one time step τ versus $\lambda\tau$. (b) Relative mass error at time $t = 0.6$ over number of splitting time steps ($\#\tau$) for problem (5.17), with $v = 1$ and $\lambda = 2$.

	A-DR		A-DRS	
$\#\tau$	$M_{err}(\%)$	rate	$M_{err}(\%)$	rate
1	4.83×10^{1}	-	-1.17×10^{1}	-
2	2.70×10^{1}	0.84	-2.98	1.97
4	1.43×10^{1}	0.92	-7.49×10^{-1}	1.99
8	7.31	0.96	-1.87×10^{-1}	2.00
16	3.70	0.98	-4.69×10^{-2}	2.00
32	1.86	0.99	-1.17×10^{-2}	2.00
64	9.35×10^{-1}	1.00	-2.93×10^{-3}	2.00

Table 5.2: Relative mass errors for linear decay with Robin boundary condition and convergence of OS methods for different splitting time steps τ at time $t = 0.6$ with parameters $v = 1$, $D = 10^{-3}$ and $\lambda = 2.0$.

and for AD-RS it becomes

$$M_{os}(n\tau) = \frac{vC_0\tau\left(1 + e^{-\lambda\tau}\right)}{2\lambda}\left(1 - e^{-n\lambda\tau}\right).$$

Fig. 5.1b shows the absolute value of the relative mass error M_{err} versus the number of time steps ($\#\tau$) for A-DR and AD-RS at time $t = 0.6$ with $v = 1$ and $\lambda = 2$. The AD-RS scheme is of second-order accuracy with regard to the splitting time τ while A-DR only obtains first-order accuracy. To reduce the mass error under 1% of the total mass, AD-R requires 64 time steps τ, whereas AD-RS needs only 4 steps.

5.2.2 Error Measurements

In many studies, the error induced by OS techniques was investigated only with respect to the total mass balance (Carrayrou et al., 2004). The A-DR and AD-RS OS schemes applied to a simple problem (5.17) with linear decay work reasonably well if we compare the total mass. However, the mass error does not say anything about the spatial distribution of the error. It

also does not fulfill the definition of a norm: even for zero mass error the OS solution does not necessarily correspond to the exact solution of a given problem.

For a more rigorous investigation we compare the exact solution u_e and the OS splitting solution u_τ. The error E_{rr} is given by

$$E_{rr} = u_e - u_\tau.$$

Furthermore, we define a relative error by

$$L_1^r = \frac{\|E_{rr}\|_1}{M}, \tag{5.24}$$

where $\|\cdot\|_1$ is the L_1-norm and M is the total mass of the exact solution u_e. The relative mass error norm L_1^r, corresponding to the L_1-error normalized by the total mass, is a better measure for the quality of the OS solution. If the OS method overestimate or underestimate consistently the exact solution in the whole domain (as e.g. for the problem (5.17) solved using the A-D-R scheme), the error computed by (5.24) corresponds to the mass error given by (5.22).

5.2.3 Characteristic Time Scales

In Section 5.2.1 we showed that the relative mass error of the OS for a simple problem (5.17) depends only on factor $\lambda\tau$, independent of the velocity and diffusion. However, in general the OS error depends on the nature of each operator. One of the major difficulties in coupling transport and chemical reactions is the wide range of spatial and temporal scales characterizing the various transport and reaction processes.

To be able to describe the relative velocities of each process in the system of ADREs, we define the characteristic times for advection t_a, for diffusion t_d and for reactions t_r as

$$t_a = \frac{l}{v}, \quad t_d = \frac{l^2}{2D}, \quad t_r = \frac{1}{\lambda_r}, \tag{5.25}$$

where l is a characteristic length and λ_r corresponds to the effective rate of chemical reactions. The characteristic length l can be related e.g., to the diameter of the spatial domain or to the spatial discretization of numerical schemes. In our applications the characteristic length l corresponds to the tracer transport distance in one splitting time step τ and is given by

$$l = v\tau + \sqrt{2D\tau}. \tag{5.26}$$

The characteristic length l in pure advection or pure diffusion corresponds to the length computed from (5.25) with characteristic time τ.

To specify the relationship between advection and diffusion in one step τ, we define a Péclet number Pe as

$$\mathrm{Pe} = 2\frac{t_d}{t_a} = \frac{vl}{D} = \frac{v\left(v\tau + \sqrt{2D\tau}\right)}{D}. \tag{5.27}$$

If the characteristic length is equal to the mesh size h, Pe given by (5.27) corresponds to the grid Péclet number $\mathrm{Pe_g}$ computed by (4.25).

The relationship between reaction and transport time scales has a significant impact on the applicability of OS methods to reactive transport problems. It can be estimated from advective and diffusive Damköhler numbers (Bahr and Rubin, 1987). The advection and diffusion Damköhler numbers Da_a and Da_d are defined as the ratio of the advection time scale (or diffusion time scale respectively) to the reaction time scale:

$$Da_a = \frac{t_a}{t_r} = \frac{l\lambda_r}{v}, \quad Da_d = \frac{t_d}{t_r} = \frac{l^2\lambda_r}{2D}.$$

If we take the advection and diffusion for a transport process with the transport time scale t_t given by

$$t_t = \frac{l^2}{vl + 2D},$$

the Damköhler number for the transport is defined as

$$Da = \frac{t_t}{t_r} = \frac{\lambda_r l^2}{v\,l + 2\,D}. \tag{5.28}$$

The Damköhler numbers can be used to estimate whether the time scale of macroscopic physical transport or the time scale of chemical reactions dominate a particular problem. However, it is usually problematic to determine the reaction rate λ_r, because it is often not constant in time and space and typically depends on the concentrations of the reactive solutes. We define the reaction rate as the maximum over all individual rates in the considered problem.

5.2.4 Exact Solution

In the following we examine the performance of OS methods for different simplified problems with various relative velocities of advection, diffusion and reaction. We classify the time scales based on Da_a, Da_d, Da and Pe and discuss the sources and the magnitude of OS errors.

We only investigate one-dimensional problems with constant velocity and diffusion coefficients. Thus, according to Theorem 2 there is no splitting error between advection and diffusion in inside of the computational domain and the two-step scheme AD-R behaves like the A-D-R OS scheme.

To be able to study the OS errors in ADREs, we need to solve the involved operators exactly. However, the exact solution of each operator in advection-diffusion-reaction problems is often not known and we substitute a highly accurate numerical solution of each operator computed as follows. We discretize the computational domain using the CCFV discretization with a fine mesh containing 6400 elements. To solve all operators, the temporal time step Δt corresponds to the advection CFL number $\nu = 1$ given by (4.23). We solve the advective transport using the method of characteristics, which solves the transport operator exactly (LeVeque, 2002). We treat the diffusion implicitly with Alexander3 and the reaction element-wise with RKF45. As an alternative when we solve the diffusion and reaction coupled, we use CCFV together with Alexander3. Thus, each operator is solved very accurately and the total error of the OS solution is thus largely dominated by the splitting. Note, that in all considered cases the splitting time step τ is much greater than the discretization time step Δt.

In some examples described below we do not know the analytical solution of the given problem. In these cases, we compute the exact solution using the second-order symmetrical Strang splitting (A-DRS): in the first step we solve characteristics of the advective transport with time step Δt, followed by the solution of diffusion-reaction operator with CCFV and Alexander3 with time step $2\Delta t$ and followed by one step of advection. The spatial discretization and the time step Δt are the same as in the numerical solution of each operator described above. However, in this case $2\Delta t = \tau$ and thus both the discretization and the operator splitting errors are reduced significantly.

5.3 One-Component Reactions

The goal of this chapter is to analyze the OS errors for different types of chemical reactions. Before we can go ahead with reactions which are relevant for practical applications, we start by investigating the OS errors in an irreversible one-component ADRE. In irreversible reactions the reactants are completely converted into products and do not form reactants again. However, this type of reactions represents a good starting position for the study of OS errors. The more complicated reaction problems are mostly composed of several reactions which have similar structure to the reactions considered below.

The Theorem 2 describes situations in which OS errors occur but does not say anything about the size of the OS error. In order to estimate the size of the OS error for different variants of Eq. (5.17) we consider various reactive source terms q including linear and non-linear reactions, and also position-dependent reactions:

1. linear decay
$$q = -\lambda C, \tag{5.29}$$
2. non-linear Monod kinetic
$$q = -\lambda \frac{C}{K_c + C}, \tag{5.30}$$
3. position-dependent Monod kinetic
$$q = -\lambda \frac{C}{K_c + C}(1 - x). \tag{5.31}$$

The half-saturation constant K_c in the Monod kinetic (5.30) and (5.31) is set to 0.5 for all regarded problems. The reaction rates λ_r are in all cases less than or equal to the parameter λ and we set $\lambda_r = \lambda$. The liquid flows with a constant unit velocity, while the diffusion coefficient and the reaction rate may vary depending on the concrete problem.

5.3.1 Reactive Gaussian Hill Problem

To test the theoretical observations given by Theorem 2, we consider the one-dimensional ADR equation (5.17) with the initial concentration given by a Gaussian function

$$C_0(x) = \exp\left\{-\left(\frac{x - x_0}{d}\right)^2\right\}. \tag{5.32}$$

The numerical computations are performed on the truncated domain $\Omega = [0, 2]$ with homogeneous boundary conditions. We choose the the appropriate constants as in Simpson et al. (2005): $d = 0.04$, $x_0 = 0.25$, $v = 1$ and the final time $t = 1$. In this case the tracer will not access the domain boundary. The decay rate λ remains constant with a value of 0.2 in all types of reaction for Gaussian hill problem.

Linear Decay

For linear decay (5.29), the analytical solution on $-\infty < x < \infty$ is known and has the form

$$C(x,t) = \frac{\exp(-\lambda t)}{\sigma(t)} \exp\left\{-\left(\frac{x - x_0 - vt}{d\sigma(t)}\right)^2\right\}, \quad \sigma(t) = \frac{1}{d}\sqrt{d^2 + 4Dt}. \tag{5.33}$$

Furthermore, all assumptions of Theorem 2 are met and thus no splitting error in OS occurs. In this example, any discrepancy between the numerical and analytical solutions is only due to the numerical error alone. To test the implementation of temporal discretization schemes, we have chosen the time step for the numerical discretization Δt equal to the step τ.

Table 5.3 shows the convergence behavior in the L_1-norm of the numerical solution to the exact solution. The convergence rates are as expected: implicit methods Alexander2 and Alexander3 are second- and third-order accurate respectively and RKF45 is the fifth-order accurate in time. These results also confirm no operator splitting error between transport and reaction.

	advection-reaction ($D = 0$)				advection-diffusion-reaction ($D = 0.01$)			
	Alexander3		RKF45		Alexander2		Alexander3	
$\#\tau$	L_1-error	rate	L_1-error	rate	L_1-error	rate	L_1-error	rate
1	1.57×10^{-7}	-	6.30×10^{-11}	-	1.55×10^{-2}	-	9.78×10^{-3}	-
2	2.02×10^{-8}	2.96	1.89×10^{-12}	5.06	2.93×10^{-3}	2.40	1.22×10^{-3}	3.00
4	2.56×10^{-9}	2.98	5.80×10^{-14}	5.03	3.14×10^{-4}	3.22	1.02×10^{-4}	3.58
8	3.22×10^{-10}	2.99	1.80×10^{-15}	5.01	7.13×10^{-5}	2.14	1.46×10^{-5}	2.80
16	4.04×10^{-11}	2.99	5.63×10^{-17}	5.00	1.75×10^{-5}	2.03	2.03×10^{-6}	2.85
32	5.06×10^{-12}	3.00	-	-	4.34×10^{-6}	2.01	2.73×10^{-7}	2.90
64	6.33×10^{-13}	3.00	-	-	1.08×10^{-6}	2.00	3.86×10^{-8}	2.82

Table 5.3: Convergence of different time discretization schemes for Gaussian hill problem with linear decay (5.33), A-DR OS scheme.

Gaussian Hill with Monod Kinetic

In the following two problems we investigate ADRE (5.17) with a fixed diffusion coefficient ($D = 10^{-3}$). When the reaction term is of simple non-linear Monod kinetic type (5.30), we expect an OS error between the diffusion and the reaction parts.

We compare the errors and the convergence behavior of different OS schemes with different number of time steps in Table 5.4. The convergence orders of A-D-R and A-DS-RS are as expected. To reduce the relative L_1-error under 1%, the first-order splitting scheme requires 4 steps, which corresponds to the diffusion Damköhler number $Da_d = 7.42$. The second-order splitting scheme reduces the OS error enough even after one splitting time step and the error L_1^r is less than 0.003.

Fig. 5.2 shows the spatial distribution of the error E_{rr}. For the A-D-R scheme OS errors mostly occur at the boundaries of the Gaussian curve, because the diffusion is underestimated in regions with high concentration gradients. On the other hand, AD-RS overestimates the reaction at extrema of the solution, which is the maximum concentration in this example. Both schemes overestimate the reaction which results in positive mass errors M_{err}.

		A-D-R		A-DS-RS	
$\#\tau$	Da_d	$L_1^r(\%)$	rate	$L_1^r(\%)$	rate
1	1.09×10^{2}	2.36	-	2.79×10^{-1}	-
2	2.83×10^{1}	1.33	0.83	8.06×10^{-2}	1.79
4	7.42	7.06×10^{-1}	0.91	2.13×10^{-2}	1.92
8	1.98	3.65×10^{-1}	0.95	5.42×10^{-3}	1.98
16	5.43×10^{-1}	1.85×10^{-1}	0.98	1.36×10^{-3}	1.99
32	1.53×10^{-1}	9.34×10^{-2}	0.99	3.42×10^{-4}	1.99

Table 5.4: Convergence of different OS schemes to the exact solution for Monod kinetic (5.30) with different splitting time steps τ.

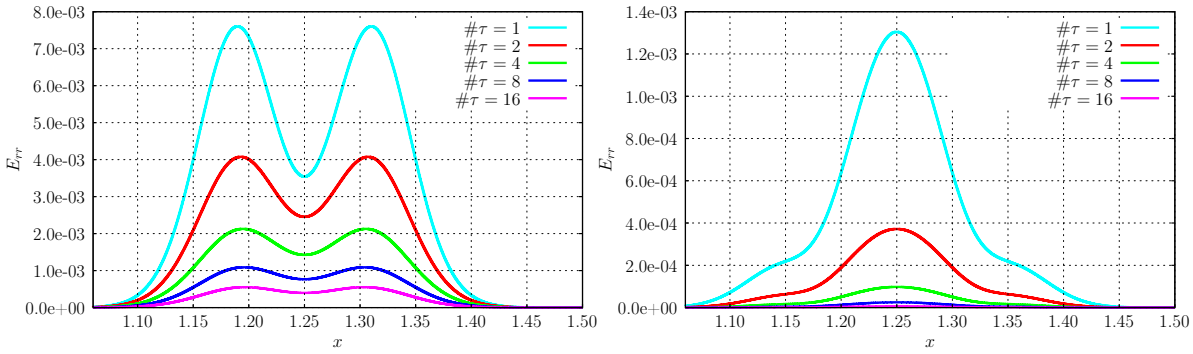

(a) A-D-R OS

(b) A-DS-RS OS

Fig. 5.2: Spatial distribution of error E_{rr} for Monod kinetic (5.30), splitting between diffusion and reaction.

Gaussian Hill with Position-Dependent Monod Kinetic

For position-dependent Monod kinetic (5.31) the OS error arises between transport and reaction. Second-order symmetric Strang splittings (A-DS-RS and A-DRS) again perform much better than first-order splittings, see Table 5.5. A Damköhler number Da of less than 10^{-2} is sufficient for a significant reduction in the OS error ($L_1^r < 1\%$) for all considered OS schemes.

The first-order A-D-R scheme underestimates the reaction part which turns in negative error E_{rr} in the whole domain (Fig. 5.3a), whereas the second-order Strang splitting (A-DS-RS) overestimates the reaction and E_{rr} remains positive (Fig. 5.3b).

		A-D-R		A-DS-RS		A-DR		A-DRS	
$\#\tau$	Da	$L_1^r(\%)$	rate	$L_1^r(\%)$	rate	$L_1^r(\%)$	rate	$L_1^r(\%)$	rate
1	2.09×10^{-1}	1.14×10^{1}	-	5.28×10^{-1}	-	1.07×10^{1}	-	4.62×10^{-1}	-
2	1.06×10^{-1}	5.30	1.10	1.48×10^{-1}	1.83	5.39	0.99	1.20×10^{-1}	1.95
4	5.41×10^{-2}	2.55	1.05	3.87×10^{-2}	1.94	2.70	1.00	3.02×10^{-2}	1.98
8	2.78×10^{-2}	1.25	1.03	9.79×10^{-3}	1.98	1.35	1.00	7.58×10^{-3}	1.99
16	1.43×10^{-2}	6.20×10^{-1}	1.01	2.46×10^{-3}	2.00	6.77×10^{-1}	1.00	1.90×10^{-3}	2.00

Table 5.5: Convergence of different OS schemes to the exact solution for position-dependent Monod kinetic (5.31) with different splitting time steps τ.

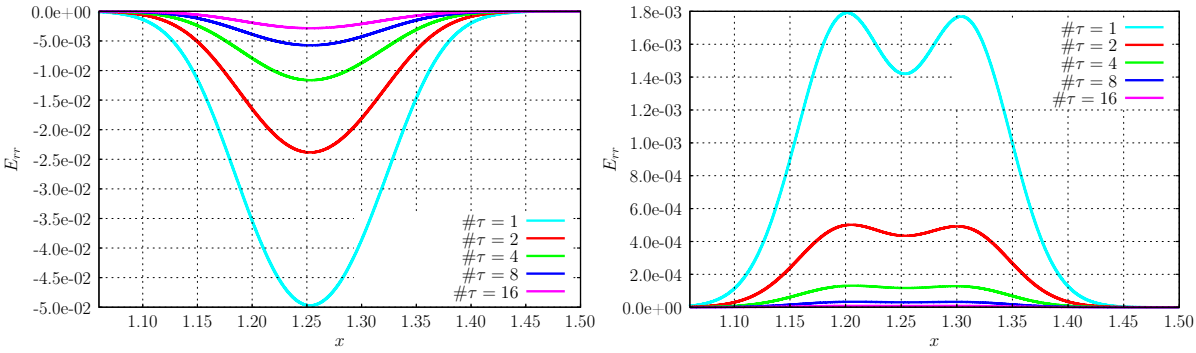

(a) A-D-R OS

(b) A-DS-RS OS

Fig. 5.3: Spatial distribution of error E_{rr} for position-dependent Monod kinetic (5.31), splitting between transport and reaction.

Summary

In both examples with homogeneous boundary conditions where the reaction term is described by the non-linear Monod kinetic, we can suppress the arising OS error easily. To reduce the relative error L_1^r under 1%, we need at most 16 splitting steps τ for the first-order OS schemes or only one step for second-order schemes. The convergence rates of OS methods in the L_1-norm are as expected. The splitting error between diffusion and reaction is smaller than the OS error between advection and reaction for the same values of Damköhler numbers, see Tables 5.4 and 5.5.

5.3.2 Linear Decay with Boundary Flux

OS methods are known to incur an innate error when a non-zero boundary flux across the domain boundary is present, see Section 5.1.4. Accordingly, we study the influence of boundary conditions on the accuracy of the OS schemes. First of all, we take a look at the linear decay problem (5.17) together with the Robin boundary condition (5.19) as we already investigated in Section 5.2.1. Looking back at the analytic mass balance error, we note that the mass error in OS depends only on the flow velocity and the reaction rate.

We will answer the question under which circumstances we reach the expected convergence rates of the OS schemes in the L_1-norm. We study not only the convergence order of OS schemes with respect to the reaction rates, but also the influence of the diffusion coefficient on the OS error and on the convergence rates of OS methods. Simulation parameters have been chosen such that the tracer does not enter the right boundary, avoiding any outflow boundary effects: domain $\Omega = [0, 1]$, velocity $v = 1$ and the simulation time $t = 0.6$.

Table 5.6 shows the relative errors L_1^r for this problem with diffusion coefficient $D = 10^{-3}$. The first-order OS splitting reaches the expected convergence rate almost immediately for low number of splitting time steps τ. However, the second-order OS scheme obtains second-order accuracy after 4 refinements of the splitting time step. The reduction of the accuracy of the A-DRS scheme depends on the diffusion coefficient D, see Fig. 5.4. If the local diffusion is high compared to the tracer travel distance in one splitting time step τ, which corresponds to the Péclet number $\mathrm{Pe} < 100$, the OS solution is sufficiently regular and the A-DRS scheme obtains second-order accuracy in the L_1-norm (Fig. 5.4b). However, for small diffusion coefficient the convergence order of A-DRS does not exceed one, see Fig. 5.4a. Moreover, the figure shows that Strang splitting consistently outperforms first-order approaches independent of the diffusion coefficient.

The highest OS error for the A-D-R scheme arises at the inflow boundary, see Fig. 5.5a. The reaction for A-D-R is overestimated in the whole domain which results in positive values for the mass error. On the other hand, the E_{rr} error for A-DRS is in some part of the domain positive and in some parts negative (Fig. 5.5b). That means that the L_1^r error for A-DRS does not correspond to the relative mass error M_{err}. The highest magnitude of the OS error for A-DRS occurs at the distance from the inflow boundary which corresponds to the transport time $\tau/2$.

		A-DR		A-DRS	
$\#\tau$	Da	$L_1^r(\%)$	rate	$L_1^r(\%)$	rate
1	1.27	4.83×10^{1}	-	3.11×10^{1}	-
2	6.45×10^{-1}	2.70×10^{1}	0.84	1.39×10^{1}	1.16
4	3.31×10^{-1}	1.43×10^{1}	0.92	5.38	1.37
8	1.71×10^{-1}	7.31	0.96	1.44	1.91
16	8.85×10^{-2}	3.70	0.98	3.03×10^{-1}	2.25
32	4.60×10^{-2}	1.86	0.99	6.69×10^{-2}	2.18
64	2.39×10^{-2}	9.35×10^{-1}	1.00	1.69×10^{-2}	1.98

Table 5.6: Convergence of different OS schemes to the exact solution for linear decay with Robin boundary condition.

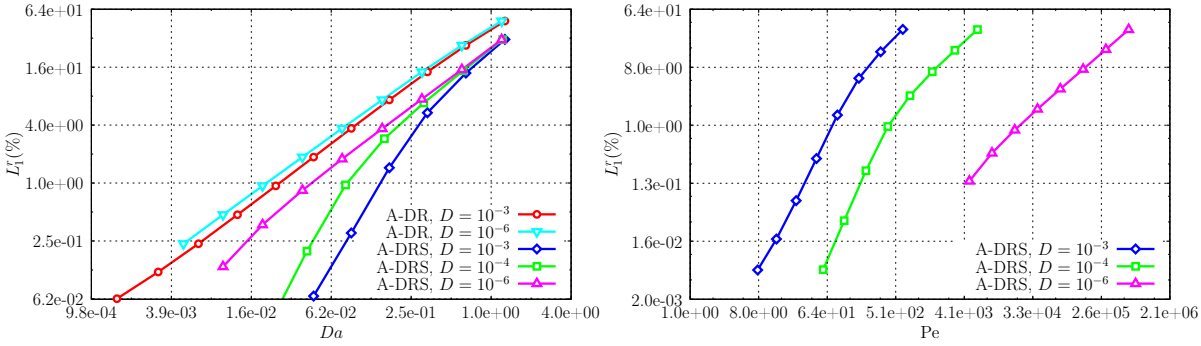

(a) (b)

Fig. 5.4: (a) Splitting error versus Damköhler number Da. (b) Splitting errors for Strang splitting with different diffusion coefficients versus Péclet number Pe.

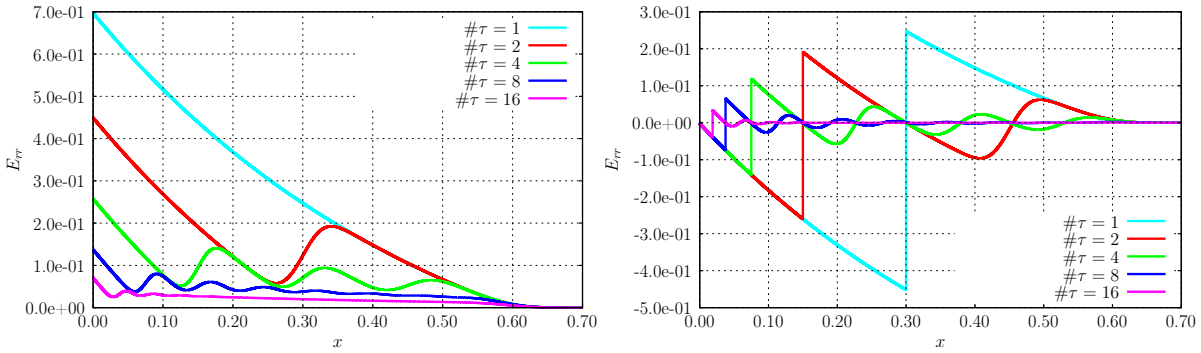

(a) A-D-R OS (b) A-DRS OS

Fig. 5.5: Spatial distribution of error E_{rr} for linear decay with Robin boundary condition at time $t = 0.6$ computed using different number of splitting time steps ($\#\tau$).

		A-DR		A-DRS	
λ	Da	$L_1^r(\%)$	rate	$L_1^r(\%)$	rate
3.20×10^{1}	1.42	4.83×10^{1}	-	2.56×10^{1}	-
1.60×10^{1}	7.08×10^{-1}	2.70×10^{1}	0.84	8.82	1.54
8.00	3.54×10^{-1}	1.43×10^{1}	0.92	2.75	1.68
4.00	1.77×10^{-1}	7.31	0.97	8.54×10^{-1}	1.69
2.00	8.85×10^{-2}	3.70	0.98	3.03×10^{-1}	1.49
1.00	4.42×10^{-2}	1.86	0.99	1.25×10^{-1}	1.28
5.00×10^{-1}	2.21×10^{-2}	9.35×10^{-1}	0.99	5.86×10^{-2}	1.09

Table 5.7: Convergence of different OS schemes to the exact solution for linear decay with Robin boundary condition with different reaction rates λ and fixed number of splitting time steps.

We have also investigated the OS errors for this example with a fixed number of splitting time steps ($\#\tau = 16$) for different reaction rates $\lambda = 0.5$-32 with constant diffusion $D = 10^{-3}$ (see Table 5.7). The results show that for Damköhler numbers Da smaller than 10^{-2} the OS error in the normalized L_1-norm for both OS schemes is less than 1%.

5.3.3 Summary

We repeated the simulations with inhomogeneous boundary conditions also with the Monod kinetic. However, the difference was negligible and we can state that the majority of the OS error occurs at the boundary and is not created by the non-linearity in the reaction model. We showed that the expected second-order accuracy of the Strang splitting can be achieved in the L_1-norm only for low Péclet numbers. However, the Strang splitting outperforms the first-order splitting and we should prefer the second-order splitting scheme.

5.4 Multi-Species Reactions

Up to now we have only studied reactive transport with one solute component. Our results show that the OS methods work well in all discussed situations with one solute component.

In this section, we expand on this work by applying OS methods to several reversible and irreversible reactions with two components. We will show that there is an ambiguity in how the OS methods are implemented which can play an important role in the accuracy of the OS solution. We consider three benchmark problems for this purpose:

1. transport of one component with interaction to the solid phase;
2. first-order decay chain of linearly sorbing contaminants with distinct retardation factors;
3. kinetically controlled Monod kinetics model describing the uptake of a substrate and growth of microorganisms together with retardation factors.

In order to be able to compare the OS errors and discuss the differences between one- and multi-component systems, we choose the same parameters as above. The computational domain is $[0, 1]$ and the velocity of flowing components is one. We compare the exact solution to the OS solution at time $t = 0.6$.

5.4.1 Linear Retardation

Fast chemical reactions are often described by equilibrium models. However, the equilibrium models are in fact a simplification of fast kinetic processes. We demonstrate this link in the following example which is often use to model adsorption of microorganisms on the solid soil phase. For a special case of the linear adsorption isotherm, the transport of microorganisms is retarded.

The transport of a single fluid component C_1 which can interact with a solid phase is described by

$$\frac{\partial C_1}{\partial t} + \frac{\partial C_2}{\partial t} + \nabla \cdot (vC_1 - D\nabla C_1) = 0, \tag{5.34}$$

where C_2 corresponds to the concentration of C_1 in the solid phase. We assume that the adhesion kinetic is linear with retardation factor R and reaction rate λ. The usual interphase mass transfer model is given by

$$\frac{\partial C_2}{\partial t} = \lambda \left((R-1)C_1 - C_2\right). \tag{5.35}$$

Letting $\lambda \to \infty$ reduces Eq. (5.35) to the linear retardation model (Herzer and Kinzelbach, 1989)

$$C_2 = (R-1)C_1. \tag{5.36}$$

Substituting (5.36) into the original problem (5.34) leads to a well-known advection-diffusion equation with retardation factor R:

$$\frac{\partial \left(RC_1\right)}{\partial t} + \nabla \cdot (vC_1 - D\nabla C_1) = 0.$$

Thus, the transport of one fluid component including linear adhesion to the solid phase can be described with a system of equations

$$\frac{\partial C_1}{\partial t} + \nabla \cdot (vC_1 - D\nabla C_1) = -\lambda \left((R-1)C_1 - C_2\right), \tag{5.37a}$$

$$\frac{\partial C_2}{\partial t} = \lambda \left((R-1)C_1 - C_2\right), \tag{5.37b}$$

and solved using an OS approach by separating transport and reactions. The reaction rate λ_r corresponds to the adhesion rate λ.

The initial concentration of the solute in the liquid phase as well as in the solid phase is zero. We impose the Robin boundary condition on (5.37a) with unit inflow concentration. We solve problem (5.37) with distinct reaction rates $\lambda = 10^2$-10^5 and various diffusion coefficients $D = 10^{-6}$-10^{-3} to investigate the influence of the velocity of reactions and the magnitude of diffusion on the OS error and on the convergence rates of OS schemes. We set the value of the retardation factor R to 2. It corresponds in the limit case for very fast reaction to the deceleration of the transport to the half of the original transport velocity, see Fig. 5.6.

Table 5.8 contains a comparison of the convergence behavior of different OS schemes for a number of reaction rates with constant diffusion coefficient ($D = 10^{-3}$). The convergence for small numbers of splitting time steps τ is less than one. For fast reactions, which almost corresponds to the local equilibrium, the difference between first-order splitting (A-DR) and second-order splitting (A-DRS) is negligible. In addition, the convergence order of A-DRS for quasi-equilibrium reactions reduces to one. To reduce the OS error L_1^r to less than 1% for fast reaction, at least 512 splitting time steps τ are needed.

In Table 5.9 we summarize the splitting errors of first- and second-order OS schemes for very fast adhesion ($\lambda = 10^5$) for two different diffusion coefficients (10^{-4} and 10^{-6}). The observed convergence rates are less than one and the convergence of all OS schemes is very slow. The

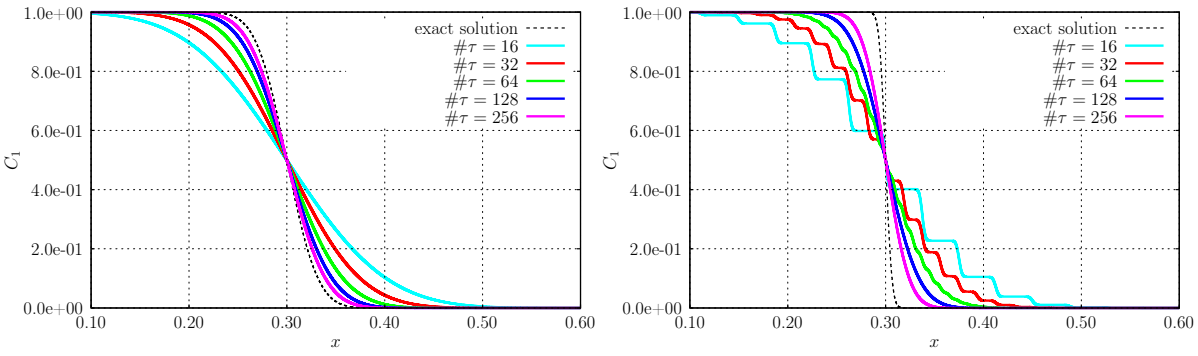

(a) $D = 10^{-3}$ (b) $D = 10^{-5}$

Fig. 5.6: The OS solution of the linear retardation problem (5.37) using A-DR with high reaction rate ($\lambda = 10^5$) and different diffusion parameters.

difference between A-D-R and A-DRS is negligible. As a result, this type of problem is better suited to first-order splitting because it requires less computational effort than the second-order scheme. The OS schemes applied to fast chemical reactions in a local equilibrium add an error in the OS solution, which looks like numerical diffusion for an advection-diffusion problem, see Fig. 5.6, and the sharp front is smeared. To obtain a sufficiently accurate solution using OS schemes (L_1^r less than 1%), it is required to use more than 1024 splitting time steps (Table 5.9).

Fig. 5.7 shows the OS error for the linear retardation problem with various diffusion coefficients and reaction rates versus the Damköhler number Da. The OS solution for fast reactions can be accurate enough even for high Damköhler numbers (greater than 50). However, achieving a sufficient accuracy requires a very large number of splitting time steps in this case.

	A-DRS ($\lambda = 10^2$)		A-DRS ($\lambda = 10^3$)		A-DRS ($\lambda = 10^5$)		A-DR ($\lambda = 10^5$)	
$\#\tau$	$L_1^r(\%)$	rate	$L_1^r(\%)$	rate	$L_1^r(\%)$	rate	$L_1^r(\%)$	rate
1	4.88×10^1	-	4.99×10^1	-	5.00×10^1	-	9.34×10^1	-
2	4.00×10^1	0.29	4.48×10^1	0.15	4.55×10^1	0.14	4.62×10^1	1.02
4	2.67×10^1	0.58	3.17×10^1	0.50	3.23×10^1	0.49	3.31×10^1	0.48
8	1.62×10^1	0.72	2.11×10^1	0.58	2.18×10^1	0.57	2.24×10^1	0.56
16	8.58	0.91	1.35×10^1	0.65	1.42×10^1	0.62	1.44×10^1	0.64
32	3.57	1.26	8.18	0.72	8.84	0.68	8.91	0.69
64	1.12	1.67	4.60	0.83	5.26	0.75	5.28	0.76
128	3.01×10^{-1}	1.90	2.30	1.00	2.97	0.83	2.97	0.83
256	8.13×10^{-2}	1.89	9.45×10^{-1}	1.28	1.58	0.91	1.58	0.91
512	2.75×10^{-2}	1.56	3.04×10^{-1}	1.64	7.93×10^{-1}	1.00	7.89×10^{-1}	1.00

Table 5.8: Convergence of different OS schemes to the exact solution for the linear adhesion model (5.37) with different splitting time steps τ and various reaction rates, $D = 10^{-3}$.

	A-DR ($D = 10^{-4}$)		A-DRS ($D = 10^{-4}$)		A-DR ($D = 10^{-6}$)		A-DRS ($D = 10^{-6}$)	
$\#\tau$	$L_1^r(\%)$	rate	$L_1^r(\%)$	rate	$L_1^r(\%)$	rate	$L_1^r(\%)$	rate
1	9.76×10^1	-	5.00×10^1	-	9.88×10^1	-	5.00×10^1	-
2	4.85×10^1	1.01	4.83×10^1	0.05	4.92×10^1	1.01	4.90×10^1	0.03
4	3.58×10^1	0.44	3.56×10^1	0.44	3.65×10^1	0.43	3.64×10^1	0.43
8	2.55×10^1	0.49	2.53×10^1	0.49	2.62×10^1	0.48	2.62×10^1	0.48
16	1.76×10^1	0.53	1.75×10^1	0.53	1.85×10^1	0.51	1.85×10^1	0.51
32	1.19×10^1	0.57	1.18×10^1	0.57	1.28×10^1	0.53	1.28×10^1	0.53
64	7.81	0.61	7.78	0.60	8.74	0.55	8.73	0.55
128	4.97	0.65	4.96	0.65	5.84	0.58	5.83	0.58
256	3.01	0.72	3.02	0.71	3.78	0.63	3.78	0.62
512	1.71	0.81	1.72	0.81	2.33	0.70	2.34	0.69
1024	8.76×10^{-1}	0.97	8.80×10^{-1}	0.97	1.32	0.82	1.32	0.82

Table 5.9: Convergence of different OS schemes to the exact solution for the linear adhesion model (5.37) with different splitting time steps τ.

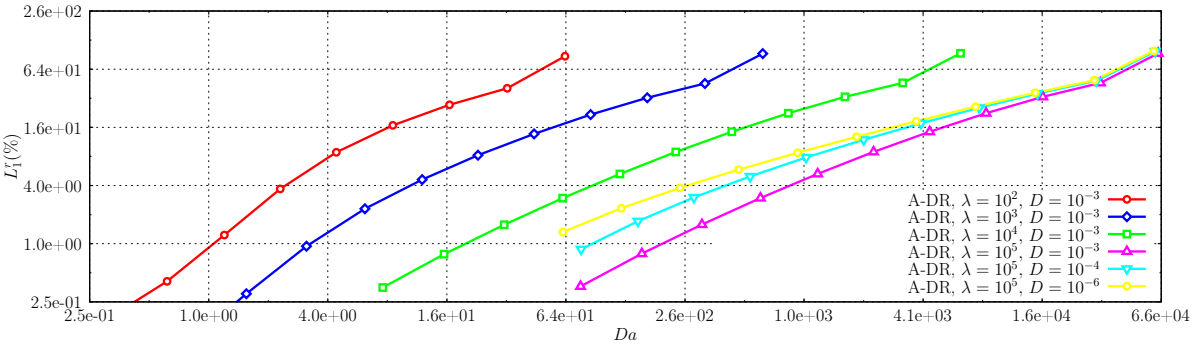

Fig. 5.7: OS errors for A-DR scheme with various diffusion coefficients and reaction rates versus Damköhler number Da.

Summary

We can conclude, that for rapid reactions which are described by high reaction rates or which are in a local equilibrium, the applicability of OS techniques is significantly limited. We showed that in the non-asymptotic regime the convergence rates are less than one for both the first-order and the second-order OS methods.

The OS approach in this example shows significant fronting. This is the result of reactive processes retarding the front velocities. This retardation is not addressed directly if transport and chemistry are calculated completely independently of each other. Fronts are moving too fast in the transport step, the related concentration changes decrease in the following chemistry step - but apparently not to a sufficient extend.

We can reduce the numerical diffusion introduced by OS choosing smaller splitting time steps. However, the large number of time steps leads to an excessive increase in computational complexity.

5.4.2 Coupled Transport with Distinct Retardation Factors

When the solute transport is retarded by fast linear adsorption, the OS methods need many time steps to achieve a sufficient accuracy. The arising question is if the different flow velocities can influence the applicability of OS methods. For this reason we study the OS errors in two different kinetically controlled two-component reactions with various flow velocities.

To demonstrate the relative performance of different OS schemes, we solve a problem with two fluid components and a positive mass flux through the inlet boundary. The governing transport equations for a coupled two-species problem are given by

$$\frac{\partial (R_1 C_1)}{\partial t} + \nabla \cdot (vC_1 - D\nabla C_1) = q_1, \tag{5.38a}$$

$$\frac{\partial (R_2 C_2)}{\partial t} + \nabla \cdot (vC_2 - D\nabla C_2) = q_2, \tag{5.38b}$$

with retardation factors R_i and source terms q_i, $i = 1, 2$.

In the first example, we solve a chain of linear reactions with two components and compare the results to the analytical solution (see Quezada et al. (2004)). In the second example, we investigate a more complex reaction with Monod-type kinetics with one substrate and one bacterium consuming the substrate. In this case the analytical solution is not known and we again substitute a highly accurate numerical solution for the exact solution, see Section 5.2.4.

Linear Decay

The reaction terms describing the degradation of two reactive contaminants mediated by sequential linear reactions are given by

$$q_1 = R_1 (-\lambda_1 C_1), \tag{5.39a}$$

$$q_2 = R_2 (\lambda_1 C_1 - \lambda_2 C_2), \tag{5.39b}$$

where the coefficients λ_1 and λ_2 describe decay rates. The first-order decay for one component has already been investigated in Section 5.3.2 and the results are also applicable here to the reactive transport of C_1. Therefore, we concentrate on a comparison of concentration C_2 with the exact solution for different OS schemes, Damköhler and Péclet numbers, diffusion coefficients and retardation factors. We set the reaction rates λ_1 and λ_2 to 2 and 1 respectively. The total reaction rate λ_r for the second component can be computed as

$$\lambda_r = \lambda_1 + \lambda_2. \tag{5.40}$$

The initial concentrations of both species are assumed to be zero. The concentration of the first component at the inlet boundary is fixed at 1, whereas C_2 has zero inflow concentration.

Fig. 5.8 illustrates the spatial distribution of the OS error for a fixed number of splitting time steps in the whole computational domain. The A-DR scheme introduces an OS error in the part of the domain where the second tracer is present (Fig. 5.8a). In the first part of the domain (up to $x = 0.3$), the reaction for the first component is underestimated which results in an underestimation of C_2. In the region between 0.3 and 0.6 the uptake of the second component

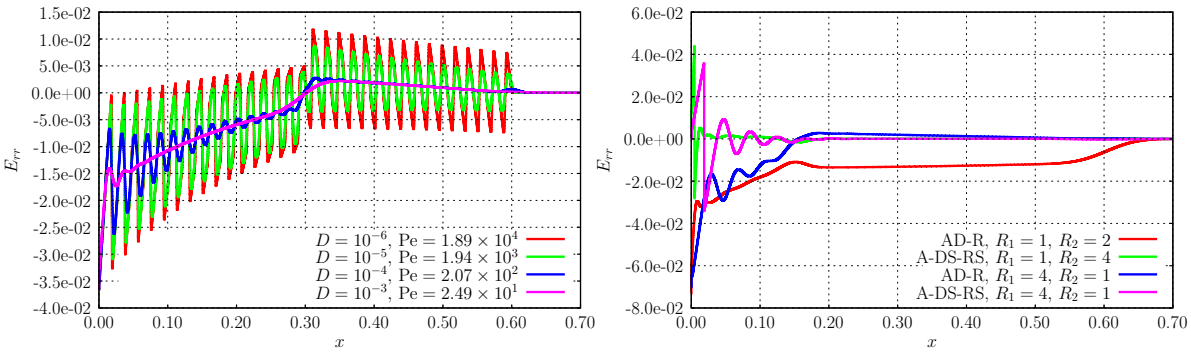

(a) (b)

Fig. 5.8: Spatial distribution of the OS error for C_2 with a fixed number of splitting time steps, $\#\tau = 32$: (a) A-DR OS scheme, first component is retarded ($R_1 = 2$, $R_2 = 1$). (b) A-DR and A-DRS OS schemes after 16 splitting time steps with constant diffusion ($D = 10^{-3}$) and different retardation factors.

is also underestimated which results in a positive error. For low diffusion coefficients the error between the exact and the OS solution is highly oscillating, see Fig. 5.8a. However, with increasing diffusion coefficients, the oscillations are smoothened out by the diffusion and disappear for Pe < 100.

Fig. 5.8b shows the spatial distribution of OS error for A-DR and A-DRS schemes with various retardation factors. A-DR distributes the OS error in the whole computational domain. One can observe the symmetrical nature of the A-DRS scheme: the error arises only at the inflow boundary with both positive and negative values. In contrast to A-DR, A-DRS scheme reduces the error almost completely in the remaining part of the domain with $x > 0.2$.

Tables 5.10 and 5.11 list the OS errors for C_2 with diffusion coefficient $D = 10^{-3}$. If the second component is slower than the first ($R_2 = 4$), there is almost no difference to the A-DR OS error for the case with identical flow velocities ($R_1 = R_2 = 1$) with more than 8 steps. OS errors in the case when the second component is faster are slightly greater. For smaller splitting time steps the A-DR scheme converges with first-order and 128 steps are enough to obtain an accuracy of less than 1%. Both OS schemes achieve the expected convergence orders already after a few refinements of the time step τ.

The convergence results of the A-DR scheme for different retardation factors and a smaller diffusion coefficient ($D = 10^{-5}$) are compared in Fig. 5.9a. One can see that the OS error for higher Damköhler numbers (which corresponds to lower number of time steps τ) depends strongly on the retardation factors R_1 and R_2. Nevertheless, for $Da < 10^{-2}$ the splitting error for A-DR with different retardation factors is similar. The difference between different scenarios with various retardation factors is greater for the A-DRS OS scheme, see Fig. 5.9b. The higher convergence rates are observed only for small Da. The Damköhler number less than 4.0×10^{-2} is sufficient to reduce the normalized L_1-error to less than 1%.

		$R_1 = R_2 = 1$		$R_1 = 1,\ R_2 = 4$		$R_1 = 4,\ R_2 = 1$	
$\#\tau$	Da	$L_1^r(\%)$	rate	$L_1^r(\%)$	rate	$L_1^r(\%)$	rate
1	1.90	4.60×10^{1}	-	6.88×10^{1}	-	1.68×10^{2}	-
2	9.68×10^{-1}	2.96×10^{1}	0.64	3.19×10^{1}	1.11	1.16×10^{2}	0.54
4	4.96×10^{-1}	1.65×10^{1}	0.84	1.65×10^{1}	0.95	4.33×10^{1}	1.42
8	2.56×10^{-1}	8.69	0.93	8.69	0.93	1.43×10^{1}	1.60
16	1.33×10^{-1}	4.45	0.96	4.45	0.96	6.90	1.05
32	6.91×10^{-2}	2.25	0.98	2.25	0.98	3.44	1.00
64	3.59×10^{-2}	1.13	0.99	1.13	0.99	1.72	1.00
128	1.85×10^{-2}	5.68×10^{-1}	1.00	5.69×10^{-1}	1.00	8.62×10^{-1}	1.00

Table 5.10: Convergence of A-DR method to the exact solution for C_2, linear decay (5.39b) with Robin boundary condition with various retardation parameters, $D = 10^{-3}$.

		$R_1 = R_2 = 1$		$R_1 = 1,\ R_2 = 4$		$R_1 = 4,\ R_2 = 1$	
$\#\tau$	Da	$L_1^r(\%)$	rate	$L_1^r(\%)$	rate	$L_1^r(\%)$	rate
1	1.90	3.92×10^{1}	-	3.66×10^{1}	-	1.33×10^{2}	-
2	9.68×10^{-1}	1.78×10^{1}	1.14	1.50×10^{1}	1.28	1.03×10^{2}	0.37
4	4.96×10^{-1}	7.21	1.30	5.31	1.50	4.24×10^{1}	1.28
8	2.56×10^{-1}	2.16	1.74	9.50×10^{-1}	2.48	1.05×10^{1}	2.01
16	1.33×10^{-1}	4.94×10^{-1}	2.13	2.23×10^{-1}	2.09	2.07	2.34
32	6.91×10^{-2}	1.10×10^{-1}	2.17	6.25×10^{-2}	1.83	4.73×10^{-1}	2.13

Table 5.11: Convergence of A-DRS method to the exact solution for C_2, linear decay (5.39b) with Robin boundary condition with various retardation parameters, $D = 10^{-3}$.

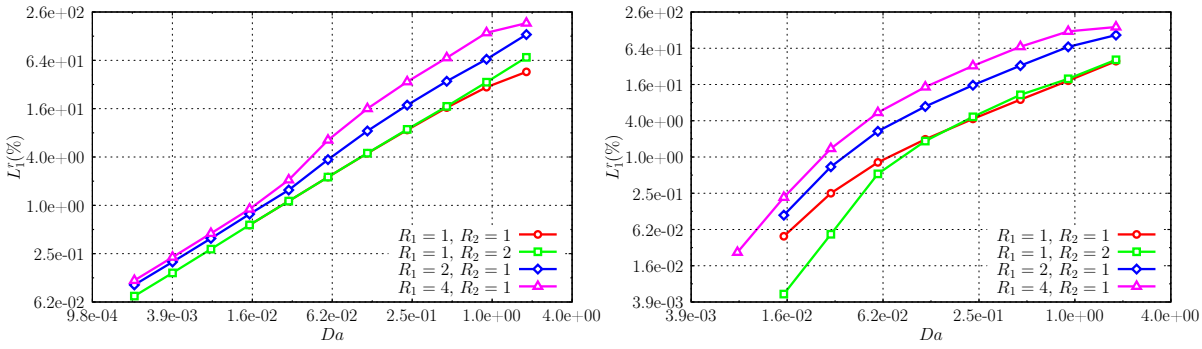

(a) A-DR OS

(b) A-DRS OS

Fig. 5.9: Splitting error for C_2 versus Damköhler number Da for various retardation factors, $D = 10^{-5}$.

Monod Kinetics

In this section the discussion is extended to address the applicability of the OS technique to solve systems of two ADREs with Monod kinetics. The results of the analysis show that the behavior of the error causing the OS error is similar to those observed with first-order kinetics. Reaction terms describing uptake of a substrate with concentration C_1 and growth of microorganisms with concentration C_2 are given by

$$q_1 = R_1 \left(-\lambda_1 \frac{C_1}{K_c + C_1} C_2 \right), \tag{5.41a}$$

$$q_2 = R_2 \left(\lambda_1 Y_{12} \frac{C_1}{K_c + C_1} C_2 - \lambda_2 C_2 \right), \tag{5.41b}$$

where the coefficients λ_i, $i = 1, 2$ denote the first-order decay rate, Y_{12} is the yield coefficient and K_c is the half-saturation constant. We fix both the yield coefficient and the half-saturation constant at 0.5.

The source term (5.41a) describes the consumption of substrate; the consumption rate is also dependent on the microbial concentration C_2. When no microorganisms are present, the substrate cannot be consumed. We set the maximum growth rate λ_1 is to 16 and the linear decay for the second component to 0.25. The initial as well as the inflow concentration C_2 of bacteria is 0.1. We assume that the initial concentration of C_1 is 0 and the inflow concentration is fixed at 1. The reaction rate λ_r is again given by (5.40), while the consumption rate of the component with concentration C_1 does not exceed one in all considered situations.

Fig. 5.10 shows the exact solution of the two-component transport problem (5.38) at time $t = 0.6$ with reaction terms (5.41), diffusion coefficient $D = 10^{-3}$ and various retardation factors. If both species are moving with the same flow velocity ($R_1 = R_2 = 1$), the sharp front in the substrate concentration disappears because of the substrate uptake. However, a sharpened front in the microbial concentration C_2 arises. In the case when the bacterial transport is retarded w.r.t. the nutrient transport, the sharp front in the substrate concentration remains, but no steep gradients in C_2 are created.

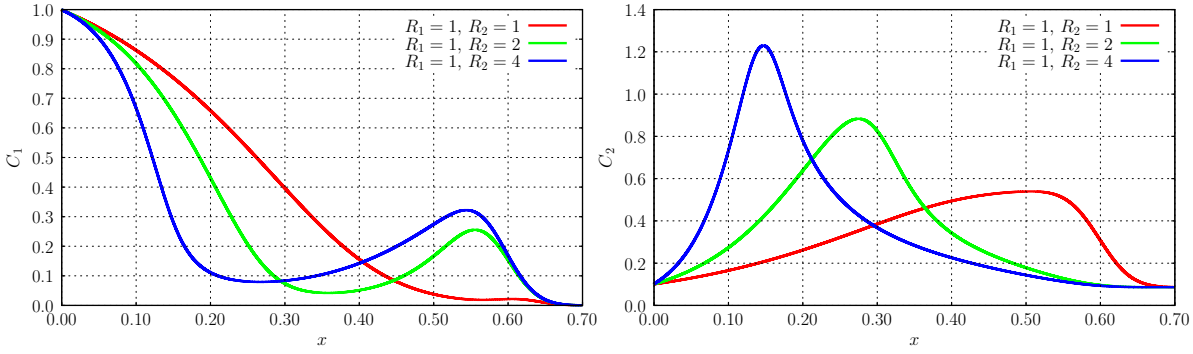

(a) concentration C_1 (b) concentration C_2

Fig. 5.10: Exact solution for two-component transport problem (5.38) with Monod kinetics (5.41) and different retardation factors at time $t = 0.6$.

In accordance with Theorem 2, an OS error arises even between diffusion and reaction. However, in this case the differences between A-D-R and A-DR, and A-DS-RS and A-DRS schemes are negligible and we thus only show results for A-DR and A-DRS respectively.

The A-DR scheme manages to achieve first-order accuracy for both components, see Table 5.12. If C_2 is retarded ($R_2 = 2$) and moves slower, it causes higher consumption of C_1 at the inflow boundary. Thus, it results in greater OS error in C_1. The A-DRS scheme captures this effect much better, see Table 5.13. The OS error for A-DRS is less than 1% for both components in less than 16 steps for higher diffusion ($D = 10^{-3}$). The second-order accuracy of A-DRS is also achieved for lower diffusion coefficient, see Fig. 5.11 and the OS error is negligible for small Damköhler numbers ($Da < 0.25$). The convergence of A-DR is only first-order, but the OS error is sufficiently small in all situations for Damköhler number smaller than 0.05.

Fig. 5.12 shows the spatial distribution of error between the exact and the OS solution of both components for A-DR and A-DRS after 64 time steps. The magnitude of the error for each component is similar in the case of A-DR. When the transport of microorganisms is retarded, the magnitude of the error is greater. The maximum of the error is reached at $x = 0.15$ which corresponds to the front of the second component.

		$R_1 = R_2 = 1$				$R_1 = 1$, $R_2 = 2$			
		C_1		C_2		C_1		C_2	
$\#\tau$	Da	$L_1^r(\%)$	rate	$L_1^r(\%)$	rate	$L_1^r(\%)$	rate	$L_1^r(\%)$	rate
1	1.03×10^{1}	9.79×10^{1}	-	4.31×10^{1}	-	9.75×10^{1}	-	5.85×10^{1}	-
2	5.24	5.55×10^{1}	0.82	2.54×10^{1}	0.76	6.41×10^{1}	0.60	2.95×10^{1}	0.99
4	2.69	2.89×10^{1}	0.94	1.34×10^{1}	0.92	3.57×10^{1}	0.85	1.44×10^{1}	1.03
8	1.39	1.45×10^{1}	0.99	6.74	0.99	1.87×10^{1}	0.93	6.90	1.06
16	7.19×10^{-1}	7.21	1.01	3.35	1.01	9.52	0.97	3.50	0.98
32	3.74×10^{-1}	3.59	1.01	1.67	1.01	4.81	0.98	1.77	0.98
64	1.94×10^{-1}	1.79	1.00	8.33×10^{-1}	1.00	2.42	0.99	8.93×10^{-1}	0.99
128	1.00×10^{-1}	8.94×10^{-1}	1.00	4.17×10^{-1}	1.00	1.22	0.99	4.49×10^{-1}	0.99
256	5.08×10^{-2}	4.47×10^{-1}	1.00	2.09×10^{-1}	1.00	6.14×10^{-1}	0.99	2.26×10^{-1}	0.99

Table 5.12: Convergence of A-DR to the exact solution for two-component transport with Monod kinetics, $D = 10^{-3}$.

		$R_1 = R_2 = 1$				$R_1 = 1$, $R_2 = 2$			
		C_1		C_2		C_1		C_2	
$\#\tau$	Da	$L_1^r(\%)$	rate	$L_1^r(\%)$	rate	$L_1^r(\%)$	rate	$L_1^r(\%)$	rate
1	1.03×10^{1}	4.27×10^{1}	-	1.93×10^{1}	-	7.23×10^{1}	-	2.80×10^{1}	-
2	5.24	2.54×10^{1}	0.75	1.20×10^{1}	0.69	2.56×10^{1}	1.50	1.51×10^{1}	0.89
4	2.69	9.17	1.47	4.36	1.46	6.98	1.88	4.84	1.64
8	1.39	1.99	2.21	9.63×10^{-1}	2.18	1.89	1.88	9.62×10^{-1}	2.33
16	7.19×10^{-1}	3.13×10^{-1}	2.67	1.52×10^{-1}	2.66	4.87×10^{-1}	1.95	2.31×10^{-1}	2.06

Table 5.13: Convergence of A-DRS to the exact solution for two-component transport with Monod kinetics, $D = 10^{-3}$.

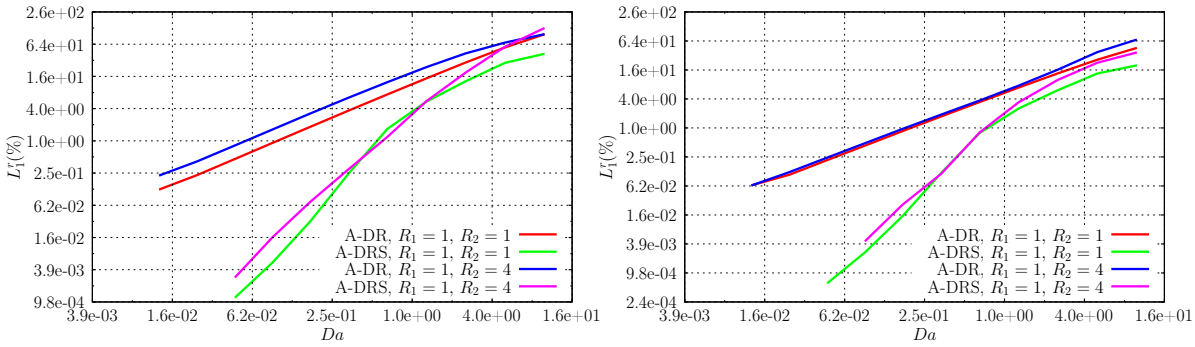

(a) concentration C_1 (b) concentration C_2

Fig. 5.11: Splitting error versus Damköhler number Da for Monod kinetic with two components and different retardation factors, diffusion coefficient is $D = 10^{-4}$.

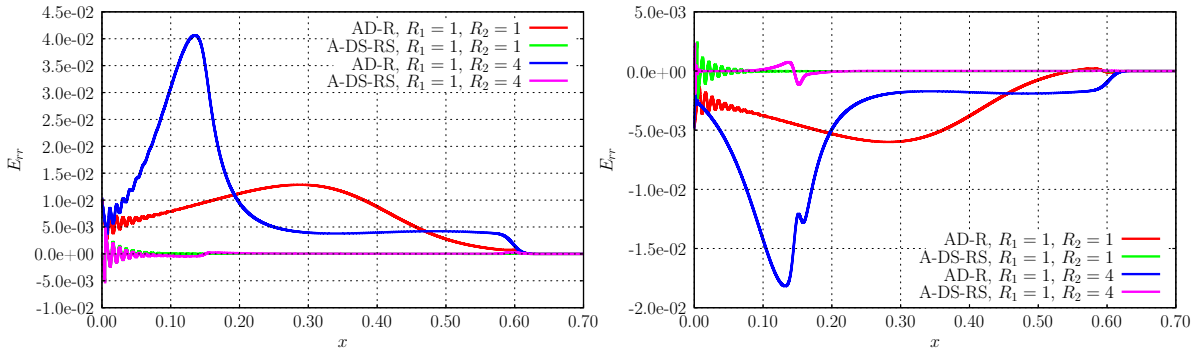

(a) concentration C_1 (b) concentration C_2

Fig. 5.12: Spatial distribution of OS error for A-DR and A-DRS OS schemes after 64 time steps with various retardation factors, $D = 10^{-4}$.

The error of the A-DRS scheme for C_1 is significant only at the inflow boundary. When the flow velocities of both components are the same, the splitting error for C_2 is concentrated at the inflow boundary. However, if C_2 is retarded, the greatest OS error for A-DRS and the second component is at the concentration front.

Summary

We have shown that the difference in flow velocities of different components may effect the accuracy of OS schemes. However, if the retardation is modeled by a retardation parameter and not by rapid reactions like in Section 5.4.1, the convergence rates of all considered OS schemes reached the expected asymptotic convergence rates after a few time steps. Thus, we are able to reduce the OS error sufficiently, particularly using second-order OS schemes.

The retarded velocities for linear and non-linear reactions with slow kinetic may affect the splitting error but not the convergence rates. Compared to the problems with one component, the OS error occurs not only at the domain boundary but also at the solute fronts.

5.5 Discussion on Errors in Operator Splitting Methods

In summary, the question of whether chemical reaction terms can effectively be decoupled from the transport equations depends on many factors including the nature of the chemical reactions involved, the effect of boundary conditions and the desired and acceptable accuracy. In this chapter we have studied the operator splitting errors in ADREs for non-iterative versions of the operator splitting (SNIA). We have studied problems with one and two components with homogeneous and inhomogeneous boundary conditions. We also have considered the influence of non-linearities in reaction terms and differences in the flow velocities to the accuracy of OS schemes.

The discussed OS errors in this chapter are independent of the discretization error and is due to the splitting of simultaneous processes. We will discuss the importance of OS errors and compare the contribution of the space and time discretization errors in Chapter 6.

The present analysis provides information useful in determining the magnitude of the OS errors depending on the velocity of the kinetically controlled reactions and the velocity of transport and diffusion processes. We can quantify this relationships between different time scales using dimensionless Péclet and Damköhler numbers defined in Section 5.2.3. We measure the OS error in the L_1-norm which is a generalization of the mass error often used in the literature.

Moreover, the OS errors in the L_1-norm are also consistent with previous studies for SNIA schemes w.r.t. the total mass. Valocchi and Malmstead (1992) have studied the splitting error per τ by using an analytical solution for transport with first-order decay and a Robin boundary condition. They have shown that a standard SNIA scheme introduces an $\mathcal{O}(\tau)$ error and the Strang splitting leads to an $\mathcal{O}(\tau^2)$ error. Kaluarachchi and Morshed (1995) and Morshed and Kaluarachchi (1995) have analyzed the error for a first-order Monod kinetic reaction, and for the transport of two species coupled with a Monod rate low. They concluded that an error in operator splitting in these situations is similar to Valocchi and Malmstead (1992): an $\mathcal{O}(\tau)$ error occurs for the standard SNIA and an $\mathcal{O}(\tau^2)$ error for the Strang splitting scheme. Carrayrou et al. (2004) compared the intrinsic OS errors for both the non-iterative and iterative OS schemes and performed a mass balance analysis for first-order kinetically controlled irreversible and reversible reactions with one and two species. They concluded the standard iterative schemes should not be used, because they can have convergence or stability problems and the OS error is still present. Thus, we shall prefer the SNIA with the Strang splitting or the symmetric iterative scheme (for detail see Carrayrou et al. (2004)) because it produces the most precise results.

On the other hand, the extended use of Strang splitting in computational reactive transport modeling leads to the conjecture that in this field splitting errors are kept within reasonable bounds if the splitting time steps τ are small enough. However, this statement should be taken very carefully. The formally second-order Strang splitting does not achieve the asymptotic convergence behavior in all situations. The non-asymptotic regime is often attained in practice when the splitting time step τ is much larger than some of the time scales associated with either the reaction terms, the diffusion or advection operator when large gradients are present (Descombes et al., 2014). We observed this reduction of convergence orders in the L_1-norm for high Péclet numbers ($\mathrm{Pe} > 500$) and higher Damköhler numbers ($Da > 0.1$).

The order reduction for the Strang splitting to order one was also observed for time-dependent Dirichlet boundary conditions for advection-reaction problem in Hundsdorfer and Verwer (1995) and Hundsdorfer and Verwer (2003). Thus, the Strang splitting scheme is in these situations not more accurate than the first-order splitting scheme (Hundsdorfer and Verwer, 1995).

The equilibrium models can be derived as a limiting case of a non-equilibrium model described by reaction kinetic, see Section 5.4.1. In this case, the observed convergence rates of Strang splitting were less than 1. Similar results were also published by Barry et al. (1996a,b). They analyzed the splitting errors for linear sorption, linear decay and interphase mass transfer chemistry and concluded that the Strang splitting scheme does not lead to an $\mathcal{O}(\tau^2)$ error in all cases.

Chapter 6

Numerical Experiments

In this chapter we present several simulations in one- and two-dimensional domains to illustrate the capabilities and performance of the numerical schemes described in Chapter 4 to solve advection-diffusion-reaction equations when the transport is dominated by advection.

We study the performance of various spatial discretization schemes: first- and second-order CCFV schemes and the DG method with linear basis function which is also second-order accurate. In Section 6.1 we also use a standard finite element method as spatial discretization. As time discretization schemes we use first-, second- and third-order explicit, implicit and implicit-explicit schemes.

The main objective of this chapter is to verify the implementation of the numerical schemes and to answer the following questions:

- Which numerical methods are suitable for a concrete problem?
- Are the chosen methods sufficiently accurate?
- How demanding are the used methods w.r.t. the computational requirements?
- Which kind of error is predominant: the error arising from the operator splitting technique or the error from the numerical discretization?

In Chapter 5 we investigated the operator splitting error with respect to characteristic time scales represent by Damköhler and Péclet numbers, see Section 5.2.3. In order to connect these two numbers to the spatial discretization, we take as the characteristic length l the mesh size h. Thus, the grid Péclet number is given by

$$\mathrm{Pe}_{\mathrm{g}} = \frac{hv}{D} \tag{6.1}$$

and the transport Damköhler number Da is computed as

$$Da = \frac{\lambda_r h^2}{v\,h + 2\,D}. \tag{6.2}$$

The goal of this chapter is to compare both types of errors: the operator splitting errors and the errors caused by the spatial and temporal discretization. The arising errors depend on the type of the problem, the used solution strategy, numerical discretization and the spatial and temporal resolution.

As expected, there is no solution strategy and numerical scheme which are the best choice in all situations to solve the underlying reactive transport problem. However, the discussion in the conclusion of this chapter can guide the reader how to choose the solution approach and numerical methods regarding to the nature of problem, computational effort and the desired accuracy.

6.1 IMEX Methods

In order to test the accuracy and performance of RK-IMEX schemes as described in Section 4.4.3 and in Appendix A.1.2, we apply them to the diffusion-reaction or advection-diffusion-reaction equations. We show two examples in which the RK-IMEX schemes may have an advantage in comparison to the classical implicit or explicit methods. We solve the problems on one-dimensional computational domain Ω with length $L = 1$. All measurements of the duration of the numerical simulation were done on a single core of AMD *Opteron*™ 6172, 2.10 GHz.

Diffusion-Reaction Problem with Time-Dependent Boundary Conditions

With the purpose of testing the accuracy and the theoretical convergence rates of RK-IMEX schemes, we study a model problem with time-dependent Dirichlet boundary conditions of the form

$$\frac{\partial C}{\partial t} - \frac{\partial^2 C}{\partial x^2} = f \quad \text{in } \Omega, \tag{6.3a}$$

$$C(0,t) = e^t \sin t, \quad C(1,t) = e^{t-1}\sin(t+1), \tag{6.3b}$$

$$C(x,0) = e^{-x}\sin x, \tag{6.3c}$$

where

$$f = C - C^2 + 3e^{t-x}\cos(t+x) + e^{2(t-x)}\sin^2(t+x).$$

The exact solution of (6.3) at time t is given by

$$C(x,t) = e^{t-x}\sin(t+x).$$

This non-linear diffusion-reaction problem was also studied in Koto (2008a). We treat the diffusion part of (6.3) implicitly, whereas the right hand side f describing the reactive term is solve explicitly. The application of RK-IMEX schemes to this problem has one advantage: explicit treatment of the non-linear reaction term does not need any linearization using Newton's method.

We apply the method of lines, where the standard finite element method with quadratic polynomial basis functions is used for the spatial discretization. The domain Ω is uniformly divided into 1024 elements to suppress the error in the spatial discretization. The initial time step $\Delta t = 0.2$ is refined to observe the time convergence of RK-IMEX methods to the analytical solution. Table 6.1 summarizes the errors and convergence rates in the L_2-norm at time 1. As expected, we observe convergence order 1 and order 2 for Euler-IM and Trapez-IM scheme

respectively. The convergence orders of Alexander2-IM and Pareschi2 schemes are also asymptotically approaching 2. The Ascher3 method converges only with order 2.25 as was already observed in Koto (2008a). The best second-order method regarding to the computational effort and the obtained accuracy is Alexander2-IM, which has only two stages.

To compare the performance of RK-IMEX methods with classical fully implicit methods (implicit Euler, Alexander2 and Alexander3), we solve (6.3) using CCFV spatial discretization with 2048 elements and various time integrators with different sizes of time steps. While the RK-IMEX methods require the solution of the linear system only one time per stage, the fully implicit methods need at least two iterations (and also solutions of linear system) in the Newton's method in each stage. Fig. 6.1 shows the computational effort of different time discretization schemes with various time steps lengths. All RK-IMEX schemes are faster than Alexander3. Alexander2-IM shows a good performance: the computational times to solve the problem (6.3) are similar to implicit Euler method. However, Alexander2-IM is second-order accurate compared to implicit Euler.

	Euler-IM		Trapez-IM		Alexander2-IM	
$\#\Delta t$	L_2-error	rate	L_2-error	rate	L_2-error	rate
160	9.91×10^{-4}	-	2.14×10^{-5}	-	3.61×10^{-6}	-
320	4.97×10^{-4}	1.00	5.36×10^{-6}	2.00	9.26×10^{-7}	1.96
640	2.49×10^{-4}	1.00	1.34×10^{-6}	2.00	2.35×10^{-7}	1.98
1280	1.24×10^{-4}	1.00	3.37×10^{-7}	1.99	5.95×10^{-8}	1.98

	Pareschi2		Ascher3	
$\#\Delta t$	L_2-error	rate	L_2-error	rate
160	6.00×10^{-5}	-	5.78×10^{-7}	-
320	1.62×10^{-5}	1.89	1.21×10^{-7}	2.25
640	4.25×10^{-6}	1.93	2.56×10^{-8}	2.25
1280	1.10×10^{-6}	1.95	5.38×10^{-9}	2.25

Table 6.1: Convergence of different RK-IMEX schemes for the model problem (6.3), finite element method with quadratic elements, 2049 DOFs.

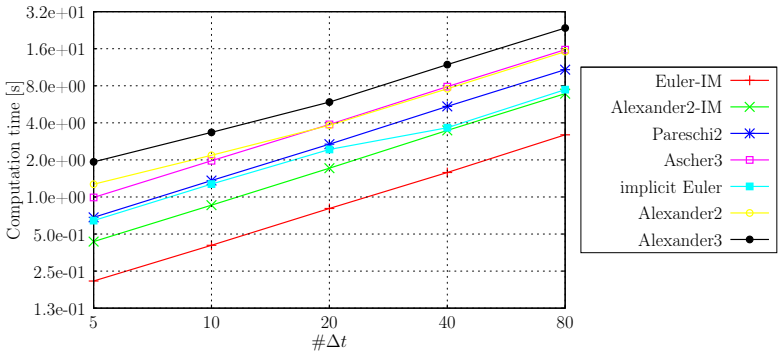

Fig. 6.1: Computational times for different time discretization schemes versus the number of time steps needed to compute the solution the problem (6.3) at time 1, CCFV discretization with 2048 elements.

Advection-Diffusion Problem with Linear Decay

To show the advantage of RK-IMEX schemes compared to fully explicit time discretization, we also solve the one-dimensional ADRE problem with first-order linear decay

$$\frac{\partial C}{\partial t} + \nabla \cdot (vC - D\nabla C) = -\lambda C \tag{6.4}$$

together with zero initial condition and Robin boundary condition (5.19) with unit inflow concentration. We have already studied this problem w.r.t. the OS error in Section 5.3.2. The numerical computations are performed to time $t = 0.6$. The value of both the velocity v and the parameter λ is 1, and the diffusion coefficient D is 5×10^{-4}.

We solve this problem using CCFV method with minmod flux reconstruction. As time discretization, we use second-order accurate methods: Alexander2-IM and Heun's method. For the fully explicit methods, we solve the ADR equation without operator splitting; in the RK-IMEX scheme we solve the advection explicitly, whereas the diffusion-reaction part is treated implicitly.

Starting from an initial mesh with 32 elements, we study the h-convergence to the analytical solution. The time step Δt corresponds to the CFL-like number $\nu_l = 0.8$ computed by Eq. (4.22) to achieve the stability in the numerical schemes. However, using the Alexander2-IM method the diffusion is treated implicitly and ν_l corresponds to the pure advective CFL number ν, for details see Section 4.4.5. For this reason RK-IMEX schemes enable larger time steps in the solution of advection-diffusion equations compared to the explicit time discretization schemes. This is significant particularly for small grid Péclet numbers (Table 6.2). For $\mathrm{Pe_g} < 2$ the diffusion becomes locally dominant and the number of time steps needed for explicit treatment grows quadratically. On the other hand, the number of time steps for RK-IMEX method still rises linearly. For coarser grids (with high Péclet numbers) the computational time for the explicit Heun method is approx. 4 times lower than for Alexander2-IM because the purely explicit method does not need to solve a non-trivial linear system compared to the RK-IMEX schemes. However, this difference vanishes for low $\mathrm{Pe_g}$ and Alexander2-IM is faster for meshes with more than 4096 elements.

		Heun		Alexander2-IM	
L/h	$\mathrm{Pe_g}$	$\#\Delta t$	Comp. time [s]	$\#\Delta t$	Comp. time [s]
32	6.25×10^{1}	50	2.02×10^{-2}	48	7.56×10^{-2}
64	3.12×10^{1}	101	7.79×10^{-2}	96	2.83×10^{-1}
128	1.56×10^{1}	211	3.15×10^{-1}	192	1.10
256	7.81	458	1.35	384	4.44
512	3.91	1063	6.29	768	1.75×10^{1}
1024	1.95	2716	3.23×10^{1}	1536	6.94×10^{1}
2048	9.77×10^{-1}	7791	1.84×10^{2}	3072	2.81×10^{2}
4096	4.88×10^{-1}	25 019	1.19×10^{3}	6144	1.13×10^{3}
8192	2.44×10^{-1}	87 786	8.29×10^{3}	12 288	4.50×10^{3}

Table 6.2: Number of time steps and computational times to solve ADR with linear decay (5.17) using CCFV with either the method of Heun or the RK-IMEX method Alexander2-IM.

Summary

We have shown in two numerical experiments that RK-IMEX methods can be successfully used in reactive transport modeling. The advantage of these methods is the elimination of the error in operator splitting. RK-IMEX methods can also have an advantage in the computational complexity.

If the non-linear reactive part is not stiff, using an explicit treatment of the reaction term avoids the solution of a non-linear system. In the case of multi-component reactive flow, the explicit solution of the advection part and implicit solution of the diffusion-reaction term can remove the error in operator splitting. RK-IMEX schemes also enable the use of higher-order non-linear space discretization schemes (like CCFV with flux reconstruction) for advection part which reduces numerical diffusion and does not add any non-linearity to the arising system.

However, the disadvantage is the necessity to solve a non-trivial linear systems in each time step. Moreover, further research is also required to study the stability of RK-IMEX methods with applications to reactive transport modeling.

6.2 One-Dimensional Problems

In the examples below, we solve problems on a one-dimensional domain with length L which are similar to those investigated in Chapter 5 w.r.t. the error in operator splitting. We solve advection, diffusion and reaction operators in one time step without operator splitting (unless explicitly stated otherwise) and all discrepancies between the numerical and the exact solutions are only due to the numerical error.

6.2.1 Gaussian Hill Problem

To get a better insight into the error arising from the numerical discretization, we solve the reactive Gaussian hill problem with linear decay (see Section 5.3.1) using different space and time discretization schemes. We firstly divide the computational domain with length $L = 2$ into 64 elements. To observe the spatial convergence, we uniformly refine the initial mesh. The considered problem is advection dominated with $v = 1$, $D = 10^{-5}$ and small reaction rate $\lambda = 0.1$. The size of the time step Δt is given by the CFL-like condition (4.22) and fulfills $\nu_l = 0.8$ for all mesh refinements.

The CCFV with full upwinding and explicit Euler time discretization is formally first-order accurate. However, the results show that this asymptotic rate is achieved only for very fine meshes requiring huge computational effort (Table 6.3). This method is highly diffusive: using a mesh with 512 elements, the maximum of the numerical solution lies above 0.6, but the maximum value of the exact solution is 0.9, see Fig. 6.2a. The poor convergence rates and very high errors on coarse grids give rise to a high error even on very fine grids. On a grid with 8192 elements the normalized error in the L_1-norm is more than 3%. Using explicit Heun or implicit schemes instead of explicit Euler introduces even higher numerical diffusion.

The convergence rates of the second-order space discretization schemes together with explicit Euler are not well predictable, see Table 6.3. The initial error for a coarse grid with 64 elements

is much smaller than the error for the first-order CCFV. However, the numerical solution diverges from the exact solution. The higher-order schemes with explicit Euler converge again for meshes with more than 1024 elements, but the convergence rate is limited by the first-order explicit Euler. Although the maximum is for CCFV with flux reconstruction reached for lower number of mesh elements (Fig. 6.2b), the numerical solution has higher gradients compared to the exact solution. This combination of numerical methods sharpens the fronts in the solution too much. We observe this behavior also for second-order DG with explicit Euler.

The theoretical asymptotic convergence rates for higher-order space discretizations together with higher-order time integrators are fully confirmed in Table 6.4; the rates are asymptotically approaching 2 for all methods. The smallest errors are achieved using CCFV with minmod flux limiter with $\theta = 2$ and both Heun and Shu3 time discretizations. To reduce the error in the normalized L_1-norm under 1%, we require a mesh with at least 2048 elements.

While the accuracy of Shu3 is slightly better than of Heun's method, Shu3 has three stages and requires a higher computational effort compared to Heun. Thus, we further in this work prefer the method of Heun. We have also computed all the numerical tests stated below with Shu3, but we have not discovered any obvious advantages of Shu3 compared to Heun.

We can conclude that even for a simple advection-diffusion-reaction example with a smooth initial condition, we need a very fine mesh with more than 2048 elements to reduce the error sufficiently ($L_1^r < 1\%$). Moreover, we showed that the combination of a first-order method in time and the second-order discretization in space should be avoided in the solution of ADREs.

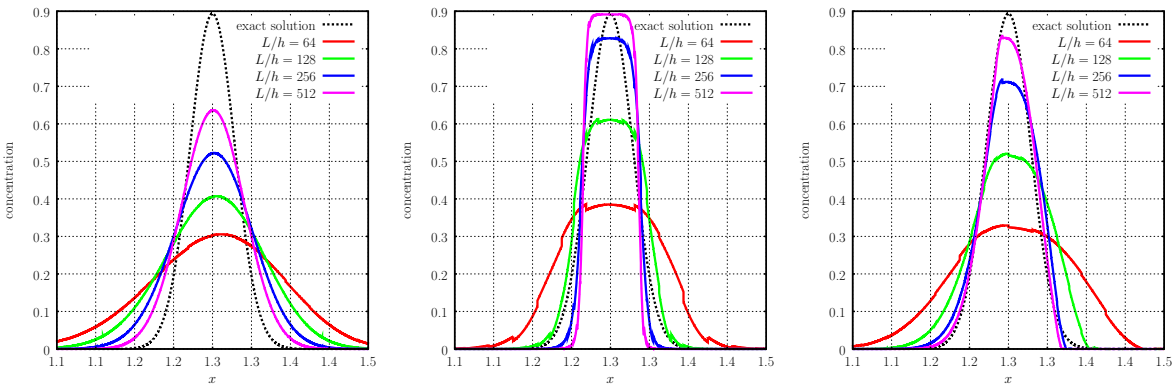

(a) explicit Euler (b) explicit Euler (c) Heun

Fig. 6.2: Comparison of different numerical schemes with various temporal and space discretizations to the analytical solution of Gaussian hill problem with linear decay (5.33): (a) first-order CCFV and (b)-(c) second-order CCFV.

	DG		CCFV			
	minmod ($\theta = 1$)		first-order		minmod ($\theta = 1$)	
L/h	$L_1^r(\%)$	rate	$L_1^r(\%)$	rate	$L_1^r(\%)$	rate
64	6.50×10^1	-	9.23×10^1	-	7.31×10^1	-
128	2.74×10^1	1.25	7.19×10^1	0.36	2.91×10^1	1.33
256	2.20×10^1	0.32	5.09×10^1	0.50	2.05×10^1	0.51
512	3.21×10^1	-0.55	3.26×10^1	0.64	2.93×10^1	-0.52
1024	3.59×10^1	-0.16	1.94×10^1	0.75	3.20×10^1	-0.13
2048	2.47×10^1	0.54	1.11×10^1	0.81	2.40×10^1	0.41
4096	1.18×10^1	1.07	6.25	0.83	1.17×10^1	1.04
8192	5.79	1.03	3.62	0.79	5.85	1.00

Table 6.3: Space and time convergence of different discretization schemes for Gaussian hill problem with linear decay (5.33), explicit Euler time discretizations.

time discretization: Heun

	DG		second-order CCFV					
	minmod ($\theta = 1$)		minmod ($\theta = 1$)		minmod ($\theta = 2$)		superbee	
L/h	$L_1^r(\%)$	rate	$L_1^r(\%)$	rate	$L_1^r(\%)$	rate	$L_1^r(\%)$	rate
64	1.12×10^2	-	1.11×10^2	-	8.83×10^1	-	7.71×10^1	-
128	7.96×10^1	0.49	7.92×10^1	0.49	4.83×10^1	0.87	2.74×10^1	1.49
256	4.56×10^1	0.80	4.53×10^1	0.81	2.01×10^1	1.26	1.88×10^1	0.54
512	1.89×10^1	1.27	1.87×10^1	1.28	8.59	1.23	7.39	1.35
1024	6.01	1.65	5.93	1.66	2.63	1.71	4.17	0.83
2048	2.01	1.58	1.98	1.59	7.33×10^{-1}	1.84	1.49	1.48
4096	5.50×10^{-1}	1.87	5.29×10^{-1}	1.90	1.78×10^{-1}	2.04	4.57×10^{-1}	1.71
8192	1.40×10^{-1}	1.97	1.30×10^{-1}	2.03	4.17×10^{-2}	2.10	1.21×10^{-1}	1.91

time discretization: Shu3

	DG		second-order CCFV					
	minmod ($\theta = 1$)		minmod ($\theta = 1$)		minmod ($\theta = 2$)		superbee	
L/h	$L_1^r(\%)$	rate	$L_1^r(\%)$	rate	$L_1^r(\%)$	rate	$L_1^r(\%)$	rate
64	1.11×10^2	-	1.11×10^2	-	8.70×10^1	-	7.47×10^1	-
128	7.91×10^1	0.49	7.87×10^1	0.49	4.61×10^1	0.91	2.53×10^1	1.56
256	4.52×10^1	0.81	4.49×10^1	0.81	1.78×10^1	1.37	1.29×10^1	0.98
512	1.88×10^1	1.26	1.86×10^1	1.27	6.91	1.37	6.50	0.98
1024	5.92	1.67	5.83	1.67	2.05	1.75	3.78	0.78
2048	1.98	1.58	1.95	1.58	5.65×10^{-1}	1.86	1.52	1.32
4096	5.47×10^{-1}	1.86	5.26×10^{-1}	1.89	1.36×10^{-1}	2.05	4.58×10^{-1}	1.73
8192	1.40×10^{-1}	1.97	1.29×10^{-1}	2.03	3.22×10^{-2}	2.08	1.21×10^{-1}	1.92

Table 6.4: Space and time convergence of different discretization schemes for Gaussian hill problem with linear decay (5.33), higher-order time discretization.

6.2.2 Linear Decay with Robin Boundary Condition

In order to compare the discretization errors to the OS errors for an advection-diffusion equation with linear decay, we solve the problem (6.4) with zero initial condition and Robin boundary condition with unit inflow concentration. We choose the parameters similar to Section 5.3.2: $v = 1$, $D = 10^{-4}$, $\lambda = 1$, domain length $L = 1$ and final time 0.6.

Due to the sharp front in the tracer concentration C, we expect difficulties in the numerical solution, specifically an occurrence of numerical diffusion. We start with a 32-element mesh and refine it to investigate the convergence of the numerical solution to the analytical solution.

The time step for explicit methods corresponds to the CFL-like number $\nu_l = 0.8$, while the time step for implicit methods is kept constant at a value corresponding to $\nu = 1$ computed for pure advection with Eq. (4.23). The advection dominates even for fine meshes ($\mathrm{Pe_g} > 1$), see Fig. 6.3a.

Fig. 6.3 shows the error in the normalized L_1-norm between the exact and the numerical solution computed using different numerical schemes versus the number of grid elements. Using first-order CCFV with full upwinding and explicit Euler requires at least 1024 elements to keep the discretization error small ($L_1^r < 1\%$). The implicit methods introduce even more numerical diffusion and an even finer mesh is required to reduce the error sufficiently, see Fig. 6.3a. Fig. 6.3b shows the performance of higher-order schemes in space for different time discretizations.

Similar to the Gaussian curve example, higher-order schemes together with explicit Euler show non-monotony convergence to the exact solution for both CCFV with flux reconstruction and DG with minmod limiter. These methods start to converge with a first order again for finer meshes when the Péclet number is less than 8. The best convergence results are obtained using CCFV with flux reconstruction with minmod limiter ($\theta = 2$) together with Heun's method. To reduce the normalized L_1-error under 1%, we require a mesh with only 256 elements; the Damköhler number Da for this mesh is approx. 2.0×10^{-3}.

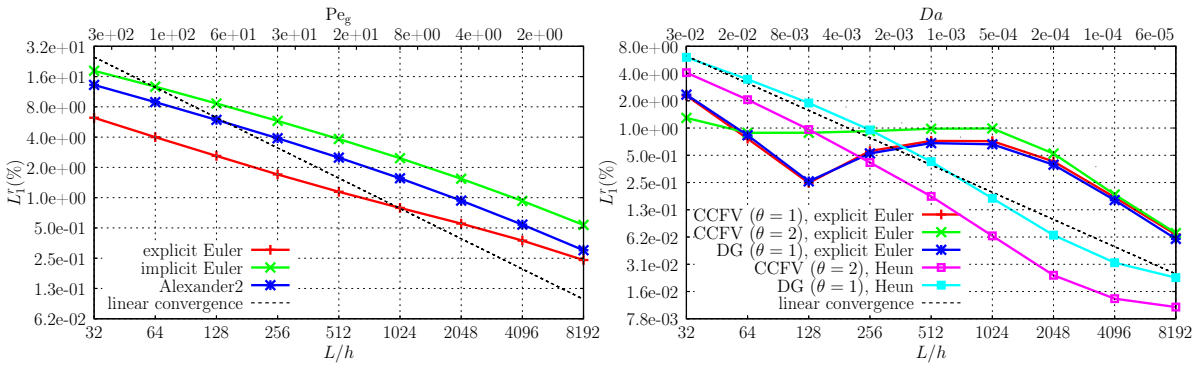

(a) first-order CCFV

(b) higher-order schemes

Fig. 6.3: Spatial convergence of different numerical schemes to the exact solution of advection-diffusion problem with linear decay (6.4) together with Robin boundary condition.

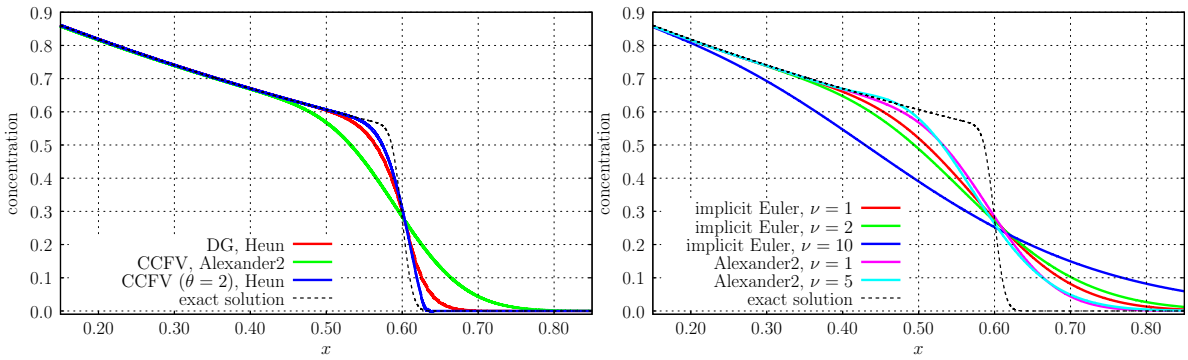

(a) various methods

(b) CCFV with implicit methods

Fig. 6.4: Comparison of numerical solutions computed using various temporal and space discretization schemes to the exact solution of the advection-diffusion problem with linear decay (6.4) together with Robin boundary condition at time $t = 0.6$.

In Fig. 6.4 we compare the exact and the numerical solution obtained using different discretization methods on a mesh with 128 elements. The accuracy of second-order in space schemes together with Heun is much better than the accuracy of first-order schemes with full upwinding. The numerical solution computed with higher-order methods captures the sharp front of the solution well even on this coarse grid, see Fig. 6.4a.

The accuracy of the numerical solution computed by CCFV with full upwinding and implicit Euler depends on the size of the time step (Fig. 6.4b). By increasing the CFL number ν and also increasing the time step Δt, the implicit Euler scheme introduces much more numerical diffusion to the solution. On the other hand, Alexander2 performs well for time steps corresponding to $\nu = 1$ and $\nu = 5$ and does not introduce additional numerical diffusion for larger time steps.

6.2.3 Monod Kinetics with Two Components

In the last one-dimensional problem we compare the numerical solution of two-species reactive transport together with Monod kinetics as described in Section 5.4.2. The system of two equations describing the transport of a substrate with concentration C_1 and the growth and transport of microorganisms with concentration C_2 is given by (5.38) together with reaction terms (5.41). All parameters are equal to the example in Chapter 5 investigating the operator splitting error ($v = 1$, $\lambda_1 = 16$, $\lambda_2 = 0.25$, $K_c = Y_{12} = 0.5$), except for the diffusion coefficient D, which we set to 10^{-4}. Table 6.5 summarizes the Damköhler and Péclet numbers for different mesh resolutions.

We compare the accuracy of two solution approaches: an operator splitting (OS) approach together with higher-order numerical schemes and the numerical solution computed using the global implicit approach (GIA) with first-order numerical discretization in space.

L/h	Da	$\mathrm{Pe_g}$	L/h	Da	$\mathrm{Pe_g}$
64	2.47×10^{-1}	1.56×10^{2}	512	2.83×10^{-2}	1.95×10^{1}
128	1.22×10^{-1}	7.81×10^{1}	1024	1.30×10^{-2}	9.77
256	5.95×10^{-2}	3.91×10^{1}	2048	5.54×10^{-3}	4.88

Table 6.5: Péclet and Damköhler numbers for different mesh resolutions.

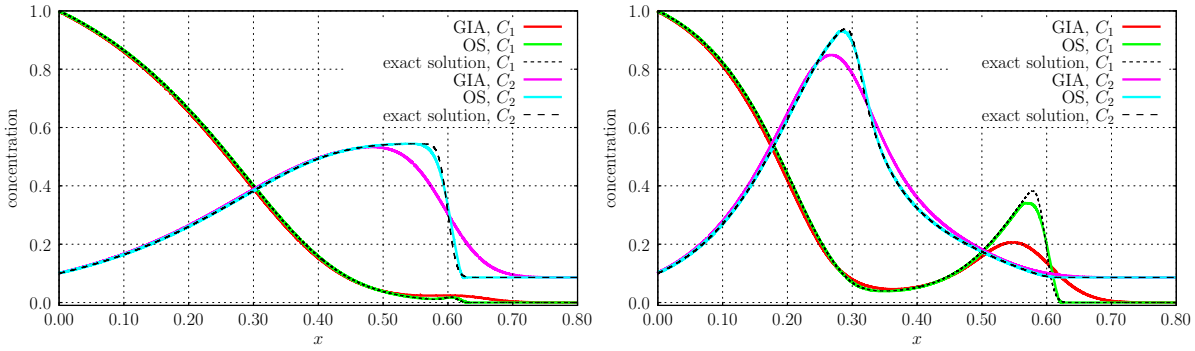

(a) $R_1 = R_2 = 1$ (b) $R_1 = 1, R_2 = 2$

Fig. 6.5: Comparison of different solution strategies computed on mesh with 256 elements to the exact solution for two-component transport with Monod kinetics.

In the GIA approach, we solve the system (5.41) with CCFV with full upwinding using implicit Alexander2. The time step Δt is chosen to fulfill the advection CFL condition (4.23) with $\nu = 1$. The previous examples shows that Alexander2 is more accurate than implicit Euler. The GIA approach does not achieve first-order convergence rates even on very fine meshes, see Table 6.6, where we compare the normalized L_1-errors for both components and different retardation factors. When both components move with the same velocity ($R_1 = R_2 = 1$), the GIA method with above described numerical methods suppresses the normalized L_1-errors under 1% on a mesh with 4096 elements. However, when the second component is retarded ($R_2 = 2$), a relatively sharp front in C_1 occurs and the GIA approach has great difficulty to accurately describe this phenomena, see Fig. 6.5b. Moreover, the error arising from the numerical discretization does not vanish even on a very fine mesh (Table 6.6).

In the OS approach, we use the symmetrical Strang splitting scheme: in each time step Δt we solve the advection-diffusion problem for each component using CCFV with second-order flux reconstruction (minmod limiter with $\theta = 2$), followed by a solution of reactive model using RKF45 with time step $2\Delta t$, followed by one step of advection-diffusion with Δt. The size of the time step in the OS scheme corresponds to the CFL-like number $\nu_l = 0.8$. The second-order Strang splitting reduces the operator splitting error significantly for Damköhler numbers less than 1, see e.g. Table 5.13 in Section 5.4.2, and the error in the numerical discretization predominates the discrepancy between the exact solution and the numerical solution. The normalized L_1-error is less than 1% for both components and both variations of retardation factors on a mesh with 512 elements, see Table 6.7. The OS method with higher-order numerical schemes reducing the numerical diffusion is able to capture the correct solution with high accuracy even on a coarse grid with 256 elements (Fig. 6.5).

	$R_1 = R_2 = 1$				$R_1 = 1,\ R_2 = 2$			
	C_1		C_2		C_1		C_2	
L/h	$L_1^r(\%)$	rate	$L_1^r(\%)$	rate	$L_1^r(\%)$	rate	$L_1^r(\%)$	rate
32	1.21×10^{1}	-	2.13×10^{1}	-	2.66×10^{1}	-	2.03×10^{1}	-
64	6.71	0.85	1.44×10^{1}	0.57	1.87×10^{1}	0.51	1.35×10^{1}	0.59
128	3.63	0.88	9.44	0.60	1.27×10^{1}	0.55	8.63	0.64
256	1.95	0.90	6.10	0.63	8.43	0.59	5.33	0.69
512	1.05	0.90	3.86	0.66	5.47	0.62	3.19	0.74
1024	5.63×10^{-1}	0.90	2.37	0.70	3.44	0.67	1.84	0.79
2048	3.01×10^{-1}	0.90	1.41	0.75	2.07	0.73	1.03	0.83
4096	1.59×10^{-1}	0.92	8.02×10^{-1}	0.81	1.19	0.80	5.63×10^{-1}	0.88

Table 6.6: Convergence of GIA using first-order CCFV with Alexander2 discretization to the exact solution for two-component transport with Monod kinetics.

	$R_1 = R_2 = 1$				$R_1 = 1,\ R_2 = 2$			
	C_1		C_2		C_1		C_2	
L/h	$L_1^r(\%)$	rate	$L_1^r(\%)$	rate	$L_1^r(\%)$	rate	$L_1^r(\%)$	rate
32	2.25	-	7.04	-	1.17×10^{1}	-	8.91	-
64	6.83×10^{-1}	1.72	3.33	1.08	5.66	1.05	3.50	1.35
128	2.19×10^{-1}	1.64	1.50	1.16	2.55	1.15	1.26	1.47
256	6.84×10^{-2}	1.68	6.23×10^{-1}	1.26	1.05	1.28	4.15×10^{-1}	1.61
512	2.95×10^{-2}	1.21	2.55×10^{-1}	1.29	3.99×10^{-1}	1.40	1.22×10^{-1}	1.76

Table 6.7: Convergence of OS together with second-order CCFV with Heun discretization to the exact solution for two-component transport with Monod kinetics.

Summary

We have tested the performance of different numerical discretization schemes on three simple one-dimensional problems, where the advection was a dominating process. In order to compare the errors in the numerical discretization to the operator splitting errors investigated in Chapter 5, we measured the error in the L_1-norm divided by the total component mass (see Section 5.2.1).

The example in this section also demonstrates the difficulties in accurately obtaining asymptotic convergence rates due to the very large problem sizes required to enter the asymptotic regime. Particularly, the first-order CCFV method with full upwinding requires very fine meshes with several thousands elements to achieve the asymptotic first-order accuracy. Thus, the effort to achieve first-order accuracy in multi-dimensional examples will be computationally very demanding, see also the example in Section 6.3.

The second-order schemes perform much better. Although the second-order accuracy is reached only on fine meshes, the convergence rates are in all examples greater than one even on coarse grids. Furthermore, the initial error on the initial mesh is much smaller for the second-order methods than for the first-order schemes.

In many studies, the authors combined second-order CCFV or DG in space with a first-order schemes in time, e.g. Geiser (2007); Mikyška and Firoozabadi (2010). However, the combination of second-order schemes in space and first-order integration in time should be avoided in reactive transport modeling because this combination of methods can create sharp fronts on smooth solutions. Furthermore, the asymptotic convergence rate of the simulation is restricted by the numerical method with the lowest convergence order.

6.3 Rotating Gaussian Hill

In this example we consider an advection-diffusion-reaction problem with a linear reaction on a two-dimensional domain with a rotating flow field. We solve problem (6.4) on the domain $\Omega = [-0.5, 0.5]^2$ together with zero Dirichlet boundary condition. The velocity field is rotating in the center of the domain with $v = (-4y, 4x)^T$. The initial condition is specified as a two-dimensional Gaussian hill

$$C(x, y) = \exp\left(-\frac{(x - x_c)^2 + (y - y_c)^2}{2\sigma^2}\right).$$

The exact solution of this problem reads

$$C(x, y, t) = \frac{2\sigma^2}{2\sigma^2 + 4Dt} \exp\left(\lambda t - \frac{(x^* - x_c)^2 + (y^* - y_c)^2}{2\sigma^2 + 4Dt}\right),$$

where (x^*, y^*) is the backtrack of the characteristic given by

$$x^* = x \cos 4t + y \sin 4t, \quad y^* = -x \sin 4t + y \cos 4t.$$

A similar problem was solved in Liu and Ewing (2005) or without the reaction term in Wang et al. (1999) and in Bastian (2003). For numerical experiments, we choose the final time $t = \frac{\pi}{4}$, which is the time for a half rotation. We use the same parameters as in Wang et al. (1999): $D = 10^{-4}$, $x_c = -0.25$, $y_c = 0$ and $2\sigma^2 = 0.01$. The reaction rate λ is 0.1 as in Liu and Ewing (2005).

To observe the convergence of the numerical solution to the exact solution, we refine the initial uniform mesh with 32 elements in each direction. The initial time step is $\Delta t = \frac{\pi}{512}$ to fulfill the stability condition for explicit methods. We refine the spatial mesh and the time steps such that $h/\Delta t$ remains constant.

The convergence results in Table 6.8 show that the theoretical convergence rates are achieved only for second-order CCFV schemes; other numerical methods would require finer meshes to obtain the theoretical convergence rates. However, the computation on very fine meshes in multiple dimensions requires huge computational effort and is not always guaranteed to achieve the theoretical asymptotic convergence rate.

The solutions computed by higher-order schemes are more accurate than those computed by first-order methods (Table 6.8). The best considered numerical discretization for this example (regarding the error in L_2 and L_∞ norm) is, as in the previous examples, CCFV with flux reconstruction and minmod limiter with $\theta = 2$ together with the method of Heun.

We compare the exact and the numerical solutions computed on a mesh with 128×128 elements in Fig. 6.6. The value spacing between isolines in the contour is 0.1. The first-order CCFV scheme with full upwinding is very diffusive; the L_∞-error on this mesh is 0.51, whereas the L_∞-error for the second-order schemes is less than 0.23.

We can conclude that the second-order schemes perform well even in situations with a complicated flow field. A more thorough discussion of the precision of second-order numerical schemes in two-dimensional problems can be found in the second part of Chapter 7, particularly in Section 7.3.

	first-order CCFV, explicit Euler				second-order CCFV, minmod ($\theta = 1$), Heun			
mesh	L_2-error	rate	L_∞-error	rate	L_2-error	rate	L_∞-error	rate
32×32	5.69×10^{-2}	-	6.53×10^{-1}	-	4.35×10^{-2}	-	5.31×10^{-1}	-
64×64	4.77×10^{-2}	0.26	6.27×10^{-1}	0.06	2.45×10^{-2}	0.83	3.90×10^{-1}	0.44
128×128	3.62×10^{-2}	0.40	5.15×10^{-1}	0.28	9.44×10^{-3}	1.37	2.04×10^{-1}	0.93
256×256	2.46×10^{-2}	0.56	3.71×10^{-1}	0.47	2.91×10^{-3}	1.70	8.74×10^{-2}	1.23
512×512	1.50×10^{-2}	0.71	2.38×10^{-1}	0.64	8.05×10^{-4}	1.85	3.20×10^{-2}	1.45
1024×1024	8.48×10^{-3}	0.83	1.38×10^{-1}	0.78	2.03×10^{-4}	1.99	9.87×10^{-3}	1.70

	second-order CCFV, minmod ($\theta = 2$), Heun				DG, minmod ($\theta = 1$), Heun			
mesh	L_2-error	rate	L_∞-error	rate	L_2-error	rate	L_∞-error	rate
32×32	3.08×10^{-2}	-	3.97×10^{-1}	-	4.10×10^{-2}	-	6.26×10^{-1}	-
64×64	1.20×10^{-2}	1.36	2.06×10^{-1}	0.94	2.47×10^{-2}	0.73	4.26×10^{-1}	0.56
128×128	3.54×10^{-3}	1.76	6.79×10^{-2}	1.60	1.02×10^{-2}	1.27	2.27×10^{-1}	0.91
256×256	9.06×10^{-4}	1.97	1.64×10^{-2}	2.05	3.46×10^{-3}	1.57	1.04×10^{-1}	1.12
512×512	2.33×10^{-4}	1.96	3.34×10^{-3}	2.30	1.13×10^{-3}	1.62	4.49×10^{-2}	1.21
1024×1024	5.97×10^{-5}	1.96	8.45×10^{-4}	1.98	3.72×10^{-4}	1.60	1.86×10^{-2}	1.27

Table 6.8: Convergence of different discretization schemes for 2D Gaussian hill problem with linear decay.

6.4 Discussion

The two approaches to solve reactive transport problems discussed in this thesis, the global implicit approach and the operator splitting approach, offer different sets of advantages and disadvantages and are applicable to different types of problems. GIA introduces an error only in the numerical discretization of the underlying problem. On the other hand, in the OS method there are two sources of errors: the intrinsic error involved with OS and the discretization errors associated with the operator approximations.

In this chapter and in Chapter 5 we denote the solution to be accurate enough or the errors to be reduces sufficiently if the error in the normalized L_1-norm is less than 1% for all considered components. Note that in both chapters we solved similar problems to be able to compare the OS and the discretization errors.

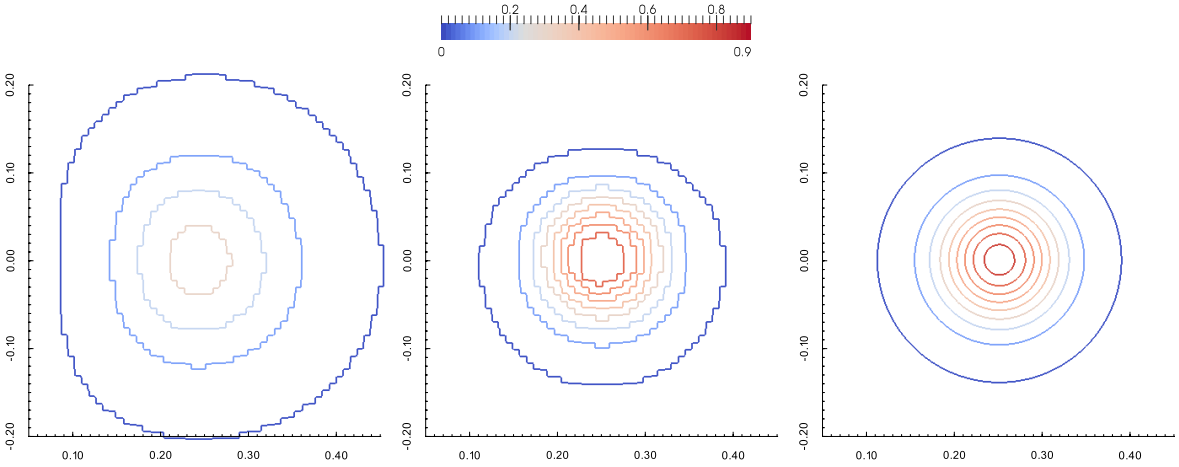

(a) first-order, explicit Euler (b) second-order, Heun (c) exact solution

Fig. 6.6: Contours of the numerical and exact solution of rotating Gaussian hill problem after half rotation on grid with 128×128 elements: (a) first-order CCFV with explicit Euler, and (b) second-order CCFV with minmod limiter and method of Heun.

OS **approach vs.** GIA

For many transport, diffusion and reactive problems of interest, it is likely that the difference in the relevant time scales is sufficiently large and the additional numerical error introduced by operator splitting is small, see the discussion in Chapter 5. This is particularly the case if the reactive processes are slow compared to the transport. We quantify this relationship using dimensionless Damköhler number. For $Da < 0.1$ the Strang splitting is mostly in an asymptotic convergence region and generates $\mathcal{O}(\tau^2)$ splitting error. Thus, the additional truncation error introduced by decoupling the transport and reaction terms is negligible when the splitting time step is sufficiently small, mostly corresponding to $Da < 0.01$.

In our implementation of OS, we solve the transport explicitly with a second-order CCFV scheme in space and Heun's method in time. The flux reconstruction with minmod slope limiter and parameter $\theta = 2$ together with Heun consistently outperformed all tested slope limiters and time discretization schemes in all considered test examples. GIA uses first-order CCFV together with unconditionally stable implicit methods in time. As expected, OS works well particularly in the advection-dominated regime, while GIA in this case fails to accurately capture sharp fronts in the solution.

In one-component transport with linear decay, GIA requires a mesh with at least 1024 elements, whereas the OS method achieves a sufficient error reduction with only 256 elements. We observe similar behavior also in two-component transport with Monod kinetics. GIA needs very fine mesh with at least 4096 elements to reduce the error in all situations for all components sufficiently. On the other hand, OS with higher-order methods requires only a mesh with 512 elements to obtain the same accuracy. The problem of GIA is particularly the accuracy of the underlying numerical methods. Although we use first-order CCFV, to reach the region of

first-order accuracy in h-convergence one needs to use very fine grids. This is a severe problem particularly in two- and three-dimensional simulations to perform a transient computation in which evolution details are important.

For high values of Da, the reaction approaches equilibrium almost immediately and the error associated with the splitting method increases. In this case, an equilibrium model may be more appropriate. This is consistent with the observation of several researchers that the use of the local equilibrium assumption in modeling reactive systems may be appropriate when the governing Damköhler number is greater than 100 (Miller and Rabideau, 1993).

For systems characterized by rapid reactions, however, a more careful assessment of the potential error introduced by operator splitting is required. As shown by the example with linear retardation in Section 5.4.1, neither of the tested operator splittings is more than first-order accurate. The convergence order is for small number of splitting time steps less than one and we need more than 1000 time steps to reduce the OS error sufficiently. This magnitude of error is comparable to the discretization error introduced by GIA for linear transport with linear decay discussed in Section 6.2.2. Furthermore, in systems with many components where the reactions are described by local equilibrium, the OS errors can accumulate and the model behavior may become quantitatively wrong.

(Carrayrou et al., 2010) tested a code based on OS approach to solve a reactive problem including instantaneous equilibrium chemistry, kinetic rate laws and precipitation-dissolution reactions. They showed that intensive mesh refinement and small splitting time steps are needed to reach the reference solution with the desired accuracy. The time discretization as well as the splitting time step correspond to transport CFL numbers between 10^{-3} and 10^{-2}. However, using small time steps requires a huge computational effort and even the accuracy of numerical methods for advective transport with small time steps can be reduced. The applicability of the OS approach to solve reactive transport systems with several fast chemical reactions needs more investigation. We note that in this thesis we concentrate on chemical reactions which we are able to describe with kinetically controlled rate laws.

The GIA appears to be particularly well suited for long term problems because it allows very large time steps in comparison to the time scale of the transport processes. Large time steps together with first-order methods in space affect the accuracy of the solution significantly for non-reactive components or components which are not described by equilibrium. However, they do not affect the distributions of component concentrations controlled by fast reactions. In Mayer et al. (2002), the author mentioned that fast reactions can have a self-sharpening effect on concentration fronts, which can even cancel the effects of transport-induced numerical diffusion. This may also explain the comparably small errors introduced when using OS techniques for the solution of reactive-transport problems largely controlled by equilibrium reactions (Walter et al., 1994). The GIA approach is particularly suitable in situations where the concentration gradients are controlled by geochemical reaction processes and not by transport processes.

Solution Strategy

The choice of solution strategy depends on the nature and the velocity of the reactive and transport processes involved in the system. Furthermore, the main purpose of the instationary

simulation plays an important role. The solution strategy is different in situations when we are interested in a steady-state solution or where the evolutions details are important.

In the solution procedure described in Section 4.6 (see also simulation flow chart in Fig. 4.2), we firstly solve the two-phase problem and obtain a velocity field. From this velocity field we can compute compute Péclet and Damköhler numbers by Eqs. (6.1) and (6.2). Then we choose the solution strategy as follows:

- $Da < 0.01$:
  We prefer the OS approach with symmetrical Strang splitting and higher-order methods to solve component transport. Furthermore, if $\mathrm{Pe_g} < 500$, the Strang splitting is mostly in an asymptotic convergence region. When $\mathrm{Pe_g} < 2$, the problem is locally diffusion dominant and the advection term can be approximated by central differences. In this case, we can also split advection and diffusion or use RK-IMEX schemes. For very low Damköhler numbers ($Da \ll 0.01$) we can use several time steps Δt to solve the sub-problems in one splitting time step τ. We use GIA for long-term experiments where we are not interested in sharp fronts and details of concentrations, only in a steady-state solution. However, the time step should be bounded to reduce an excessive numerical diffusion.

- $0.01 < Da < 100$:
  No solution strategy is optimal: we use an OS approach with symmetrical Strang splitting and higher order discretization methods. However, the splitting error can be comparable to the discretization error.

- $Da > 100$:
  In principle, GIA is the preferred approach in this regime because the magnitude of the OS error is unpredictable. On the other hand, the high computational effort involved in GIA often mandates the use of the first-order OS approach instead. In this case, the splitting time step τ should not exceed the time step given by the CFL condition for the explicit time discretization.

Finally we note that to ensure a quantitatively correct solution, it is necessary to compare the two approaches in a model simulation with reduced size and investigate the h-convergence to verify that the numerical solution is not influenced by errors arising in operator splitting and numerical discretization.

Chapter 7

Applications to Processes in Unsaturated Porous Media

We apply the numerical simulator developed and tested in previous chapters to simulate, describe and analyze two laboratory experiments. In the first part, we investigate the transport of nanoparticles in unsaturated porous media and find a suitable model which is able to describe measured breakthrough curves. We then use parameter estimation to obtain the kinetically controlled parameters. All data and modeling results for the nanoparticles were published in Kumahor et al. (2015b).

In the second part of this chapter, we study oxygen transport in saturated and unsaturated porous media. We compare the oxygen profiles measured by C. Haberer in a flow-through cell filled with glass beads to numerical simulations. Furthermore, we study the influence of different numerical discretization schemes on the accuracy of the numerical simulations in setups, which are similar to the laboratory experiment.

7.1 Transport of Citrate-Coated Silver Nanoparticles

7.1.1 Introduction

The transport of nanoparticles (NP) in the subsurface is a topic of significant scientific interest, because soils and aquifers act as the primary filter systems to protect water resources (Liang et al., 2013a). NPs can be highly mobile and may potentially contaminate groundwater. Furthermore, NPs based on silver (Ag) and its compounds are known to have anti-microbial properties and can act as effective microbial growth inhibitors instead of antibiotics (Kim et al., 2007). The transport and retention of NPs in porous media is controlled by the coupling of chemical factors, physical constraints of the particles, the solution chemistry and the hydrodynamic properties of the system. Moreover, in unsaturated porous media, particle mobility is determined by the existence of an air-water interface in addition to a solid-water interface. Thus, the development of mathematical models capturing all effects is very challenging.

We developed the model described below based on data from laboratory experiments executed by S. Kumahor. He performed several flow-through experiments in unsaturated porous medium and measured breakthrough curves and retention profiles of citrate-coated Ag nanoparticles. We refer the reader to Kumahor et al. (2015a) and Kumahor et al. (2015b), where the laboratory setup and measured techniques are described in more detail. We briefly describe the experiment with a focus on the experimental aspects which are important for the model development.

7.1.2 Experimental Setup

The experimental column was a polyvinyl chloride cylinder with an inner diameter of 16.2 cm and a height of 10 cm. The column was filled with quartz sand with a mean grain diameter of 0.2 mm and a bulk density of $1.52\,\mathrm{g\,cm^{-3}}$.

The water retention curves and the unsaturated hydraulic conductivity functions of this sand were measured using the multistep-outflow (MSO) experiments. The results were used to design the transport experiments with nanoparticles, for details see Kumahor et al. (2015a).

The flow-through experiments were conducted with two pH values (5 and 9) and three different flow rates ($2.5, 9.7$ and $17.0\,\mathrm{cm\,h^{-1}}$). The different flow rates correspond to different volumetric water contents θ_l (i.e., 0.17, 0.29 and 0.35 respectively) and pore-water velocities (i.e., 14.7, 33.4 and $48.6\,\mathrm{cm\,h^{-1}}$ respectively). The constant inlet flux was established via a peristaltic pump such that a uniform θ_l was realized during the water flow.

The NP transport experiments were conducted along the following steps. Prior to the application of Ag NP dispersion, the column was flushed with 5 pore volumes of the background electrolyte solution (containing 1 mmol KNO_3) to establish a stationary flow field. Then, 8 pore volumes of the Ag NP dispersion were delivered through 19 evenly distributed hypodermic needles at the surface. This was followed by another 8 pore volumes of Ag NP-free solution to quantify the mass of NPs irreversible retained. After the flow-through experiment, the column was then dissected into layers of 1 cm, the concentration of attached NPs was measured and the retention profiles were established (see e.g. Fig. 7.1b).

This procedure was repeated for both the inert tracer (KBr solution) and for the NPs with different flow rates and pH values. The outflow concentrations were measured during the experiment and breakthrough curves (BTC) were established (Figs. 7.1a, 7.2a and 7.3a). Note that the BTCs measured under quasi-steady state unsaturated flow showed retardation of the NPs compared to the inert solute.

7.1.3 Model Formulation

We propose a model formulation which is motivated by the qualitative interpretation of the BTCs. The colloid filtration theory (CFT) has commonly been employed to predict the deposition of NPs on collector surfaces (Liang et al., 2013a; Tufenkji, 2007). However, in contrast to the classical CFT, the BTCs are asymmetric and retarded. There is a steep initial breakthrough followed by a long tailing as typical for non-equilibrium sorption. At the same time the initial breakthrough is shifted in time with respect to the tracer as typical for a simple retardation at equilibrium. Hence, the BTCs suggest two parallel processes controlling the transport of NPs:

1. retardation of the NPs relative to the tracer which can be represented by a retardation factor R in analogy to the equilibrium sorption;
2. a non-equilibrium process depicted as unbalanced attachment and detachment rates.

Based on these observations, we use a two-site sorption model, where the sorption sites can be divided into two parts: kinetically controlled adsorption and an adsorption, which is in equilibrium with aqueous concentration as in Chen et al. (2003).

Thus, we model the transport of the citrate-coated Ag NPs in unsaturated porous medium using a one-dimensional form of the ADR equation

$$\frac{\partial\left(\theta_l R C_{np}\right)}{\partial t} + \nabla \cdot \{j_w C_{np} - \theta_l D \nabla C_{np}\} = -\rho_b \frac{\partial S_{np}}{\partial t}, \tag{7.1}$$

where C_{np} is the concentration of NPs in the aqueous phase, j_w the flow rate, θ_l the volumetric water content, D the dispersion coefficient, ρ_b the bulk density of the packed column and S_{np} is the amount of attached NPs. The pore velocity v is related to the flow rate as $v\theta_l = j_w$. The one-dimensional computational domain represents a vertical cut in z-direction. We can use this approximation because of the symmetry of the experimental domain and because the flow velocity is constant in the whole domain.

For the special case of linear adsorption, the retardation coefficient R relates to an equilibrium sorption coefficient (K_{eq}) given by

$$R = 1 + \frac{\rho_b K_{eq}}{\theta_l},$$

where $K_{eq} = S^e_{np}/C_{np}$ and S^e_{np} is the amount of NPs sorbed under equilibrium conditions. The mass balance equation for the NPs in the solid phase is given by

$$\rho_b \frac{\partial S_{np}}{\partial t} = \theta_l \psi k_{att} C_{np} - \rho_b k_{det} S_{np}, \tag{7.2}$$

where k_{att} and k_{det} are the attachment and detachment coefficients, respectively. The relation (7.2) incorporates a dimensionless time and depth dependent straining function ψ as in Kasel et al. (2013) given by

$$\psi = \left(1 - \frac{S_{np}}{S^m_{np}}\right)\left(\frac{p_d + z}{p_d}\right)^{-\beta}, \tag{7.3}$$

where p_d is the mean grain size of the porous medium, β is the shape factor for retention along the flow path, z is the distance from the column inlet and S^m_{np} is the maximal attainable amount of NPs attached to the sand grains. Hence, the first and second terms on the right hand side of (7.3) represent temporal dynamics and depth dependent interaction of NPs, respectively (Torkzaban et al., 2008).

The model (7.2-7.3) describes a kinetic attachment and detachment mechanism together with equilibrium adsorption. However, it should be noted that equilibrium adsorption does not result in removal of NPs from the aqueous phase. Rather, this process gives rise to a retarded breakthrough of NPs in comparison to that of a conservative (inert) tracer. That means it is a completely reversible process (Tufenkji, 2007).

7.1.4 Parameter Estimation

The chosen mathematical model (7.1-7.3) contains several unknown parameters. We obtained these parameters including $\theta_l, j_w, D, k_{att}, k_{det}, R, S^m_{np}$ and β either directly from the laboratory

experiments or estimated them using inverse modeling.

The flow rates j_w and water content θ_l were directly obtained from the tracer and the NPs transport experiments, while D was obtained by fitting a one-dimensional exact solution of the advection-diffusion equation to the breakthrough curves of the tracer (Kumahor et al., 2015a). We determined the parameter D also using parameter estimation to test the correctness of our implemented Levenberg-Marquardt-Algorithm (LMA). The maximal attainable concentration S_{np}^m was determined from the NP retention profiles and is first fixed to the maximal measured value for given experiment. In the second part of the discussion, we also estimated the value of S_{np}^m independently of the measured values. The remaining parameters k_{att}, k_{det}, R and β were obtained via parameter estimation using LMA, for details see Section 4.7. The error in measured normalized concentrations is fixed to 0.04.

In the forward problem, we solve the transport equation for the NPs in the aqueous phase (7.1) together with the reversible attachment models (7.2) and (7.3) with given inflow concentrations. The initial concentration of NPs in both phases is zero, whereas the inflow aqueous concentration denoted by C_{np}^i differs depending on the concrete experiment. In order to minimize numerical errors when solving the forward problem, the 10 cm one-dimensional domain was discretized into 512 elements for the CCFV discretization. We use the second-order Strang splitting to solve the ADR system, where we split physical transport and chemical reactions. We solve the transport part with Heun time integration together with second-order flux reconstruction and use the RKF45 method for the reaction. The concentration in the last element was taken as the outflow concentration in each time step.

7.1.5 Results and Discussion

Table 7.1 shows the estimated parameters, the residua for parameter estimation and the coefficients of determination. All BTCs could be modeled reasonably well and the simulated BTCs are able to capture the main features of the NP transport. The goodness of fit is given by the coefficient of determination $\mathcal{R}^2$, which is for all experiments greater than 0.964.

The resulting differences in k_{att} and k_{det} (Table 7.1) suggest intermediate to fast attachment to the solid-water interface but slow detachment. The values of k_{att} are several order of magnitude smaller than k_{det} and the kinetic desorption of NPs can be neglected (e.g., Liang et al. (2013b)). The retardation term required to describe the BTCs is an added feature and has not been typically observed for saturated transport. We suggest that the equilibrium sorption may be linked to the air-water interface and its surface area.

For higher j_w and θ_l, a broader spectrum of pores is activated, leading to much faster NP breakthrough compared to lower j_w and θ_l. Kumahor et al. (2015a) observed that dispersivity increased non-linearly with decreasing θ_l. They interpreted it as a change in the geometry of the flow field when θ_l is reduced.

Figs. 7.1 to 7.3 show the BTCs of NPs and the corresponding retention profiles. The experimental results and model outputs are indicated as points and lines respectively. The BTCs depict a non-linear increase in mobility with increasing j_w and θ_l, and lower NP mobility at pH = 5 compared to pH = 9.

j_w [cm h^{-1}]	pH	S_{np}^m [–]	k_{att} [s^{-1}]	k_{det} [s^{-1}]	β [–]	R [–]	$\mathcal{R}$	$\mathcal{R}^2$(%)
2.4	9	2.29×10^{-6}	8.73×10^{1}	3.99×10^{-6}	1.88	3.44	0.23	98.9
9.7	5	4.50×10^{-6}	8.79×10^{-1}	1.12×10^{-6}	1.47	2.46	23.34	99.7
9.7	9	1.26×10^{-6}	3.01×10^{-1}	4.15×10^{-6}	1.22	2.65	6.80	99.9
17.0	5	1.79×10^{-6}	2.73×10^{-1}	1.50×10^{-8}	1.03	1.48	227.28	96.4
17.0	9	2.06×10^{-7}	2.84×10^{-2}	1.06×10^{-5}	0.84	1.58	51.56	99.4

Table 7.1: Model parameters obtained from the one-dimensional transport and retention model (7.1-7.3) for Ag NPs using inverse modeling. The maximal attainable concentration S_{np}^m was determined from the NP retention profiles.

j_w [cm h^{-1}]	pH	S_{np}^m [–]	k_{att} [s^{-1}]	k_{det} [s^{-1}]	β [–]	R [–]	$\mathcal{R}$	$\mathcal{R}^2$(%)
9.7	5	1.87×10^{-5}	5.53	3.63×10^{-6}	2.08	2.43	12.73	99.7
9.7	9	3.05×10^{-6}	1.41	4.72×10^{-6}	1.64	2.66	6.00	99.9
17.0	5	5.80×10^{-5}	5.01×10^{-1}	1.47×10^{-8}	1.45	1.67	66.15	99.0
17.0	9	4.12×10^{-7}	5.95×10^{-2}	2.18×10^{-5}	1.06	1.59	44.55	99.7

Table 7.2: Model parameters obtained from the one-dimensional transport and retention model (7.1-7.3) for Ag NPs. Parameters S_{np}^m, k_{att}, k_{det}, β and R were determined using inverse modeling.

The maximal retention of NPs was observed close to the column surface (Figs. 7.1 to 7.3). Our model parametrization could mimic the influence of j_w and θ_l for a given pH level. Hence, the model concept is sensitive to the investigated flow dynamics and the delineated chemical boundaries. The magnitude of NPs retained at the column surface is highly sensitive to j_w and pH. This ranges from almost no retention for the highest j_w at pH = 9, to almost complete retention for the lowest j_w at pH = 9 (Figs. 7.1 to 7.3). This suggests that flow dynamics and chemical forces are coupled to determine the shape of the retention profiles. It is however noted that the filtration theory is not always valid for deposition under unfavorable conditions (Tufenkji, 2007) and probably unable to mimic coupled physical and chemical processes. Further discussion about the measured data for the NPs and their properties goes beyond the scope of this thesis. We refer the reader to Kumahor et al. (2015b), where the experimental results are explained in more detail.

Although the model with a fixed parameter S_{np}^m describes the effluent concentration curves and the final spatial distribution of NPs well, we also tried to estimate all the parameters including S_{np}^m. Table 7.2 shows the estimated parameters together with the computed residua. As expected, the performance of the model tends to increase with an increasing number of fitted parameters ($\mathcal{R}^2 > 0.99$ for all experiments). Comparison of the residua in Tables 7.1 and 7.2 shows that the model with more fitting parameters performs better, particularly in experiments with lower pH and higher flow velocities, see also Fig. 7.4. Moreover, the difference between the values of k_{att} in Tables 7.1 and 7.2 shows the model sensitivity to the model assumption: fixing the parameter S_{np}^m to the maximum of measured NP concentration in the solid phase.

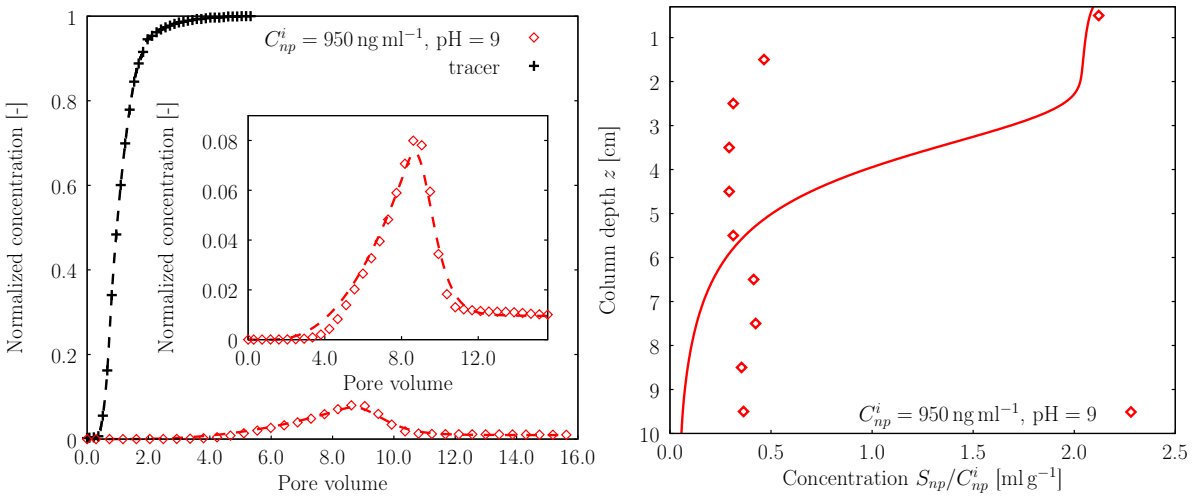

(a) (b)

Fig. 7.1: Experimental breakthrough curves (a) and retention profiles (b) for NPs. The symbols and lines represent experiment outcomes and model results respectively for $j_w = 2.4\,\mathrm{cm\,h^{-1}}$ and $D = 14.15\,\mathrm{cm^2\,h^{-1}}$. The inset Fig. zooms in on the shape of the breakthrough curve.

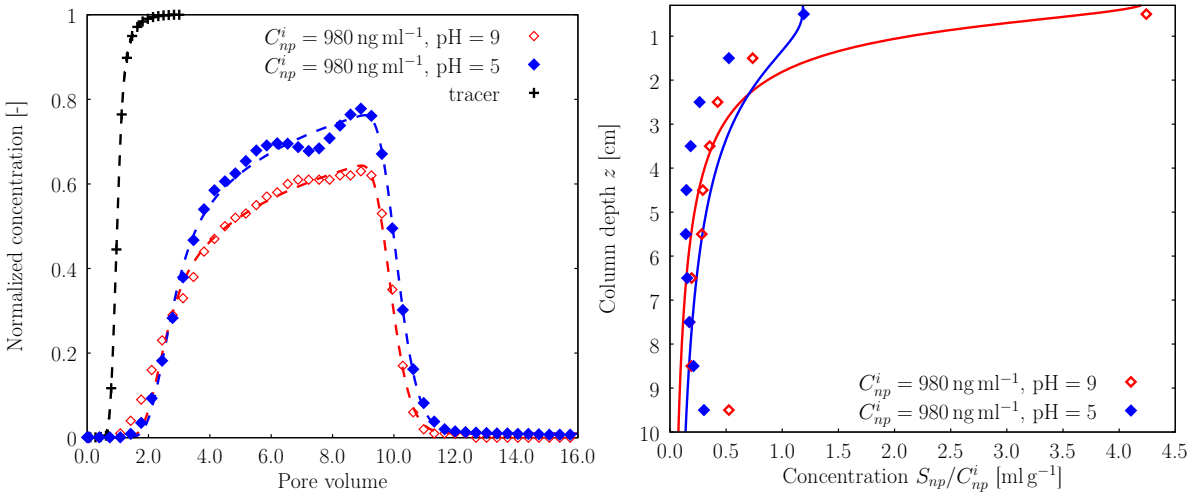

(a) (b)

Fig. 7.2: Experimental breakthrough curves (a) and retention profiles (b) for NPs. The symbols and lines represent experiment outcomes and model results respectively for $j_w = 9.7\,\mathrm{cm\,h^{-1}}$ and $D = 6.95\,\mathrm{cm^2\,h^{-1}}$.

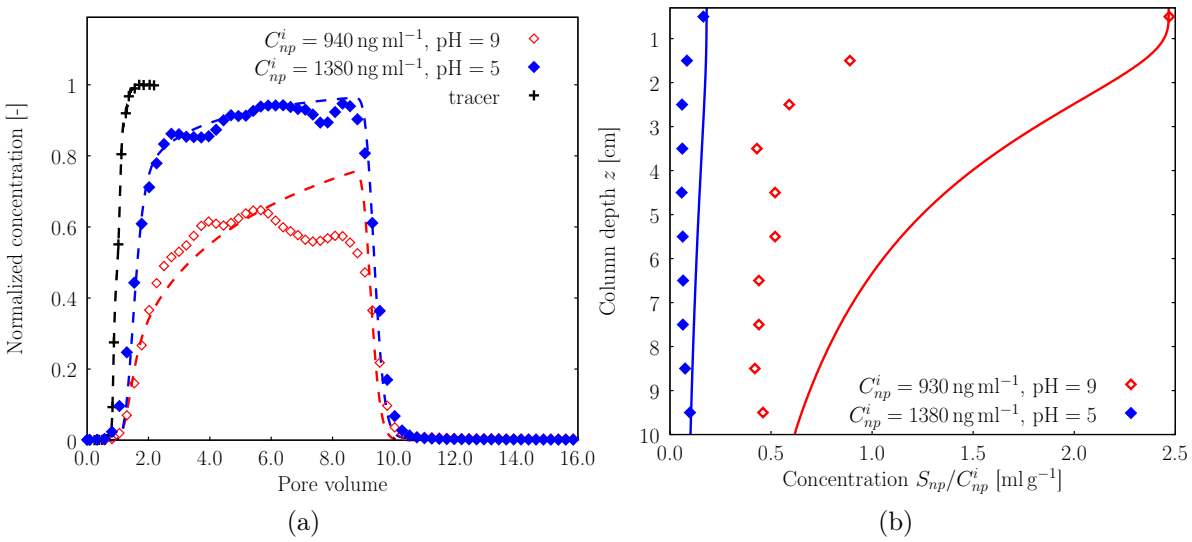

Fig. 7.3: Experimental breakthrough curves (a) and retention profiles (b) for NPs. The symbols and lines represent experiment outcomes and model results respectively for $j_w = 17.0\,\mathrm{cm\,h^{-1}}$ and $D = 0.13\,\mathrm{cm^2\,h^{-1}}$.

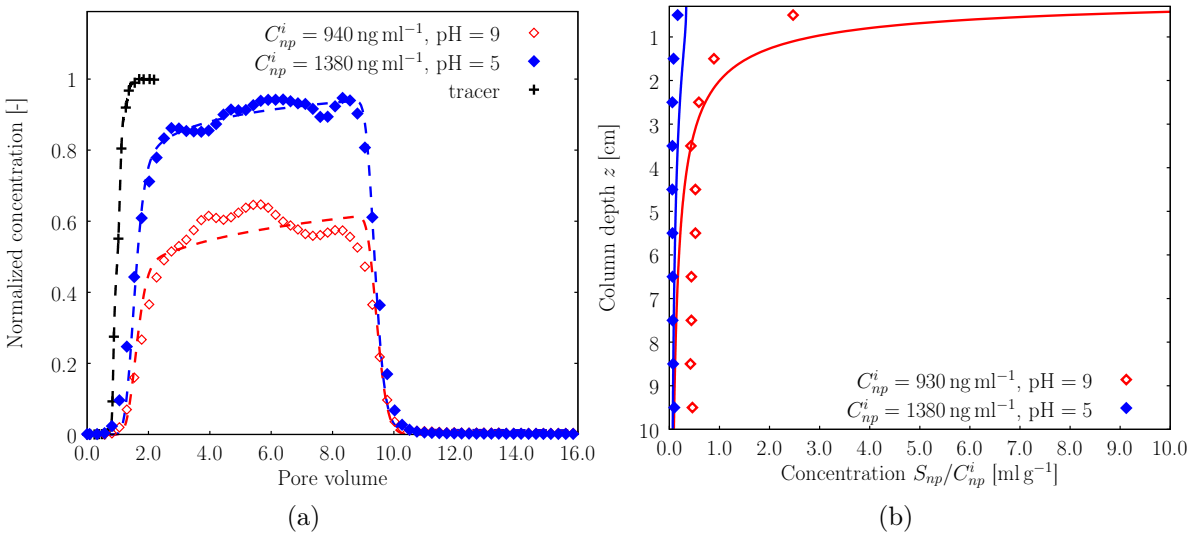

Fig. 7.4: Experimental breakthrough curves (a) and retention profiles (b) for NPs. The symbols and lines represent experiment outcomes and model results respectively for $j_w = 17.0\,\mathrm{cm\,h^{-1}}$ and $D = 0.13\,\mathrm{cm^2\,h^{-1}}$. Parameter S^m_{np} was also estimated (Table 7.2).

7.2 Oxygen Transport Experiment

7.2.1 Introduction

To assess the performance of the transport model, we investigated the transport of oxygen across the capillary fringe. We define the capillary fringe (CF) in a wide sense as the region of the subsurface which is above the groundwater table but still dominated by capillary rise.

This section is based on laboratory experiments conducted by C. Haberer published in Haberer et al. (2011). The author focused on the mass transport of oxygen across the interface between the unsaturated and the saturated zones and within the groundwater. These investigations help to deepen our quantitative understanding of flow and transport processes in the CF. The active flow and transport processes within the CF make this zone interesting because steep gradients in oxygen concentrations exist and a high microbial activity is expected (Maier and Grathwohl, 2005). Thus, oxygen transport across the CF is relevant for many bio-geochemical processes, see also Chapter 8.

7.2.2 Experimental Setup

Fig. 7.5 shows a photograph of a flow-through cell (FTC) system which was used in the laboratory experiment. The FTC with inner dimensions of $80 \times 40 \times 1\,\text{cm}$ was filled with a homogeneous packing of glass beads with grain size diameters of 1.0-1.5 mm. During the filling procedure, the water table was slowly raised and constantly maintained above the top of the porous medium in order to avoid entrapment of air bubbles. After the flow-through chamber has been completely packed, the water table was lowered to its final stage such that the top of the capillary fringe was kept below the surface of the porous medium and an unsaturated zone was created in the upper region of the packing.

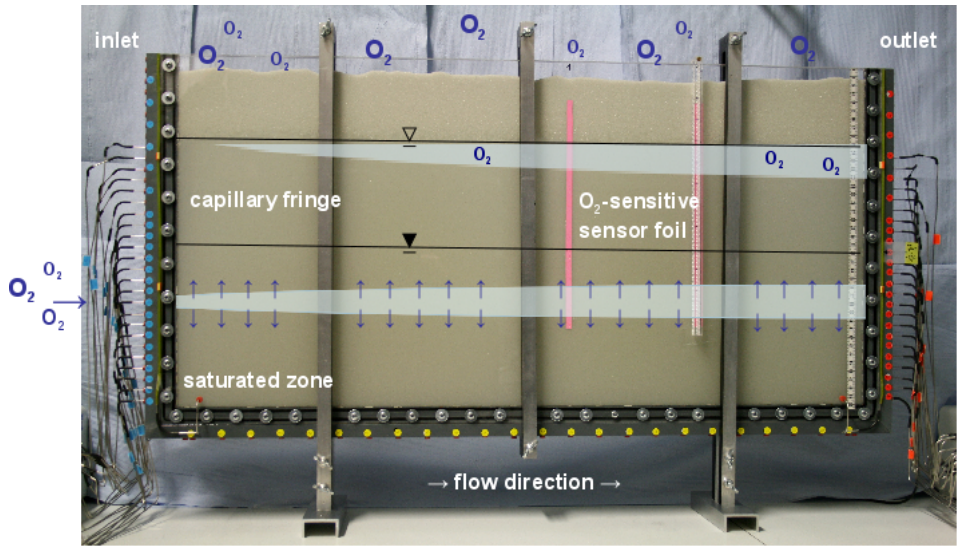

Fig. 7.5: Experimental setup for oxygen transport experiment in the flow-through cell filled with glass beads, picture by C. Haberer.

The water table was kept constant at a height of 27 cm and the CF extended to a height of 29 cm with a rapid transition to low saturations. The average porosity ϕ of the porous medium determined by tracer experiments was 0.413 and the permeability K was $1.31 \times 10^{-9}\,\mathrm{m}^2$. The capillary pressure-saturation relationship is described by a Brooks-Corey model, see Eqs. (2.3) and (2.5), with an air-entry pressure $p_e = 186.39\,\mathrm{Pa}$ and pore size distribution index $\lambda_{bc} = 2$.

On each side of the chamber there are 23 inlet (outlet) ports, with a vertical separation of 12.5 mm, connected to a peristaltic pump. A constant pumping rate of $7.5\,\mathrm{ml\,min^{-1}}$ created a quasi-stationary horizontal water flow with a pore velocity of $18\,\mathrm{m\,d^{-1}}$. Initially, the water in the FTC was nearly oxygen free, with a background oxygen concentration $C_{bg} = 0.026\,\mathrm{mol\,m^{-3}}$. In order to study the transport of oxygen in the saturated zone, oxygen with concentration $C^i = 0.26\,\mathrm{mol\,m^{-3}}$ was added to the water entering at the 11^{th} inlet port (13.13 cm from the bottom), while the water at the other inlet ports kept the small background concentration C_{bg}. The total duration of the transport experiment was 4 hours.

The oxygen concentrations were measured using two vertical stripes of oxygen-sensitive polymer optode foil placed at distances of 45 cm and 60 cm from the inlet. At each stripe, a profile of the oxygen concentration was measured with a high vertical resolution. Each stripe has more than 100 measurement locations spaced by 2.5 mm, see Haberer et al. (2011) for more details.

Over time, the oxygen was transported to the right and the vertical extension of the oxygen rich plume became wider due to diffusion, see Fig. 7.5 and the numerical simulation in Fig. 7.6. At the interface between the unsaturated and the saturated zone, the oxygen transfer between the two phases occurred by diffusion, and a steady-state profile of the oxygen concentration was developed.

7.2.3 Simulation

The mass transfer between the liquid and the gas phase at the air water interface is fast enough to assume local equilibrium and can be computed by Henry's law (2.13). Only molecular diffusion with a diffusion coefficient of $D_{l,O_2} = 1.25 \times 10^{-8}\,\mathrm{m^2\,s^{-1}}$ was considered for oxygen.

We simulated the laboratory experiment with our operator splitting approach solving first for the steady-state flow field of the water transport described by Eq. (3.2). Afterwards, the transport of oxygen in the water (Eq. (3.3)) was simulated with the second-order CCFV scheme

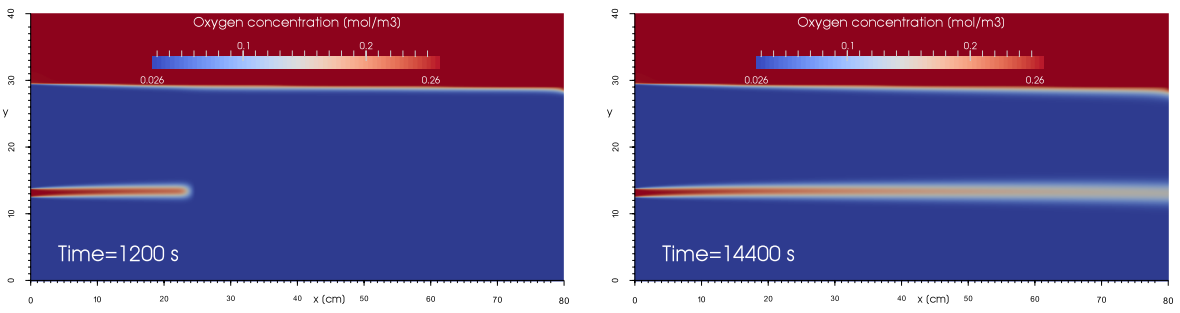

Fig. 7.6: Distribution of oxygen plume in the FTC, second-order CCFV with flux reconstruction and Heun time discretization, mesh 2048 × 1024 elements.

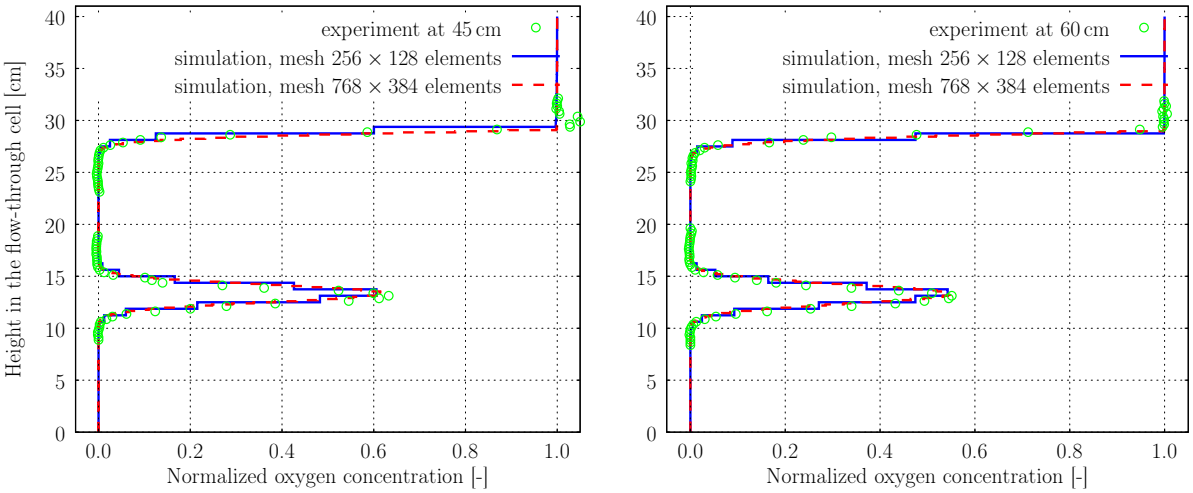

Fig. 7.7: Comparison of profiles of the normalized oxygen concentration after four hours at 45 and at 60 cm from the inlet.

together with the method of Heun. Two different grid resolutions (256×128 and 768×384 elements) were used to test for grid convergence. The concentration profile was compared after four hours of simulated time. As the water was not completely oxygen free, we used a normalized oxygen concentration defined by

$$C_n = \frac{C_{l,O_2} - C_{bg}}{C^i - C_{bg}}, \tag{7.4}$$

where C_{l,O_2} is the measured oxygen concentration in water, C_{bg} is the measured background concentration of oxygen and C^i refers to the oxygen concentration at the air-water interface and at the inlet. Fig. 7.7 shows an excellent agreement between measured and simulated data, both for the position of the peak and its width. The fine and coarse grid results are nearly identical, indicating a negligible discretization error already on the coarse grid.

Fig. 7.8a shows a comparison of profiles of the normalized oxygen concentration after 3000 s at 45 cm from the inlet computed using two different numerical schemes: second-order CCFV with flux reconstruction and first-order CCFV with full upwinding. Both simulations are performed on a grid with resolution 256×128 elements and the chosen time step corresponds to the advection CFL number (Eq. 4.23) less than 1. While the flow is quasi horizontal and the flow field is perpendicular to the grid interfaces, one is able to get a good description of the vertical profile of the oxygen plume even using first-order CCFV with the implicit Euler method. In this case, almost no numerical diffusion is added to the vertical profile of the numerical solution.

Up to now we have investigated only one-dimensional numerical examples or experiments where the flow velocity was perpendicular to the grid orientation. However, the difficulty of numerical diffusion is more severe in problems where the flow is diagonal to the face orientations (Steefel and Lasaga, 1994) and we expect more numerical diffusion introduced by the first-order CCFV scheme in transport problems with complicated flow fields.

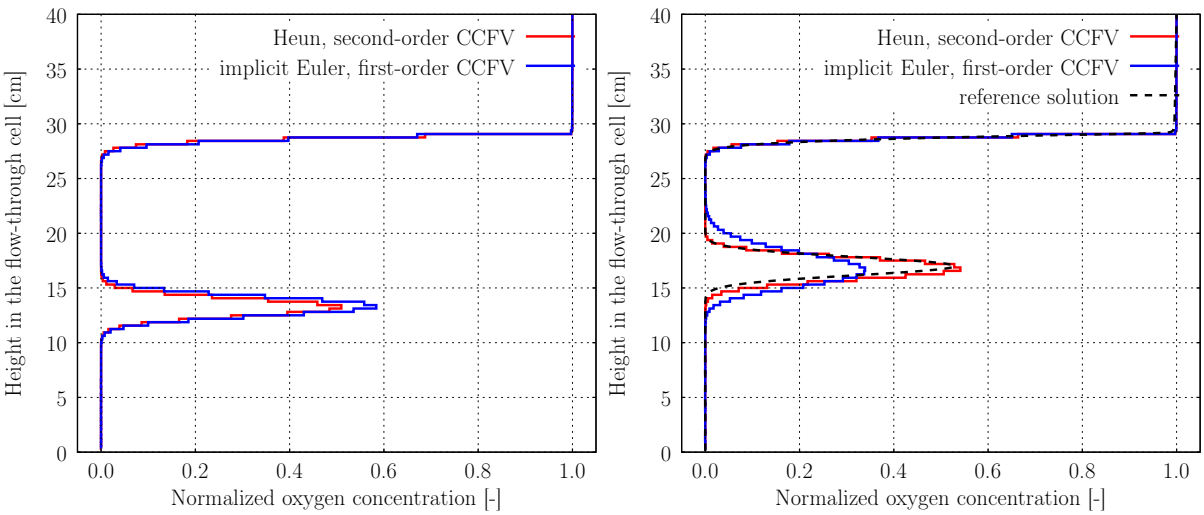

Fig. 7.8: Comparison of vertical profiles after 3000 s at 45 cm from the inlet computed (a) for horizontal flow as described in Section 7.2.3 and (b) for non-horizontal flow described in Section 7.2.4, CCFV discretization with 256×128 elements.

7.2.4 Non-Horizontal Water Flow

It is not easy to reach a quasi steady-state horizontal flow field in the laboratory experiments which study the flow and transport in the saturated and the unsaturated zone. This is particularly the case in situations without a rapid transition to a low saturation.

We simulated a slightly modified experiment (compared to the experiment described above), where the five uppermost ports are switched off. This creates a water flow which is not horizontal and thus a flow direction which is not perpendicular to the grid interfaces.

In order to study the reduction of numerical diffusion, we solved the oxygen transport using different numerical methods. As a reference solution, we denote the numerical solution which was computed on a fine grid (2048×1536 elements) using second-order CCFV with flux reconstruction and Heun's method. Fig. 7.9 shows the distribution of the oxygen concentration after 3000 s obtained from simulations with a 256×128 element grid using two different time and space discretizations: second-order CCFV with explicit Heun method and CCFV with first-order upwinding together with an implicit Euler. For both methods, the time step was chosen to guarantee that the advection CFL number is less than 1. As there are no stability restrictions for the implicit time discretization, the time step could be larger. However, the implicit scheme would then produce an even higher numerical diffusion. The numerical diffusion introduced by the first-order upwind scheme together with implicit time discretization give rise to an inaccuracy in both the sharp front of the plume in flow direction as well as in the vertical concentration distribution, see Fig. 7.8b.

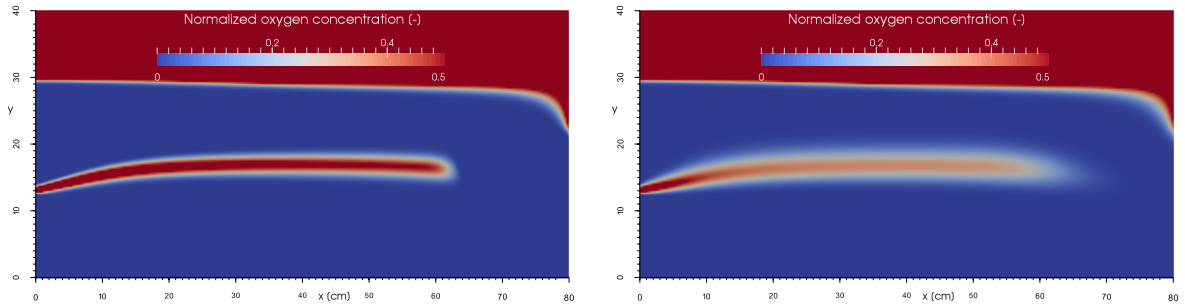

(a) (b)

Fig. 7.9: Distribution of the normalized oxygen concentration after 3000 s simulated with (a) an explicit time discretization (method of Heun) and the second-order CCFV scheme with flux reconstruction and (b) an implicit Euler scheme with full upwinding.

7.3 Reactive Mixing

7.3.1 Introduction

Laboratory experiments and reactive transport modeling of various abiotic and biotic processes in saturated and unsaturated porous media show that the biodegradation of organic pollutants is, in many cases, controlled by mixing (Bauer et al., 2008, 2009). Therefore, the bio-chemical reaction occurs locally at the plume's fringes, where electron donors (e.g., carbon compounds such as lactate or pyruvate among many others) and electron-acceptors (e.g., oxygen) mix. Many authors have investigated mixing and reactive transport in porous media. We refer the reader to e.g., Anna et al. (2014); Chu et al. (2005); Cirpka et al. (1999); Cirpka and Valocchi (2007); Dentz et al. (2011) for more details about this topic.

As a simplification, we model the kinetics of an irreversible fast bimolecular reaction of two solutes C_1 and C_2 that goes to completion

$$C_1 + C_2 \rightarrow C_3, \tag{7.5}$$

where the product C_3 is discernible within the chamber (representing e.g., the concentration of aerobic microorganisms). The reaction described by (7.5) takes place at the front between the reactants immediately. The main goal of the following numerical experiment is to show the performance of different numerical discretization schemes and their abilities to describe the reactant fronts good enough to prevent an overestimation of component mixing.

7.3.2 Setup

We investigate a simulation of a virtual experiment in the two-dimensional FTC filled with a porous medium, where the oxygen plume (concentration C_1) will spread in the oxygen-free region containing enough nutrients (C_2). The two-dimensional FTC system is the same as in Section 7.2.2 dealing with the oxygen transport experiment, specifically the size of the FTC

and the used porous medium. At the beginning of the experiment the initial amount of water does not contain any of the considered solutes.

On each side of the chamber we inject water with a pumping rate of $7.5\,\mathrm{ml\,min^{-1}}$. This new water solution is flowing from inlets positioned between 5 and 13 cm and it contains oxygen with concentration $C_1 = 1$; the boundary value of the other solutes is zero. The water injected from the other inlets is also free of all considered solutes.

In addition to the side pumps, we added a source and a sink with a pumping rate of $3\,\mathrm{ml\,min^{-1}}$ at the height of 10 cm and at distances of 19 cm and 61 cm from the inlet respectively. The water pumped into the domain from this inner source contains only one component with concentration $C_2 = 1$. The solute with concentration C_1 is transported with the water and mixes with the solute C_2 to produce C_3, see Fig. 7.10.

We assume that the diffusion coefficient of C_1 is that of oxygen ($D_{l,O_2} = 1.25 \times 10^{-8}\,\mathrm{m^2\,s^{-1}}$) and the diffusion of the other solutes is negligible ($D = 0$).

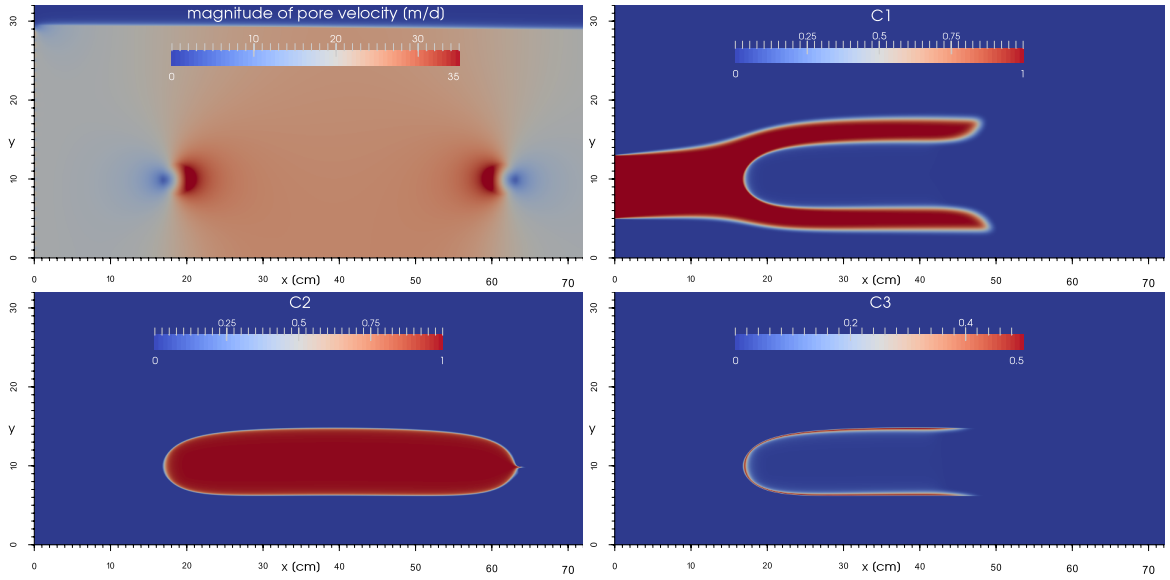

Fig. 7.10: Distribution of pore velocity and concentrations of all components after 2000 s simulated with an explicit time discretization (method of Heun) and the second-order CCFV scheme with flux reconstruction, mesh 2048×1536 elements.

7.3.3 Numerical Simulation and Discussion

As a reference solution to the problem described above, we denote the numerical solution computed with the same discretization methods as in Section 7.2.4 on a fine grid with 2048×1536 elements using second-order CCFV with flux reconstruction and explicit Heun method.

Fig. 7.10 shows the magnitude of the velocity field and the distribution of solute concentrations at time 2000 s. The oxygen plume moves with the flow field and diffuses into the part of the domain which contains the plume of the solute with concentration C_2. As a result, C_3 is nonzero at the interface between both plumes, where the mixing occurs.

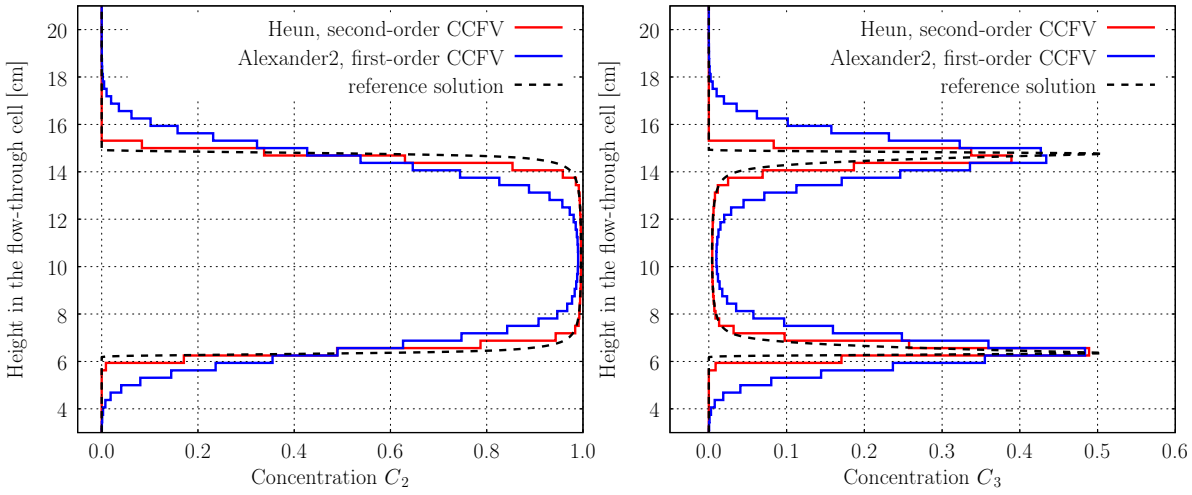

Fig. 7.11: Comparison of vertical profiles after 2000 s at 40 cm from the inlet computed using various numerical discretization scheme on mesh with 256×128 elements: (a) concentration C_2 and (b) concentration of mixing product C_3.

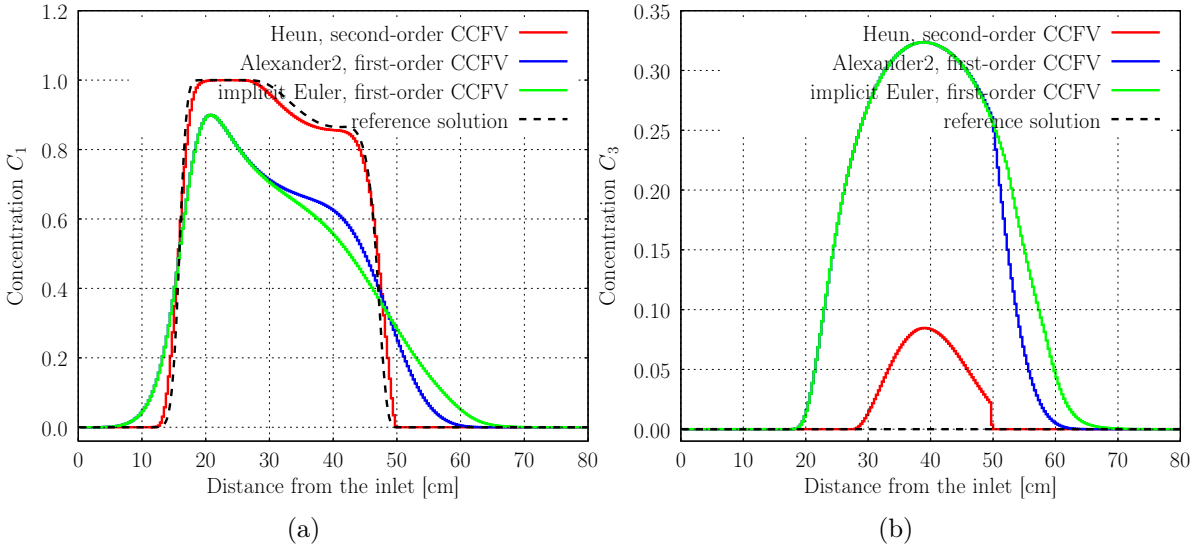

Fig. 7.12: Comparison of horizontal profiles after 2000 s at the height of 15 cm computed using various numerical discretization scheme on mesh with 256×128 elements: (a) concentration C_1 and (b) concentration of mixing product C_3. Time step for implicit Euler corresponds to the advective CFL number ν given by Eq. (4.23) equal to 5.

We compare the numerical solution at time 2000 s, which is computed using different numerical discretization methods. Fig. 7.11 shows vertical profiles of the concentrations at 40 cm from the inlet of the FTC. The discrepancy between the profiles gained by the second-order CCFV with method of Heun on a mesh with 256×128 elements and the exact solution is almost negligible for both C_1 and C_3. However, the numerical diffusion in the solution computed by the first-order CCFV method with implicit integration causes inaccuracy in comparison to the reference solution. The numerical diffusion extends the region where the components C_1 and C_2 mix. Thus, the resulting concentration of C_3 is over-predicted, see Fig. 7.11b.

The difference between the solute concentrations measured in horizontal direction at a height of 15 cm after 2000 s is even more significant. As already shown in Chapter 6, the numerical diffusion caused by the first-order CCFV scheme is severe in the flow direction if the solution contains some sharp fronts as, e.g., oxygen with concentration C_1, see Fig. 7.12a. At the height of 15 cm should be no solute with concentration C_2. Fig. 7.12b shows that the solution computed by second-order CCFV scheme is non-zero and we require finer grid to get the correct solution. Note that both methods converge to the exact solution when we refine the mesh.

7.4 Summary

In this chapter we applied the developed numerical simulator to processes in saturated and unsaturated porous media and compared the performance of several numerical discretization schemes in two-dimensional transport examples.

The model describing the transport of nanoparticles together with kinetically controlled adsorption can fit the breakthrough curves and predict the retention curves reasonably well. However, the estimated parameters vary depending on many factors like pH and water content, among others. Moreover, it is difficult to do any prognosis about the transport of nanoparticles in more complicated systems like highly dynamic zones of porous media.

In the second example, we simulated an oxygen transport experiment in the two-dimensional flow-through cell. The measured and computed oxygen profiles are in excellent agreement. Thus, we can conclude that we are able to simulate and predict the distribution of the tracer given the system parameters and the characteristics of the porous medium.

In the last experiment, we simulated local mixing in a virtual two-dimensional system similar to that for oxygen transport. The quantification of local mixing is key to the understanding and the prediction of regions of high bio-chemical activity. We showed that the CCFV method with second-order flux reconstruction, together with the explicit method of Heun, reduces the numerical diffusion significantly. In comparison to first-order CCFV method with full upwinding, the use of second-order methods leads to a much more accurate simulation at the same grid resolution for reactive flow in porous media with non-trivial flow fields.

Chapter 8

Modeling Microbiological Growth and Transport in the Capillary Fringe

There is a considerable ongoing effort aimed at understanding the microbial growth and transport in porous media (Chen and Walker, 2012; Clement and Peyton, 1997; Tufenkji, 2007; Yarwood et al., 2006). The soil microbial population can be affected by the availability of electron acceptors (Sierra and Renault, 1995), nutrients (Reischke et al., 2013) and bio-available water (Chang and Halverson, 2003; Skopp et al., 1990). The capillary fringe (CF) is a region where all of these factors are abundantly available and it offers attractive growth conditions for aerobic and anaerobic soil microorganisms (Affek et al., 1998; Jost et al., 2010, 2011). It is thus a region where high microbial activity is to be expected.

While the behavior of microorganisms in porous media under saturated flow conditions has been studied intensively (Bradford et al., 2006; Kouznetsov et al., 2004; Walker et al., 2004), the more complicated transport in unsaturated porous media is still not very well understood (Dechesne et al., 2008; Powelson and Mills, 2001; Rockhold et al., 2007; Schäfer et al., 1998a). In this chapter we analyze the results of laboratory experiments with *Escherichia coli* conducted by D. Jost (see Jost et al. (2014b)) under transient, unsaturated conditions using the developed numerical model.

E. coli is well suited for an investigation of bacterial growth and transport in partially saturated porous media, as *E. coli* cells can grow under aerobic and anaerobic conditions (Clark, 1989; Madigan et al., 2010). Additionally, there are fluorescent strains of *E. coli* which are especially easy to detect and quantify (Jost et al., 2014b). The net negative surface charge and low inactivation rates of *E. coli* ensure that it may travel long distances in the subsurface (Foppen and Schijven, 2005). These characteristics make *E. coli* an important indicator for contamination of drinking water supplies and for faecal pollution of the environment (Chen and Walker, 2012). It has therefore been an object of research in a number of studies (Duffy et al., 1999; Jiang et al., 2007; Lacoursiere et al., 1986; Powelson and Mills, 2001).

To investigate growth and transport of *E. coli* under steady-state and transient conditions, experiments have been conducted in a flow-through chamber (FTC) filled with quartz sand, see Section 8.4 or Jost et al. (2014b) for details. The main purpose of this chapter is to answer the question if it is possible to predict the growth of microorganisms under transient flow conditions in such a flow trough cell without any calibration by experimental data from the flow-through cell. Therefore, first models for microbial growth and cell adhesion are to be developed, integrate into the numerical simulator, and then applied to simulate experiments in the FTC. We published the major part of this chapter in Hron et al. (2015) and further reference this paper without citation.

8.1 Modeling of Microbial Growth

E. coli is a facultative anaerobic bacterium which gains ATP by aerobic respiration if oxygen is present, but is capable of switching to fermentation or anaerobic respiration if oxygen is absent. As aerobic growth is much more energy efficient, we expect some switch between anaerobic and aerobic growth if enough oxygen becomes available. Thus, we suppose the growth depends on the concentration of oxygen and bio-available dissolved organic carbon (DOC).

8.1.1 Batch Experiments

To understand the growth of *E. coli* and to describe the population dynamics (such as cell densities and their dependence on substrate concentrations), a number of different batch-culture experiments were performed under varying conditions. We do not describe the batch experiments in detail and refer the reader to Hron et al. (2014).

For the aerobic and anaerobic batch experiments, shake flasks filled with different liquid solutions of lysogeny broth (LB) medium were used to observe growth of initially added *E. coli* cells. Duplicate culture assays were shaken and the optical density (OD) at 578 nm was measured after inoculation and after every 1 h during the initial phase (log-phase) of bacterial growth and at several points in time afterwards with a photometer to get the growth curves. Calibration experiments showed that OD values were linear dependent on the cell density.

The LB medium, which is a source of DOC, was used pure and diluted with 0.9 % NaCl solution to 1/2 (1:1), 1/5 (1:4) and 1/10 (1:9) of the original concentration. The oxygen concentration in the air phase was kept constant at 20 % for aerobic experiments. A nitrogen atmosphere was used in anaerobic experiments instead of air. In addition the biomass (dry weight, denoted by dw) of *E. coli* cells after the growth phase was measured gravimetrically for each replicate. At the end of the batch experiments, the DOC concentration in the liquid solution was measured with a carbon analyzer and the amount of consumed DOC was determined.

To determine the dependence of the growth rate on oxygen availability, experiments with different oxygen concentrations were conducted in closed glass vessels filled with undiluted LB medium only. Each vessel was flushed with a mixture of different ratios of sterile artificial air and pure nitrogen to achieve different oxygen concentrations. Similar experiments with different LB dilutions were also conducted to measure oxygen consumption and biomass production. The oxygen concentration in the liquid phase was measured with a non-invasive optode technique. After 24 hours, a sample of gas was taken from each bottle and the oxygen concentration in the gas phase was measured with a gas chromatograph and the total biomass production was determined gravimetrically.

The following conclusions about the main factors controlling growth of *E. coli* have been obtained from the batch experiments:

- Cell growth is faster in presence of oxygen. This is a consequence of the higher energy efficiency of aerobic respiration compared to anaerobic fermentation.
- Anaerobic growth takes place only if the amount of available oxygen is very low. If enough oxygen is available only aerobic respiration is active.

- Oxygen is still consumed after the growth phase (log-phase), when all convertible DOC is already depleted. The necessary nutrients are most probably taken from intracellular resources.
- At high cell and DOC concentrations the dissolution of oxygen in water is slower than oxygen consumption.
- In all batch experiments only up to 30 % of the total DOC was consumed or converted for both the aerobic and the anaerobic growth.

In the following we test different growth models depending on oxygen and DOC availability, which are based on common approaches in the literature. We answer the question if it is possible to describe all batch experiments with one single set of parameters. This is crucial for the applicability of the growth model in predicting growth and transport of *E. coli* in porous media.

8.1.2 Single-Substrate Kinetics

Various mathematical models have been proposed to quantitatively describe microbial growth kinetics, see Contois (1959); Monod (1949); Moser (1958); Powell et al. (1967).

The biomass concentration under anaerobic conditions is described by a first order differential equation relating the change of the biomass concentration over time to the current biomass concentration $C_{l,X}$ multiplied with a specific growth rate μ^*_{an}

$$\frac{\mathrm{d}C_{l,X}}{\mathrm{d}t} = \mu^*_{an} C_{l,X}.$$

μ^*_{an} is the product of a maximal specific growth rate $\mu_{max,an}$ and a relative specific growth rate. $\mu_{max,an}$ is a characteristic of all organisms and it is related to their ability to reproduce and it is simply defined as the increase of biomass per unit of time under optimal conditions (no limiting nutrients). Common growth kinetics expressing the relative speed of growth depending on the concentration s_i of a single substrate are given by:

$$\text{Monod} \quad \frac{s_i}{K_{si} + s_i}, \tag{8.1}$$

$$\text{Moser} \quad \left(1 + K_{si} {s_i}^{-\lambda_i}\right)^{-1}, \tag{8.2}$$

$$\text{Tessier} \quad 1 - \exp\left(-\frac{s_i}{K_{si}}\right), \tag{8.3}$$

$$\text{Contois} \quad \frac{s_i}{B_{si} C_{l,X} + s_i}. \tag{8.4}$$

The substrate affinity constant (half-saturation constant) K_{si} can be interpreted as a reflection of the affinity of the bacterial cell towards the substrate s_i. It represents the substrate concentration at which growth with half the maximal speed occurs. Moser's constant λ_i and the constant B_{si} in the Contois model do not have direct biological meaning. In our case $s_i = C_{l,S}$, which denotes the concentration of bioconvertible nutrients and is only a part of the total DOC in the medium.

Together with a Monod kinetic (8.1) we obtain for example

$$\mu_{an}^{*} = \mu_{max,an} \frac{C_{l,S}}{K_{S,an} + C_{l,S}}. \tag{8.5}$$

8.1.3 Multiple-Substrate Kinetics

While under anaerobic conditions, the growth of *E. coli* or other facultative anaerobic microorganisms depends only on the bio-available organic carbon concentration, under aerobic conditions the oxygen concentration C_{l,O_2} in the liquid phase has to be taken into account as well. Kornaros and Lyberatos (1997) used a double Monod model to describe this double nutrient limitation for the growth of *Pseudomonas denitrificans*. It combines two Monod kinetics in a multiplicative form. The (aerobic) specific growth rate with a double Monod model is given by

$$\mu_a = \mu_{max,a} \frac{C_{l,S}}{K_{S,a} + C_{l,S}} \frac{C_{l,O_2}}{K_{O_2} + C_{l,O_2}}. \tag{8.6}$$

In both growth models (8.5) and (8.6), the Monod kinetics can be substituted with each of the other models of the relative specific growth rate (8.2)-(8.4).

8.1.4 Combination of Aerobic and Anaerobic Growth

While aerobic growth of *E. coli* cells is already occurring at low oxygen concentrations, anaerobic growth might still be important. As aerobic respiration is much more efficient, we assume that only aerobic growth occurs if μ_a is higher than the growth rate for purely anaerobic growth under the same substrate limitation ($\mu_a \geq \mu_{an}^{*}$). Under these assumptions, the specific growth rate function for anaerobic growth in presence of oxygen μ_{an} can be defined as

$$\mu_{an} = \max(\mu_{an}^{*} - \mu_a, 0), \tag{8.7}$$

The total growth rate $\mu = \mu_a + \mu_{an}$ is then a non-decreasing function of C_{l,O_2} for constant $C_{l,S}$, where only the ratio between aerobic and anaerobic growth is changing.

8.1.5 Mass Balance Equations

We consider a constant volume V_l of liquid phase (culture medium) and gas phase V_g. As there is no injection or removal of cells during the batch experiment, the balance equation for the cell density $C_{l,X}$ is given by

$$\frac{\mathrm{d}C_{l,X}}{\mathrm{d}t} = (\mu_a + \mu_{an} - r_d)\, C_{l,X}, \tag{8.8a}$$

where r_d is the decay rate. The generic balance equation for the consumable substrate $C_{l,S}$ has the form

$$\frac{\mathrm{d}C_{l,S}}{\mathrm{d}t} = -\left(\frac{\mu_a}{Y_{S,a}} + \frac{\mu_{an}}{Y_{S,an}}\right) C_{l,X}, \tag{8.8b}$$

where $Y_{S,a}$ and $Y_{S,an}$ are the yield coefficients. They represent the link between growth rate and substrate utilization, a measure for the efficiency of the conversion of a substrate into biomass.

Oxygen transfer between liquid and gas phase occurs at the interface between both phases. The local equilibrium concentration of oxygen in water C^*_{l,O_2} can be described by Henry's law (2.13). As the batch experiments have shown, the assumption of equilibrium between gas phase and liquid phase is not valid for oxygen exchange during rapid growth phases. Thus, we introduce a kinetic mass transfer model depending on the difference of the actual and equilibrium concentration of oxygen in the liquid phase, a gas-liquid mass transfer capacity coefficient $k_L\alpha$ depending on gas/liquid interfacial area (which was constant for the batch experiments) and the ratio of the phase volumes. The mass balance equations for oxygen in the liquid and gas phase are then given by

$$\frac{\mathrm{d}C_{l,O_2}}{\mathrm{d}t} = -\left(\frac{\mu_a}{Y_{O_2}} + m_o C_{l,O_2}\right) C_{l,X} + k_L\alpha \left(C^*_{l,O_2} - C_{l,O_2}\right), \tag{8.8c}$$

$$\frac{\mathrm{d}C_{g,O_2}}{\mathrm{d}t} = -k_L\alpha \left(C^*_{l,O_2} - C_{l,O_2}\right) \frac{V_l}{V_g}, \tag{8.8d}$$

where Y_{O_2} is the yield coefficient for oxygen and m_o is the oxygen consumption factor for maintenance.

The system of ordinary differential equations (8.8), together with appropriate initial conditions, specifies a modified growth rate model for *E. coli* including simultaneous aerobic and anaerobic growth, cell decay and a kinetic description for oxygen transfer. It can be customized with different models of the relative specific growth rate.

With the growth model (8.8) derived from the batch experiments, we obtain the following reaction terms $r_{\alpha,\kappa}$ as denoted in the model development (see Chapter 3, Eq. (3.4)) for cell density $C_{l,X}$, substrate $C_{l,S}$ and oxygen concentration C_{l,O_2} in the liquid phase:

$$r_{l,X} = (\mu_a + \mu_{an} - r_d)\, C_{l,X}, \tag{8.9a}$$

$$r_{l,S} = -\left(\frac{\mu_a}{Y_{S,a}} + \frac{\mu_{an}}{Y_{S,an}}\right) C_{l,X}, \tag{8.9b}$$

$$r_{l,O_2} = -\left(\frac{\mu_a}{Y_{O_2}} + m_o C_{l,O_2}\right) C_{l,X}. \tag{8.9c}$$

8.2 Parameter Estimation for Growth Kinetics

The growth model (8.8) contains a number of different parameters like maximal growth rates, half saturation constants, yield coefficients, maintenance and mass transfer coefficient etc, which need to be determined using the data obtained from the batch experiments.

Scientists have developed many different ways to determine the model's kinetic parameters. However, some of them are predisposed to inaccuracy and can be applied only under limited conditions. In the last two decades, software based on non-linear regression is used to determine growth parameters, e.g. in Kovárová et al. (1996); Kovárová-Kovar and Egli (1998); Senn et al.

(1994). In this approach a separate set of parameters is obtained for every single experiment or even for different stages of an experiment. Usually the parameters are averaged later.

In this work, we want to use a parameter estimation approach to obtain model parameters, which describe the measured quantities (like optical densities, biomass densities, DOC concentrations and oxygen concentrations in air and in water) for all experiments simultaneously. Our approach uses an inverse model together with the initial value approach (Marsili-Libelli, 1992; Richter and Söndgerath, 1990), for details see Section 4.7. The forward model in the LMA algorithm solves the system of equations (8.8) using a RKF45 method for systems of ordinary differential equations. The initial conditions are derived from the batch experiments.

8.2.1 Parameter Estimation for the Batch Experiments

To combine the deviations between measured and simulated data for different measured quantities into a single objective function (4.26), a suitable weighting factor w_{ij} has to be chosen. In theory, this should be the measurement error. We assume that the error for each measurement is 10% of the maximal value of the measured quantity in the specific experiment.

To assess the predictive power of the growth model with the different models of the relative specific growth rate (Monod, Moser, Tessier and Contois model, (8.1)-(8.4)) a separate set of parameters was estimated for each of the combinations and the residua were compared.

Anaerobic Growth

In the absence of oxygen the growth of *E. coli* is purely anaerobic ($\mu = \mu_{an}$). This reduces the unknowns to the maximum growth rate $\mu_{max,an}$, the anaerobic substrate yield factor $Y_{S,an}$, the decay rate r_d and parameters for the growth kinetics like half saturation constant or Contois saturation constant.

The decay rate was determined from four, six-day long anaerobic batch experiments, each using a different dilution of the LB medium. The remaining growth parameters were estimated from 8 experiments using 4 different dilutions of the LB medium at an incubation temperature of 21°C with a total of 125 single measurements.

Aerobic Growth

The two types of aerobic experiments emphasize different aspects of microbial growth. In the open system experiments, the concentration of oxygen in air was kept constant with a fast air circulation and thus the mass balance equation for oxygen in the gas phase (8.8d) can be omitted, while the closed system experiments allow a quantification of the oxygen consumption.

A total of 334 individual measurements from 35 aerobic experiments were used to estimate the remaining 7 or 8 parameters (depending on the model used for the relative growth rate) which are only relevant in the presence of oxygen.

8.2.2 Performance of the Different Growth Kinetics

Table 8.1 summarizes the residua obtained with the different models of the relative specific growth rate. There was generally a good agreement between measured and simulated cell biomasses (residuum $\mathcal{R}_X$) and the final substrate concentrations (residuum $\mathcal{R}_S$) as dry biomass and substrate concentration were measured at the start of batch experiment and after the log-phase only.

	anaerobic growth				aerobic growth					
	$\mathcal{R}_S$	$\mathcal{R}_{OD}$	$\mathcal{R}_X$	$\mathcal{R}$	$\mathcal{R}_S$	$\mathcal{R}_{OD}$	$\mathcal{R}_{g,O_2}$	$\mathcal{R}_{l,O_2}$	$\mathcal{R}_X$	$\mathcal{R}$
Contois	1.8	5.2	6.7	13.8	8.6	14.1	8.6	9.2	15.6	56.2
Monod	1.2	12.3	7.2	20.8	7.8	39.4	13.8	25.1	15.8	101.9
Moser	1.8	9.0	6.9	17.7	8.4	34.3	11.8	43.5	18.0	116.1
Tessier	1.4	12.9	7.2	21.5	8.4	47.4	14.9	28.0	15.2	113.8

Table 8.1: Residua gained by an inverse modeling for different kinetic growth models (8.1-8.4) of the relative specific growth rate. $\mathcal{R}_S$ denotes the residuum in the substrate concentration, $\mathcal{R}_{OD}$ the residuum in the growth curves w.r.t. the optical density, $\mathcal{R}_X$ the residuum in cell density, $\mathcal{R}_{g,O_2}$ and $\mathcal{R}_{l,O_2}$ are residua in oxygen concentration and $\mathcal{R}$ is the total residuum.

The best overall agreement between simulated and measured values was obtained with the Contois model of relative specific growth. This is mostly due to a much better reproduction of the measurements of optical density (and also growth curves) and oxygen concentration in the liquid phase. The models based on a Monod, Moser or Tessier kinetic perform significantly worse. The obtained growth curves show a sharp switch between log-phase and stationary/death phase, which was not observed in the batch experiments and does not occur with the Contois kinetics. The difference is even more striking, as the Contois based model has the same amount of parameters as the models using the Monod and Tessier kinetic and one parameter less than the model with the Moser kinetic. Thus, only the model with the Contois kinetic (8.4) is used in the rest of this chapter.

8.2.3 Estimated Parameters and Discussion

The estimated growth parameters for the model with the Contois kinetic are given in Table 8.2. For all parameters, the standard deviations are relatively small indicating that the model is both appropriate and not over-parametrized. Higher standard deviations for the Contois saturation constants confirm the difficulty described already in Kovárová-Kovar and Egli (1998). The authors mentioned that the saturation constant K_{si} in the Monod model could vary even during a single growth cycle.

However, the agreement between simulations and experiment was very good for all types of measurements in all setups. As a typical example, the simulated and measured biomass concentration for aerobic and anaerobic growth in closed serum bottles is shown in Fig. 8.1 and 8.2 for different substrate dilutions. Fig. 8.3 shows the corresponding decrease of the oxygen concentration in the gas phase.

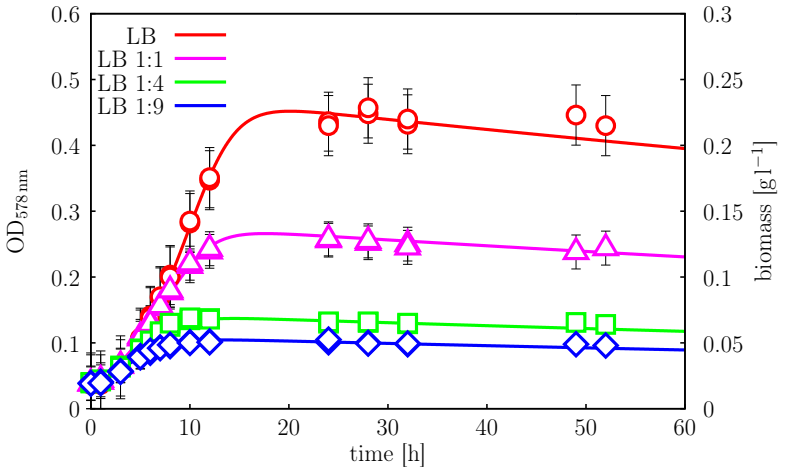

Fig. 8.1: Comparison of measured optical densities (points) for anaerobic growth and growth curves as a solution of model (8.8) (lines) with estimated parameters summarized in Table 8.2.

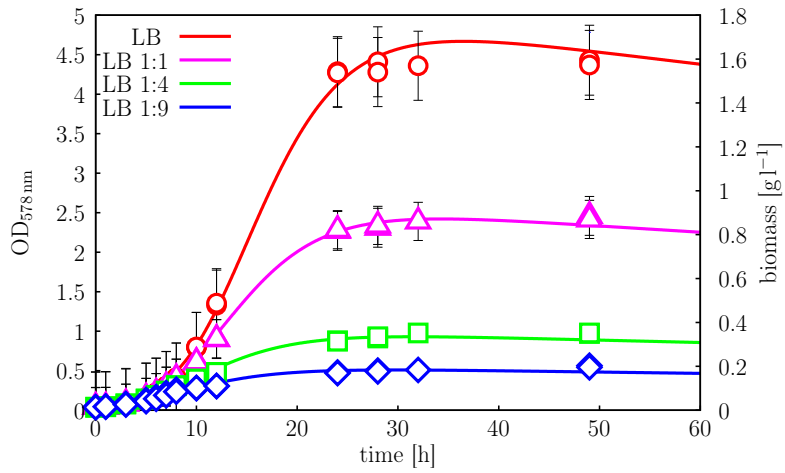

Fig. 8.2: Comparison of measured optical densities (points) aerobic growth and growth curves as a solution of model (8.8) (lines) with estimated parameters summarized in Table 8.2.

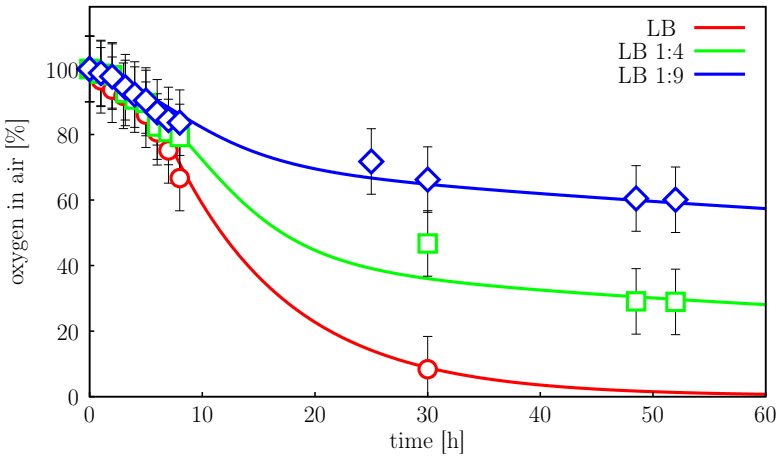

Fig. 8.3: Comparison of measured data (points) and oxygen concentrations in gas as a solution of model (8.8) (lines) with estimated parameters summarized in Table 8.2.

Parameter	Aerobic	Anaerobic
Maximum growth rate $\mu_{max,\cdot}$ [h^{-1}]	$0.324 \pm 3.7\%$	$0.255 \pm 6.9\%$
Decay rate r_d [h^{-1}]	$3.54 \times 10^{-3} \pm 4.2\%$	
Contois saturation c. $B_{S,\cdot}$ [-]	$1.81 \pm 15.3\%$	$3.07 \pm 26.3\%$
Yield for substrate $Y_{S,\cdot}$ [g dw g^{-1} consumable DOC]	$0.95 \pm 4.3\%$	$0.163 \pm 2.1\%$
Contois saturation c. B_{O_2} [-]	$0.019 \pm 27.6\%$	-
Yield for oxygen Y_{O_2} [g dw g^{-1} O_2]	$0.49 \pm 8.2\%$	-
Maintenance for oxygen m_o [l h^{-1} g^{-1} dw]	$0.003 \pm 19.9\%$	-
Oxygen mass transfer c. $k_L\alpha$ [h^{-1}]	$33.2 \pm 9.3\%$	

Table 8.2: Growth parameters for Contois model derived by inverse modeling.

The yield coefficients of 0.95 g dw g^{-1} consumed DOC and 0.49 g dw g^{-1} O_2 estimated for the *E. coli* cells are in accordance with the yield coefficients reported by Reiling et al. (1985), where also $\mu_{max,a}$ values of 0.39-1.39 h^{-1} at a high cultivation temperature of 37 °C were determined. In Kovárová-Kovar and Egli (1998) values for $\mu_{max,an}$ between 0.19 and 0.65 in Chemostat and batch cultures with glucose at 17-20 °C are listed.

Under anaerobic conditions, bacteria use a mixed acid fermentation (instead of respiration) to gain energy for growth (Paege and Gibbs, 1961; Stokes, 1949), thus the growth is slower and the yield coefficient decreases. According to our results, a yield of 0.163 g dw g^{-1} consumed DOC was determined, which is close to the anaerobic yield coefficient of 0.18 g dw g^{-1} glucose which Ataai and Shuler (1985) found for some other strains of *E. coli*.

Comparing these values with the results of our batch experiments for aerobic growth of *E. coli*, it is obvious that the chosen growth conditions (21°C) and LB medium were not optimal. Under natural conditions the soil flora has to grow with a mixture of carbon sources, mostly digestion products or amino acids draining from the surface layer.

The LB medium reflects naturally available carbon sources relatively well. While the DOC concentration in the LB medium is very high compared to naturally oligotrophic conditions in

groundwater, an optimal nutrient supply was necessary in this study to produce measurable quantities of biomass.

These results clearly show that it is possible to describe the growth of *E. coli* under a wide range of substrate and oxygen concentrations including both aerobic and anaerobic growth with a single set of realistic parameters.

8.3 Phase Exchange with High Oxygen Consumption

Even in growth experiments with batch-cultures, continuous shaking and instantaneous oxygen supply, the measured oxygen concentrations in water were significantly below the concentration calculated for an equilibrium with the gas phase. The consumption of oxygen was thus faster than oxygen dissolution and therefore local equilibrium can not be assumed.

To specify macroscopic closure relationships for the mass exchange of oxygen between the gas and the liquid phase in a porous medium, we follow the model proposed by Holocher et al. (2003) and Geistlinger et al. (2005) based on a stagnant film model for spherical gas bubbles.

The mass flux between the two phases is assumed to be proportional to the concentration deficit in the water phase (Mayer and Miller, 1996) and the effective area of the gas-water interface a_{gw} and can be described by

$$- e_{g,O_2} = e_{l,O_2} = \beta_e a_{gw} \left(C^*_{l,O_2} - C_{l,O_2} \right), \tag{8.10}$$

where β_e is a mass exchange coefficient and C^*_{l,O_2} is the equilibrium oxygen concentration given by the Henry's law.

According to Clift et al. (1978) the mass exchange coefficient β_e can be calculated for a spherical structure with a harmonic mean particle diameter p_d as

$$\beta_e = D_{l,O_2} \left(\frac{2}{p_d} + \frac{1}{\delta} \right), \tag{8.11}$$

where D_{l,O_2} is the oxygen diffusion coefficient in water and δ is the thickness of the stagnant film layer. The boundary layer thickness depends on the flow velocity at the interface

$$\delta = \sqrt{\frac{\pi p_d D_{l,O_2}}{\|v_l\|}}.$$

The velocity at the interface is approximated by the pore water velocity of the liquid phase v_l, see Niessner (2011).

The gas-liquid interface plays a crucial role for the phase exchange in unsaturated porous media. As a consequence, there is a large number of models to estimate the effective gas-liquid specific interfacial area a_{gw}, see e.g. Ahrenholz et al. (2011) for an overview.

One model to estimate a_{gw} was formulated by Gvirtzman and Roberts (1991) based on geometrical considerations for the surface area of a packing of spheres. In this model the total

effective interfacial area is given by

$$a_{gw} = \kappa s_g \frac{6\phi}{p_d}, \tag{8.12}$$

where κ is the fraction of the air bubble surface area exposed to mobile water, which is assumed to be equal to the porosity (Geistlinger et al., 2005).

In this model a_{gw} is proportional to the gas content. However, this relationship was proven with pore network models (Joekar-Niasar et al., 2007; Reeves and Celia, 1996) and experiments with glass beads (Culligan et al., 2004; Porter et al., 2010) only for $s_l > 0.3$. The model (8.12) thus may overestimate the gas-liquid interfacial area and thus also the phase exchange in regions with low water saturation.

The mass transfer model (8.10) together with a mass exchange coefficient β_e calculated according to (8.11) and the effective interfacial area from (8.12) describes a first-order kinetic, where the exchange rate depends on water content with only one free parameter p_d. We discuss the sensitivity of the model regarding to p_d in Section 8.4.3.

8.4 Microbial Growth Experiments in a Flow-Through Chamber

Up to now we have developed a growth model for *E. coli* under aerobic or anaerobic conditions and their combination. In this section, we will solve the combined model containing the growth model, the component transport and the model for kinetically controlled oxygen phase exchange and compare the simulation results with experimental data.

8.4.1 Experimental Setup

To investigate growth and transport of *E. coli* under steady-state and transient conditions, a flow-through chamber (FTC) with inner dimensions of $50 \times 40 \times 0.6\,\text{cm}$ was used. It was filled with quartz sand (grain size: 0.2-0.6 mm, porosity 0.39) up to a height of 30 cm. The hydraulic properties of the sand were parametrized with a van Genuchten model (Genuchten, 1980) and the parameters determined by a multi-step outflow (MSO) experiment, see Table 8.3.

van Genuchten parameters	
Pore size distribution parameter $\hat{n}$	5.48
Shape parameter α	$1.21 \times 10^{-3}\,\text{Pa}^{-1}$
Porosity (ϕ) = saturated volumetric water content	0.39
Residual volumetric water content (θ_r)	0.0
Hydraulic conductivity K	$2.6 \times 10^{-11}\,\text{m}^2$

Table 8.3: Hydraulic parameters for the quartz sand used for the transport experiments with microbial growth in the FTC.

At the start of the experiment, the porous medium was completely dry (previously heat sterilized). A suspension of *E. coli* cells and LB medium was initially injected to the chamber

through six ports in the bottom (at $5, 11.5, 21.5, 28, 39$ and $44.5\,\text{cm}$ from the left) with a flow-rate of $190\,\text{ml}\,\text{h}^{-1}$. After one hour, the water injection was stopped and a CF formed at a height of up to $25\,\text{cm}$, while a hydraulic potential of zero was reached at a height of $6\,\text{cm}$. Fig. 8.4 shows the simulation of the inflow phase and the development of the CF.

Water flow through the FTC was suspended for five days, during which *E. coli* cells grew while consuming the bioconvertible DOC. After five days, sterile, oxygen-saturated LB medium was injected from the left side of the FTC and the same amount of liquid was extracted on the right side of the chamber by peristaltic pumps for another five days. The four inflow and outflow ports were located at a height of $0.5, 2.0, 3.5$ and $5.0\,\text{cm}$. The depth integrated flow-rate in the horizontal direction was $15\,\text{ml}\,\text{h}^{-1}$. The whole system was kept under a constant temperature of 21°C. Detailed descriptions of the laboratory experiment can be found in Jost et al. (2014b).

Growth was monitored by the detection of a green fluorescent protein, which is produced by the *E. coli* strain HB101 K12 pGLO used in the experiment. The FTC was irradiated with UV light ($365\,\text{nm}$) and the mean fluorescence intensity, which was detected by a camera system, was converted to cell concentrations in cells ml^{-1} CF volume, see Jost et al. (2014b). The CF volume denotes the total volume occupied by the porous medium including the pore space. The average dry weight m of one cell of *E. coli* was determined from independent experiments to be approx. $5.0 \times 10^{-13}\,\text{g}$.

8.4.2 Numerical Simulation

To simulate the laboratory experiment, we solve the two-phase problem (3.2) and the component transport equations (3.3). In the liquid phase, we are interested in the concentration of microorganisms and the consumable substrate. The oxygen concentration is important in the water as well as in the air. The reactions describing the microbial growth and the phase exchange are solved locally or are coupled to the reactive transport and we solve the system of Eq. (3.5) with right hand sides (8.9c) and (8.10) respectively.

As the FTC is very thin in one dimension compared to the others, it can be considered as an essentially two-dimensional system. The $50 \times 30\,\text{cm}$ large domain was discretized using 392×256 rectangular grid cells, resulting in a grid resolution of $1.3 \times 1.2\,\text{mm}$. This resolution corresponds to twice the diameter of the maximal grain size. The grid resolution is fine enough to keep the spatial discretization error small, while the runtime of one simulation is still acceptable. We discuss the solution strategy, the chosen methods, the performance of the implementation and the code scalability in Section 8.6.

The initial conditions for p_c and p_l where chosen to correspond to a volumetric water content of 0.1% and atmospheric pressure for the gas phase. All domain boundaries, excluding inlet/outlet ports, are treated as impermeable for the liquid phase (zero Neumann boundary condition). The flux at the ports is set to the value used in the experiments. For the gas phase all but the top side is impermeable. The air pressure at the top of the domain is fixed to the atmospheric pressure.

The initial amount of water is free of DOC and *E. coli* cells. The relative initial and boundary oxygen concentration in air is 20.95%. The ideal gas law yields absolute oxygen concentration of $8.68\,\text{mmol}\,\text{l}^{-1}$ gas. At $21\,°\text{C}$, the Henry constant k_H^{cc} is 3.28×10^{-2} (Dean and Lange, 1999) and the equilibrium oxygen concentration C_{l,O_2}^* is $9.1\,\text{mg}\,\text{l}^{-1}$ water.

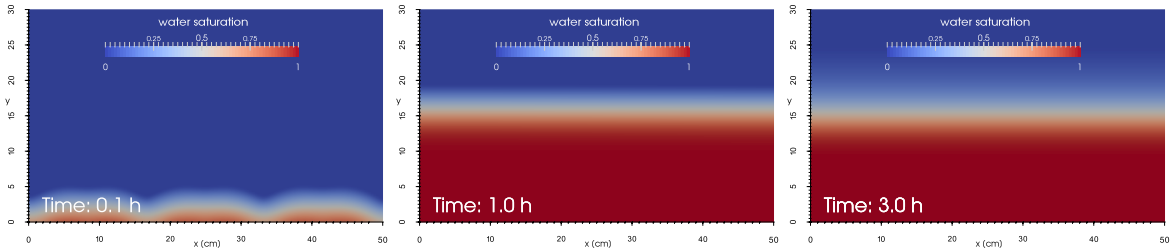

Fig. 8.4: Initial injection of water suspension containing *E. coli* cells and LB medium after 0.1 h, 1 h and 3 h.

The injected suspension contains LB medium with $0.8\,\mathrm{g\,l^{-1}}$ of consumable DOC. At the start of the experiment (inflow phase), it additionally contains a negligible amount of dissolved oxygen ($0.1\,\mathrm{mg\,l^{-1}}$) and $2 \times 10^7\,\mathrm{cells\,ml^{-1}}$ of *E. coli* which is equivalent to a biomass concentration of $1.0 \times 10^{-2}\,\mathrm{mg\,ml^{-1}}$. In the second part of the experiment the injected water does not contain *E. coli* cells and the dissolved oxygen concentration corresponds to the equilibrium oxygen concentration C^*_{l,O_2}.

For the numerical simulations we assumed, that *E. coli* cells are not able to move without water flow (no active movement, no molecular diffusion, $D_{l,X} = 0\,\mathrm{m^2\,s^{-1}}$). The other diffusion coefficients were taken from literature: $D_{l,S} = 1.9 \times 10^{-10}\,\mathrm{m^2\,s^{-1}}$ given by Hendry et al. (2003), $D_{l,O_2} = 2.2 \times 10^{-9}\,\mathrm{m^2\,s^{-1}}$ and $D_{g,O_2} = 1.8 \times 10^{-5}\,\mathrm{m^2\,s^{-1}}$ as listed in Aachib et al. (2004).

8.4.3 Simulation Results

Inflow and Stagnancy (Day 0-6)

While the infiltration of water from the bottom was stopped after 1 h, the establishing of a stationary moisture distribution took significantly longer. After approx. 6 h, no visible changes of the water content were observed, in both the model as well as the experiment. Fig. 8.4 shows the water saturation and the development of the CF during the injection and shortly after the initial infiltration.

A vertical profile of the measured cell concentrations at $x = 25\,\mathrm{cm}$ after 5 d is given in Fig. 8.5 at the left. The lower part of the domain, up to a height of 11 cm, is fully water saturated. In this region the *E. coli* cells are growing anaerobically, as all oxygen is quickly consumed and there is no additional supply. The measured *E. coli* concentration is $0.7 \times 10^8\,\mathrm{cells\,ml^{-1}}$ CF volume.

Starting at a height of 11 cm, the cells are growing under anaerobic as well as aerobic conditions, as oxygen diffuses from the air phase on top into the liquid phase. The highest growth rates and biomass production were observed in a zone between 12 and 16 cm, where the water saturation is 0.6-0.8. In this region, there is enough bioconvertible DOC available, which was contained in the infiltrating water, but there is also sufficient dissolved oxygen available. In the uppermost part of the domain, the cell concentrations decrease with the water saturation.

To assess the impact of the value used for the mean particle diameter in the oxygen exchange model, simulations with three different values of p_d were conducted. A higher value of p_d

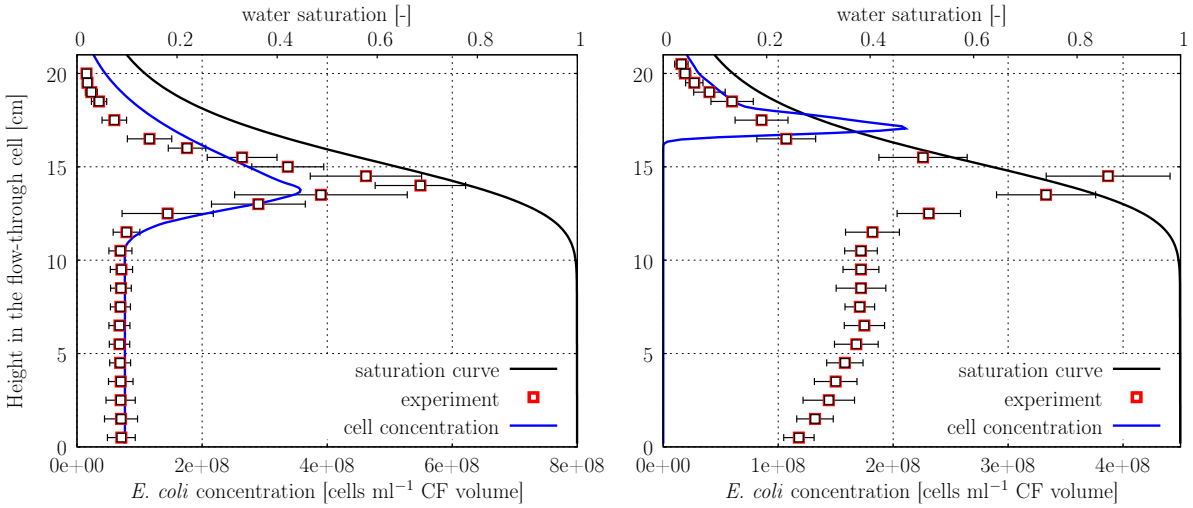

Fig. 8.5: Vertical profile of cell concentration at $x = 25\,\text{cm}$ after 5 d of growth without new nutrient supply and without flow (left) and after another 5 d with new nutrient supply and flow (right). Comparison between cell concentrations computed by numerical simulation with $p_d = 0.9\,\text{mm}$ and experimental data.

results in a lower effective interfacial area. Thus, a lower phase exchange rate and finally a slower microbial growth. Comparison of the results (Fig. 8.6) shows a significant impact on the shape of the cell concentration profile in regions with a water saturation between 0.4 and 0.95. With p_d equal to the diameter of the biggest grains in the quartz sand used, the model over-predicts the oxygen exchange rate and the maximum of the cell concentration is too deep. For larger values of p_d the maximum moves upwards. However, the parameter κ in the model of the exchange rate (the fraction of the air bubble surface exposed to mobile water) and p_d are indirect proportional. Thus, the deviation could be caused by an overestimation of κ. In all following numerical simulations a value of 0.9 mm is used for the parameter p_d.

The simulated maximal cell concentration (Fig. 8.5, left) with $p_d = 0.9$ is approx. 30% lower than the maximal cell concentration in the laboratory experiment (5.3×10^8 compared to $3.6 \times 10^8\,\text{cells}\,\text{ml}^{-1}$ CF volume). However, the experimental cell concentrations calculated from fluorescence intensities (FI) have a rather high uncertainty, especially at high intensities. There is also other evidence for an overestimation of the maximal cell concentration obtained from the FI. If the cell concentration in the water phase is calculated from the cell concentration and the saturation, the maximal cell concentration in water (at 14 cm) is almost 11 times higher than in the saturated region below. However, this value is much higher than the factor of 6 as expected from the different yield coefficients for aerobic and anaerobic growth.

In the uppermost part of the domain, the simulated cell concentrations are proportional to the water saturation. The systematically higher cell concentration compared to the experimental data may be a result of an overestimation of the phase exchange of oxygen or by a slightly different shape of the capillary-pressure saturation curve than determined in the MSO experiments (with a different sample of the same sand).

Considering that there was nearly no calibration of the simulation model on the FTC experiment (except for p_d), instead all parameters were determined from independent measurements

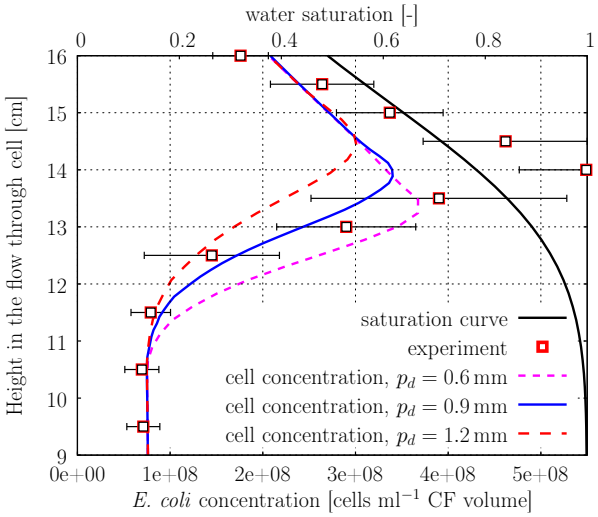

Fig. 8.6: Vertical profile of cell concentration at $x = 25\,\text{cm}$ after 5 d of growth without new nutrient supply and without flow calculated with different values of p_d and experimental data.

in batch or MSO experiments, the agreement is astonishingly good. This is not only qualitatively but also quantitatively.

Horizontal Flow (Day 6-10)

After 5 d without water flow, $15\,\text{ml}\,\text{h}^{-1}$ of oxygen saturated LB medium was injected to the domain from the left. In the numerical simulations, a tiny change of the water content was observed due to the potential gradient required to sustain the flow. On the inflow side of the domain, the water content profile was shifted upwards by 4 mm and it was shifted downwards by the same value on the outflow side of the FTC. This change in the water content profile is too small to be detected in a laboratory experiment. After two hours, the flow field and water content distribution became essentially stationary.

The velocity field after the steady-state is shown in Fig. 8.7. In the middle of the domain, water flow is practically horizontal with a pore water velocity of $1.3\,\text{m}\,\text{d}^{-1}$ up to a height of about 11 cm. In the unsaturated zone, the pore water velocity decreases drastically with decreasing water content. Close to the inlet/outlet ports the pore water velocity reaches a maximum of $6.5\,\text{m}\,\text{d}^{-1}$. Flow is not just horizontal but follows curved streamlines and new nutrients are transported to the upper part of the domain. Thus, also cells in the unsaturated zone will get fresh DOC supply. After 3 d of flow, the transport and growth of *E. coli* becomes quasi-stationary and does no longer change considerably. The spatial distribution after 10 d (after 5 d with horizontal flow) is shown in Fig. 8.8 together with a picture of the fluorescence intensity. A vertical profile of the cell concentration is shown in Fig. 8.5.

It is obvious from the plots that there is a fundamental mismatch between simulation results and experimental data. The microorganisms are too strongly washed out in the simulation, as retention of the bacteria e.g. by adhesion to the solid phase or filtration is not considered in the model. This results in a shift of the cell concentration distribution to more unsaturated

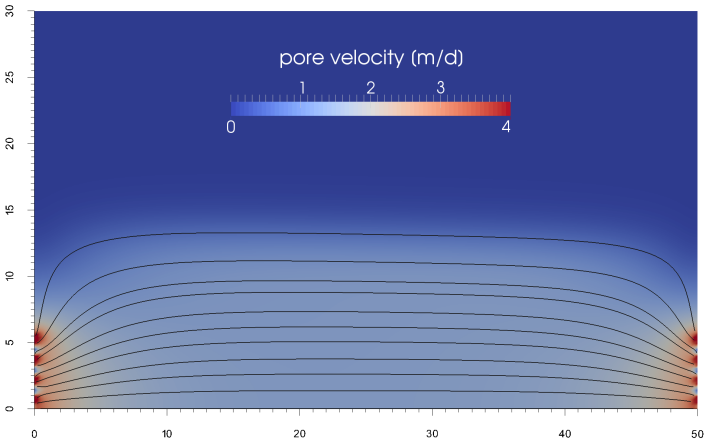

Fig. 8.7: Magnitude of pore velocity flow field [$\mathrm{m\,d^{-1}}$] (scaled to the maximal pore velocity $4\,\mathrm{m\,d^{-1}}$) and streamlines of water flow.

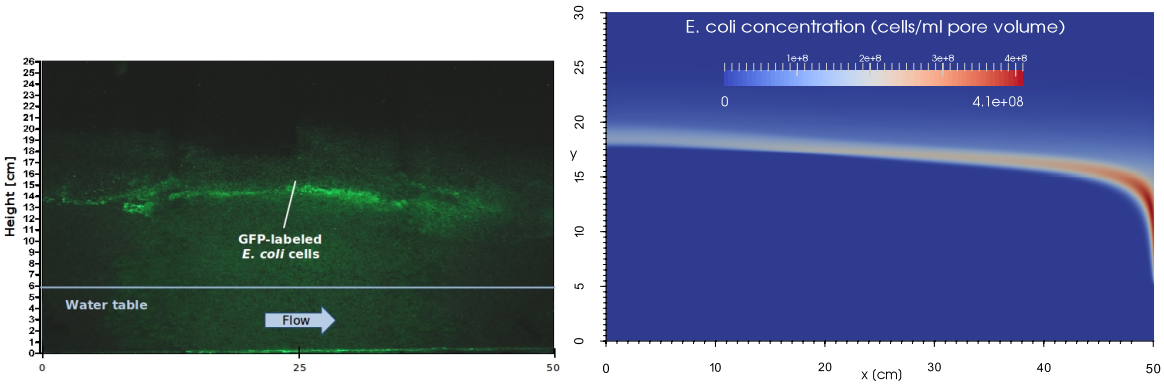

Fig. 8.8: Fluorescence intensity in the experiment (left) from Jost et al. (2014a) and cell concentration (right) after 10 days of simulation (after 5 days of flow with new DOC supply).

conditions, where the pore water velocity is low. In the lower part of the domain, virtually no bacteria are present. Thus, all DOC is available to the bacteria at the top, resulting in very high cell concentrations in this region.

8.5 Investigation of Bacteria Attachment at the Solid Phase

In the following we want to examine if the adhesion of the *E. coli* bacteria to the solid phase could be the reason for the discrepancies.

8.5.1 Attachment Model

In many laboratory and field studies, models based on a colloid filtration theory (CFT) have been used extensively to evaluate microbial transport and adhesion in saturated and unsatu-

rated porous media (e.g. Ginn et al., 2002; Tufenkji, 2007).

Assuming that the attachment of *E. coli* cells to sand grains is reversible, the general formulation of the adhesion term $a_{l,X}$ describing cell adhesion from liquid phase is written as (Bradford et al., 2006)

$$a_{l,X} = -\theta_l k_{att} \psi C_{l,X} + \theta_s k_{det} C_{s,X}, \tag{8.13}$$

where $C_{l,X}$ is the *E. coli* concentration in the liquid phase, $C_{s,X}$ is the *E. coli* concentration at the solid surface, k_{att} is the first-order deposition coefficient, k_{det} is the first-order detachment coefficient and ψ is a dimensionless deposition function. The mass balance equation for *E. coli* attached to the solid phase is then given by

$$\frac{\partial \left(\theta_s C_{s,X}\right)}{\partial t} = -a_{l,X}. \tag{8.14}$$

To account for time dependent deposition behavior and a decrease in the solid surface area available for bacterial adhesion, a general form for ψ is utilized as in Schäfer et al. (1998a):

$$\psi = \left(1 - \frac{C_{s,X}}{s_l C_{s,X}^{max}}\right), \tag{8.15}$$

where $C_{s,X}^{max}$ is the maximum attainable bacterial concentration on the solid surface. The solid-liquid interfacial area available for cell attachment decreases with water content. As $C_{s,X}$ rises, the bacteria render the solid surface less attractive for further attachment and the deposition function (8.15) will decrease. The maximum concentration of the attached cells is given by $s_l C_{s,X}^{max}$.

Because the cells attached to the surface of the sand grains are still in direct contact with the liquid phase, we can define a *total* liquid *E. coli* concentration as $C_X = C_{l,X} + C_{s,X}\theta_s/\theta_l$. We assume, that attached and detached cells can be described by the same growth model.

8.5.2 Experimental Determination of the Adhesion Parameters

In the work by Lutterodt (2012), many flow through experiments were conducted to investigate adhesion kinetics of different *E. coli* strains. The adhesion rates for different strains may differ by many orders of magnitude (10^{-2}-$10^{-7}\,\mathrm{s}^{-1}$) and the adhesive kinetic needs to be established for every strain separately. For this reason we designed similar experiments to estimate the model parameters (8.13) for strain HB101 K12 pGLO. The flow-through experiments were conducted in stainless steel capillaries (diameter 0.4 cm, length 10 cm, filled with quartz sand) and saturated with a 0.9 % NaCl solution. Bacteria suspended in 0.9 % NaCl solution were then pumped through the cell with a constant bacterial concentration in the inflow ranging from 0.7×10^8 up to 1.0×10^9 cells ml^{-1}. The experiment was conducted with pore velocities between 1.3 and 4.0 $\mathrm{m\,d}^{-1}$. The amount of bacteria in the outflow was recorded over time.

The resulting data was then used for parameter estimation. The forward model solves the transport equation for *E. coli* concentration in water (3.3) together with the adhesion kinetic model (8.13-8.14) with the inflow concentration as boundary condition. To exclude an influence of numerical discretization and splitting errors in the solution of the forward problem on the

Attachment rate k_{att} [s^{-1}]	$3.0 \times 10^{-4} \pm 10\%$
Detachment rate k_{det} [s^{-1}]	$6.2 \times 10^{-6} \pm 42\%$
Maximum attached conc. $C_{s,X}^{max}$ [cells ml^{-1}porous medium]	$0.5 \times 10^{8} \pm 4\%$

Table 8.4: Adhesion parameters for *E. coli* estimated by inverse modeling from the breakthrough curves.

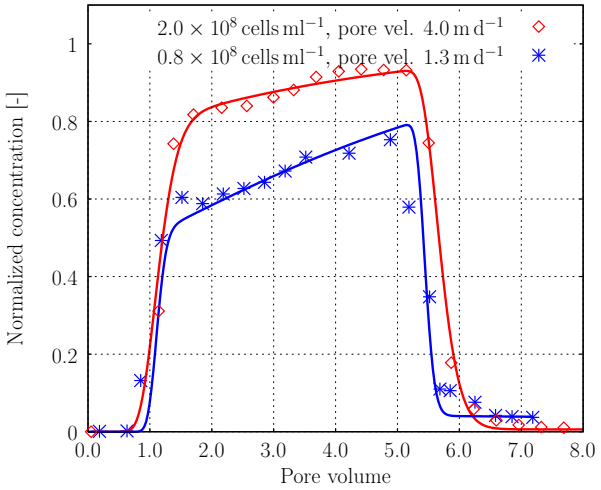

Fig. 8.9: Breakthrough curves for *E. coli* HB101 K12 pGLO measured in experiments under water-saturated conditions (points) and solution of transport/adhesion problem with estimated parameters (lines).

results of the parameter estimation, a one-dimensional domain was divided into 512 elements for the simulation. We used the same solution strategy for the forward problem as in Section 7.1. In each time step, the concentration in the last element was taken as outflow concentration. The data of all experiments was fitted simultaneously. Two example curves and the adjusted model are shown in Fig. 8.9 and the estimated parameters are summarized in Table 8.4.

The attachment coefficients reported by Bradford et al. (2006) have values between 7.7×10^{-3} and $1.3 \times 10^{-4}\,s^{-1}$, which is in a good agreement with our estimated attachment coefficient. The detachment coefficient also comparable with the values of 1.7×10^{-8}-$3.3 \times 10^{-6}\,s^{-1}$ reported in Bradford et al. (2006) with a pore velocity of approx. $4\,m\,d^{-1}$. Schäfer et al. (1998a) measured the maximum attached concentration of approx. 0.5×10^{8} cells ml^{-1} porous medium for *Pseudomonas putida*. In principle, the attachment rates can be dependent on flow velocities. However, we have not observed any dependency on flow conditions. The influence of the bacterial growth stage on cell adhesion of *E. coli* has been studied by Walker et al. (2004). Cells in the stationary growth phase were notably more adhesive than those in the exponential phase. In our batch experiments, the age of *E. coli* cells did not have any influence on cell adhesion kinetics.

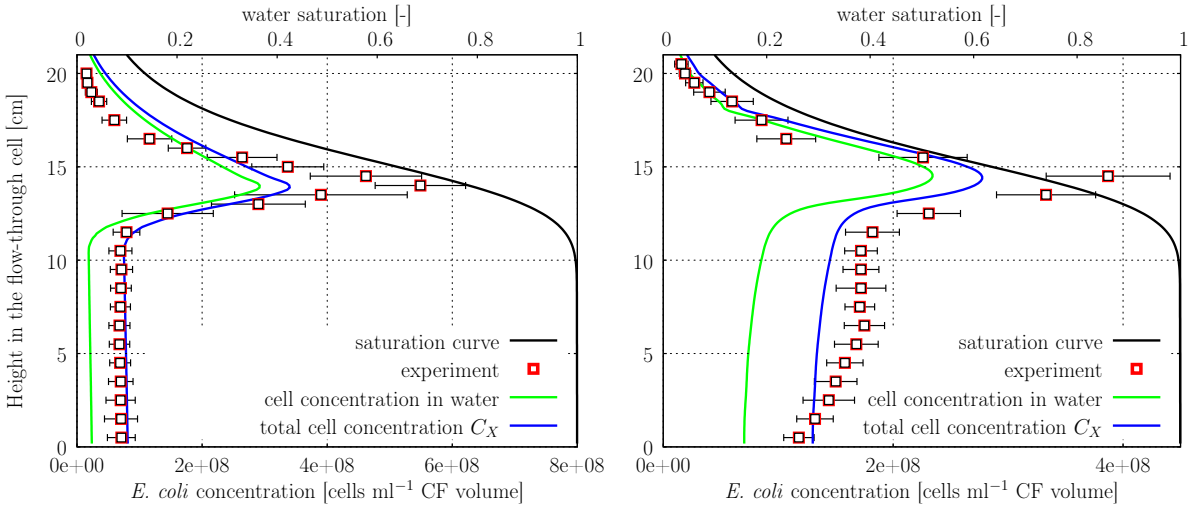

Fig. 8.10: Vertical profile of total cell concentration and cell concentration in the liquid phase at $x = 25\,\text{cm}$ after 5 d of growth without new nutrient supply and without flow (left) and after another 5 d with new nutrient supply and flow (right). Comparison between cell concentrations computed by numerical simulation with $p_d = 0.9\,\text{mm}$ and experimental data.

8.5.3 Simulation Results with Attachment

In order to capture attachment behavior, the simulation of the FTC experiment as described in Section 8.4.1 was repeated with the adhesion model (8.13-8.15). In addition to the system of equations described in Section 8.4.2, we added the reaction term $a_{l,X}$ given by (8.13) to the reactive transport problem (3.5) and also solved Eq. (8.14) modeling the concentration of attached microorganisms.

All other parameters were the same as in the simulations without attachment (see Section 8.4.2). A vertical profile of the total cell concentration and the cell concentration in the liquid phase at $x = 25\,\text{cm}$ (in the middle of the FTC) is given in Fig. 8.10. The distribution of attached and total cell concentration is shown in Fig. 8.12. While the simulation results (and the agreement with the experimental data) are nearly identical for the first five days of the experiment (the stationary phase), there are drastic differences in the transient phase.

In the lower part of the FTC, where the growth of *E. coli* was anaerobic in the first five days, the cell concentration after 10 days is higher than after 5 days. This has two reasons: firstly the nutrients and oxygen are continuously provided with the current, secondly the attachment prevents the bacteria from being washed out. This is reflected by the fact that in this region nearly half of the microorganisms are attached to the solid phase (Fig. 8.10). The maximum cell concentration is at a height of about 15 cm, which is well in accordance with the measurements. As in the experiment, the maximal cell concentration is lower than at the end of the stagnant phase. In the upper part of the domain with very low saturation ($s_l < 0.2$) *E. coli* cells do not get any new nutrients from the flowing water and are starving. Overall, the agreement between measured and simulated total cell concentration is even better than after the stagnant phase.

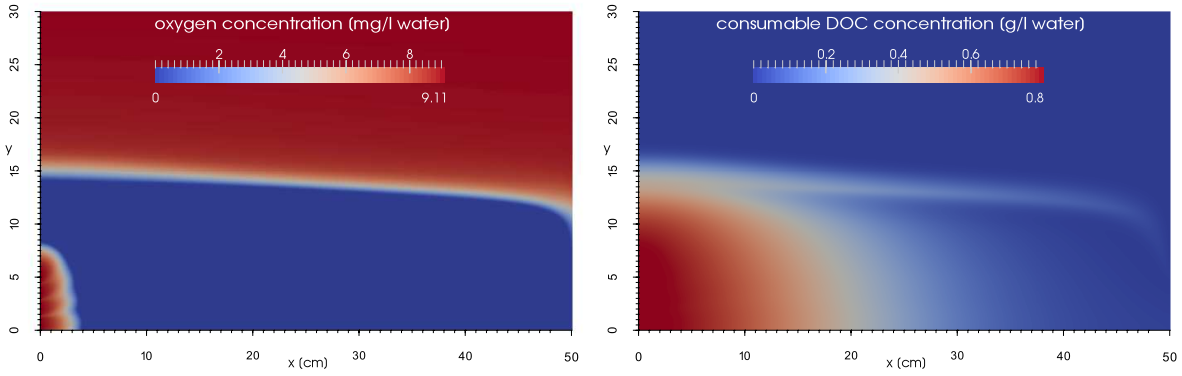

Fig. 8.11: Spatial distribution of oxygen (left) and consumable DOC (right) after 10 days of simulation with new DOC supply.

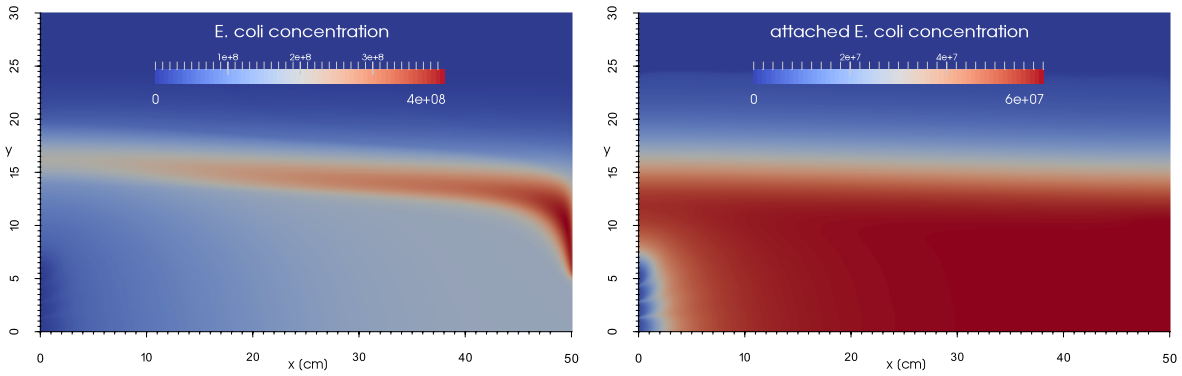

Fig. 8.12: Spatial distribution of cell concentrations [cells ml^{-1} CF volume] after 10 days of simulation with new DOC supply; total *E. coli* concentration (left) and attached cell concentration (right).

Close to the inlet ports, the microorganisms are washed out and even the number of attached cells is reduced (Fig. 8.12). The area with the highest cell concentration is shifted upwards on the inflow by 2-3 cm. Both effects can be observed in principle but are less pronounced in the fluorescence intensities (Fig. 8.8, left).

The carbon and oxygen sources in the added water are depleted during the transport through the chamber, see Fig. 8.11. Oxygen is exhausted almost immediately if the microorganism concentration is high in the saturated and unsaturated zones. DOC is transported with the current and is consumed continuously. Numerical simulation confirmed that almost all bioconvertible DOC was consumed within the chamber.

The numerical simulation predicts an accumulation of *E. coli* cells at the right side of the domain above the outflow ports, as the flow velocities are low there and the cells are washed out slowly in this region. This effect was also observed in tracer experiments with fluorescein, but not in the experiment with *E. coli* cells. The production of a green fluorescent protein depends on the oxygen concentration (Jost et al., 2014b) and also on the activity of the cell. This is not considered in the simulation. Thus, the cell concentration at the right side of the domain might be considerably higher but the cells are inactive. This has to be investigated in future experiments.

Production of Carbon Dioxide

When the *E. coli* cells respire, they release carbon in the form of CO_2. A very high CO_2 concentration in the air changes the density of the gas phase, which in turn influences its Darcy's velocity. Assuming that for each mole of consumed O_2 one mole of CO_2 will immediately be released into the gas phase, we repeated the previous simulations with initial and boundary concentration corresponding to 0.05% of CO_2 in the gas phase. In regions with high DOC supply and high oxygen consumption the density of the gas phase increased up to $1.3\,\mathrm{kg\,m^{-3}}$. However, the magnitude of the gas phase velocity caused by differences in density was of the order of $10^{-8}\,\mathrm{m\,s^{-1}}$ which is still small compared to the diffusive fluxes considering a diffusion coefficient of $1.6 \times 10^{-5}\,\mathrm{m^2\,s^{-1}}$ for CO_2 (Lide, 2008) and the dimension of the domain. Thus, the effect is negligible.

8.6 Solution Strategy and Implementation Efficiency

The laboratory experiment is characterized by a highly transient initial behavior with rapid changes caused by initial transport, followed by a stagnancy phase without groundwater flow. The third part of the experiment simulates a quasi-steady state transient flow.

We will discuss the solution approaches for the following four phases of the simulation:

1. inflow (t = 0-1 h),
2. stagnancy (t = 1 h-5 d),
3. horizontal flow, short term with duration 5 h (t = 5 d-5 d and 5 h),
4. horizontal flow, long term with duration 2 d (t = 5 d-7 d).

Dominant Processes and Solution Approaches

The 50×30 cm large domain was discretized using 392×256 rectangular grid cells, i.e. the grid size h is approx. 1.3×10^{-3} m. There are two dominant reactive processes in the inflow phase of the experiment: microbial growth and adhesion of microorganisms. We can estimate the maximum velocity of the microbial growth by the aerobic maximum growth rate $\mu_{max,a} = 0.324\,\mathrm{h}^{-1} = 9.0 \times 10^{-5}\,\mathrm{s}^{-1}$ and the adhesion kinetic by the attachment coefficient $k_{att} = 3.0 \times 10^{-4}\,\mathrm{s}^{-1}$. The maximum flow velocity determining the time step for explicit methods at the inlet ports is approx. $6.5\,\mathrm{m\,d}^{-1} = 7.5 \times 10^{-5}\,\mathrm{m\,s}^{-1}$. Thus, the transport Damköhler number for microbial growth and cell attachment is 0.0015 and 0.005 respectively. We can state that the error in the operator splitting approach using the second-order Strang splitting between transport and reaction is negligible and we can thus use the OS approach.

In the second part of the experiment, the transport is dominated by diffusion and it is convenient to use GIA. The bacterial concentration becomes higher and the bacteria consume the oxygen in the transition zone very quickly. However, the oxygen dissolution described by model (8.10) is limited by the mass exchange coefficient β_e and the effective interfacial area a_{gw}. In the region with gas saturation 0.1 (i.e. the region of high microbial activity), the kinetic rate $\lambda_r = \beta_e a_{gw}$ is approx. $5.7 \times 10^{-4}\,\mathrm{s}^{-1}$ for $p_d = 0.9$ mm.

The maximum flow velocity in the third part of the experiment with horizontal flow is about $6\,\mathrm{m\,d}^{-1}$. Thus, the transport Damköhler number for oxygen phase exchange is approx. 0.01. The Damköhler numbers for microbial growth and adhesion are similar to those computed above and the OS approach can be applied successfully.

Code Performance

We performed all simulations described in this chapter on AMD *Opteron*™ 6172, 2.10 GHz. We tested the performance of the implementation of the two-phase problem and the reactive transport using both approaches. To perform a strong scaling, we fixed the problem size (mesh with 392×256 elements) and investigated how the solution time varies with the number of processors.

Table 8.5 summarizes the computational times for the two-phase simulation in the inflow part of the experiment. The two-phase code scales well, with an efficiency above 70% for 16 processors.

P	CT	speedup	efficiency
1	52.7	1.00	1.00
2	28.0	1.88	0.94
4	17.1	3.07	0.77
8	8.2	6.43	0.80
16	4.5	11.79	0.74

Table 8.5: Strong scaling for two-phase problem in the inflow phase of the experiment. The computational times (CT) in minutes for different numbers of processors P on a mesh 392×256 elements, 65 time steps.

In each time step of the two-phase problem, we solve the system of ADREs using both solution approaches (GIA and OS). In the GIA approach we use a first-order CCFV scheme with full upwinding of the convection terms together with implicit Euler in time. GIA uses adaptive time stepping as described in Section 4.6.1 with a maximum time step corresponding to the CFL number 10. On the other hand, the OS approach solves the advection-diffusion problem for each component using second-order CCFV with flux reconstruction and Heun time discretization for all solute components in the liquid phase. The transport in the gas phase is solved with either the same methods as the transport in the advection-dominated case ($\mathrm{Pe}_g > 2$) or with CCFV using central differences for the advection term and implicit Euler if $\mathrm{Pe}_g < 2$. The splitting time step τ in the OS splitting corresponds to the CFL-like number $\nu_l = 0.8$. The system of reactions describing the microbial growth, phase exchange and adhesion of microorganisms is solved element-wise with RKF45.

Table 8.6 shows the computational performance of both the operator splitting and the global implicit approach in the first part of the experiment (inflow). The time needed to compute the reactions in the OS approach does not exceed 5% of the time needed to compute the transport of all components. The computational time needed by one processor with GIA is less than half of the computational time needed using the OS approach. This difference is caused by the different number of time steps required for the simulation. The maximum time step for the OS approach is much smaller than for the GIA approach and OS requires almost 15 times more time steps than GIA. However, the computational effort per time step is 6-8 smaller for the OS approach, which is due to the required linear system solve in GIA. We solve the ADRE system with three components in the liquid phase (bacteria, consumable substrate, oxygen), one component in the gas phase and bacteria in the solid phase. Thus, the two-dimensional problem with 5 components solved on a mesh with 392×256 elements using CCFV requires the solution of a non-linear system with more than 5×10^5 DOFs.

With respect to the scalability of both approaches, OS is much more efficient than GIA. One can observe a super-linear speedup when using at least 16 processes in the transport part of the OS approach. This super-linear speedup is caused by cache effects: the used machine has 512 kB of L_2 cache. When we solve the transport problems component-wise, all of the working sets fits into L_2 cache, and the memory access time reduces dramatically.

The element-wise computed reactions in the OS approach do not scale very well. The velocity and the stiffness of the reaction terms in this example strongly depend on the position in the computational domain, i.e. the solution time is governed by the processor which needs to compute most of the stiff reaction. The domain decomposition used in this work is well suited for transport problems (particularly with explicit treatment), but if the time for reactions were dominant, a more sophisticated load balancing would be required. The computational times of OS and GIA simulating the first 5 h of the horizontal flow using 16 processors are comparable for both approaches (Table 8.7). This time (5 h) corresponds to propagation through a half of the pore volume. However, GIA is more efficient for long-term simulations which correspond to several pore volumes, see Table 8.7, because we can use longer time steps.

The results of the numerical simulations shown in this chapter were computed with both approaches. Although the GIA approach may introduce a small amount of the numerical diffusion at the concentration fronts, we have not seen any difference between the concentrations computed by either approach. We have also performed the simulation on a finer mesh without any visible changes of resulting concentrations.

	OS approach						GIA	
	transport		reactions		sum		reactive transport	
P	CT	eff.	CT	eff.	CT	eff.	CT	eff.
1	450.4	1.00	9.9	1.00	460.4	1.00	187.4	1.00
2	227.6	0.99	4.9	1.00	232.5	0.99	115.5	0.81
4	121.2	0.93	3.2	0.78	124.4	0.93	72.4	0.65
8	60.4	0.93	1.6	0.78	62.0	0.93	36.4	0.64
16	22.8	1.23	0.9	0.66	23.7	1.21	22.6	0.52

Table 8.6: Strong scaling for reactive transport in the inflow phase of the experiment (up to 1 h). Comparison between computational times (CT) in minutes for OS approach (988 time steps) and GIA (69 time steps).

	OS approach							GIA		
	transport		reactions		sum			reactive transport		
P	CT	eff.	CT	eff.	CT	eff.	CT pts	CT	eff.	CT pts
1	1557.6	1.00	20.6	1.00	1578.2	1.00	24.9	846.0	1.00	110.6
2	783.6	0.99	10.6	0.97	794.3	0.99	12.6	448.2	0.94	58.6
4	432.6	0.90	5.9	0.88	438.5	0.90	6.9	271.1	0.78	35.4
8	221.3	0.88	3.2	0.81	224.5	0.88	3.5	148.6	0.71	19.4
16	86.0	1.13	2.0	0.64	88.0	1.12	1.4	67.4	0.78	8.8

Table 8.7: Strong scaling for reactive transport in the phase of the experiment with horizontal flow. 5 h of experiment correspond to approx. 0.5 pore volume. Comparison between computational times (CT) in minutes for OS approach (3746 time steps) and GIA (459 time steps) and corresponding computational times for one time step (CT pts) in seconds.

	OS approach							GIA		
	transport		reactions		sum			reactive transport		
P	CT	eff.	CT	eff.	CT	eff.	CT pts	CT	eff.	CT pts
1	11 797.8	1.00	178.4	1.00	11 976.3	1.00	25.3	2951.1	1.00	117.3
2	5979.7	0.99	94.7	0.94	6074.4	0.99	12.8	1712.9	0.86	68.1
4	3314.3	0.89	48.8	0.91	3363.1	0.89	7.1	956.2	0.77	38.0
8	1686.6	0.87	25.5	0.87	1712.1	0.87	3.6	555.2	0.66	22.1
16	653.6	1.13	16.9	0.66	670.4	1.12	1.4	273.3	0.67	10.9

Table 8.8: Strong scaling for reactive transport in the phase of the experiment with horizontal flow. 48 h of experiment correspond to approx. 5 pore volumes. Comparison between computational times (CT) in minutes for OS approach (28393 time steps) and GIA (1510 time steps) and corresponding computational times for one time step (CT pts) in seconds.

8.7 Summary and Discussion

The primary objective of this chapter was to test if we can understand the behavior of microorganisms well enough to predict their growth in a porous medium using only independently measured data, or if we can just reproduce their behavior afterwards by fitting a model to the data. The well known bacterium *E. coli* was used as a typical representative. The growth model, which was developed and parametrized with data from batch experiments, was applied to data from experiments with a flow through cell.

We also showed that the parallel implementation of the numerical schemes exhibits good scalability, which allows us to keep the spatial discretization error negligible, while the runtime of the complete simulation is still acceptable (several hours with 32 cores on AMD *Opteron*™ 6172, 2.10 GHz).

8.7.1 Microbiological Growth

In order to predict microbial processes in the field, a good understanding of the dominant processes is essential. The applied growth model was developed and parametrized with data from batch experiments, where the bacteria grow in a liquid suspension without a porous medium was investigated. Together with an appropriate transport model, it was (nearly) sufficient to get a very good prediction for the cell concentration of *E. coli* during the infiltration and stagnant phase of the experiment. The only free parameter was the ratio $\frac{\kappa}{p_d}$ in the model for the dependency of the effective gas/liquid interfacial area on gas phase saturation. The not negligible sensitivity on this parameter demonstrates that the kinetic of the phase exchange between gas and water phase is of crucial importance at higher water saturations and that a local equilibrium assumption is not valid. Thus, additional research into the dynamics of this phase exchange and its parametrization is highly desirable. The good prediction of the cell concentrations for both the zone of aerobic and anaerobic growth demonstrates that the new parameterless approach for a switch between aerobic and anaerobic growth works well.

For the second phase of the experiment with horizontal ground water flow, an inclusion of the attachment of the *E. coli* bacteria to the solid phase was essential to obtain a good agreement between simulated and measured data. A suitable adhesion model could be successfully transferred from the literature and calibrated with additional independent measurements. With the adhesion model, it was possible to reproduce the cell concentration distribution in the flow through cell within an accuracy of 30%. As the flow velocity is relatively high in our application and a significant part of microorganisms remains in the liquid phase, we did not need to introduce a maximal microbial capacity in the growth model as in Schäfer et al. (1998c).

After about three days, the distribution of the cell concentrations becomes nearly static. The still high concentration of non adsorbed bacteria is a clear indicator that the system is in a dynamic equilibrium between permanent bacterial growth (sustained by the constant supply of nutrients) and elution of microorganisms by the groundwater flow.

8.7.2 Model Limitations

There are some processes, which were neglected or simplified in our macroscopic modeling approach, as they were not relevant in the experiment.

For adhesion kinetic we use a model based on colloid filtration theory, which is not always valid under repulsive conditions (Tufenkji, 2007). Although we assumed the same consumption kinetic in both phases, attached bacteria may consume less nutrients than cells in liquid phase. In addition, the attachment mechanism can be different in fully water saturated and unsaturated regions.

More understanding is also required on how soluble organic substances interact with the surface of bacteria and affect their retention to soil surfaces (Unc and Goss, 2004). In Schäfer et al. (1998a) and Jiang et al. (2007) the accumulation of bacteria at the air-water interface was also considered and it was modeled as an irreversible adsorption. We did not deem this necessary here, as no attachment at the air-water interface was observed in the laboratory experiments.

Furthermore, we neglected the capability of microorganisms to move actively, as the *E. coli* strain used is not capable of moving in response to a chemical gradient. Both random motility and chemotaxis can have an influence on transport for subsurface organisms (Ginn et al., 2002). Motility and chemotaxis can play a role e.g. in movement of microbes into contaminated areas of low permeability, where advective transport is minimal compared with adjacent preferred flow paths (Amy and Halderman, 1997).

Moreover, the growth and transport of microorganisms can have an influence on the hydraulic properties of porous media (Yarwood et al., 2006). High accumulation of microbial cells can change the hydraulic properties of porous media (Taylor and Jaffé, 1990), create preferential flow paths and change flow and transport direction. This is not yet included in the model. The microbially generated gases and entrapment or microbially induced changes in the chemical properties of the liquid or solid phases of the media may also play a role in permeability reduction (Rockhold et al., 2002). As the nutrient supply in this experiment was not sufficient to result in very high cell concentrations, this was not relevant. However, this is not unrealistic, as nutrient supply in natural uncontaminated groundwater is usually rather scarce.

Models describing the formation of microcolonies and/or biofilms require microscale data that are difficult to measure accurately (Clement et al., 1998). Microbial colonization may cause apparent drying within the colonized zone, with localized decreases in saturation, giving rise to partial diversion of flow around the colonized zone (Yarwood et al., 2006). In the experiments described here, no biofilm formation was detected.

8.7.3 Conclusion

Given a suitable growth model and sufficient data for the independent determination of the parameters, it is possible to predict microbial growth in a porous medium, even if the parameters were obtained from measurements with aqueous solutions only. This is even true for experimental conditions with a horizontal groundwater flow. However, the inclusion of a model for the attachment of the *E. coli* bacteria to the solid surface was crucial for a successful prediction. In the unsaturated zone a suitable description of the kinetic of the air/water gas exchange is crucial and a local equilibrium assumption is wholly insufficient.

Chapter 9

Summary and Conclusions

The main objective of this thesis was to develop a multi-phase multi-component reactive transport model for the investigation of transport and reaction processes in unsaturated and saturated groundwater systems. We have shown our new numerical model based on an operator splitting approach is a valuable tool for the investigation of various transport and reactive processes in a porous medium. The model includes transient two-phase flow, multi-component solute transport, phase exchange, as well as a chemical model that considers chemical reactions, microbial growth and attachment.

9.1 Model Development

We designed the model to be applicable to a wide variety of reactive transport problems and to be computationally robust. These goals were achieved by using an operator splitting approach. We separated either phase flow and reactive component transport or phase flow, component transport and reaction. Furthermore, the operator splitting concept enables the flexible use of discretization schemes that are adapted in an optimal way to the individual situation dependent on the flow conditions.

Monotonicity of the solution and the suppression of artificial oscillations are the fundamental requirements for the accurate simulation of reactive transport problems. In contrast to non-reactive transport simulations, where small oscillations are unproblematic, in the reactive transport oscillations result in negative concentrations, which leads to instabilities in the calculation of reactive processes. The problem with the monotonic behavior of the solution typically occurs when linear high-order methods are applied to advection-dominated problems. Conversely, linear low-order methods may introduce significant artificial diffusion. Since reaction only takes place when components mix, numerical diffusion can lead to an over-prediction of mixing, and thus an over-prediction of chemical reactions (Gramling et al., 2002). Therefore, traditional linear first-order transport schemes are not good choices for simulating advection-dominated transport of interacting compounds. The operator splitting allows the use of higher-order discretization schemes for the component transport, which as a consequence of Godunov's theorem (LeVeque, 2002) are non-linear and non-differentiable and thus cannot be included into implicit time stepping schemes. Using higher-order explicit one-step methods for the time discretization, we are able to greatly reduce the numerical diffusion.

We incorporated and tested several numerical discretization schemes to ensure an efficient and robust solution. The numerical methods have been implemented in the DUNE software framework and have been tailored towards applications in reactive transport modeling. The solution of the transport parts requires a numerical scheme which preserves the underlying

mass-conservation laws, avoids the generation of over- and undershoots and reduces numerical diffusion, whereas the solution of the chemistry part requires a numerical method adapted to efficiently solve stiff problems. As the geometry of the laboratory experimental setup is just a rectangular box, simple structured grids were sufficient. The selected cell-centered finite volume scheme for the discretization in space is robust, flexible, accurate, locally mass conservative and efficient on such grids. However, the operator splitting approach is not limited to structured grids. On complicated geometries unstructured grids with discretization schemes like the discontinuous Galerkin method can be used.

As was shown in the last chapter, reactive transport problems are often characterized by a highly transient initial behavior with rapid changes caused by transport or reaction processes, followed by a quasi-steady state condition or a series of quasi-steady state conditions, where the concentrations of dissolved species do not change significantly. Thus, an efficient solution of the whole problem requires a suitable strategy. The present model includes adaptive time stepping. Moreover, the numerical methods used to compute reactive transport can be adapted to the concrete simulation conditions to significantly reduce the numerical discretization error and the computational time.

9.2 Operator Splitting vs. Global Implicit Approach

One of the objectives of this work was to determine the convergence properties of the operator splitting method for reactive transport as a function of the used splitting algorithm and the values of the dimensionless variables describing the system under consideration.

In the case of the OS approach, when the transport part is solved explicitly with higher-order schemes in space and time, no linear or non-linear systems need to be solved. Explicit methods are easy to parallelize and require a modest amount of computer memory. However, the time step may not exceed a certain threshold that depends on the CFL-like number. Otherwise, the transport scheme may become unstable. The lack of stability for longer time steps is the price to be paid for the simplicity of the explicit schemes. To compute a single time step in transport is cheap but an inordinately large number of time steps may be required to perform simulations over a given interval of time. However, the solution of component transport in the OS approach is not limited to explicit time schemes; unconditionally stable implicit or implicit-explicit time step schemes can be used as well.

The reaction terms in the OS approach are solved element-wise. We showed that the symmetrical second-order Strang splitting reduces the OS error between transport and reactions sufficiently for slow kinetically controlled reactions ($Da < 0.01$). In all examples in this thesis, the time needed to solve the chemical reactions did not exceed 5% of the time to solve the transport problems. However, in problems including instantaneous equilibrium chemistry, the computation time to solve the chemical problem can be many times longer than the time needed to compute the component transport. In this situation, a non-adaptive parallelization based on domain decomposition without additional load-balancing can be very inefficient.

GIA with implicit methods produces non-diagonal matrices. The design of an efficient implicit algorithm is particularly difficult if the underlying PDE and/or the discretization procedure are non-linear. The cost per time step is larger compared to that of an OS approach with explicit

treatment of the transport problem. The used implicit schemes are unconditionally stable, and the use of large time steps makes it possible to reach the final time faster than with an explicit scheme subject to a restrictive stability limit (see Section 8.6). However, the accuracy of the space and time discretization and the convergence behavior of linear and non-linear iterative solvers also depends on the time step size and on the underlying problem.

The reactive processes involved in the system also affect the choice of the solution strategy. If all the reactive processes are slow compared to the transport, we can use an OS approach without any loss of accuracy. However, if there are any reactions which are in local equilibrium, we should prefer the GIA approach. We should also distinguish between truly transient problems and those in which the solution varies slowly and/or converges to a steady state. Tables 9.1 and 9.2 summarize the restriction and possible applications of both approaches.

If it is not known in advance whether the transport process to be simulated is steady or unsteady, it is possible to start with an OS approach and switch to GIA if the changes in solution in one time step become small. However, the deterministic criteria for this switch need to be further investigated. The most severe problem with the OS approach with explicit schemes for component transport is the time step restriction given by the CFL condition. Particularly in multi-dimensional examples the difference in magnitude of the velocity can be very high (as e.g. in the two-dimensional examples in Chapters 7 and 8) and the time step is determined by the element with maximal velocity. On the other hand, in the remaining part of the domain the time step could be larger. To overcome this difficulty, one can use local time-stepping (different time steps for different elements) and/or an unconditionally stable implicit scheme together with shock detectors. However, these improvements need to be investigated in future extensions of our model.

Method	Time discretization	Space discretization	CFL	Pe	Da	Solution of global (non-)linear system
GIA	implicit	first-order	-	-	-	yes
OS	explicit	higher-order	< 1	> 2	< 0.01	no

Table 9.1: Restrictions of solution approaches w.r.t. Péclet, Damköhler and CFL numbers, and the necessity to solve global (non-)linear system of equations.

Method	Applications
GIA	slowly moving fronts, reaction dominated problems, equilibrium reactions, diffusion dominated problems, long-term flow behavior or steady-state solution
OS	transient problems, transport dominated problems, kinetically controlled reactions, sharp fronts in solution, importance of evolution details

Table 9.2: Applications of the global implicit and operator splitting approaches to reactive transport processes.

9.3 Modeling of Laboratory Experiments

The quality of a scientific field and its progress depends on how well the mathematical models developed on the theoretical side agree with the results of repeatable laboratory experiments. The final focus of this thesis was to apply the developed simulator to reproduce three different laboratory experiments. We investigated transport and adhesion of nanoparticles in an unsaturated porous medium, oxygen transport and diffusion in a flow-through cell filled with glass beads, and growth and transport of microorganisms in the capillary fringe.

The lack of agreement between our initial mathematical models and the experimental measurements led to important advances as better mathematical models were developed. We took into account the discrepancy between measured data and numerical simulations, the description of feasible processes already mentioned in the literature and also the experimental observations. A very flexible, robust and fast numerical simulator which can be easily adapted to solve various transport and reactive processes and simultaneously solve the underlying problem with a sufficient accuracy is an essential tool to achieve this goal. Furthermore, parameter estimation takes a key role in the determination of kinetically controlled chemical rates.

With the help of experimentally determined information about the investigated system (properties of the porous medium, initial and boundary conditions, flow rates etc.) together with suitable models and sufficient data from the independent determination of model parameters, it was possible to predict microbial growth and transport in a porous medium. Results of modeling of cell distribution showed a very good prediction of the cell density profile of cells within the capillary fringe, even if the kinetically controlled rates were obtained from measurements with aqueous solutions only. However, the inclusion of a model for the cell attachment to the solid surface was crucial for a successful prediction. In the unsaturated zone, a suitable description of the kinetic of the air/water gas exchange was also essential. We performed all the numerical simulations without any additionally calibration of the parameters estimated from the batch experiments. The very good predictive quality of the model developed from batch experiments for the quite different conditions in a porous medium makes it a promising basis for further experiments.

9.4 Final Remarks and Future Work

In order to compare our numerical simulator to other codes described in Steefel et al. (2014), we summarize the capabilities and the used methods in the model:

- flow and transport features:
  - saturated and unsaturated flow in 1D, 2D, 3D;
  - multi-phase and multi-component flow
  - advection and diffusion transport in the liquid as well as in the gas phase
- geochemical and microbial features:
  - microbial growth

  - liquid-gas exchange
  - kinetically controlled adhesion and adsorption
- computational capabilities:
  - operator splitting and global implicit approach for reactive transport
  - transport with high Péclet numbers
  - code parallelization
  - inverse modeling and parameter estimation

The newly developed model provides a solid basis for modeling reactive flow in porous media and is not limited to the simulation of processes discussed in this work. However, there are many other desirable capabilities, which are not yet included in the model like variable density and/or non-isothermal flow. In the future, new geochemistry model like surface complexation, ion exchange, mineral precipitation and dissolution can be integrated to the model.

Moreover, additional research on the suitability of different varieties of splitting between phase transport and reactive component transport is necessary. This splitting does not play a key role in systems with water and air. However, it may be very important for other applications like CO_2 modeling, DNAPL transport or for the modeling of reactions causing a fast phase consumption.

This numerical simulator can be applied to reproduce and verify additional laboratory experiments, which requires a close collaboration with scientists executing laboratory experiments. However, the outcome of the numerical simulation cannot be better than the quality of the underlying mathematical model. Thus, the development of better and more accurate models is a great scientific challenge.

Appendix A

A.1 Time Discretization Methods

A.1.1 Explicit SSP-RK Methods

A general m stage RK-SSP method can be algorithmically represented as

$$\tilde{U}^0 = U^n, \tag{A.1a}$$

$$\tilde{U}^i = \sum_{k=0}^{i-1} \left(\alpha_{ik} \tilde{U}^k + \Delta t^n \beta_{ik} L(\tilde{U}^k) \right), \quad i = 1, \ldots, m, \tag{A.1b}$$

$$U^{n+1} = \tilde{U}^m, \tag{A.1c}$$

where $\alpha_{ik} \geq 0$ and $\alpha_{ik} = 0$ only if $\beta_{ik} = 0$. We use the second- and third-order non-linear SSP-RK methods described in Shu (1988).

Heun

The second order, two-stage non-linear SSP-RK method is given by

$$\begin{aligned} \tilde{U}^0 &= U^n, \\ \tilde{U}^1 &= \tilde{U}^0 + \Delta t^n L(\tilde{U}^0), \\ U^{n+1} &= \frac{1}{2}\tilde{U}^0 + \frac{1}{2}\tilde{U}^1 + \frac{1}{2}\Delta t^n L(\tilde{U}^1). \end{aligned}$$

This method corresponds to the well known method of Heun.

Shu3

Similarly, the third order, three-stage non-linear SSP-RK method is given by

$$\begin{aligned} \tilde{U}^0 &= U^n, \\ \tilde{U}^1 &= \tilde{U}^0 + \Delta t^n L(\tilde{U}^0), \\ \tilde{U}^2 &= \frac{3}{4}\tilde{U}^0 + \frac{1}{4}\tilde{U}^1 + \frac{1}{4}\Delta t^n L(\tilde{U}^1), \\ U^{n+1} &= \frac{1}{3}\tilde{U}^0 + \frac{2}{3}\tilde{U}^2 + \frac{2}{3}\Delta t^n L(\tilde{U}^2). \end{aligned}$$

A.1.2 IMEX Methods

We summarize the Butcher tableaus for the second- and third order IMEX schemes tested in this thesis. The tableau on the left corresponds to explicit scheme, whereas the tableau on the right describes the implicit scheme.

In all of these schemes the implicit tableau corresponds to an L-stable scheme, whereas the explicit tableau is SSP scheme. We use the notation SSP(s, e, o), where s is the number of schemes of the implicit scheme, e the number of stages of the explicit scheme and o denotes the order of the RK-IMEX scheme.

Alexander2-IM

IMEX-SSP(2,2,2) from Ascher et al. (1997), stability discussed in Koto (2008b):

$$\begin{array}{c|ccc} 0 & 0 & & \\ \gamma & \gamma & 0 & \\ 1 & \delta & 1-\delta & 0 \\ \hline & \delta & 1-\delta & 0 \end{array} \quad \begin{array}{c|ccc} 0 & 0 & & \\ \gamma & 0 & \gamma & \\ 1 & 0 & 1-\gamma & \gamma \\ \hline & 0 & 1-\gamma & \gamma \end{array}, \quad \gamma = \frac{2-\sqrt{2}}{2}, \delta = \frac{1-\sqrt{2}}{2-\sqrt{2}}$$

Pareschi2

IMEX-SSP(3,3,2) from Koto (2008b):

$$\begin{array}{c|cccc} 0 & 0 & & & \\ 1 & 1 & 0 & & \\ \frac{1}{2} & \frac{1}{2} & 0 & & \\ 1 & 0 & 0 & 1 & 0 \\ \hline & 0 & 0 & 1 & 0 \end{array} \quad \begin{array}{c|cccc} 0 & 0 & & & \\ 1 & 0 & 1 & & \\ \frac{1}{2} & 0 & -\frac{1}{2} & 1 & \\ 1 & 0 & -1 & 1 & 1 \\ \hline & 0 & -1 & 1 & 1 \end{array}$$

Ascher3

IMEX-SSP(4,4,3) from (Ascher et al., 1997; Pareschi and Russo, 2005):

$$\begin{array}{c|ccccc} 0 & 0 & & & & \\ \frac{1}{2} & \frac{1}{2} & 0 & & & \\ \frac{2}{3} & \frac{11}{18} & \frac{1}{18} & 0 & & \\ \frac{1}{2} & \frac{5}{6} & -\frac{5}{6} & \frac{1}{2} & 0 & \\ 1 & \frac{1}{4} & \frac{7}{4} & \frac{3}{4} & -\frac{7}{4} & 0 \\ \hline & \frac{1}{4} & \frac{7}{4} & \frac{3}{4} & -\frac{7}{4} & 0 \end{array} \quad \begin{array}{c|ccccc} 0 & 0 & & & & \\ \frac{1}{2} & 0 & \frac{1}{2} & & & \\ \frac{2}{3} & 0 & \frac{1}{6} & \frac{1}{2} & & \\ \frac{1}{2} & 0 & -\frac{1}{2} & \frac{1}{2} & \frac{1}{2} & \\ 1 & 0 & \frac{3}{2} & -\frac{3}{2} & \frac{1}{2} & \frac{1}{2} \\ \hline & 0 & \frac{3}{2} & -\frac{3}{2} & \frac{1}{2} & \frac{1}{2} \end{array}$$

Bibliography

Aachib, M., Mbonimpa, M., Aubertin, M.. Measurement and Prediction of the Oxygen Diffusion Coefficient in Unsaturated Media, with Applications to Soil Covers. Water, Air, & Soil Pollution 2004;156(1):163–193. doi:10.1023/B:WATE.0000036803.84061.e5.

Abadpour, A., Panfilov, M.. Method of negative saturations for modeling two-phase compositional flow with oversaturated zones. Transport in Porous Media 2009;79(2):197–214. doi:10.1007/s11242-008-9310-0.

Abriola, L.M., Pinder, G.F.. A multiphase approach to the modeling of porous media contamination by organic compounds: 1. equation development. Water Resources Research 1985;21(1):11–18. doi:10.1029/WR021i001p00011.

Adenekan, A.E., Patzek, T.W., Pruess, K.. Modeling of multiphase transport of multicomponent organic contaminants and heat in the subsurface: Numerical model formulation. Water Resources Research 1993;29(11):3727–3740. doi:10.1029/93WR01957.

Affek, H.P., Ronen, D., Yakir, D.. Production of CO2 in the capillary fringe of a deep phreatic aquifer. Water Resources Research 1998;34(5):989–996. doi:10.1029/98WR00095.

Ahrenholz, B., Niessner, J., Helmig, R., Krafczyk, M.. Pore-scale determination of parameters for macroscale modeling of evaporation processes in porous media. Water Resources Research 2011;47(7). doi:10.1029/2010WR009519.

Alexander, R.. Diagonally implicit Runge-Kutta methods for stiff ODE's. SIAM Journal on Numerical Analysis 1977;14(6):1006–1021.

Allen, M., Behie, G., Trangenstein, J.. Multiphase Flow in Porous Media. volume 34 of *Lecture Notes in Engineering*. Springer–Verlag, 1992.

Allen, M.B.. Numerical modelling of multiphase flow in porous media. Advances in Water Resources 1985;8(4):162–187. doi:10.1016/0309-1708(85)90062-4.

Amir, L., Kern, M.. A global method for coupling transport with chemistry in heterogeneous porous media. Computational Geosciences 2010;14(3):465–481. doi:10.1007/s10596-009-9162-x.

Amy, P.S., Halderman, D.L.. Microbiology of the Terrestrial Deep Subsurface (The Microbiology of Extreme and Unusual Environments). CRC, 1997.

Anna, P.d., Jimenez-Martinez, J., Tabuteau, H., Turuban, R., Le Borgne, T., Derrien, M., Méheust, Y.. Mixing and reaction kinetics in porous media: An experimental pore scale quantification. Environmental Science & Technology 2014;48(1):508–516. doi:10.1021/es403105b.

Appelo, C., Rolle, M.. PHT3D: A reactive multicomponent transport model for saturated porous media. Ground Water 2010;48(5):627–632. doi:10.1111/j.1745-6584.2010.00732.x.

Ascher, U.M., Ruuth, S.J., Spiteri, R.J.. Implicit-explicit Runge-Kutta methods for time-dependent partial differential equations. Applied Numerical Mathematics 1997;25(2-3):151–167. doi:10.1016/S0168-9274(97)00056-1.

Ataai, M., Shuler, M.. Simulation of the growth pattern of a single cell of Escherichia coli under anaerobic conditions. Biotechnology and bioengineering 1985;XXVII(8):1027–1035.

Aziz, K., Aziz, K., Settari, A.. Petroleum reservoir simulation. Elsevier, 1979.

Bahr, J.M., Rubin, J.. Direct comparison of kinetic and local equilibrium formulations for solute transport affected by surface reactions. Water Resources Research 1987;23(3):438–452. doi:10.1029/WR023i003p00438.

Barry, D., Bajracharya, K., Miller, C.. Alternative split-operator approach for solving chemical reaction/groundwater transport models. Advances in Water Resources 1996a;19(5):261 – 275. doi:10.1016/0309-1708(96)00002-4.

Barry, D., Miller, C., Culligan-Hensley, P.. Temporal discretisation errors in non-iterative split-operator approaches to solving chemical reaction/groundwater transport models. Journal of Contaminant Hydrology 1996b;22(1–2):1 – 17. doi:10.1016/0169-7722(95)00062-3.

Bastian, P.. Numerical computation of multiphase flows in porous media. Habilitation; Kiel university; 1999.

Bastian, P.. Higher order discontinuous galerkin methods for flow and transport in porous media. In: Bänsch, E., editor. Challenges in Scientific Computing - CISC 2002. Springer Berlin Heidelberg; volume 35 of *Lecture Notes in Computational Science and Engineering*; 2003. p. 1–22. doi:10.1007/978-3-642-19014-8_1.

Bastian, P.. A fully-coupled discontinuous Galerkin method for two-phase flow in porous media with discontinuous capillary pressure. Computational Geosciences 2014;:1–18doi:10.1007/s10596-014-9426-y.

Bastian, P., Blatt, M., Dedner, A., Engwer, C., Klöfkorn, R., Kornhuber, R., Ohlberger, M., Sander, O.. A generic grid interface for parallel and adaptive scientific computing. Part II: implementation and tests in DUNE. Computing 2008a;82(2-3):121–138. doi:10.1007/s00607-008-0004-9.

Bastian, P., Blatt, M., Dedner, A., Engwer, C., Klöfkorn, R., Ohlberger, M., Sander, O.. A generic grid interface for parallel and adaptive scientific computing. Part I: Abstract framework. Computing 2008b;82(2):103–119. doi:10.1007/s00607-008-0003-x.

Bastian, P., Heimann, F., Marnach, S.. Generic implementation of finite element methods in the distributed and unified numerics environment (DUNE). Kybernetika 2010;46(2):294–315.

Bastian, P., Helmig, R.. Efficient fully-coupled solution techniques for two-phase flow in porous media: Parallel multigrid solution and large scale computations. Advances in Water Resources 1999;23(3):199 – 216. doi:10.1016/S0309-1708(99)00014-7.

Bastian, P., Ippisch, O., Rezanezhad, F., Vogel, H., Roth, K.. Numerical simulation and experimental studies of unsaturated water flow in heterogeneous systems. In: et al., R.R., editor. Reactive Flows, Diffusion and Transport. Berlin-Heidelberg: Springer; 2005. .

Bauer, R.D., Maloszewski, P., Zhang, Y., Meckenstock, R.U., Griebler, C.. Mixing-controlled biodegradation in a toluene plume–results from two-dimensional laboratory experiments. Journal of Contaminant Hydrology 2008;96(1-4):150–68. doi:10.1016/j.jconhyd.2007.10.008.

Bauer, R.D., Rolle, M., Kürzinger, P., Grathwohl, P., Meckenstock, R.U., Griebler, C.. Two-dimensional flow-through microcosms - Versatile test systems to study biodegradation processes in porous aquifers. Journal of Hydrology 2009;369(3-4):284–295. doi:10.1016/j.jhydrol.2009.02.037.

Bear, J.. Dynamics of fluids in porous media. Number Bd. 2 in Dynamics of Fluids in Porous Media. American Elsevier, 1972.

Bear, J., Cheng, A.. Modeling Groundwater Flow and Contaminant Transport. Theory and Applications of Transport in Porous Media. Springer, 2010.

Bell, C., McIntyre, N., Cox, S., Tissue, D., Zak, J.. Soil microbial responses to temporal variations of moisture and temperature in a chihuahuan desert grassland. Microbial ecology 2008;56(1):153–67. doi:10.1007/s00248-007-9333-z.

Bergamaschi, L., Bru, R., Martinez, A., Putti, M.. Quasi-newton acceleration of ILU preconditioners for nonlinear two-phase flow equations in porous media. Advances in Engineering Software 2012;46(1):63 – 68. doi:10.1016/j.advengsoft.2010.10.011.

Bielinsky, A.. Numerical Simulation of CO_2 Sequestration in Geological Formations. Ph.D. thesis; Universität Stuttgart; 2006.

Blatt, M.. A Parallel Algebraic Multigrid Method for Elliptic Problems with Highly Discontinuous Coefficients. Ph.D. thesis; University of Heidelberg; 2010.

Borch, T., Kretzschmar, R., Kappler, A., Cappellen, P.V., Ginder-Vogel, M., Voegelin, A., Campbell, K.. Biogeochemical redox processes and their impact on contaminant dynamics. Environmental science & technology 2010;44(1):15–23. doi:10.1021/es9026248.

Boscarino, S., Pareschi, L., Russo, G.. Implicit-Explicit Runge–Kutta Schemes for Hyperbolic Systems and Kinetic Equations in the Diffusion Limit. SIAM Journal on Scientific Computing 2013;35(1):A22–A51. doi:10.1137/110842855.

Bourgeat, A., Jurak, M., Smaï, F.. Two-phase, partially miscible flow and transport modeling in porous media; application to gas migration in a nuclear waste repository. Computational Geosciences 2009;13(1):29–42. URL: http://dx.doi.org/10.1007/s10596-008-9102-1. doi:10.1007/s10596-008-9102-1.

Bradford, S.A., Šimůnek, J., Walker, S.L.. Transport and straining of *E. coli* O157:H7 in saturated porous media. Water Resources Research 2006;42(12). doi:10.1029/2005WR004805.

Brooks, R., Corey, A.. Hydraulic Properties of Porous Media. Colorado State University Hydrology Papers. Colorado State University, 1964.

Calvo, M., de Frutos, J., Novo, J.. Linearly implicit runge–kutta methods for advection–reaction–diffusion equations. Applied Numerical Mathematics 2001;37(4):535 – 549. doi:10.1016/S0168-9274(00)00061-1.

Carrayrou, J.. Looking for some reference solutions for the reactive transport benchmark of MoMaS with SPECY. Computational Geosciences 2009;14(3):393–403. doi:10.1007/s10596-009-9161-y.

Carrayrou, J., Hoffmann, J., Knabner, P., Kräutle, S., de Dieuleveult, C., Erhel, J., Van der Lee, J., Lagneau, V., Mayer, K., MacQuarrie, K.. Comparison of numerical methods for simulating strongly nonlinear and heterogeneous reactive transport problems—the momas benchmark case. Computational Geosciences 2010;14(3):483–502. doi:10.1007/s10596-010-9178-2.

Carrayrou, J., Mosé, R., Behra, P.. Operator-splitting procedures for reactive transport and comparison of mass balance errors. Journal of Contaminant Hydrology 2004;68(3-4):239–68. doi:10.1016/S0169-7722(03)00141-4.

Chang, W., Halverson, L.. Reduced water availability influences the dynamics, development, and ultrastructural properties of *Pseudomonas putida* biofilms. Journal of bacteriology 2003;185(20):6199–6204. doi:10.1128/JB.185.20.6199-6204.2003.

Chavent, G., Jaffré, J.. Mathematical Models and Finite Elements for Reservoir Simulation: Single Phase, Multiphase and Multicomponent Flows through Porous Media. Studies in Mathematics and its Applications. Elsevier, 1986.

Chen, G., Rockhold, M., Strevett, K.A.. Equilibrium and kinetic adsorption of bacteria on alluvial sand and surface thermodynamic interpretation. Research in Microbiology 2003;154(3):175 – 181. doi:10.1016/S0923-2508(03)00033-0.

Chen, G., Walker, S.L.. Fecal indicator bacteria transport and deposition in saturated and unsaturated porous media. Environmental Science & Technology 2012;46(16):8782–90. doi:10.1021/es301378q.

Chen, Z.. Reservoir Simulation: Mathematical Techniques in Oil Recovery (CBMS-NSF Regional Conference Series in Applied Mathematics). Philadelphia, PA, USA: Society for Industrial and Applied Mathematics, 2007.

Chu, M., Kitanidis, P.K., McCarty, P.L.. Modeling microbial reactions at the plume fringe subject to transverse mixing in porous media: When can the rates of microbial reaction be assumed to be instantaneous? Water Resources Research 2005;41(6):n/a–n/a. doi:10.1029/2004WR003495.

Cirpka, O., Helmig, R.. Comparison of approaches for the coupling of chemistry to transport in groundwater systems. In: Helmig, R., Jäger, W., Kinzelbach, W., Knabner, P., Wittum, G., editors. Modeling and Computation in Environmental Sciences. Vieweg+Teubner Verlag; volume 59 of *Notes on Numerical Fluid Mechanics (NNFM)*; 1997. p. 102–120. doi:10.1007/978-3-322-89565-3_10.

Cirpka, O.A., Frind, E.O., Helmig, R.. Numerical methods for reactive transport on rectangular and streamline-oriented grids. Advances in Water Resources 1999;22(7):711–728. doi:10.1016/S0309-1708(98)00051-7.

Cirpka, O.A., Valocchi, A.J.. Two-dimensional concentration distribution for mixing-controlled bioreactive transport in steady state. Advances in Water Resources 2007;30(6–7):1668 – 1679. doi:10.1016/j.advwatres.2006.05.022.

Clark, D.. The fermentation pathways of Escherichia coli. FEMS Microbiology Letters 1989;63(3):223–234. doi:10.1111/j.1574-6968.1989.tb03398.x.

Class, H., Helmig, R.. Numerical simulation of non-isothermal multiphase multicomponent processes in porous media. Advances in Water Resources 2002;25(5):551–564. doi:10.1016/S0309-1708(02)00015-5.

Class, H., Helmig, R., Bastian, P.. Numerical simulation of non-isothermal multiphase multicomponent processes in porous media. Advances in Water Resources 2002;25(5):533–550. doi:10.1016/S0309-1708(02)00014-3.

Clement, T., Peyton, B.. Microbial growth and transport in porous media under denitrification conditions: experiments and simulations. Journal of Contaminant Hydrology 1997;24(3-4):269–285. doi:10.1016/S0169-7722(96)00014-9.

Clement, T., Sun, Y., Hooker, B., Petersen, J.. Modeling Multispecies Reactive Transport in Ground Water. Ground Water Monitoring & Remediation 1998;18(2):79–92. doi:10.1111/j.1745-6592.1998.tb00618.x.

Clift, R., Grace, J.R., Weber, M.E.. Bubbles, drops, and particles. New York: Academic Press Inc., 1978.

Cockburn, B., Shu, C.W.. The runge–kutta discontinuous galerkin method for conservation laws v: Multidimensional systems. Journal of Computational Physics 1998;1421(2):199 – 224. doi:10.1006/jcph.1998.5892.

Contois, D.E.. Kinetics of bacterial growth: relationship between population density and specific growth rate of continuous cultures. Journal of General Microbiology 1959;21:40–50.

Culligan, K.A., Wildenschild, D., Christensen, B.S.B., Gray, W.G., Rivers, M.L., Tompson, A.F.B.. Interfacial area measurements for unsaturated flow through a porous medium. Water Resources Research 2004;40(12):W12413/1–W12413/12. doi:10.1029/2004WR003278.

Cussler, E.. Diffusion: Mass Transfer in Fluid Systems. Cambridge Series in Chemical Engineering. Cambridge University Press, 1997.

Dawson, C.. Godunov-mixed methods for advective flow problems in one space dimension. SIAM Journal on Numerical Analysis 1991;28(5):1282–1309. doi:10.1137/0728068.

Dawson, C., Klíe, H., Wheeler, M.F., Woodward, C.S.. A parallel, implicit, cell-centered method for two-phase flow with a preconditioned newton-krylov solver. Computational Geosciences 1997;1(3-4):215–249. doi:10.1023/A:1011521413158.

Dean, J., Lange, N.. Lange's Handbook of Chemistry. Number Bd. 15 in LANGE'S HANDBOOK OF CHEMISTRY. McGraw-Hill, 1999.

Dechesne, A., Or, D., Gülez, G., Smets, B.F.. The porous surface model, a novel experimental system for online quantitative observation of microbial processes under unsaturated conditions. Applied and Environmental Microbiology 2008;74(16):5195–200. doi:10.1128/AEM.00313-08.

Dentz, M., Borgne, T.L., Englert, A., Bijeljic, B.. Mixing, spreading and reaction in heterogeneous media: A brief review. Journal of Contaminant Hydrology 2011;120(0):1 – 17. doi:10.1016/j.jconhyd.2010.05.002.

Descombes, S., Duarte, M., Dumont, T., Laurent, F., Louvet, V., Massot, M.. Analysis of operator splitting in the nonasymptotic regime for nonlinear reaction-diffusion equations. application to the dynamics of premixed flames. SIAM Journal on Numerical Analysis 2014;52(3):1311–1334. doi:10.1137/130926006.

de Dieuleveult, C., Erhel, J.. A global approach to reactive transport: application to the MoMas benchmark. Computational Geosciences 2009;14(3):451–464. doi:10.1007/s10596-009-9163-9.

de Dieuleveult, C., Erhel, J., Kern, M.. A global strategy for solving reactive transport equations. Journal of Computational Physics 2009;228(17):6395 – 6410. doi:10.1016/j.jcp.2009.05.044.

Duffy, G., Whiting, R., Sheridan, J.. The effect of a competitive microflora, pH and temperature on the growth kinetics of *Escherichia coli* O157:H7. Food Microbiology 1999;16(3):299–307. doi:10.1006/fmic.1998.0242.

Durlofsky, L.J.. A triangle based mixed finite element—finite volume technique for modeling two phase flow through porous media. Journal of Computational Physics 1993;105(2):252 – 266. doi:10.1006/jcph.1993.1072.

Eymard, R., Gallouët, T., Herbin, R.. Finite volume approximation of elliptic problems and convergence of an approximate gradient. Applied Numerical Mathematics 2001;37(1–2):31 – 53. doi:10.1016/S0168-9274(00)00024-6.

Fahs, M., Carrayrou, J., Younes, A., Ackerer, P.. On the Efficiency of the Direct Substitution Approach for Reactive Transport Problems in Porous Media. Water, Air, and Soil Pollution 2008;193(1-4):299–308. doi:10.1007/s11270-008-9691-2.

Faou, E., Ostermann, A., Schratz, K.. Analysis of exponential splitting methods for inhomogeneous parabolic equations. IMA Journal of Numerical Analysis 2014;doi:10.1093/imanum/dru002.

Fernández-Calviño, D., Rousk, J., Brookes, P.C., Bååth, E.. Bacterial pH-optima for growth track soil pH, but are higher than expected at low pH. Soil Biology and Biochemistry 2011;43(7):1569–1575. doi:10.1016/j.soilbio.2011.04.007.

Foppen, J.W., Schijven, J.F.. Transport of *E. coli* in columns of geochemically heterogeneous sediment. Water Research 2005;39(13):3082–8. doi:10.1016/j.watres.2005.05.023.

Forsyth, P., Sammon, P.. Practical considerations for adaptive implicit methods in reservoir simulation. Journal of Computational Physics 1986;62(2):265 – 281. doi:10.1016/0021-9991(86)90127-0.

Forsyth, P.A.. A control volume finite element approach to napl groundwater contamination. SIAM J Sci Stat Comput 1991;12(5):1029–1057. doi:10.1137/0912055.

Forsyth, P.A., Simpson, R.B.. A two-phase, two-component model for natural convection in a porous medium. International Journal for Numerical Methods in Fluids 1991;12(7):655–682. doi:10.1002/fld.1650120705.

Friedly, J.C., Rubin, J.. Solute transport with multiple equilibrium-controlled or kinetically controlled chemical reactions. Water Resources Research 1992;28(7):1935–1953. doi:10.1029/92WR00699.

Fuller, R.C., Prevost, J.H., Piri, M.. Three-phase equilibrium and partitioning calculations for co2 sequestration in saline aquifers. Journal of Geophysical Research: Solid Earth 2006;111(B6):n/a–n/a. doi:10.1029/2005JB003618.

Fučík, R., Mikyška, J., Sakaki, T., Beneš, M., Illangasekare, T.H.. Significance of Dynamic Effect in Capillarity during Drainage Experiments in Layered Porous Media. Vadose Zone Journal 2010;9(3):697. doi:10.2136/vzj2009.0106.

Geiser, J.. Discretization methods with embedded analytical solutions for convection–diffusion dispersion–reaction equations and applications. Journal of Engineering Mathematics 2007;57(1):79–98. doi:10.1007/s10665-006-9057-y.

Geistlinger, H., Beckmann, A., Lazik, D.. Mass transfer between a multicomponent trapped gas phase and a mobile water phase: Experiment and theory. Water Resources Research 2005;41(11). doi:10.1029/2004WR003885.

Genuchten, M.T.V.. Analytical solutions for chemical transport with simultaneous adsorption, zero-order production and first-order decay. Journal of Hydrology 1981;49(3–4):213 – 233. doi:10.1016/0022-1694(81)90214-6.

Genuchten, M.V.. A closed-form equation for predicting the hydraulic conductivity of unsaturated soils. Soil Science Society of America Journal 1980;44:892–8.

Ginn, T.R., Wood, B.D., Nelson, K.E., Scheibe, T.D., Murphy, E.M., Clement, T.. Processes in microbial transport in the natural subsurface. Advances in Water Resources 2002;25(8-12):1017–1042. doi:10.1016/S0309-1708(02)00046-5.

Gottlieb, S., Gottlieb, L.a.J.. Strong Stability Preserving Properties of Runge – Kutta Time Discretization Methods for Linear Constant Coefficient Operators. Journal of Scientific Computing 2003;18(1):83—-109. doi:10.1023/A:1020338228736.

Gottlieb, S., Shu, C.w., Tadmor, E.. Strong Stability-Preserving High-Order Time Discretization Methods. SIAM Review 2001;43(1):89–112. doi:10.1137/S003614450036757X.

Gramling, C.M., Harvey, C.F., Meigs, L.C.. Reactive Transport in Porous Media: A Comparison of Model Prediction with Laboratory Visualization. Environmental Science & Technology 2002;36(11):2508–2514. doi:10.1021/es0157144.

Gvirtzman, H., Roberts, P.V.. Pore scale spatial analysis of two immiscible fluids in porous media. Water Resources Research 1991;27(6):1165–1176. doi:10.1029/91WR00303.

Haberer, C.M., Rolle, M., Liu, S., Cirpka, O.A., Grathwohl, P.. A high-resolution non-invasive approach to quantify oxygen transport across the capillary fringe and within the underlying groundwater. Journal of Contaminant Hydrology 2011;122(1–4):26 – 39. doi:10.1016/j.jconhyd.2010.10.006.

Hackbusch, W., Reusken, A.. Analysis of a damped nonlinear multilevel method. Numerische Mathematik 1989;55(2):225–246. doi:10.1007/BF01406516.

Hairer, E., Nørsett, S., Wanner, G.. Solving Ordinary Differential Equations I: Nonstiff Problems. Solving Ordinary Differential Equations. Springer, 1993.

Hammond, G.E., Valocchi, A.J., Lichtner, P.C.. Modeling multicomponent reactive transport on parallel computers using jacobian-free newton krylov with operator-split preconditioning. In: S. Majid Hassanizadeh Ruud J. Schotting, W.G.G., Pinder, G.F., editors. Computational Methods in Water Resources Proceedings of the XIVth International Conference on Computational Methods in Water Resources (CMWR XIV). Elsevier; volume 47 of *Developments in Water Science*; 2002. p. 727 – 734. doi:10.1016/S0167-5648(02)80131-9.

Harten, A., Engquist, B., Osher, S., Chakravarthy, S.R.. Uniformly high order accurate essentially non-oscillatory schemes, III. Journal of Computational Physics 1987;71(2):231 – 303. doi:10.1016/0021-9991(87)90031-3.

Hassanizadeh, S.M., Celia, M.A., Dahle, H.K.. Dynamic Effect in the Capillary Pressure–Saturation Relationship and its Impacts on Unsaturated Flow. Vadose Zone Journal 2002;1(1):38–57. doi:10.2136/vzj2002.3800.

Helmig, R.. Multiphase flow and transport processes in the subsurface. Springer Berlin, 1997.

Hendry, M.J., Ranville, J.R., Boldt-Leppin, B.E.J., Wassenaar, L.I.. Geochemical and transport properties of dissolved organic carbon in a clay-rich aquitard. Water Resources Research 2003;39(7). doi:10.1029/2002WR001943.

Herzer, J., Kinzelbach, W.. Coupling of transport and chemical processes in numerical transport models. Geoderma 1989;44(2-3):115–127. doi:10.1016/0016-7061(89)90022-0.

Holocher, J., Peeters, F., Aeschbach-Hertig, W., Kinzelbach, W., Kipfer, R.. Kinetic Model of Gas Bubble Dissolution in Groundwater and Its Implications for the Dissolved Gas Composition. Environmental Science & Technology 2003;37(7):1337–1343. doi:10.1021/es025712z.

Hornung, U., editor. Homogenization and Porous Media. New York, NY, USA: Springer-Verlag New York, Inc., 1997.

Hron, P., Jost, D., Gallert, C., Bastian, P., Winter, J., Ippisch, O.. Numerical simulation of growth of *Escherichia coli* in unsaturated porous media; 2014. arXiv:1407.3743; Water Resources Research, submitted.

Hron, P., Jost, D., Gallert, C., Bastian, P., Winter, J., Ippisch, O.. Application of reactive transport modelling to growth and transport of microorganisms in the capillary fringe. Vadose Zone Journal 2015;14(5):n.a. doi:10.2136/vzj2014.07.0092.

Huber, R., Helmig, R.. Multiphase flow in heterogeneous porous media: A classical finite element method versus an implicit pressure–explicit saturation-based mixed finite element–finite volume approach. International Journal for Numerical Methods in Fluids 1999;29(8):899–920. doi:10.1002/(SICI)1097-0363(19990430)29:8<899::AID-FLD715>3.0.CO;2-W.

Hundsdorfer, W., Verwer, J.. A note on splitting errors for advection-reaction equations. Applied Numerical Mathematics 1995;18(1–3):191 – 199. doi:10.1016/0168-9274(95)00069-7.

Hundsdorfer, W., Verwer, J.. Numerical solution of time-dependent advection-diffusion-reaction equations. Number 3 in Springer Series in Computational Mathematics. Springer, 2003. doi:10.1007/978-3-662-09017-6.

Ippisch, O.. Contributions to the large-scale Simulation of Flow and Transport in Heterogeneous Porous Media. Habilitation; University of Heidelberg; 2014.

Ippisch, O., Vogel, H.J., Bastian, P.. Validity limits for the van Genuchten–Mualem model and implications for parameter estimation and numerical simulation. Advances in Water Resources 2006;29(12):1780–1789. doi:10.1016/j.advwatres.2005.12.011.

Jaffré, J., Sboui, A.. Henry' law and gas phase disappearance. Transport in Porous Media 2010;82(3):521–526. doi:10.1007/s11242-009-9407-0.

Jiang, G., Noonan, M.J., Buchan, G.D., Smith, N.. Transport of *Escherichia coli* through variably saturated sand columns and modeling approaches. Journal of Contaminant Hydrology 2007;93(1-4):2–20. doi:10.1016/j.jconhyd.2007.01.010.

Jin, Y., Jury, W.. Characterizing the dependence of gas diffusion coefficient on soil properties. Soil Science Society of America Journal 1996;60(1):66–71. doi:10.2136/sssaj1996.03615995006000010012x.

Joekar-Niasar, V., Hassanizadeh, S.M., Leijnse, A.. Insights into the Relationships Among Capillary Pressure, Saturation, Interfacial Area and Relative Permeability Using Pore-Network Modeling. Transport in Porous Media 2007;74(2):201–219. doi:10.1007/s11242-007-9191-7.

Jost, D., Haberer, C., Grathwohl, P., Winter, J., Gallert, C.. Oxygen transfer in a fluctuating capillary fringe: Impact of microbial respiratory activity. Vadose Zone Journal 2014a;doi:10.2136/vzj2014.04.0039.

Jost, D., Winter, J., Gallert, C.. Distribution of aerobic motile and non-motile bacteria within the capillary fringe of silica sand. Water Research 2010;44(4):1279–87. doi:10.1016/j.watres.2010.01.001.

Jost, D., Winter, J., Gallert, C.. Water and Oxygen Dependence of Pseudomonas putida Growing in Silica Sand Capillary Fringes. Vadose Zone Journal 2011;10(2):532. doi:10.2136/vzj2010.0092.

Jost, D., Winter, J., Gallert, C.. Non-invasive quantification of gfp-labeled escherichia coli in the capillary fringe by fluorescence intensity. Vadose Zone Journal 2014b;doi:10.2136/vzj2014.03.0028.

Kaluarachchi, J.J., Morshed, J.. Critical assessment of the operator-splitting technique in solving the advection-dispersion-reaction equation: 1. first-order reaction. Advances in Water Resources 1995;18(2):89 – 100. doi:10.1016/0309-1708(95)00001-Y.

Kanney, J.F., Miller, C.T., Barry, D.. Comparison of fully coupled approaches for approximating nonlinear transport and reaction problems. Advances in Water Resources 2003;26(4):353 – 372. doi:10.1016/S0309-1708(02)00188-4.

Karlsen, K.H., Risebro, N.H.. A front tracking approach to a two-phase fluid flow model with capillary forces. In: In Situ. 1998. p. 59–89.

Kasel, D., Bradford, S.A., Šimůnek, J., Heggen, M., Vereecken, H., Klumpp, E.. Transport and retention of multi-walled carbon nanotubes in saturated porous media: Effects of input concentration and grain size. Water Research 2013;47(2):933 – 944. doi:10.1016/j.watres.2012.11.019.

Kim, J.S., Kuk, E., Yu, K.N., Kim, J.H., Park, S.J., Lee, H.J., Kim, S.H., Park, Y.K., Park, Y.H., Hwang, C.Y., Kim, Y.K., Lee, Y.S., Jeong, D.H., Cho, M.H.. Antimicrobial effects of silver nanoparticles. Nanomedicine: Nanotechnology, Biology and Medicine 2007;3(1):95 – 101. doi:10.1016/j.nano.2006.12.001.

Kirkner, D.J., Reeves, H.. Multicomponent mass transport with homogeneous and heterogeneous chemical reactions: Effect of the chemistry on the choice of numerical algorithm: 1. theory. Water Resources Research 1988;24(10):1719–1729. doi:10.1029/WR024i010p01719.

Knoll, D., Rider, W.. A multigrid preconditioned newton–krylov method. SIAM Journal on Scientific Computing 1999;21(2):691–710. doi:10.1137/S1064827598332709.

Kolditz, O., Bauer, S., Bilke, L., Böttcher, N., Delfs, J., Fischer, T., Görke, U., Kalbacher, T., Kosakowski, G., McDermott, C., Park, C., Radu, F., Rink, K., Shao, H., Shao, H., Sun, F., Sun, Y., Singh, A., Taron, J., Walther, M., Wang, W., Watanabe, N., Wu, Y., Xie, M., Xu, W., Zehner, B.. Opengeosys: an open-source initiative for numerical simulation of thermo-hydro-mechanical/chemical (THM/C) processes in porous media. Environmental Earth Sciences 2012;67(2):589–599. doi:10.1007/s12665-012-1546-x.

Kornaros, M., Lyberatos, G.. Kinetics of aerobic growth of a denitrifying bacterium, Pseudomonas denitrificans, in the presence of nitrates and/or nitrites. Water Research 1997;31(3):479–488. doi:10.1016/S0043-1354(96)00288-6.

Koto, T.. IMEX Runge–Kutta schemes for reaction–diffusion equations. Journal of Computational and Applied Mathematics 2008a;215(1):182–195. doi:10.1016/j.cam.2007.04.003.

Koto, T.. Stability of IMEX Runge–Kutta methods for delay differential equations. Journal of Computational and Applied Mathematics 2008b;211(2):201–212. doi:10.1016/j.cam.2006.11.011.

Kouznetsov, M.Y., Pachepsky, Y.A., Gillerman, L., Gantzer, C.J., Oron, G.. Microbial transport in soil caused by surface and subsurface drip irrigation with treated wastewater. International Agrophysics 2004;18(3):239–247.

Kovárová, K., Zehnder, A.J., Egli, T.. Temperature-dependent growth kinetics of *Escherichia coli* ML 30 in glucose-limited continuous culture. Journal of Bacteriology 1996;178(15):4530–9.

Kovárová-Kovar, K., Egli, T.. Growth kinetics of suspended microbial cells: from single-substrate-controlled growth to mixed-substrate kinetics. Microbiology and Molecular Biology Reviews 1998;62(3):646–666.

Kräutle, S., Knabner, P.. A new numerical reduction scheme for fully coupled multicomponent transport-reaction problems in porous media. Water Resources Research 2005;41(9):n/a–n/a. doi:10.1029/2004WR003624.

Kräutle, S., Knabner, P.. A reduction scheme for coupled multicomponent transport-reaction problems in porous media: Generalization to problems with heterogeneous equilibrium reactions. Water Resources Research 2007;43(3):n/a–n/a. doi:10.1029/2005WR004465.

Kumahor, S., de Rooij, G., Schlüter, S., Vogel, H.J.. Water Flow and Solute Transport in Unsaturated Sand—A Comprehensive Experimental Approach. Vadose Zone Journal 2015a;14:1–35. doi:10.2136/vzj2014.08.0105.

Kumahor, S.K., Hron, P., Metreveli, G., Schaumann, G.E., Vogel, H.J.. Transport of citrate-coated silver nanoparticles in unsaturated sand. Science of The Total Environment 2015b;(0):–. doi:10.1016/j.scitotenv.2015.03.023.

Kurganov, A., Tadmor, E.. New High-Resolution Central Schemes for Nonlinear Conservation Laws and Convection–Diffusion Equations. Journal of Computational Physics 2000;160(1):241–282. doi:10.1006/jcph.2000.6459.

Lacoursiere, A., Thompson, B., Kole, M., Ward, D., Gerson, D.. Effects of carbon dioxide concentration on anaerobic fermentations of *Escherichia coli*. Applied Microbiology and Biotechnology 1986;23(5):404–406. doi:10.1007/BF00257042.

Lagneau, V., van der Lee, J.. Hytec results of the momas reactive transport benchmark. Computational Geosciences 2010;14(3):435–449. doi:10.1007/s10596-009-9159-5.

Lanser, D.. Numerical methods for atmospheric flow and circulation problems. Ph.D. thesis; University of Amsterdam; 2002.

Lanser, D., Verwer, J.. Analysis of operator splitting for advection–diffusion–reaction problems from air pollution modelling. Journal of Computational and Applied Mathematics 1999;111(1-2):201–216. doi:10.1016/S0377-0427(99)00143-0.

Lauser, A.. Theory and numerical applications of compositional multi-phase flow in porous media. Ph.D. thesis; University Stuttgart; 2014.

Lee, E.J., Kim, M., Kim, Y., Lee, K.K.. Numerical and field investigation of enhanced in situ denitrification in a shallow-zone well-to-well recirculation system. Ecological Modelling 2009;220(19):2441–2449. doi:10.1016/j.ecolmodel.2009.06.014.

van der Lee, J., Windt, L.D.. Present state and future directions of modeling of geochemistry in hydrogeological systems. Journal of Contaminant Hydrology 2001;47(2–4):265 – 282. doi:10.1016/S0169-7722(00)00155-8.

van der Lee, J., Windt, L.D., Lagneau, V., Goblet, P.. Module-oriented modeling of reactive transport with HYTEC. Computers & Geosciences 2003;29(3):265 – 275. doi:10.1016/S0098-3004(03)00004-9.

van Leer, B.. Towards the ultimate conservative difference scheme. V. A second-order sequel to Godunov's method. Journal of Computational Physics 1979;32(1):101–136. doi:10.1016/0021-9991(79)90145-1.

Lenhard, R., Oostrom, M., White, M.. Modeling fluid flow and transport in variably saturated porous media with the STOMP simulator. 2. verification and validation exercises. Advances in Water Resources 1995;18(6):365 – 373. doi:10.1016/0309-1708(95)00019-F.

LeVeque, R.J.. Numerical Methods for Conservation Laws. Basel: Birkhäuser Basel, 1990. doi:10.1007/978-3-0348-5116-9.

LeVeque, R.J.. Finite Volume Methods for Hyperbolic Problems. Cambridge University Press, 2002. doi:10.1017/CBO9780511791253.

Liang, Y., Bradford, S.A., Šimůnek, J., Heggen, M., Vereecken, H., Klumpp, E.. Retention and remobilization of stabilized silver nanoparticles in an undisturbed loamy sand soil. Environmental science & technology 2013a;47(21):12229 – 12237. doi:10.1021/es402046u.

Liang, Y., Bradford, S.A., Šimůnek, J., Vereecken, H., Klumpp, E.. Sensitivity of the transport and retention of stabilized silver nanoparticles to physicochemical factors. Water Research 2013b;47(7):2572 – 2582. doi:10.1016/j.watres.2013.02.025.

Lichtner, P.. Multiphase multicomponent nonisothermal reactive transport in partially saturated porous media. In: Proceedings of the 1996 international conference on deep geological disposal of radioactive waste. ACM; 1996. p. 133–142.

Lichtner, P., Steefel, C., Oelkers, E.. Reactive transport in porous media. Reviews in mineralogy. Mineralogical Society of America, 1996.

Lichtner, P.C., Hammond, G.E., Lu, C., Karra, S., Bisht, G., Andre, B., Mills, R.T., Kumar, J.. PFLOTRAN User Manual. Technical Report; 2013a.

Lichtner, P.C., Hammond, G.E., Lu, C., Karra, S., Bisht, G., Andre, B., Mills, R.T., Kumar, J.. PFLOTRAN Web page. 2013b. Http://www.pflotran.org.

Lide, D., editor. CRC handbook of chemistry and physics. 89th ed. Boca Raton, Fla., London: CRC Press, 2008.

Liu, J., Ewing, R.. An operator splitting method for nonlinear reactive transport equations and its implementation based on dll and com. In: Zhang, W., Tong, W., Chen, Z., Glowinski, R., editors. Current Trends in High Performance Computing and Its Applications. Springer Berlin Heidelberg; 2005. p. 93–102. doi:10.1007/3-540-27912-1_9.

Liu, X.D., Osher, S., Chan, T.. Weighted essentially non-oscillatory schemes. Journal of Computational Physics 1994;115(1):200 – 212. doi:10.1006/jcph.1994.1187.

Lutterodt, G.. Transport of multiple *Escherichia coli* strains in saturated porous media. CRC Press, 2012. doi:10.1201/b11796.

Madigan, M.T., Martinko, J.M., Stahl, D., Clark, D.P.. Brock Biology of Microorganisms. 13th ed. Benjamin Cummings, 2010.

Maier, U., Grathwohl, P.. Natural attenuation in the unsaturated zone and shallow groundwater: coupled modeling of vapor phase diffusion, biogeochemical processes and transport across the capillary fringe. In: Nützmann, G., Viotti, P., Aagaard, P., editors. Reactive Transport in Soil and Groundwater. Springer Berlin Heidelberg; 2005. p. 141–155. doi:10.1007/3-540-26746-8_10.

Mao, X., Prommer, H., Barry, D., Langevin, C., Panteleit, B., Li, L.. Three-dimensional model for multi-component reactive transport with variable density groundwater flow. Environmental Modelling & Software 2006;21(5):615–628. doi:10.1016/j.envsoft.2004.11.008.

Marsili-Libelli, S.. Parameter estimation of ecological models. Ecological Modelling 1992;62(4):233–258. doi:10.1016/0304-3800(92)90001-U.

Mayer, A.S., Miller, C.T.. The influence of mass transfer characteristics and porous media heterogeneity on nonaqueous phase dissolution. Water Resources Research 1996;32(6):1551–1567. doi:10.1029/96WR00291.

Mayer, K.U., Frind, E.O., Blowes, D.W.. Multicomponent reactive transport modeling in variably saturated porous media using a generalized formulation for kinetically controlled reactions. Water Resources Research 2002;38(9):13–1–13–21. doi:10.1029/2001WR000862.

Meeussen, J.C.L.. Orchestra: An object-oriented framework for implementing chemical equilibrium models. Environmental Science & Technology 2003;37(6):1175–1182. doi:10.1021/es025597s.

Mikyška, J., Firoozabadi, A.. Implementation of higher-order methods for robust and efficient compositional simulation. Journal of Computational Physics 2010;229(8):2898–2913. doi:10.1016/j.jcp.2009.12.022.

Miller, C.T., Christakos, G., Imhoff, P.T., McBride, J.F., Pedit, J.A., Trangenstein, J.A.. Multiphase flow and transport modeling in heterogeneous porous media: challenges and approaches. Advances in Water Resources 1998;21(2):77 – 120. doi:10.1016/S0309-1708(96)00036-X.

Miller, C.T., Rabideau, A.J.. Development of split-operator, petrov-galerkin methods to simulate transport and diffusion problems. Water Resources Research 1993;29(7):2227–2240. doi:10.1029/93WR00528.

Molenaar, J.. Multigrid Methods For Fully Implicit Oil Reservoir Simulation. Technical Report; Proceedings Copper Mountain Conference on Multigrid Methods; 1995.

Molins, S., Mayer, K.U.. Coupling between geochemical reactions and multicomponent gas and solute transport in unsaturated media: A reactive transport modeling study. Water Resources Research 2007;43(5):n/a–n/a. doi:10.1029/2006WR005206.

Monod, J.. The growth of bacterial cultures. Annual Reviews in Microbiology 1949;(Xl).

Morshed, J., Kaluarachchi, J.J.. Critical assessment of the operator-splitting technique in solving the advection-dispersion-reaction equation: 2. Monod kinetics and coupled transport. Advances in Water Resources 1995;18(2):101–110. doi:10.1016/0309-1708(95)00002-Z.

Moré, J.J.. The Levenberg-Marquardt algorithm: Implementation and theory. In: Watson, G., editor. Numerical Analysis. Springer Berlin Heidelberg; volume 630 of *Lecture Notes in Mathematics*; 1978. p. 105–116. doi:10.1007/BFb0067700.

Moser, H.. The dynamics of bacterial populations maintained in the chemostat. Carnegie Institution of Washington Washington, 1958.

Mulder, W., Meyling, R.G.. Numerical simulation of two-phase flow using locally refined grids in three space dimensions. SPE Advanced Technology Series 1993;1(01). doi:10.2118/21230-PA.

Neumann, R.. Two-Phase Compositional Flow Simulation with Persistent Variables. Ph.D. thesis; University of Heidelberg; 2015.

Neumann, R., Bastian, P., Ippisch, O.. Modeling and simulation of two-phase two-component flow with disappearing nonwetting phase. Computational Geosciences 2013;17(1):139–149. doi:10.1007/s10596-012-9321-3.

Niessner, J.. The role of interfacial area in two-phase flow in porous media: bridging scales and coupling models. Südwestdeutscher Verlag für Hochschulschriften, 2011.

Or, D., Smets, B., Wraith, J., Dechesne, A., Friedman, S.. Physical constraints affecting bacterial habitats and activity in unsaturated porous media - a review. Advances in Water Resources 2007;30(6-7):1505–1527. doi:10.1016/j.advwatres.2006.05.025.

Osher, S., Tadmor, E., for Computer Applications in Science, I., Engineering, . On the Convergence of Difference Approximations to Scalar Conservation Laws. Number Bd. 172614 in ICASE report. Institute for Computer Applications in Science and Engineering, NASA Langley Research Center, 1985.

Paege, L., Gibbs, M.. Anaerobic dissimilation of glucose-C14 by Escherichia coli. Journal of bacteriology 1961;:107–110.

Pareschi, L., Russo, G.. Recent trends in numerical analysis. In: Trigiante, D., editor. Implicit-explicit Runge-Kutta Schemes for Stiff Systems of Differential Equations. Commack, NY, USA: Nova Science Publishers, Inc.; 2000. p. 269–288.

Pareschi, L., Russo, G.. Implicit–Explicit Runge–Kutta Schemes and Applications to Hyperbolic Systems with Relaxation. Journal of Scientific Computing 2005;25(1):129–155. doi:10.1007/s10915-004-4636-4. arXiv:1009.2757.

Parkhurst, D.L., Appelo, C.A.J.. Description of input and examples for PHREEQC version 3–A computer program for speciation, batch-reaction, one-dimensional transport, and inverse geochemical calculations; 2013. p. 497.

Patankar, S.. Numerical Heat Transfer and Fluid Flow. Series in computational methods in mechanics and thermal sciences. Taylor & Francis, 1980.

Peaceman, D.. Fundamentals of Numerical Reservoir Simulation. Developments in Petroleum Science. Elsevier, 1977.

Pietro, D.A.D., Ern, A.. Mathematical Aspects of Discontinuous Galerkin Methods. Springer-Verlag Berlin Heidelberg, 2012.

Podgorney, R., Huang, H., Plummer, M., Gaston, D.. A globally-implicit computational framework for physics-based simulation of coupled thermal-hydro-mechanical problems: Application to sustainability of geothermal reservoirs. Orkustofnun (National Energy Authority); 2012.

Polívka, O., Mikyška, J.. Compositional modeling in porous media using constant volume flash and flux computation without the need for phase identification. Journal of Computational Physics 2014;272(0):149 – 169. doi:10.1016/j.jcp.2014.04.029.

Porter, M.L., Wildenschild, D., Grant, G., Gerhard, J.I.. Measurement and prediction of the relationship between capillary pressure, saturation, and interfacial area in a napl-water-glass bead system. Water Resources Research 2010;46(8). doi:10.1029/2009WR007786.

Powell, E., Evans, C., Strange, E., Tempest, D.. Microbial physiology and continuous culture. London: HMSO, 1967.

Powelson, D.K., Mills, A.L.. Transport of *Escherichia coli* in Sand Columns with Constant and Changing Water Contents. Journal of Environmental Quality 2001;30(1):238–245. doi:10.2134/jeq2001.301238x.

Prommer, H., Barry, D., Zheng, C.. MODFLOW/MT3DMS-Based Reactive Multicomponent Transport Modeling. Ground Water 2003;41(2):247–257. doi:10.1111/j.1745-6584.2003.tb02588.x.

Quezada, C.R., Clement, T., Lee, K.K.. Generalized solution to multi-dimensional multi-species transport equations coupled with a first-order reaction network involving distinct retardation factors. Advances in Water Resources 2004;27(5):507 – 520. doi:10.1016/j.advwatres.2004.02.013.

Reeves, H., Kirkner, D.J.. Multicomponent mass transport with homogeneous and heterogeneous chemical reactions: Effect of the chemistry on the choice of numerical algorithm: 2. numerical results. Water Resources Research 1988;24(10):1730–1739. doi:10.1029/WR024i010p01730.

Reeves, H.W., Abriola, L.M.. An iterative compositional model for subsurface multiphase flow. Journal of Contaminant Hydrology 1994;15(4):249 – 276. doi:10.1016/0169-7722(94)90030-2.

Reeves, P.C., Celia, M.a.. A Functional Relationship Between Capillary Pressure, Saturation, and Interfacial Area as Revealed by a Pore-Scale Network Model. Water Resources Research 1996;32(8):2345–2358. doi:10.1029/96WR01105.

Rehfeldt, S., Stichlmair, J.. Measurement and calculation of multicomponent diffusion coefficients in liquids. Fluid Phase Equilibria 2007;256(1-2):99–104. doi:10.1016/j.fluid.2006.10.008.

Reiling, H., Laurila, H., Fiechter, a.. Mass culture of Escherichia coli: Medium development for low and high density cultivation of Escherichia coli B/r in minimal and complex media. Journal of Biotechnology 1985;2(3-4):191–206. doi:10.1016/0168-1656(85)90038-0.

Reischke, S., Rousk, J., Bååth, E.. The effects of glucose loading rates on bacterial and fungal growth in soil. Soil Biology and Biochemistry 2013;70:88–95. doi:10.1016/j.soilbio.2013.12.011.

Richards, L.A.. Capillary conduction of liquids through porous mediums. Journal of Applied Physics 1931;1(5):318–333. doi:10.1063/1.1745010.

Richter, O., Söndgerath, D.. Parameter estimation in ecology: the link between data and models. Weinheim, Germany: VCH Verlangsgesellschaft, 1990.

Risebro, N., Tveito, A.. Front tracking applied to a nonstrictly hyperbolic system of conservation laws. SIAM Journal on Scientific and Statistical Computing 1991;12(6):1401–1419. doi:10.1137/0912076.

Rockhold, M., Yarwood, R., Niemet, M., Bottomley, P., Selker, J.. Considerations for modeling bacterial-induced changes in hydraulic properties of variably saturated porous media. Advances in Water Resources 2002;25(5):477 – 495. doi:10.1016/S0309-1708(02)00023-4.

Rockhold, M.L., Yarwood, R.R., Niemet, M.R., Bottomley, P.J., Brockman, F.J., Selker, J.S.. Visualization and modeling of the colonization dynamics of a bioluminescent bacterium in variably saturated, translucent quartz sand. Advances in Water Resources 2007;30(6-7):1593–1607. doi:10.1016/j.advwatres.2006.05.026.

Roe, P.L.. Characteristic-Based Schemes for the Euler Equations. Annual Review of Fluid Mechanics 1986;18(1):337–365. doi:10.1146/annurev.fl.18.010186.002005.

Ropp, D.L., Shadid, J.N.. Stability of operator splitting methods for systems with indefinite operators: reaction-diffusion systems. Journal of Computational Physics 2005;203(2):449 – 466. doi:10.1016/j.jcp.2004.09.004.

Rubin, J.. Transport of reacting solutes in porous media: Relation between mathematical nature of problem formulation and chemical nature of reactions. Water Resources Research 1983;19(5):1231–1252. doi:10.1029/WR019i005p01231.

Saaltink, M., Pifarré, F., Ayora, C.. RETRASO, a code for modeling reactive transport in saturated and unsaturated porous media. Geologica Acta 2004;2(3):235–251.

Saaltink, M.W., Ayora, C., Carrera, J.. A mathematical formulation for reactive transport that eliminates mineral concentrations. Water Resources Research 1998;34(7):1649–1656. doi:10.1029/98WR00552.

Saaltink, M.W., Carrera, J., Ayora, C.. On the behavior of approaches to simulate reactive transport. Journal of Contaminant Hydrology 2001;48(3-4):213–235. doi:10.1016/S0169-7722(00)00172-8.

Samper, J., Xu, T., Yang, C.. A sequential partly iterative approach for multicomponent reactive transport with core2d. Computational Geosciences 2009;13(3):301–316. doi:10.1007/s10596-008-9119-5.

Samper, J., Zhang, G.. Coupled microbial and geochemical reactive transport models in porous media: Formulation and Application to Synthetic and In Situ Experiments. Journal of Iberian Geology 2006;32(2):215–231.

Sander, R.. Modeling atmospheric chemistry: Interactions between gas-phase species and liquid cloud/aerosol particles. Surveys in Geophysics 1999;20(1):1–31. doi:10.1023/A:1006501706704.

Schäfer, A., Ustohal, P., Harms, H.. Transport of bacteria in unsaturated porous media. Journal of Contaminant Hydrology 1998a;33(1-2):149–169.

Schäfer, D., Schäfer, W., Kinzelbach, W.. Simulation of reactive processes related to biodegradation in aquifers: 1. Structure of the three-dimensional reactive transport model. Journal of Contaminant Hydrology 1998b;31(1-2):167–186. doi:10.1016/S0169-7722(97)00060-0.

Schäfer, D., Schäfer, W., Kinzelbach, W.. Simulation of reactive processes related to biodegradation in aquifers: 2. Model application to a column study on organic carbon degradation. Journal of Contaminant Hydrology 1998c;31(1-2):187–209. doi:10.1016/S0169-7722(97)00061-2.

Seber, G., Wild, C.. Nonlinear regression. Wiley series in probability and statistics. Hoboken, NJ: Wiley-Interscience, 2003.

Senn, H., Lendenmann, U., Snozzi, M., Hamer, G., Egli, T.. The growth of Escherichia coli in glucose-limited chemostat cultures: a re-examination of the kinetics. Biochimica et Biophysica Acta (BBA) - General Subjects 1994;1201(3):424–436. doi:10.1016/0304-4165(94)90072-8.

Shu, C.W.. Total-variation-diminishing time discretizations. SIAM Journal on Scientific and Statistical Computing 1988;9(6):1073–1084. doi:10.1137/0909073.

Sierra, J., Renault, P.. Oxygen consumption by soil microorganisms as affected by oxygen and carbon dioxide levels. Applied Soil Ecology 1995;2(3):175–184. doi:10.1016/0929-1393(95)00051-L.

Simpson, M.J., Landman, K.A., Clement, T.. Assessment of a non-traditional operator split algorithm for simulation of reactive transport. Mathematics and Computers in Simulation 2005;70(1):44–60. doi:10.1016/j.matcom.2005.03.019.

Skopp, J., Jawson, M., Doran, J.. Steady-state aerobic microbial activity as a function of soil water content. Soil Science Society of America Journal 1990;54(6):1619–25. doi:10.2136/sssaj1990.03615995005400060018x.

Sleep, B.E.. A method of characteristics model for equation of state compositional simulation of organic compounds in groundwater. Journal of Contaminant Hydrology 1995;17(3):189 – 212. doi:10.1016/0169-7722(94)00032-D.

Sleep, B.E., Sykes, J.F.. Compositional simulation of groundwater contamination by organic compounds: 1. model development and verification. Water Resources Research 1993;29(6):1697–1708. doi:10.1029/93WR00283.

Steefel, C., Appelo, C., Arora, B., Jacques, D., Kalbacher, T., Kolditz, O., Lagneau, V., Lichtner, P., Mayer, K., Meeussen, J., Molins, S., Moulton, D., Shao, H., Šimůnek, J., Spycher, N., Yabusaki, S., Yeh, G.. Reactive transport codes for subsurface environmental simulation. Computational Geosciences 2014;:1–34doi:10.1007/s10596-014-9443-x.

Steefel, C., Depaolo, D., Lichtner, P.. Reactive transport modeling: An essential tool and a new research approach for the Earth sciences. Earth and Planetary Science Letters 2005;240(3-4):539–558. doi:10.1016/j.epsl.2005.09.017.

Steefel, C., MacQuarrie, K.. Approaches to modeling of reactive transport in porous media. Reviews in Mineralogy 1996;34:83–125.

Steefel, C.I.. CrunchFlow User's Manual; 2008. .

Steefel, C.I., Lasaga, A.C.. A coupled model for transport of multiple chemical species and kinetic precipitation/dissolution reactions with application to reactive flow in single phase hydrothermal systems. American Journal of Science 1994;294(5):529–592. doi:10.2475/ajs.294.5.529.

Stokes, J.. Fermentation of glucose by suspensions of Escherichia coli. Journal of bacteriology 1949;:147–158.

Strang, G.. On the construction and comparison of difference schemes. SIAM Journal on Numerical Analysis 1968;5(3):506–517. doi:10.1137/0705041.

Taylor, S.W., Jaffé, P.R.. Biofilm growth and the related changes in the physical properties of a porous medium: 3. dispersivity and model verification. Water Resources Research 1990;26(9):2171–2180. doi:10.1029/WR026i009p02171.

Tebes-Stevens, C., J. Valocchi, A., VanBriesen, J.M., Rittmann, B.E.. Multicomponent transport with coupled geochemical and microbiological reactions: model description and example simulations. Journal of Hydrology 1998;209(1-4):8–26. doi:10.1016/S0022-1694(98)00104-8.

Torkzaban, S., Bradford, S.A., van Genuchten, M.T., Walker, S.L.. Colloid transport in unsaturated porous media: The role of water content and ionic strength on particle straining. Journal of Contaminant Hydrology 2008;96(1–4):113 – 127. doi:10.1016/j.jconhyd.2007.10.006.

Trevors, J.. Respiratory activity of a genetically engineered Pseudomonas fluorescens strain in soil measured using gas chromatography. Journal of microbiological methods 1991;14:11–20.

Tufenkji, N.. Modeling microbial transport in porous media: Traditional approaches and recent developments. Advances in Water Resources 2007;30(6-7):1455–1469. doi:10.1016/j.advwatres.2006.05.014.

Unc, A., Goss, M.J.. Transport of bacteria from manure and protection of water resources. Applied Soil Ecology 2004;25(1):1–18. doi:10.1016/j.apsoil.2003.08.007.

Valocchi, A.J., Malmstead, M.. Accuracy of operator splitting for advection-dispersion-reaction problems. Water Resources Research 1992;28(5):1471–1476. doi:10.1029/92WR00423.

Valocchi, A.J., Street, R.L., Roberts, P.V.. Transport of ion-exchanging solutes in groundwater: Chromatographic theory and field simulation. Water Resources Research 1981;17(5):1517–1527. doi:10.1029/WR017i005p01517.

Verwer, J., Sommeijer, B., Hundsdorfer, W.. RKC time-stepping for advection–diffusion–reaction problems. Journal of Computational Physics 2004;201(1):61–79. doi:10.1016/j.jcp.2004.05.002.

Vohralík, M.. A posteriori error estimates for lowest-order mixed finite element discretizations of convection-diffusion-reaction equations. SIAM Journal on Numerical Analysis 2007;45(4):1570–1599. doi:10.1137/060653184.

Vohralík, M.. Residual flux-based a posteriori error estimates for finite volume and related locally conservative methods. Numerische Mathematik 2008;111(1):121–158. doi:10.1007/s00211-008-0168-4.

Šimůnek, J., Jacques, D., Langergraber, G., Bradford, S.A., Šejna, M., van Genuchten, M.T.. Numerical modeling of contaminant transport using hydrus and its specialized modules. Journal of the Indian Institute of Science 2013;93(2):265–284. doi:10.1137/0705041.

Šimůnek, J., Suarez, D.L.. Two-dimensional transport model for variably saturated porous media with major ion chemistry. Water Resources Research 1994;30(4):1115–1133. doi:10.1029/93WR03347.

Wagner, C., Schäfer, W., Jäger, W., Wittum, G., Kohlmeier, E.. Simulating a field case of reactive chloroethene transport. Computing and Visualization in Science 2002;5(3):149–163. doi:10.1007/s00791-002-0097-1.

Walker, S.L., Redman, J., Elimelech, M.. Role of Cell Surface Lipopolysaccharides in *Escherichia coli* K12 adhesion and transport. Langmuir 2004;20(18):7736–46. doi:10.1021/la049511f.

Walter, A.L., Frind, E.O., Blowes, D.W., Ptacek, C.J., Molson, J.W.. Modeling of multicomponent reactive transport in groundwater: 1. Model development and evaluation. Water Resources Research 1994;30(11):3137–3148. doi:10.1029/94WR00955.

Wang, H., Dahle., H.K., Ewing, R.E., Espedal, M.S., Sharpley, R.C., Man, S.. An ellam scheme for advection-diffusion equations in two dimensions. SIAM Journal on Scientific Computing 1999;20(6):2160–2194. doi:10.1137/S1064827596309396.

White, M., Oostrom, M.. STOMP, Subsurface Transport Over Multiple Phases, theory guide; 1996. doi:10.2172/658243.

White, M., Oostrom, M., Lenhard, R.. Modeling fluid flow and transport in variably saturated porous media with the STOMP simulator. 1. nonvolatile three-phase model description. Advances in Water Resources 1995;18(6):353 – 364. doi:10.1016/0309-1708(95)00018-E.

Wissmeier, L., Barry, D.. Reactive transport in unsaturated soil: Comprehensive modelling of the dynamic spatial and temporal mass balance of water and chemical components. Advances in Water Resources 2008;31(5):858–875. doi:10.1016/j.advwatres.2008.02.003.

Xu, T., Pruess, K.. Modeling multiphase nonisothermal fluid flow and reactive transport in variably saturated fractured rocks. American Journal of Science 2001;301(1):134–59. doi:10.2475/ajs.301.1.34.

Xu, T., Pruess, K., Brimhall, G.. An improved equilibrium-kinetics speciation algorithm for redox reactions in variably saturated subsurface flow systems. Computers & Geosciences 1999a;25(6):655–666. doi:10.1016/S0098-3004(99)00005-9.

Xu, T., Samper, J., Ayora, C., Manzano, M., Custodio, E.. Modeling of non-isothermal multi-component reactive transport in field scale porous media flow systems. Journal of Hydrology 1999b;214(1-4):144–164. doi:10.1016/S0022-1694(98)00283-2.

Xu, T., Sonnenthal, E., Spycher, N., Pruess, K.. TOUGHREACT—A simulation program for non-isothermal multiphase reactive geochemical transport in variably saturated geologic media: Applications to geothermal injectivity and CO2 geological sequestration. Computers & Geosciences 2006;32(2):145–165. doi:10.1016/j.cageo.2005.06.014.

Xu, T., Sonnenthal, E., Spycher, N., Pruess, K.. TOUGHREACT User's Guide: A Simulation Program for Non-isothermal Multiphase Reactive Geochemical Transport in Variably Saturated Geologic Media, V1. 2.1. Technical Report May; Ernest Orlando Lawrence Berkeley National Laboratory, Berkeley, CA (US); 2008.

Xu, T., Spycher, N., Sonnenthal, E., Zhang, G., Zheng, L., Pruess, K.. TOUGHREACT Version 2.0: A simulator for subsurface reactive transport under non-isothermal multiphase flow conditions. Computers & Geosciences 2011;37(6):763–774. doi:10.1016/j.cageo.2010.10.007.

Yarwood, R.R., Rockhold, M.L., Niemet, M.R., Selker, J.S., Bottomley, P.J.. Impact of microbial growth on water flow and solute transport in unsaturated porous media. Water Resources Research 2006;42(10). doi:10.1029/2005WR004550.

Yeh, G., Tripathi, V.. HYDROGEOCHEM: A coupled model of HYDROlogic transport and GEOCHEMical equilibria in reactive multicomponent systems; 1990. doi:10.2172/6230985.

Yeh, G.T., Tripathi, V.S.. A critical evaluation of recent developments in hydrogeochemical transport models of reactive multichemical components. Water Resources Research 1989;25(1):93–108. doi:10.1029/WR025i001p00093.

Yeh, G.T., Tripathi, V.S.. A Model for Simulating Transport of Reactive Multispecies Components: Model Development and Demonstration. Water Resources Research 1991;27(12):3075–3094. doi:10.1029/91WR02028.

Zhu, C., Hu, F.Q., Burden, D.S.. Multi-component reactive transport modeling of natural attenuation of an acid groundwater plume at a uranium mill tailings site. Journal of Contaminant Hydrology 2001;52(1-4):85–108. doi:10.1016/S0169-7722(01)00154-1.

Zhu, J., Qiu, J., Shu, C.W., Dumbser, M.. Runge–kutta discontinuous galerkin method using WENO limiters ii: Unstructured meshes. Journal of Computational Physics 2008;227(9):4330 – 4353. doi:10.1016/j.jcp.2007.12.024.